The Role of Anisotropy in Artificial Polymerization Motors

Luis C. Pantaleone

Stellingen

Accompanying the PhD thesis

The Role of Anisotropy in Artificial Polymerization Motors

by

Luis C. Pantaleone

1. The vast majority of the scientific literature is based on research funded by public money. The primary source of revenue for scientific journals comes from subscription fees paid by public institutions. The only explanation for taxpayers' failure to dictate their own conditions in the publishing sector is lobbying, since governments ultimately control both the supply and demand of scientific knowledge.

2. Experimental design is like a chess game: studying the playbook will benefit your opening, but in the uncharted territory of the middle game, there is a need for creative solutions.

3. In the supramolecular community crystallinity is often perceived as a discrete property, which is not. Rather than classifying materials, we should focus on describing their dynamics, anisotropy, presence of defects, being aware that we are dealing with continuous parameters.

4. The difference between "pathway complexity" and "reproducibility problems" is a detailed description of our methods for sample preparation.

5. In the traditional approach, molecular self-assembly is controlled by the structure and reactivity of its building blocks. Perhaps it is time to shift our focus to how self-assembled structures can influence the chemical reactivity of their molecular components.

6. Interdisciplinary research requires navigating outside one's field of expertise. The key to overcoming this challenge is to engage in scientific discussions with specialists, not being afraid to reach out and foster collaboration. It is also important to remember your own contribution: not everyone is trained to bridge diverse scientific disciplines.

652563-L-st-Pantaleone

Processed on: 5-9-2024

University of Groningen

The role of anisotropy in artificial polymerization motors

L.C. Pantaleone

university of groningen / faculty of science and engineering / stratingh institute for chemistry

The work described in this thesis was performed at the Stratingh Institute for Chemistry, the University of Groningen, The Netherlands.

This work was financially supported by:

The European Research Council (ERC Consolidator Grant, MechanoTubes, 819075)

The Netherlands Organization for Scientific Research (NWO)

The Dutch Ministry of Education, Culture and Science (Gravitation Program 024.001.035).

Cover design by Pedro Pantaleone (www.studio-method.xyz), representing the "self-assembly" of architectural elements into the Martinitoren of Groningen.

Printed by Ipskamp Printing B.V., Enschede, The Netherlands

university of groningen

The role of anisotropy in artificial polymerization motors

PhD thesis

to obtain the degree of PhD at the
University of Groningen
on the authority of the
Rector Magnificus Prof. J.M.A. Scherpen
and in accordance with
the decision by the College of Deans.

This thesis will be defended in public on

Tuesday 1 October 2024 at 12.45 hours

by

Luis Claudio Pantaleone

born on 7 November 1994
in Rome, Italy

Supervisors

Prof. T. Kudernác
Prof. W.R. Browne

Assessment Committee

Prof. B.L. Feringa
Prof. C. Mayer
Prof. T.M. Hermans

Table of contents

"Knowledge forbidden?
Suspicious, reasonless. Why should their Lord
Envy them that? Can it be a sin to know?
Can it be death?"

—John Milton, Paradise Lost

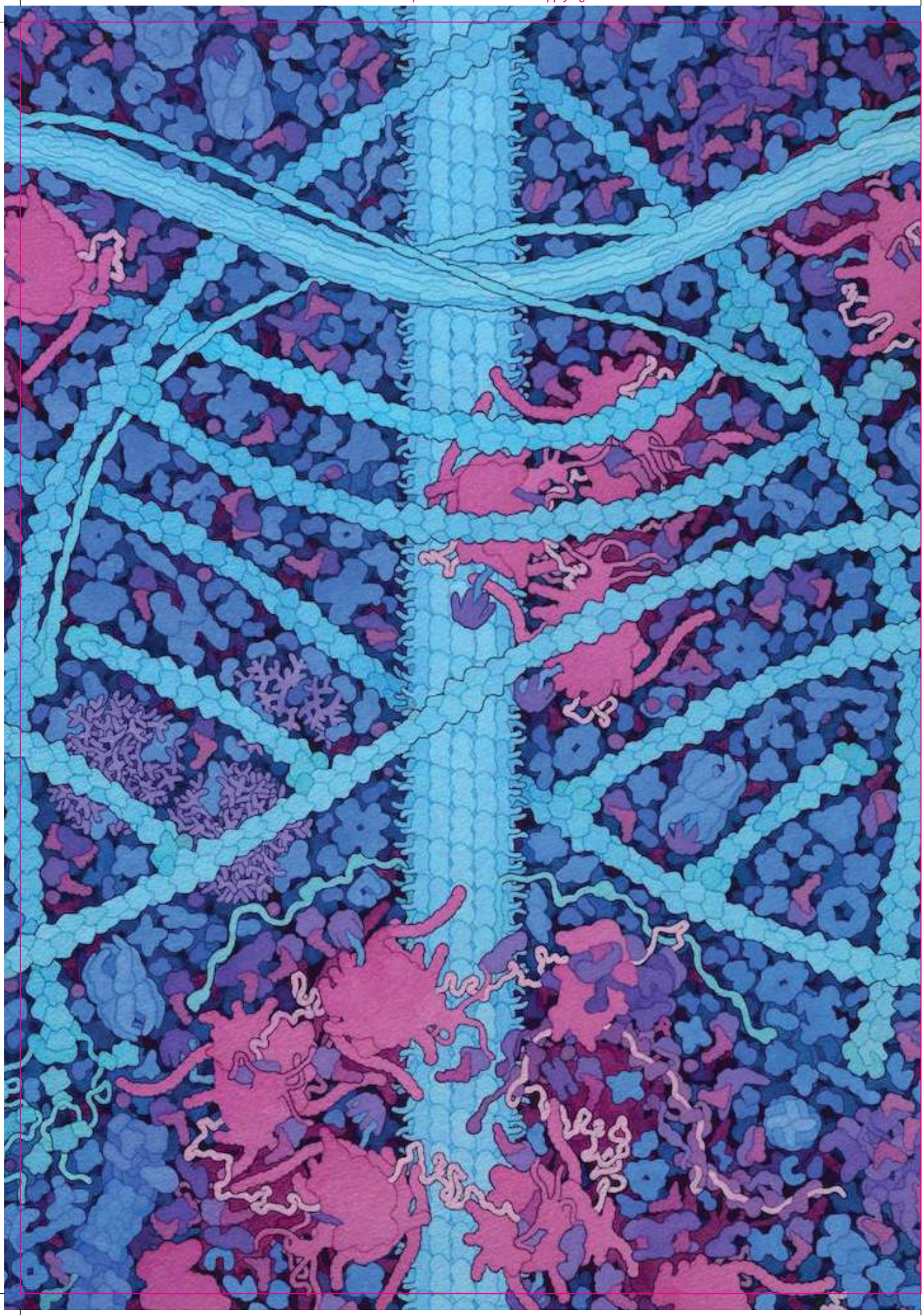

1

Artificial Polymerization Motors

ABSTRACT:

Artificial molecular machines have the potential to become a core part of nanotechnology. However, a wide gap in length scales remains unaccounted for, between the operation of these molecules in solution, where their individual mechanical action is randomly dispersed in the Brownian storm, and on the other hand their action at the macroscopic level, e.g., in polymer networks and crystals. Bridging this gap, requires chemo-mechanical transduction strategies that will allow dynamic molecules to perform a range of unprecedented tasks, e.g. by generating strong directional forces at the nanoscale and in fluid environment. Showing the way for synthetic systems, biological machinery has emerged from the pool of dynamic biomolecules operating in fluid environment. The key strategy that nature uses to overcome the Brownian storm and perform useful mechanical work is to connect the dynamics of individual biomolecular building blocks with the self-assembly processes. Such molecular machineries operating at the level of the self-assembly processes are known as polymerisation and depolymerisation motors. Developing synthetic mechanically active molecular systems that operate on the same principles constitutes the next major challenge in the field of artificial molecular machines. In this chapter, we discuss conceptual aspects of using self-assembly processes to generate mechanical force, operation of biological polymerisation and depolymerisation motors and initial steps undertaken towards developing mechanically active synthetic supramolecular systems.

L.C. Pantaleone†, N. Cissé†, Q. Huang†, T. Kudernac*; *manuscript in preparation.*

1.1. Biopolymerization motors

1.1.1 Outlook

All motion in living organisms emerges from the cooperative action of dynamic molecules that work together to transform chemical energy into ordered activity. Inspired by such biomolecular machineries, chemists have moved from synthesizing static molecular structures to the design and synthesis of dynamic molecules such as pincers, [1] motors,[2] pumps,[3,4] and switches[5] that display controlled mechanical function with an ever increasing degree of sophistication,[6] and in a few instances, even directional motion.[7] Yet, interfacing the operation of molecular motors and switches with complex systems remains a key challenge. Arguably, one major issue is with harnessing any mechanically-purposeful molecular motion against the Brownian storm, which is a few orders of magnitude larger in energy than any mechanical action produced by small dynamic molecules.

Biological molecular machinery operates within larger supramolecular assemblies using out-of-equilibrium self-assembly processes, to circumvent these fundamental limitations and generate strong directional forces in a fluid environment. The most notable of these biomolecular machines that operate under these principles are cellular microtubules and actin filaments.[8] Through their supramolecular polymerisation and depolymerization, they are capable of generating pushing and pulling forces and perform useful mechanical tasks at the level of individual fibres or at the level of crosslinked polymer networks. As the generation of force originates in the processes of supramolecular polymerization or depolymerization these types of machines are also called polymerization and depolymerization motors.

The operation of these biological machineries is a versatile tool in biomechanics, supporting life-essential tasks such as motion (e.g., propelling bacterial pathogens in a host's cytoplasm) and morphogenesis (e.g., driving chromosome segregation during mitosis).[9,10] Certainly, among the possible mechanisms to achieve chemo-mechanical transduction, exploiting self-assembly processes is not the only strategy for harnessing the mechanical action of molecular motors and switches. The potential of artificial molecular machinery operating at the level of a condensed system has already been shown in numerous examples. Controlled molecular motion is successfully applied in rotating liquid crystal films and vortices[11,12], shape morphing liquid crystal elastomers,[13] swellable hydrogels and in bending crystals.[14] However, these strategies have limitations, particularly in addressing the challenge of performing mechanical work in fluids amidst Brownian motion and a constant flux of building blocks. In contrast, re-

engineering biological principles of force generation via supramolecular polymerization and depolymerization represents a relatively unexplored domain. This approach shows potential for opening new opportunities and applications in nanotechnology, enabling directional motion and transport of nano-objects, as well as shape-changing and splitting of artificial formations.

1.1.2 Microtubules

All polymerization motors share common features in their mechanism of energy transduction. Examining the assembling properties of cytoskeletal proteins like tubulin or actin we find a similar chain of molecular events that defines their chemo-mechanical cycle. In the process of self-assembly of microtubules, tubulin dimers are linked in a head-to-tail conformation, growing 13 parallel protofilaments which are joined in a tubular structure. The growth of these structures is highly directional; microtubules are nucleated from γ-tubulin which is found in microtubule organizing centre (MTOC) or centrosomes.[15] Once the nanofibres are formed, microtubules continuously switch from polymerization to depolymerization mode, this phenomenon is called dynamic instability.[16] Polymerization is fuelled by guanosine triphosphate (GTP). GTP binds to the tubulin subunits and induces a conformational change that favours binding to the growing end of the microtubule. Shortly after incorporation of the tubulin subunit, the GTP is hydrolysed into GDP and the tubulin undergoes another conformational change that builds up strain energy in the microtubule structure. Continuous addition of GTP bound tubulin prevents the microtubule from disassembling by forming a GTP rich cap. When the fuel is totally consumed, and the GTP cap is lost by hydrolysis, the microtubule depolymerizes rapidly in a process known as "catastrophe".[17]

1.1.3 Actin fibres

A similar interplay between monomer reactivity in self-assembly regulates the dynamics of actin-based assemblies. Actin filaments are linear supramolecular polymers composed of two strands forming a 7 nm wide double helix. Like microtubules, the ends of the actin filaments have different dynamics, thus they are polarized (Figure 1). The fast growing end is termed the barbed end and the slow growing end is termed the pointed end.[18] The pointed end has a critical actin concentration that is 6 times higher than the barbed end, respectively 0.6 and 0.1 μM.[19] When the monomeric actin concentration lies between these two values, only the barbed end grows and the pointed end shrinks, a phenomenon known as treadmilling (Figure 1).[20] As with microtubules, the kinetics of actin assembly is controlled by the nucleation step, consisting of the formation of actin dimers and trimers. In cells, nucleation is regulated by actin-nucleating proteins that

mimic or stabilize actin oligomers. Another recurring feature is that the growth of actin filaments is also fuelled by a chemical reaction, in this case with ATP. Only an ATP-bound actin monomer can add to the barbed end, and after addition, actin catalyses the hydrolysis of the bound ATP into ADP. Actin filaments are less rigid than microtubules and can adopt diverse architectures such as bundles or branched networks, with diverse mechanical functions. Both bundling and branching of actin filaments into a network is mediated by specialized proteins such as fascin or the Arp2/3 complex.[21]

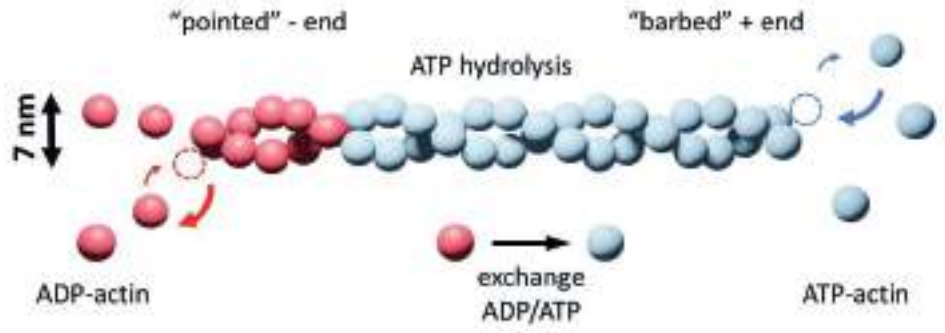

Figure 1: Treadmilling mechanism of an actin based polymerization motor

1.2. Theoretical models of force exertion

Supramolecular polymerization and depolymerization motors can generate mechanical forces using the available chemical potential, and in the attempt to explain the mechanisms of energy transduction three main theoretical models were proposed in the literature.[22] In this section we will discuss the theoretical framework of these models.

1.2.1 Brownian ratcheting during polymerization

The mechanism of Brownian ratcheting behind the generation of pushing force during microtubule growth has been widely accepted. When a load interacts with the polymerizing end of a microtubule the thermal energy of the fluid fuels the random motion of the microscopic cargo (Figure 2a). The free energy of polymerization (self-assembly) is used to rectify the Brownian motion of the load giving it a sense of directionality.[23] In an ideal scenario, consider that the Brownian fluctuation of the cargo would be directed against

a load force (F) and that this movement generates a displacement from the growing tip that allows for monomer insertion.[22] The rate of tubulin growth under this load force can be expressed as:

$$v(F) = d(k_{on}(F) \cdot c - k_{off}(F))$$

where d = 8 nm/13 is the increment of microtubule length per tubulin dimer addition; $k_{on}(F)$, $k_{off}(F)$ are the tubulin on- and off-rate constants. According to experimental observations, the k_{off} rate constant does not depend on the load force, which is consistent with modelling of growing microtubules as Brownian ratchets.[24] Subsequent reinterpretations of this basic model were focused on elucidating the implications of previously unaccounted flexibility of fibres,[25] and the distribution of load force among protofilaments in the mechanism of elongation.[26] In addition, analogue Brownian ratcheting models were also developed to interpret the force production of actin polymers grown against microfabricated barriers.[27]

1.2.2 Hill's biased diffusion

Regarding the exertion of pulling forces during the depolymerization step, the analysis of the thermodynamics is much more controversial, with two distinct models being used to describe the process of catastrophe. The two models are known as Hill's biased diffusion and the conformational wave model.[28] The major reason behind this division in the interpretations is that modelling is complicated by the role of the coupling devices that maintain the contact between microtubules and the cargo during the conversion of free energy of depolymerization into force. In the original theory introduced by Hill the cargo is modelled as a "sleeve" with multiple tubulin binding sites on its inner surface, representing the multivalent binding between kinetochore proteins and microtubules (Figure 2b).[29,30] The position of the cargo with respect to the microtubule can change due to thermal fluctuations, and its diffusion is controlled by the strength of the multivalent interaction. Each interaction between the microtubule and the cargo's binding sites reduces the free energy of the system. During depolymerization, the loss of tubulin subunits shortens the microtubule, shifting its tip out of the sleeve-cargo. In a partially inserted microtubule, the cargo will experience a pulling force so as to occupy all the binding sites and minimize the free energy.

1.2.3 Conformational wave model

The conformational wave model, on the other hand, was based on the observation that the disassembly mechanism of microtubules proceeds via

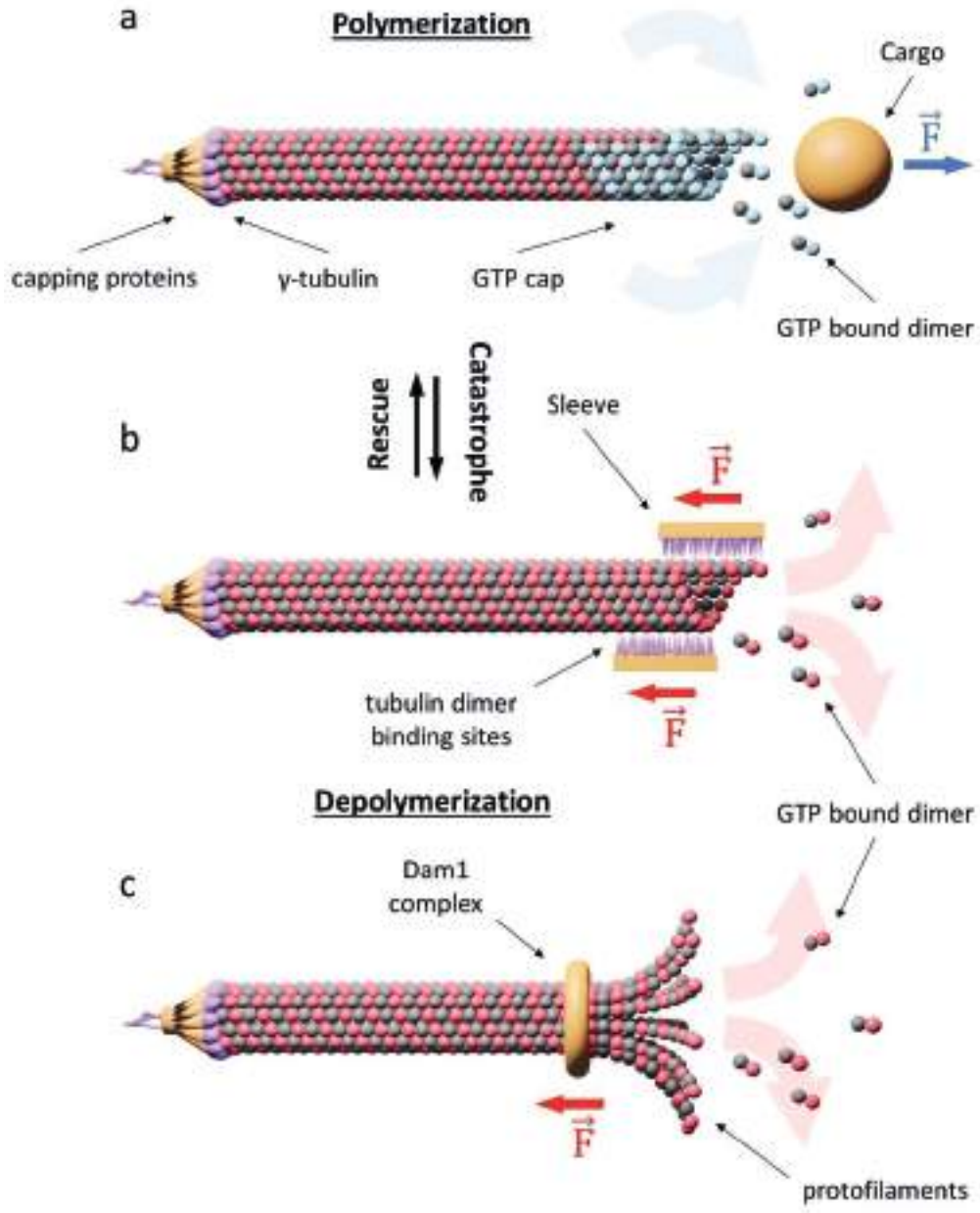

*Figure 2: (**a**) Microtubule polymerization exerting pushing force on a cargo via Brownian ratcheting mechanism. (**b**) Microtubule depolymerization and mechanism of pulling according to the Hill's biased diffusion model. (**c**) Microtubule depolymerization and mechanism of pulling according to the conformational wave model.*

the outward curling of the protofilaments.[31] In this model the cargo is represented by a cylindrical collar which is directly pushed by the bending motion of the protofilaments, sliding towards the microtubule minus end. In this mechanism the conformational change of individual tubulin subunits converts the energy from GTP hydrolysis into elastic strain stored in the microtubule lattice. Rather than rectifying the Brownian motion of the cargo the free energy is directly converted into the motion.[32] According to this model, often associated with the controversial concept of the power stroke,[33] the conformational change can displace a load, as a result of the build-up of supramolecular strain, as long as the free energy drop during this event is quantitatively in the same range as the thermal energy (Figure 2c).[34]

The structure of coupling devices anchoring the load to the polymerization motors largely influenced the discussion on force production during depolymerization.[28] While the biased diffusion model represents a more generalizable mechanism, with the dynamics of multivalent interactions as the only essential requirement, the discovery of ring-shaped kinetochore-associated proteins, such as the Dam1 complex, supported the conformational wave mechanism.[22] Comparing the theoretical analyses, its seems that that conformational wave has more potential in terms of force generating capacity but on the other hand not all of kinetochore-coupled proteins present a structure which is relatable to the cylindrical collar hypothesis.[28,35] In principle, the two mechanisms do not mutually exclude each other and in this broad discussion there was space for mixed models. For example, biased diffusion and "forced walk", a conformational wave oriented model, where described as two mechanistic extremes of the same continuous relationship which depends on the strength of the interaction between Dam1 complex and microtubules.[22]

1.2.4 The role of force spectroscopy

The discussion on these Brownian ratcheting models has been inspired, validated, and often challenged by the work of experimentalists. Among the various investigative techniques, force spectroscopy has made the most significant contribution to our understanding of this field. Before the development of force spectroscopy, studying the operation of biopolymerization motors was limited to indirect methods, such as observing the effects of mechanical work through compartment deformation,[36,37] the buckling of growing fibres,[38] or the energetically uphill movements required for repositioning chromosomes.[31] Force spectroscopy has since played a crucial role in advancing our understanding of this machinery.
The advantages of these measurements, based on optical tweezers or atomic force microscopy (AFM) techniques, are numerous. Time resolved force data provided

a direct evidence of mechanical work and opened the way to quantitative analysis.[39] In addition, in the case of optical tweezers their use as micro manipulators expanded the scope of experimental design for in vitro and in vivo studies.[40] The type of information that can be extracted by the analysis of force traces provide fundamental clues on how energy is supplied by those systems such as the maximal force exerted,[41-43] the influence of load force and loading rates,[44-46] or the effect of the coupling devices on the efficiency of the energy transduction.[43,47-50] As synthetic chemists interested in developing artificial analogues for polymerization motors, we should familiarize ourselves with these techniques and be aware of the standards used for characterizing these systems in biophysics.

1.3. Design of artificial polymerization motors

1.3.1 Design principles

The insights into the operation of biological polymerization and depolymerisation machineries reveal four key challenges on the way towards developing sophisticated synthetic supramolecular systems with similar mechanical function. Firstly, achieving regimes of molecular **self-assembly driven by external fuelling** requires pre-programming the structural changes of its building blocks. This can include conformational and/or configurational switching, modification of the charged character of the molecules or reversible chemical modifications. Any self-assembling system with such fuelled processive behaviour has a potential to generate pushing forces via Brownian ratcheting provided the stiffness of the structures formed is sufficient enough.

The second major challenge in this field is to develop regulatory mechanisms that allow for **spatial and temporal control** over the self-assembly process. This function, which is normally performed by specialized proteins that initiate the assembly of microtubules and actin filaments, is crucial to achieve an efficient mass/energy transfer during the polymerization.

The third requirement for measuring the forces produced by these nanometric assemblies consists in engineering microscopic loads such as vesicles, beads, droplets, as well as coupling devices that can **process the mechanical work** into motion or mechanical deformations.

Lastly, a fundamental aspect in both Brownian ratcheting and conformational wave models is the **transfer of the directionality** from supramolecular structure to the motion or deformation of the load during the energy transduction process.

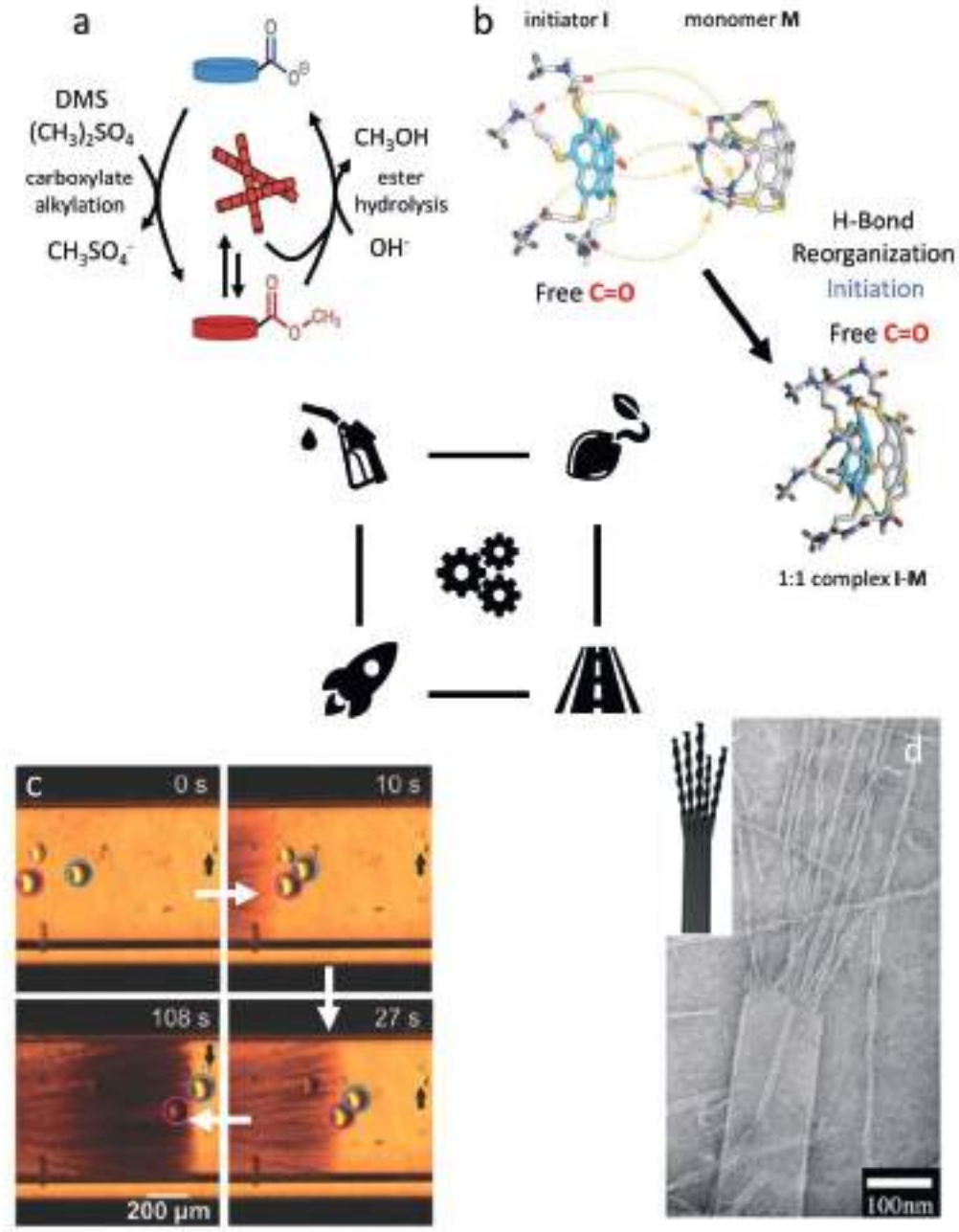

*Figure 3: Design principles for an artificial polymerization motor. (**a**) Self-assembling system where polymerization is driven by the external fuelling with a methylating agent (adapted with permission from ref. [54]). (**b**) Addition of initiator controls the kinetic of supramolecular polymerization through nucleation of corannulene-based fibres (adapted with permission from ref. [63]). (**c**) Processing mechanical work produced by the microcrystallization of peptides for directional transport of submillimetre polymer particles (adapted with permission from ref. [72]). (**d**) Self-assembling peptidic amphiphiles forming a hierarchically structured material, reminiscent of microtubules sub-organization into protofilaments (adapted with permission from ref. [81]).*

1.3.2 Dissipative self-assembly

These challenges have been in part addressed by supramolecular polymers, with synthetic systems being already capable of reproducing some of the basic principles behind the chemo-mechanics of natural polymerization motors. For example, the interest in dissipative self-assembly contributed to a rich literature on systems whose self-assembly is controlled by the addition of external fuels (Figure 3a). Several types of reactions were employed to transiently alter supramolecular interactions between building blocks, ranging from simple (de)protonation of monomer residues[51,52] to more complex chemical conversions involving methylating agents,[53-55] activation with carbodiimides,[56-58] or reducing agents,[59] and some systems were even fuelled by light.[60]

1.3.3 Nucleation strategies

Regarding the introduction of initiation mechanisms that could replicate the seeded supramolecular polymerization of actin and tubulin, growing attention has been paid to supramolecular polymers that have a reminiscent nucleation-elongation assembly behaviour. The most common strategy to introduce cooperativity in supramolecular polymerizations is based on designs where molecules are trapped in the monomeric state by a kinetic barrier.[61] The presence of seeds is then used to catalyse the process of monomer activation for example by interconverting intramolecular to intermolecular hydrogen bonding (Figure 3b).[62,63] In other cases, the activation consist in a conformational change that can reorganize π-π interactions between monomers and drive large morphological changes that stabilize the entire structure of the aggregate.[64,65] All these mechanisms, characterized by a strong cooperative trait, proved to be effective methods for controlling polymerization kinetics through the nucleation process.[66]

1.3.4 Processing mechanical work

Attempts to observe the effects of mechanical forces produced by the self-assembly of synthetic systems relied on approaches similar to those used for bio-polymerization motors before the introduction of force spectroscopy techniques. Indirect observation of mechanical work was demonstrated by inducing confined growth or disassembly and consequent deformation of compartments such as liposomes[67,68] and microdroplets.[69,70] In a couple of examples, Brownian ratcheting was used effectively to induce the movement of microscopic cargos. It is worth mentioning in this context the propulsion of Janus liposomes through the polymerization of peptidic nanofibres,[71] and the pushing of microspheres by means of microcrystallization (Figure 3c).[72]

1.3.5 Transfer of directionality

The last, and perhaps more elusive, feature to introduce in artificial polymerization motors is a mechanism for a transfer of directionality. The reason is that several factors contribute to preserving the anisotropy of these materials in the motion of the cargo.
For conformational wave model or biased diffusion, analysing the mechanism of dynamic instability reveals the essential element for a transfer of directionality during the disassembly. The accumulation of energy in the supramolecular structure of microtubules and its subsequent controlled release during catastrophe, requires a differentiation of monomers within the self-assembled structures.[73] The fact that the integrity of a strained supramolecular architecture is conserved as long as the fibre end is stabilized by a GTP-bound tubulin cap means that there is a kinetic asymmetry in the depolymerization step between monomers in the polymer bulk and those at the end of the fibre. Such difference must arise from the intermolecular interactions between monomers in the polymer bulk.[73] In the absence of such differentiation of monomers it is not possible to transfer directionality during disassembly, and structural stress or chemical potential will be dissipated isotropically.[74]

A possible strategy to achieve a (supramolecular)structure-reactivity relationship is to exploit cooperative effects arising from packed molecular environments. It has been reported that neighbouring molecules can mutually influence their dynamics in crowded conditions by affecting the translocation of macrocycles in rotaxanes,[75] or affecting the kinetics of isomerization of photoswitches.[76] This phenomenon has been largely studied in the context of collective motion and coupled molecular switching.[77] In condensed matter it is well established that anisotropy increases the possibility to develop ordered collective responses.[78] On the other hand, crystallinity also decreases molecular motion, to the point of restricting the operational freedom of switches and motors that should control the self-assembly process.[78] These effects could be used to differentiate the actuation of monomers based on their structural position, whether in the crystal bulk or at interface.

The idea that structural order plays a fundamental role in the transfer of directionality during the chemo-mechanical transduction process is also suggested by the anisotropic nature of biopolymerization motors. For their ordered lattice, actin bundles have been classified as paracrystals,[79] and microtubules, being constituted by protofilaments, are another example of hierarchically oriented superstructures.[80]

Strategies for increasing crystallinity of supramolecular polymers, for example introducing secondary interactions that could organize the primary assemblies in

hierarchically structured materials, would also decrease monomers dynamics.[81,82] Minimizing the dynamics of the bulk is desirable, since monomer exchange prevents their structural-based differentiation and, in addition, limits the maximal force exerted by disassembly mechanisms, increasing the probability of rupture events when fibres are subjected to tension.

Increasing interactions and structural order can mitigate monomer dynamics and actuation in the bulk of crystalline assemblies. However, differentiation also requires the activation of these properties at specific sites of the supramolecular structure, such as the end of a growing/disassembling fibre. Despite the relative inertness of the bulk, crystal surface chemistry can be incredibly dynamic.[83] In addition, thanks to the precise spatial organization of molecules in the lattice, crystal morphology can modulate the properties of the interfaces enhancing anisotropic effects, with examples of microcrystals that display distinct solubility,[84] adsorption,[85,86] reactivity,[87] and even catalytic activity at specific crystal facets.[88,89] Interestingly, some of the previously discussed nucleation strategies also explore the relationship between (supramolecular)structure and reactivity, as in the case of polymer domains assembling specific sites that catalyse their own monomer activation/deactivation.[90,91] This analogy suggests that to achieve directionality transfer and controlled nucleation pathways, we need to reverse the traditional approach. Instead of using chemistry to control self-assembly, we should focus on the opposite idea.

1.4 Conclusions

Recent insights from the operation of biological systems directed at force generation through supramolecular self-assembly and the exciting recent advances in developing their synthetic analogues carry a number of important messages for this rapidly emerging field of science. Supramolecular self-assembly has to meet several conditions in order to mediate chemo-mechanical transduction: operating under a dissipative thermodynamic regime, developing cooperative supramolecular polymerization, interfacing with nanodevices that can process mechanical work, transferring directionality during the energy transduction process. Reviewing the progress in these areas we have found that while there has been much attention on integrating supramolecular polymerization with a fuel processive behaviour and mechanism of nucleation-elongation, other aspects for this research haven't reach the spotlight yet. Among the ongoing challenges there is the pressing demand for directionality transfer mechanisms, required to convert any re-organization of monomers into useful mechanical work. Studying this phenomenon involves investigating how self-assembly influences both monomers' reactivity and dynamics. Achieving the

modulation of monomer activity based on the supramolecular structure will require an increase in complexity and anisotropy of the architectures, moving from supramolecular polymers to hierarchically oriented superstructures (Figure 3d).

The other research opportunity of this field is represented by the unexplored use of optical tweezers and AFM to study mechanical force produced by assembling synthetic systems. Considering the advancements in our understanding of biopolymerization motors brought by force spectroscopy, it is time for synthetic chemistry to interface with the same techniques and standards used for biophysics investigations. Applying such methods to the study of synthetic systems will not only allow for better comparison with natural counterparts, but also offer new insights into these mechanisms at the most fundamental level.

Although several challenges have been addressed and artificial systems can already reproduce some of the basic principles behind chemo-mechanics of natural polymerization motors, the most difficult task remains combining all these features. Coupling dynamicity and transient nature of these molecular machinery without sacrificing precise control and operational efficiency; the harmonized complexity of these systems is where our aspirations lie and nature still masters

1.5 Acknowledgements

I wish to thank N. Cissé and Q. Huang for their help and contribution in carrying out the bibliographic research on which this chapter is based.

1.6. References

1.6.1 Front page illustration (Chapter 1)

Goodsell, D. S. *CytoSkeleton*. (PDB-101, 2021).

1.6.2 References (Chapter 1)

1 Koumura, N., Zijlstra, R. W., van Delden, R. A., Harada, N. & Feringa, B. L. Light-driven monodirectional molecular rotor. *Nature* **401**, 152-155 (1999).
2 Muraoka, T., Kinbara, K., Kobayashi, Y. & Aida, T. Light-driven open− close motion of chiral molecular scissors. *Journal of the American Chemical Society* **125**, 5612-5613 (2003).
3 Anelli, P. L., Spencer, N. & Stoddart, J. F. A molecular shuttle. *Journal of the American Chemical Society* **113**, 5131-5133 (1991).
4 Ragazzon, G., Baroncini, M., Silvi, S., Venturi, M. & Credi, A. Light-powered autonomous and directional molecular motion of a dissipative self-assembling system. *Nature nanotechnology* **10**, 70-75 (2015).
5 Qian, H., Wang, Y.-Y., Guo, D.-S. & Aprahamian, I. Controlling the isomerization rate of an azo-BF2 switch using aggregation. *Journal of the American Chemical Society* **139**, 1037-1040 (2017).
6 Wilson, M. R. *et al.* An autonomous chemically fuelled small-molecule motor. *Nature* **534**, 235-240 (2016).
7 Kudernac, T. *et al.* Electrically driven directional motion of a four-wheeled molecule on a metal surface. *Nature* **479**, 208-211 (2011).
8 Dogterom, M. & Koenderink, G. H. Actin–microtubule crosstalk in cell biology. *Nature reviews Molecular cell biology* **20**, 38-54 (2019).
9 Lamason, R. L. & Welch, M. D. Actin-based motility and cell-to-cell spread of bacterial pathogens. *Current opinion in microbiology* **35**, 48-57 (2017).
10 Röper, K. Microtubules enter centre stage for morphogenesis. *Philosophical Transactions of the Royal Society B* **375**, 20190557 (2020).
11 Eelkema, R. *et al.* Nanomotor rotates microscale objects. *Nature* **440**, 163-163 (2006).
12 Orlova, T. *et al.* Revolving supramolecular chiral structures powered by light in nanomotor-doped liquid crystals. *Nature nanotechnology* **13**, 304-308 (2018).
13 Iamsaard, S. *et al.* Conversion of light into macroscopic helical motion. *Nature chemistry* **6**, 229-235 (2014).
14 Naumov, P., Sahoo, S. C., Zakharov, B. A. & Boldyreva, E. V. Dynamic single crystals: kinematic analysis of photoinduced crystal jumping (the photosalient effect). *Angewandte Chemie* **125**, 10174-10179 (2013).
15 Lüders, J. & Stearns, T. Microtubule-organizing centres: a re-evaluation. *Nature reviews Molecular cell biology* **8**, 161-167 (2007).
16

16 Mitchison, T. & Kirschner, M. Dynamic instability of microtubule growth. *nature* **312**, 237-242 (1984).
17 Mandelkow, E.-M., Mandelkow, E. & Milligan, R. A. Microtubule dynamics and microtubule caps: a time-resolved cryo-electron microscopy study. *The Journal of cell biology* **114**, 977-991 (1991).
18 Lappalainen, P., Kotila, T., Jégou, A. & Romet-Lemonne, G. Biochemical and mechanical regulation of actin dynamics. *Nature Reviews Molecular Cell Biology* **23**, 836-852 (2022).
19 Sheterline, P., Clayton, J. & Sparrow, J. C. Actin. (1999).
20 Andreu, J. M. How protein filaments treadmill. *Biophysical Journal* **119**, 717-720 (2020).
21 Bai, Y., Zhao, F., Wu, T., Chen, F. & Pang, X. Actin polymerization and depolymerization in developing vertebrates. *Frontiers in physiology* **14**, 1213668 (2023).
22 Gudimchuk, N. B. & Alexandrova, V. V. Measuring and modeling forces generated by microtubules. *Biophysical Reviews* **15**, 1095-1110 (2023).
23 Oster, G. & Mogilner, A. in *Supramolecular polymers* 755-766 (CRC Press, 2005).
24 Dogterom, M. & Yurke, B. Measurement of the force-velocity relation for growing microtubules. *Science* **278**, 856-860, doi:10.1126/science.278.5339.856 (1997).
25 Mogilner, A. & Oster, G. The physics of lamellipodial protrusion. *European biophysics journal* **25**, 47-53 (1996).
26 Mogilner, A. & Oster, G. The polymerization ratchet model explains the force-velocity relation for growing microtubules. *European Biophysics Journal* **28**, 235-242 (1999).
27 Mogilner, A. & Oster, G. Cell motility driven by actin polymerization. *Biophysical journal* **71**, 3030-3045 (1996).
28 Asbury, C. L., Tien, J. F. & Davis, T. N. Kinetochores' gripping feat: conformational wave or biased diffusion? *Trends in cell biology* **21**, 38-46 (2011).
29 Joglekar, A. P. & Hunt, A. J. A simple, mechanistic model for directional instability during mitotic chromosome movements. *Biophysical journal* **83**, 42-58 (2002).
30 Hill, T. L. Theoretical problems related to the attachment of microtubules to kinetochores. *Proc Natl Acad Sci U S A* **82**, 4404-4408, doi:10.1073/pnas.82.13.4404 (1985).
31 Koshland, D. E., Mitchison, T. & Kirschner, M. W. Polewards chromosome movement driven by microtubule depolymerization in vitro. *Nature* **331**, 499-504 (1988).
32 Wang, H. & Oster, G. Ratchets, power strokes, and molecular motors. *Applied Physics A* **75**, 315-323 (2002).
33 Amano, S. *et al.* Using catalysis to drive chemistry away from equilibrium: relating kinetic asymmetry, power strokes, and the Curtin–Hammett principle in Brownian ratchets. *Journal of the American Chemical Society* **144**, 20153-20164 (2022).
34 Mogilner, A. & Oster, G. Polymer motors: pushing out the front and pulling up the back. *Current biology* **13**, R721-R733 (2003).

35 McIntosh, J. R. *et al.* Conserved and divergent features of kinetochores and spindle microtubule ends from five species. *Journal of Cell Biology* **200**, 459-474 (2013).
36 Kaneko, T., Itoh, T. J. & Hotani, H. Morphological transformation of liposomes caused by assembly of encapsulated tubulin and determination of shape by microtubule-associated proteins (MAPs). *Journal of molecular biology* **284**, 1671-1681 (1998).
37 Hotani, H. & Miyamoto, H. Dynamic features of microtubules as visualized by dark-field microscopy. *Advances in biophysics* **26**, 135-156 (1990).
38 Dogterom, M. & Yurke, B. Measurement of the force-velocity relation for growing microtubules. *Science* **278**, 856-860 (1997).
39 Volpe, G. *et al.* Roadmap for optical tweezers. *Journal of Physics: Photonics* **5**, 022501 (2023).
40 Norregaard, K., Metzler, R., Ritter, C. M., Berg-Sørensen, K. & Oddershede, L. B. Manipulation and motion of organelles and single molecules in living cells. *Chemical reviews* **117**, 4342-4375 (2017).
41 Kerssemakers, J. W. *et al.* Assembly dynamics of microtubules at molecular resolution. *Nature* **442**, 709-712 (2006).
42 Alkemade, C. *et al.* Cross-linkers at growing microtubule ends generate forces that drive actin transport. *Proceedings of the National Academy of Sciences* **119**, e2112799119 (2022).
43 Driver, J. W., Geyer, E. A., Bailey, M. E., Rice, L. M. & Asbury, C. L. Direct measurement of conformational strain energy in protofilaments curling outward from disassembling microtubule tips. *Elife* **6**, e28433 (2017).
44 Parekh, S. H., Chaudhuri, O., Theriot, J. A. & Fletcher, D. A. Loading history determines the velocity of actin-network growth. *Nat Cell Biol* **7**, 1219-1223, doi:10.1038/ncb1336 (2005).
45 Zhang, X., Hu, X., Lei, H., Hu, J. & Zhang, Y. Mechanical force-induced polymerization and depolymerization of F-actin at water/solid interfaces. *Nanoscale* **8**, 6008-6013, doi:10.1039/c5nr08713a (2016).
46 Powers, A. F. *et al.* The Ndc80 kinetochore complex forms load-bearing attachments to dynamic microtubule tips via biased diffusion. *Cell* **136**, 865-875 (2009).
47 Grishchuk, E. L., Molodtsov, M. I., Ataullakhanov, F. I. & McIntosh, J. R. Force production by disassembling microtubules. *Nature* **438**, 384-388 (2005).
48 Nick Maleki, A., Huis In't Veld, P. J., Akhmanova, A., Dogterom, M. & Volkov, V. A. Estimation of microtubule-generated forces using a DNA origami nanospring. *Journal of cell science* **136**, jcs260154 (2023).
49 Huis In't Veld, P. J., Volkov, V. A., Stender, I. D., Musacchio, A. & Dogterom, M. Molecular determinants of the Ska-Ndc80 interaction and their influence on microtubule tracking and force-coupling. *Elife* **8**, e49539 (2019).
50 Volkov, V. A. *et al.* Long tethers provide high-force coupling of the Dam1 ring to shortening microtubules. *Proceedings of the National Academy of Sciences* **110**, 7708-7713 (2013).
51 Frisch, H. & Besenius, P. pH-switchable self-assembled materials. *Macromol Rapid Commun* **36**, 346-363, doi:10.1002/marc.201400623 (2015).

52 Heuser, T., Weyandt, E. & Walther, A. Biocatalytic feedback-driven temporal programming of self-regulating peptide hydrogels. *Angewandte Chemie* **127**, 13456-13460 (2015).

53 Wang, G. & Liu, S. Strategies to Construct a Chemical-Fuel-Driven Self-Assembly. *ChemSystemsChem* **2**, doi:10.1002/syst.201900046 (2020).

54 Boekhoven, J., Hendriksen, W. E., Koper, G. J., Eelkema, R. & van Esch, J. H. Transient assembly of active materials fueled by a chemical reaction. *Science* **349**, 1075-1079, doi:10.1126/science.aac6103 (2015).

55 van Ravensteijn, B. G. P., Hendriksen, W. E., Eelkema, R., van Esch, J. H. & Kegel, W. K. Fuel-Mediated Transient Clustering of Colloidal Building Blocks. *J Am Chem Soc* **139**, 9763-9766, doi:10.1021/jacs.7b03263 (2017).

56 Tena-Solsona, M. *et al.* Non-equilibrium dissipative supramolecular materials with a tunable lifetime. *Nat Commun* **8**, 15895, doi:10.1038/ncomms15895 (2017).

57 Grotsch, R. K. *et al.* Pathway Dependence in the Fuel-Driven Dissipative Self-Assembly of Nanoparticles. *J Am Chem Soc* **141**, 9872-9878, doi:10.1021/jacs.9b02004 (2019).

58 Grotsch, R. K. *et al.* Dissipative Self-Assembly of Photoluminescent Silicon Nanocrystals. *Angew Chem Int Ed Engl* **57**, 14608-14612, doi:10.1002/anie.201807937 (2018).

59 Jalani, K., Dhiman, S., Jain, A. & George, S. J. Temporal switching of an amphiphilic self-assembly by a chemical fuel-driven conformational response. *Chemical Science* **8**, 6030-6036 (2017).

60 Weissenfels, M., Gemen, J. & Klajn, R. Dissipative self-assembly: fueling with chemicals versus light. *Chem* **7**, 23-37 (2021).

61 Huang, Q., Cissé, N., Stuart, M. C., Lopatina, Y. & Kudernac, T. Molecular Engineering of the Kinetic Barrier in Seeded Supramolecular Polymerization. *Journal of the American Chemical Society* **145**, 5053-5060 (2023).

62 Ogi, S., Matsumoto, K. & Yamaguchi, S. Seeded polymerization through the interplay of folding and aggregation of an amino-acid-based diamide. *Angewandte Chemie* **130**, 2363-2367 (2018).

63 Kang, J. *et al.* A rational strategy for the realization of chain-growth supramolecular polymerization. *Science* **347**, 646-651 (2015).

64 Ogi, S., Sugiyasu, K., Manna, S., Samitsu, S. & Takeuchi, M. Living supramolecular polymerization realized through a biomimetic approach. *Nature chemistry* **6**, 188-195 (2014).

65 Escudero, C. *et al.* Hierarchical dependence of porphyrin self-aggregation: controlling and exploiting the complexity. *Journal of Porphyrins and Phthalocyanines* **14**, 708-712 (2010).

66 Korevaar, P. A., de Greef, T. F. & Meijer, E. Pathway complexity in π-conjugated materials. *Chemistry of Materials* **26**, 576-586 (2014).

67 Fu, M. *et al.* Disassembly of dipeptide single crystals can transform the lipid membrane into a network. *ACS nano* **11**, 7349-7354 (2017).

68 Brizard, A. *et al.* Preparation of nanostructures by orthogonal self-assembly of hydrogelators and surfactants. *Angewandte Chemie-International Edition In English-* **47**, 2063 (2008).

69 Méndez-Ardoy, A., Granja, J. R. & Montenegro, J. pH-Triggered self-assembly and hydrogelation of cyclic peptide nanotubes confined in water micro-droplets. *Nanoscale Horizons* **3**, 391-396 (2018).

70 Levin, A. *et al.* Elastic instability-mediated actuation by a supra-molecular polymer. *Nature Physics* **12**, 926-930 (2016).

71 Inaba, H. *et al.* Light-induced propulsion of a giant liposome driven by peptide nanofibre growth. *Scientific Reports* **8**, 6243 (2018).

72 Cera, L. *et al.* PolyWhips: Directional Particle Transport by Gradient-Directed Growth and Stiffening of Supramolecular Assemblies. *Advanced Materials (Deerfield Beach, Fla.)* **29** (2016).

73 Brouhard, G. J. & Rice, L. M. Microtubule dynamics: an interplay of biochemistry and mechanics. *Nature reviews Molecular cell biology* **19**, 451-463 (2018).

74 Fredy, J. W. *et al.* Molecular photoswitches mediating the strain-driven disassembly of supramolecular tubules. *Proceedings of the National Academy of Sciences* **114**, 11850-11855 (2017).

75 Heinrich, T. *et al.* Coupled molecular switching processes in ordered mono-and multilayers of stimulus-responsive rotaxanes on gold surfaces. *Journal of the American Chemical Society* **137**, 4382-4390 (2015).

76 Dunne, A., Delaney, C., Florea, L. & Diamond, D. Solvato-morphologically controlled, reversible NIPAAm hydrogel photoactuators. *RSC advances* **6**, 83296-83302 (2016).

77 Dattler, D. *et al.* Design of Collective Motions from Synthetic Molecular Switches, Rotors, and Motors. *Chem Rev* **120**, 310-433, doi:10.1021/acs.chemrev.9b00288 (2020).

78 Vogelsberg, C. S. & Garcia-Garibay, M. A. Crystalline molecular machines: function, phase order, dimensionality, and composition. *Chemical Society Reviews* **41**, 1892-1910 (2012).

79 Wong, G. C. *et al.* Lamellar phase of stacked two-dimensional rafts of actin filaments. *Physical review letters* **91**, 018103 (2003).

80 Mandelkow, E., Song, Y.-H., Schweers, O., Marx, A. & Mandelkow, E.-M. On the structure of microtubules, tau, and paired helical filaments. *Neurobiology of aging* **16**, 347-354 (1995).

81 Yuan, C. *et al.* Hierarchically oriented organization in supramolecular peptide crystals. *Nature Reviews Chemistry* **3**, 567-588 (2019).

82 Cui, H., Muraoka, T., Cheetham, A. G. & Stupp, S. I. Self-assembly of giant peptide nanobelts. *Nano letters* **9**, 945-951 (2009).

83 Meldrum, F. C. & Cölfen, H. Controlling mineral morphologies and structures in biological and synthetic systems. *Chemical reviews* **108**, 4332-4432 (2008).

84 Omori, M. & Sugano, K. Solution-mediated phase transformation on crystal facets of carbamazepine–saccharin cocrystals. *Crystal Growth & Design* **21**, 6237-6244 (2021).

85 Davey, R. & Mullin, J. Growth of the {100} faces of ammonium dihydrogen phosphate crystals in the presence of ionic species. *Journal of Crystal Growth* **26**, 45-51 (1974).

86 Folk, R. L. The natural history of crystalline calcium carbonate; effect of magnesium content and salinity. *Journal of Sedimentary Research* **44**, 40-53 (1974).

87 Gosálvez, M., Sato, K., Foster, A., Nieminen, R. & Tanaka, H. An atomistic introduction to anisotropic etching. *Journal of Micromechanics and Microengineering* **17**, S1 (2007).

88 Ji, X. *et al.* Reactivity triggered by an organic microcrystal interface: a case study involving an environmentally benign, aromatic boric acid reaction. *Chemical Communications* **56**, 11114-11117 (2020).

89 Chen, Z. *et al.* Solvent-free autocatalytic supramolecular polymerization. *Nature Materials* **21**, 253-261 (2022).

90 Colomb-Delsuc, M., Mattia, E., Sadownik, J. W. & Otto, S. Exponential self-replication enabled through a fibre elongation/breakage mechanism. *Nature communications* **6**, 7427 (2015).

91 Bal, S., Das, K., Ahmed, S. & Das, D. Chemically fueled dissipative self-assembly that exploits cooperative catalysis. *Angewandte Chemie* **131**, 250-253 (2019).

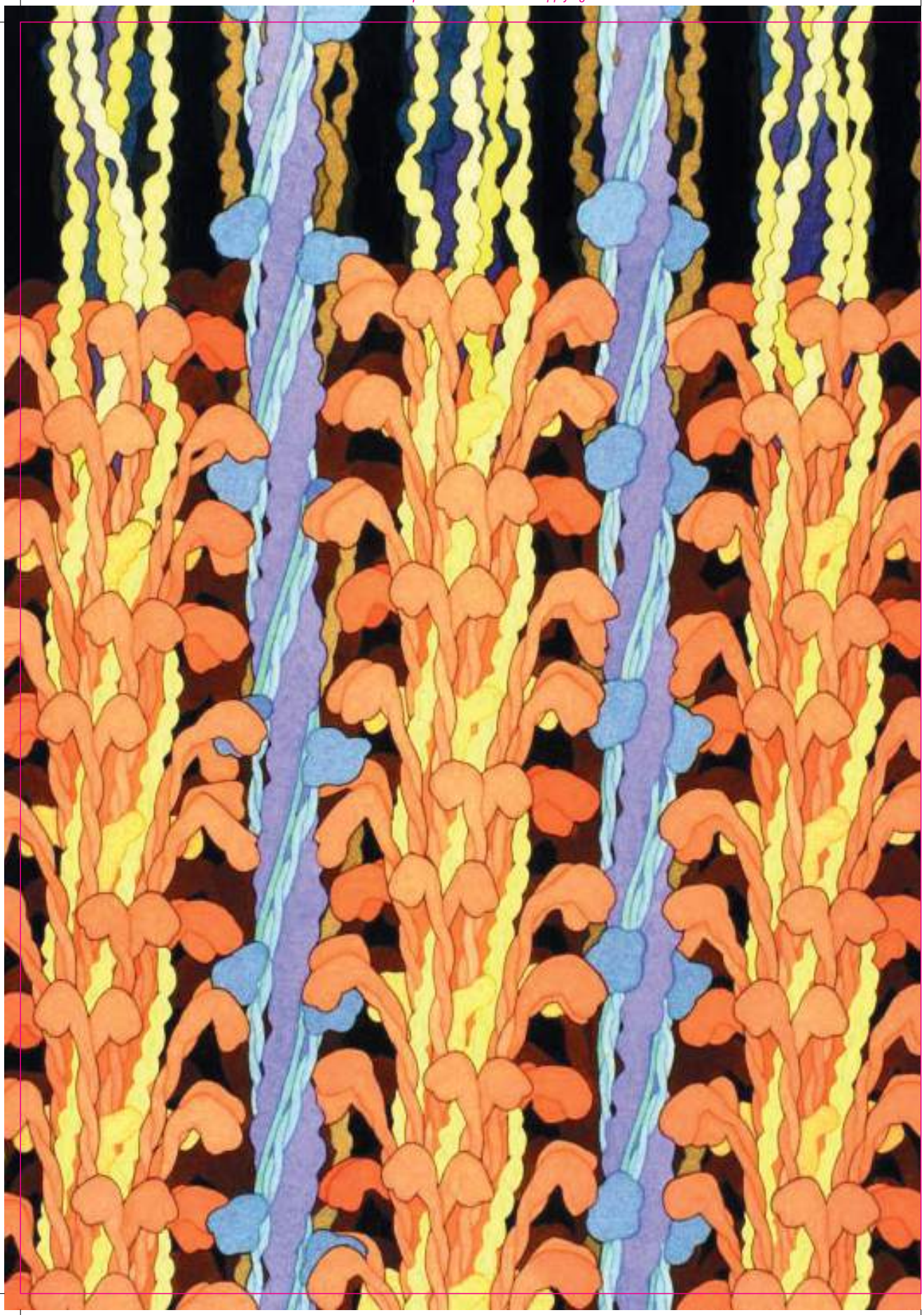

2

Anisotropic etching: imprinting reactivity with directionality

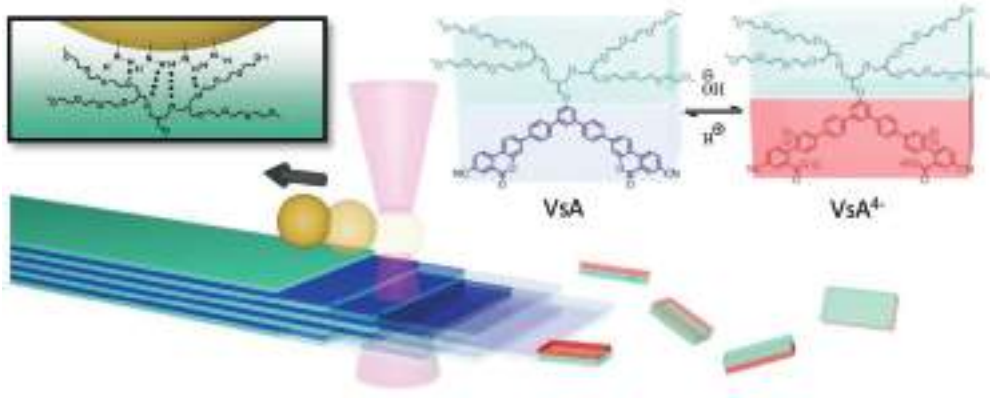

ABSTRACT:

Bio-molecular polymerization motors are molecular systems that use supramolecular (de-)polymerization to mediate the conversion of chemical potential into useful mechanical work. Microcrystallization is ideally suited to reverse-engineer this strategy in artificial systems since self-organization of molecules in a crystal lattice resembles the process of polymer growth/disassembly but with increased predictability of molecular events in a highly ordered microscopic structure. With the intent to explore new chemo-mechanical transduction strategies, we developed a synthetic mechanically-active molecular system that can generate forces via controlled disassembly while being freely suspended in fluid. The amphiphilic monomer self-assembles into rigid, high-aspect ratio microcrystalline fibres with assembly regulated by a coumarin-based pH switching motif. In the structures formed, the crystal morphology determines the monomer reactivity at the interface, resulting in anisotropic etching of the fibres. This effect can exert directional pulling forces on microscopic beads adsorbed on the crystal surface through weak multivalent interactions, paving the way for a novel chemo-mechanical transduction strategy based on a ratcheting mechanism.

This Chapter is based on a publication: L. C. Pantaleone†, E. Calicchia, J. Martinelli, M. C. A. Stuart, Y. Y. Lopatina, W. R. Browne, G. Portale, K. M. Tych*, T. Kudernac*; Nature Nanotechnology (2024)

2.1. Outline

This Chapter is part of a broader project on the exertion of pulling forces in fluids by directional disassembly of microcrystalline fibres. In this section, we will discuss the design of the monomer and its mechanism of pH switch, the characterisation of self-assembly, and how the assembly influences the switching behaviour. The pulling experiments instead, which are part and parcel of this work, will be treated in Chapter 4, a section of this thesis that will be entirely dedicated to the application of force spectroscopy for investigating mechanisms of energy transduction. Besides the use of different techniques, this Chapter is mainly grounded on optical spectroscopy and X-ray scattering experiments, the reason for this separation is that despite the results with optical tweezers being the highlight of this study, we wanted to emphasise the role of anisotropy in mediating the conversion of chemical energy into mechanical work. Looking for the properties emerging from ordered assemblies is a recurring strategy, a topic that is at the very centre of this thesis; this way of presenting it, in our opinion, gives it the attention it deserves.

2.2. Introduction

With the tremendous potential of supramolecular polymerization realized over the past decades, the scope of its application is extending into the field of molecular machinery, a niche that in nature is occupied by a class of proteins known as cytoskeletal polymerization motors (PMs).[1] These biomolecular machines convert chemical energy provided by ATP/GTP hydrolysis into mechanical work via self-assembly processes.[2] These machines drive intracellular modulations, morphology changes, motion and other essential tasks for the survival of the organisms including chromosomal segregation during mitosis.[3] Both actin filaments and microtubules organize and orient monomers by self-assembly to amplify molecular events across length scales. Despite the recent advances in controlling molecular motion, harvesting this motion in fluids, an environment dominated by viscous forces and Brownian fluctuations, still remains a major challenge in the field of synthetic molecular machines.[4,5] Additional attributes are needed to realise an artificial PM on the level of sophistication of biomolecular PMs, such as regulation, cooperativity, polarization, and dissipation of chemical energy.[6,7,8,9] However, any self-assembling system with a fuelled processive behaviour and sufficient structural stiffness has the potential to exert pulling or pushing mechanical forces during

the (de-)polymerization. Microcrystallization has often been regarded as a model for self-assembly of molecular architectures of reduced dimensionality where the lack of dynamicity of the crystal's bulk and the reduced presence of defects represent the main differences between crystalline structures and supramolecular polymers, i.e., supramolecular fibres or tubular assemblies. Less than a handful of examples demonstrating the conversion of crystallization energy into mechanical work have been reported: transport of particles pushed by crystalline growth, deformation of lipid compartments, or piercing of water droplets.[10,11,12] These pioneering examples provide tantalizing hints on what can be achieved with micro crystallization, even though forces originate from a purely physical process. By contrast, chemo-mechanical transduction in natural PMs is fuelled by chemical transformations rather than a concentration gradient or drying. Direct and quantitative measurements of mechanical forces exerted by the (dis)assembly of monomers constitute another challenge in this field.[13] Force spectroscopy techniques, and more specifically the use of optical tweezers (OTs), played a pivotal role in building our current understanding of mechanisms like the conformational wave or Brownian ratcheting, observed in natural PMs.[14,15,16] To the best of our knowledge, an artificial system showing direct evidence of chemo-mechanical transduction by means of force spectroscopy has not been reported to date. Performing such measurements in chemically-fuelled systems is an essential step for characterizing their mechanical behaviour and assessing mechanistic resemblance with their natural analogues.

With this in mind, we designed a force spectroscopy experiment where disassembling microcrystalline fibres are used to exert pulling forces on microscopic polystyrene beads multivalently bound to the surface of the crystal (Figure graphical abstract). The crystal morphology imparts directionality to this process: the disassembly is controlled by a pH switching of the monomer whose reactivity is modulated by the surface of the crystal. In fact, the basic digestion of the crystalline material is expected to occur anisotropically, switching and removing the monomer preferentially along the main axis of the fibre. Once the crystal edge reaches the contact area of the bead, according to Hill's (biased) diffusion model the bead is pulled in the etching direction to maximize the multivalent binding with the surface.[17,18]

2.3. Results and Discussion

2.3.1 Actuation range of the pH switch

The monomer used in this study is a V-shaped amphiphile (VsA).[19,20,21] Most self-assembled structures responding to pH rely on the deprotonation/protonation of monomer residues.[22] However, compared to these dynamic systems, the

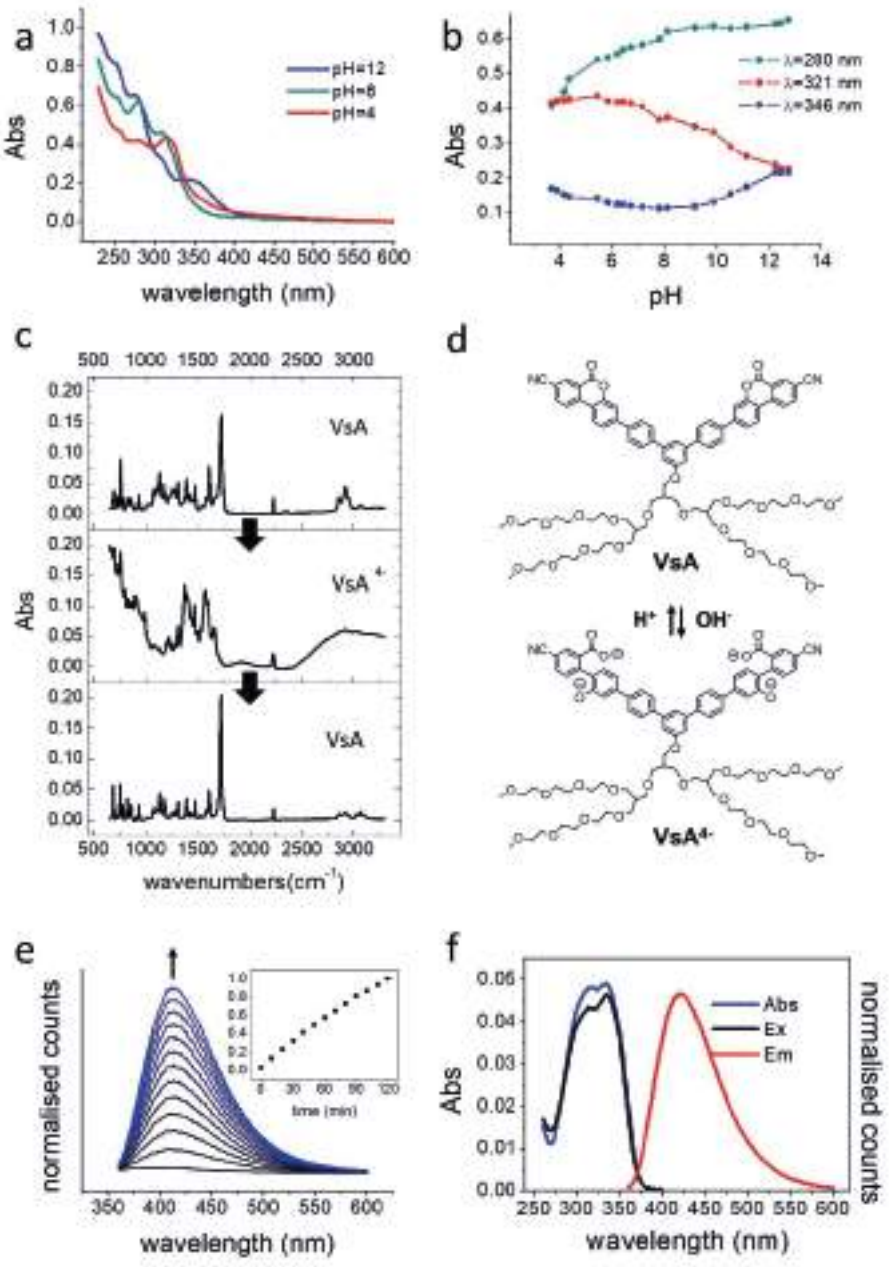

Figure 1: pH switch characterization. (a)(b) Spectroscopic titration of VsA monomer followed by UV-Vis. (c) FTIR spectra of VsA monomer, VsA^{4-} sodium salt obtained after hydrolysis of the monomer with NaOH, VsA monomer reformed upon neutralization with HCl. (d) VsA design and pH switching into VsA^{4-}. (e) Monitoring the lactonization process through the recovery of fluorescence emission upon injection VsA^{4-} in a buffered solution (pH=5). (f) Absorption (blue), excitation (black) and emission spectra (red) of VsA monomer (pH=5).

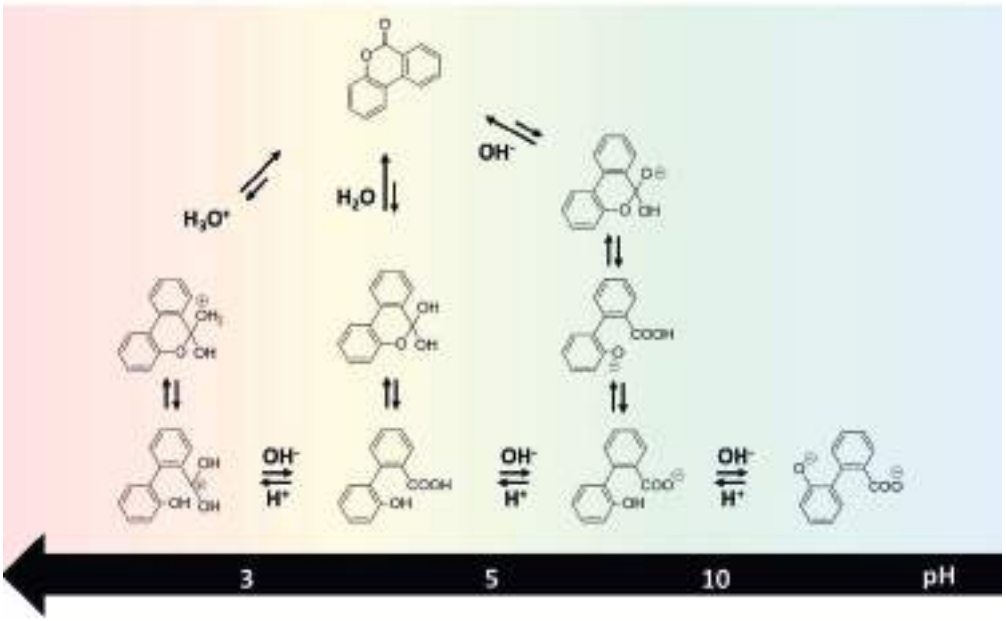

Figure 2: Hypothesized mechanism of hydrolysis/lactonization of a coumarin switch. The donor-acceptor character of the VsA monomer and its poor solubility in water contribute to pushing the equilibrium toward the lactonized form.

benzo[c]coumarin switch in the VsA aromatic scaffold operates through a more complex chemical conversion based on reversible hydrolysis/lactonization. A similar mechanism is often found in chemically fuelled supramolecular polymerizations.[23] Specifically, in those systems where self-assembly is controlled by reactions between carboxylic acids and methylating agents[24,25] or carbodiimides,[26,27,28] and alkaline conditions are employed to deactivate the resulting esters or anhydride products.[29] Spectroscopic titration of the VsA monomer confirmed a pH actuation range between 5<pH<12 consistent with those reported for biaryl lactones with similar donor-acceptor features (Figure 1a-b).[30] When the coumarin switch is closed the monomer is characterized by an absorption band at 320 nm responsible for the observed fluorescence, arising from an ICT mechanism (Figure 1e-f). Hydrolysis of the coumarin under basic conditions quenches the fluorescence, and a new absorption band at 346 nm appears, indicating the opening of the switch and the accumulation of the tetra anionic monomeric species (VsA^{4-}). This species is stabilized against intramolecular esterification. Upon protonation of the phenolates, the dianion species (VsA^{2-}) reverts slowly into the closed form and the switching process accelerates after titration of the carboxylate groups (Figure 2). The reversibility of the process was also confirmed by FTIR spectroscopy: upon basification with

sodium hydroxide the sharp ester carbonyl stretching band at 1727 cm^{-1} is replaced by two bands at 1572 cm^{-1} and 1375 cm^{-1}, consistent with the formation of a carboxylate sodium salt (Figure 1c). Subsequent acidification reverts the spectrum to its original state with VsA in its closed form (Figure 1c).

2.3.2 Structural characterization

Formation of microcrystals was achieved by spontaneous self-assembly of VsA, induced by a solvent processing method.[31] The monomer was molecularly dissolved in acetonitrile, the solution dispersed in water (water/ACN = 80/20) and the samples were annealed at 60 °C. Optical microscopy following overnight annealing showed the formation of needle-shaped fluorescent fibres that reach up to tens of microns in length. Fibres imaged under cross-polarizers showed birefringence, indicating a crystalline state (Figure 3f).

The assembly pathway was elucidated by transmission electron microscopy (TEM) and dynamic light scattering (DLS) investigations. In the early stages of assembly, the VsA forms transient nanofibers with a diameter of d = 4.1 nm (+/- 0.2 nm) (Figure 3a). The size of these nanofibers suggests that the amphiphiles pair their aromatic cores to form dimer units that π-π stack on top of each other.[32] At the later assembly stage, the polar environment promotes further association. Here, a stratified material is formed upon association of nanofibers into large crystalline domains, which grow up to a micron in length within thirty minutes (Figure 3d-e) and turn into rigid fibres with a high persistence length (l=370μm +/- 96 μm) and tendency to fracture under mechanical stress (Figure 3b-c, 3f-g). Due to their stiffness and their anisotropic properties, the latter form of assemblies, the microcrystalline fibres, are the main object of this study and only this type of aggregation state will be used to exert directional pulling forces.

Composition and molecular alignment in the fibres were explored by polarized Raman micro-spectroscopy. Single crystalline fibres were sampled with sub-micron spatial resolution. The presence of the ester carbonyl stretching band (ν_1=1725 cm^{-1}), in line with the FTIR spectra (Supplementary Figure 1a-b), confirmed that under the aforementioned assembling conditions, VsA crystalizes in its closed form. The assignment of vibrational frequencies was based on DFT calculations. Among the three conformers considered in the DFT study, the simulated spectra of a symmetric VsA isomer with internal lactone rings best

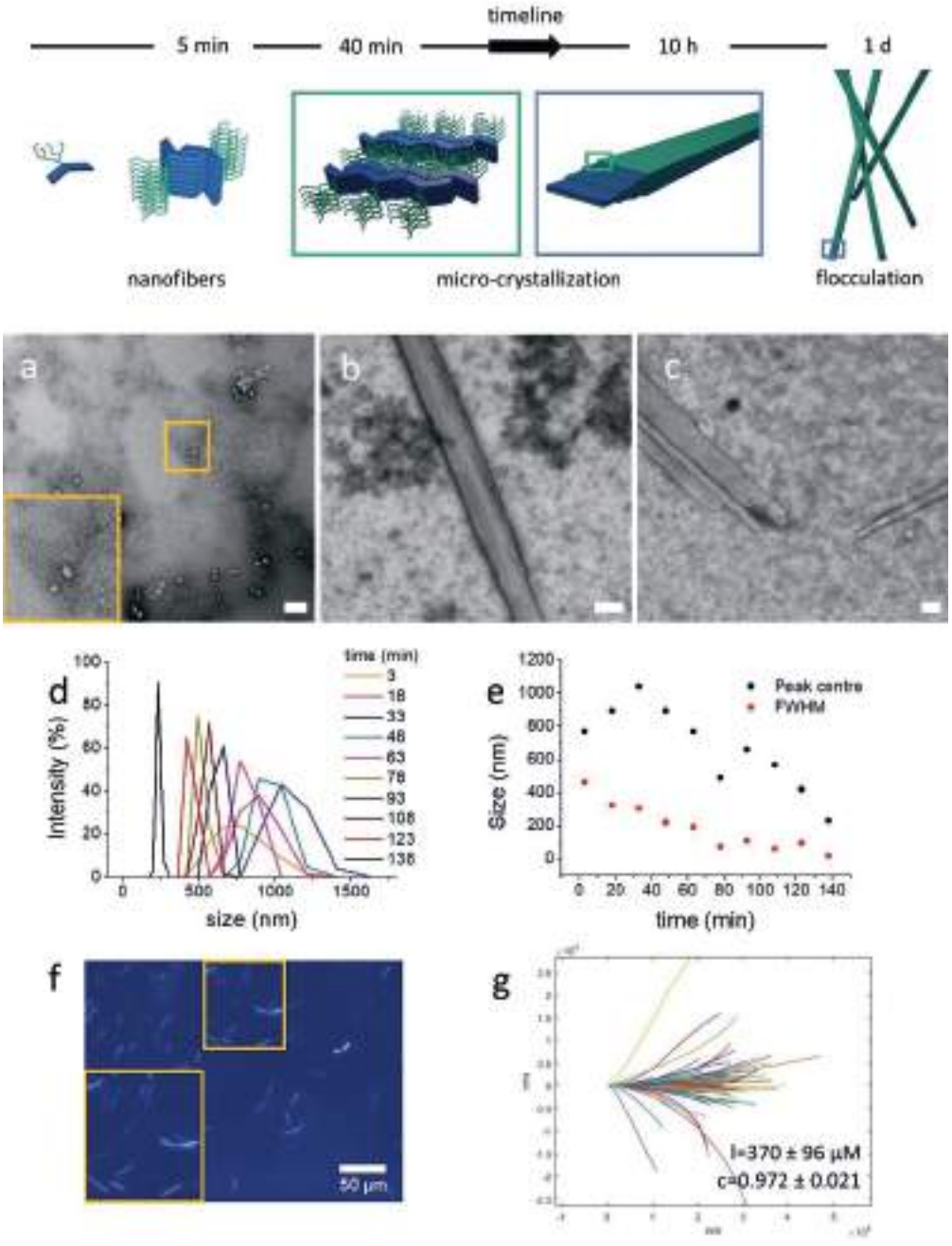

Figure 3: Hierarchical assembly timeline. (a)Transmission electron microscopy (TEM) of VsA nanofibers imaged in the early stages of self-assembly. (b) TEM of VsA fibres after micro-crystallization. (c) TEM of VsA fibres, the crystalline material seems to fracture when subjected to prolonged mechanical stress of sonication. TEM scale bars 100 nm. (d)(e) The size and distribution of VsA aggregates were analysed by dynamic light scattering over time. (f)(g) Micro crystalline fibers imaged with cross-polarized optical microscopy and corresponding deviation-secant midpoint analysis of the micrograph.

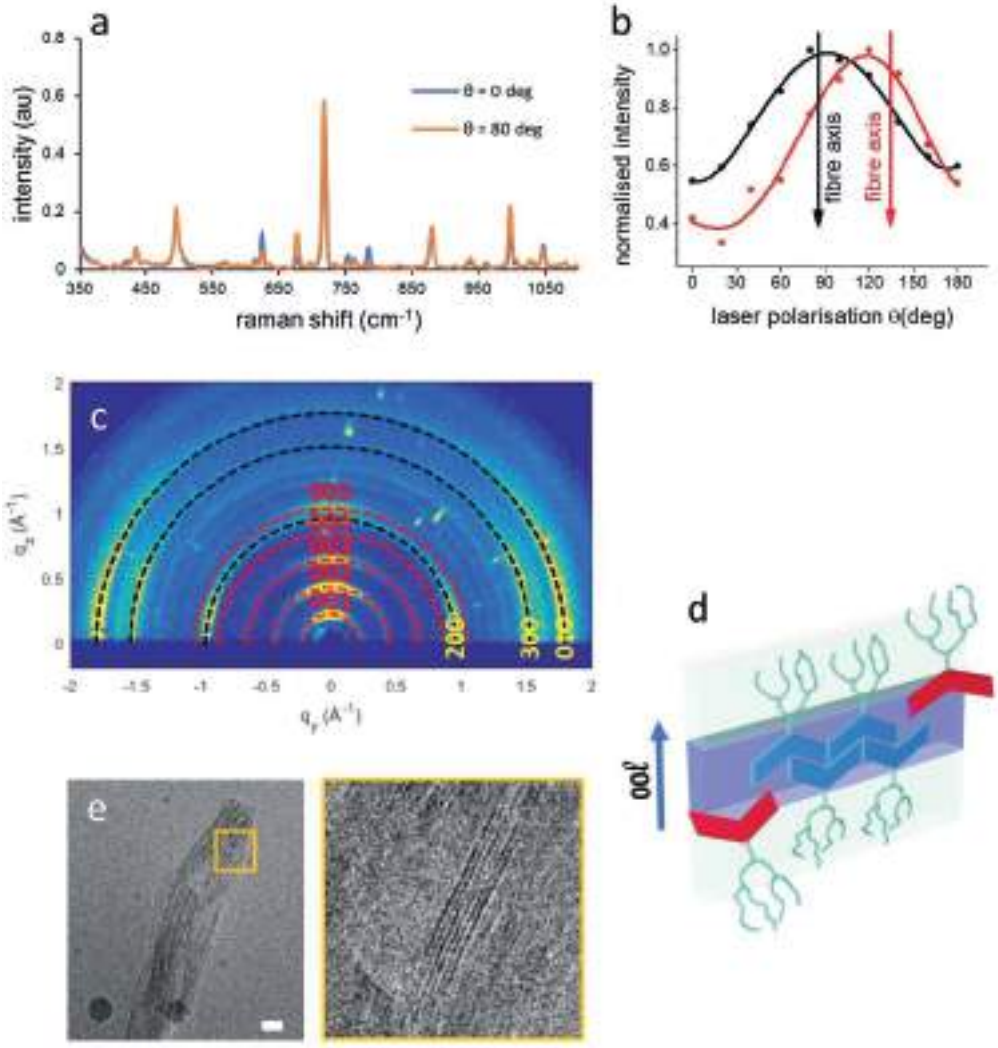

Figure 4: Structural characterization of VsA microcrystalline fibres. (a) Effect of orthogonal polarizations on the Raman spectra of single crystalline fibre. (b) Normalized intensity of Raman scattering (υ_2=998 cm^{-1}) as a function of laser polarisation, black and red arrows indicate the orientation of the corresponding fibre axis. (c) GIWAXS pattern of crystalline fibres. (d) Representation of crystal packing and anisotropic etching at crystal interface. (e) Cryo-EM micrograph of microfibre, scale bar 50 nm.

approximated the experimental spectra (Supplementary Figure 1b). The spectra were recorded varying the orientation of the polarisation of the laser with respect to the long axis of the fibres (Figure 4a-b). The oscillating intensity of the central ring breathing band (υ_2=998 cm^{-1}) was maximized when the polarization was aligned with the fibres (Figure 4b). Other vibrations oscillated fully out of phase (υ_3=624 cm^{-1}; υ_4=784 cm^{-1}) or were unaffected by the polarization of the laser (υ_5=496 cm^{-1}) (Supplementary Figure 1c).[33] These anisotropy effects, originating

from the vibrational symmetry and molecular orientation, are consistent with the molecular alignment in the specimen, which persists across the domain of a single fibre.[34]

Grazing incidence wide-angle X-ray scattering (GIWAXS) analysis was performed on a thin film of fibres drop cast onto a silicon substrate, in order to further elucidate the molecular packing of VsA inside the fibres (Figure 4c). The GIWAXS pattern exhibits several diffraction rings confirming the crystalline nature of the aggregates. The rings present some anisotropy, suggesting a small, but measurable, preferential orientation in the deposition of fibres. Specifically, five intense (00l) reflections show a marked directionality, being more intense along the vertical direction. The presence of (00l) diffraction signals with l=1-5 is due to a layer-like structure with periodicity $d_{001}=2\pi/q_{001}=2.8$ nm, which we attribute to alternated regions of the hydrophobic aromatic component of the molecule and hydrophilic glycol-based part of the molecules (Figure 4d). A similar interplanar distance is observed in Cryo-EM micrographs. Figure 4e shows regular spacing of stacked planes in the microcrystalline fibres with periodicity of 2.7 nm (+/- 0.3 nm). The alternating phase contrast due to the difference in the scattering factor is consistent with the layered architecture formed upon the entangling of the dendron's tails.

The GIWAXS pattern features three more clearly visible signals orthogonally oriented with respect to the (00l) signals and preferentially located along the horizontal q_y direction, with position q_y =1, 1.5 and 1.8 $Å^{-1}$, respectively. The first two signals are ascribed to the diffraction plane generated by the regular staggering along the aromatic backbone, while the last one is assigned to the stacking along the $\pi-\pi$ direction (Figure 4c, 4d). X-ray diffraction (XRD) data from a thin film of fibres deposited on a silicon wafer were used to confirm the structural model and refine the assignment of the unit cell (Supplementary Figure 2a). By integrating the XRD and the GIWAXS data, we derived a unit cell with axis a=12.44 Å, b=3.50 Å, c=28.57 Å for the VsA crystalline fibres.

2.3.3 Crystal morphology and monomer reactivity

The basic hydrolysis of the coumarin switch induces changes in geometry and polarity of the monomer resulting in the disassembly of pre-formed crystalline fibres. The reversibility of this process is limited by the wide operative pH range of the coumarin switch: the switching cycle generates substantial amounts of salt that affect the re-assembly of the fibres resulting in a larger number of small fibres and an increased tendency to flocculation (Supplementary Figure 3a).

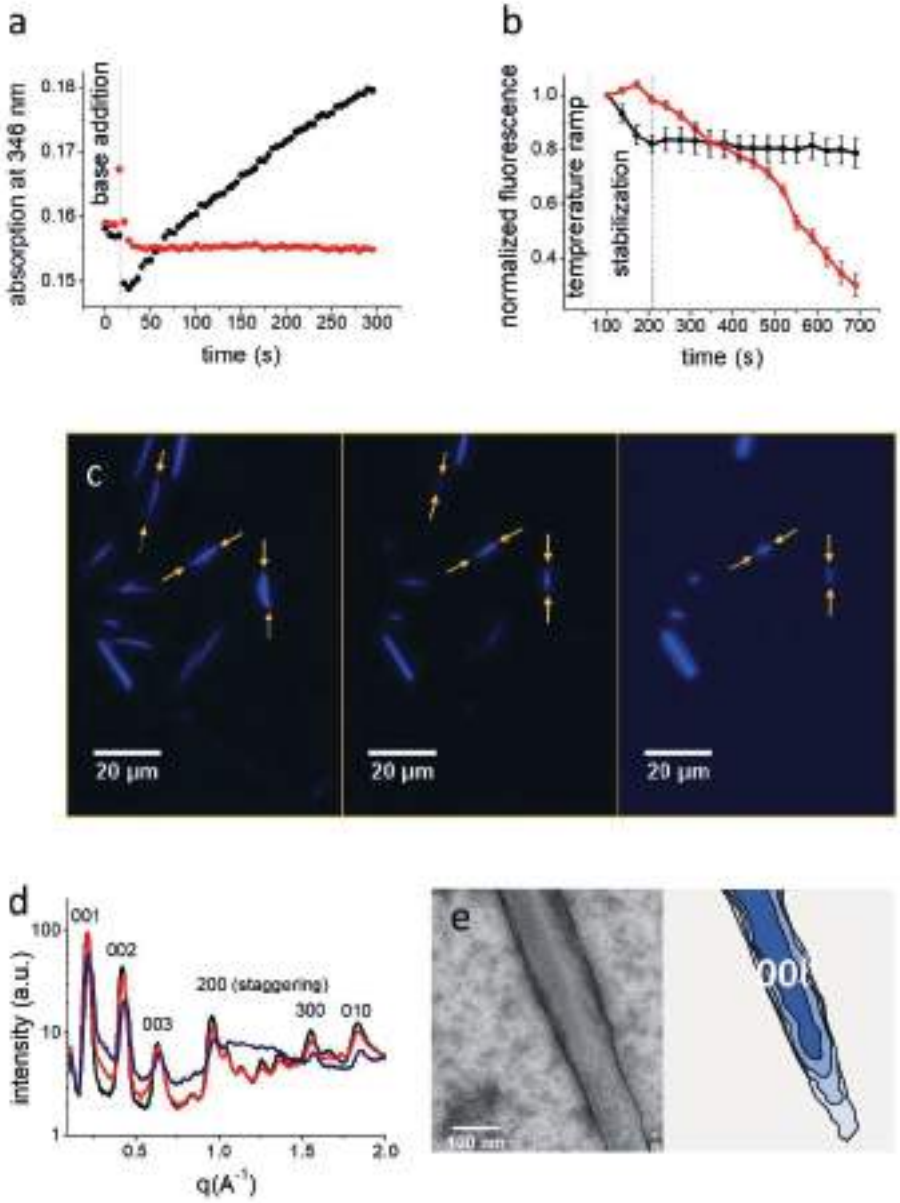

Figure 5: Evidence for anisotropic etching of microcrystalline fibers. (a) UV-Vis Absorption Spectroscopy: coumarin hydrolysis rate in microcrystalline fibres (red) and nanofibres (black) solutions (NaOH at 20°C). (b) Normalised fluorescence intensity of micrographs before (black) and after (red) NaOH addition (60°C). (c) Fluorescence microscopy: disassembly of microcrystals during basic hydrolysis (NaOH at 60°C), micrographs time frame (from left to right): 3 min, 6 min, 13 min. (d) Radially integrated GIWAXS profiles of partially digested fibres. Thin film of crystalline fibres after deposition (black), after first basic treatment (1M NaOH at 45°C for 5 minutes, water washed) (red), second treatment (1M NaOH at 45°C for 10 minutes, water washed) (blue). (e) TEM micrograph of single crystalline fibre with schematic representation of {00l} crystal facet.

The rate of hydrolysis of the monomer critically depends on the state of its assembly. In fresh samples, dominated by the presence of nanofibers, upon base addition the monomer switches into the open VsA^{4-} form at room temperature (Figure 5a). By contrast, after micro-crystallization of VsA took place, basic hydrolysis required heating of the solutions above 30°C to yield measurable conversion (Figure 5a). We hypothesize that in the crystal bulk the monomer is stabilized and, due to the lack of exchange with solvent, the monomer is inaccessible to solvolysis.

In hierarchically organized highly anisotropic material, different facets of the same crystal are expected to show different reactivity.[35,36] Analysis of the fluorescence microscopy images shows that crystalline material is etched preferentially from the ends of the fibres which results in a directional disassembly along the main axis (Figure 5c) (See Supplementary Video 1). Further, the crystals were heated at 60 °C in the absence of the base to exclude that this effect was only caused by a difference in solubility between crystal facets. Comparing the changes in normalized fluorescence intensity from individual fibres before and after addition of base confirms that disassembly does not occur without basic hydrolysis of the monomer (Figure 5b).

The occurrence of the anisotropic etching was also confirmed by the X-ray scattering analysis of partially digested samples. After removing residual sodium hydroxide and degraded monomer, the radially integrated GIWAXS profiles show an increase in the background caused by the general degradation of the sample (Figure 5d)(Supplementary Figure 2b-c). Nevertheless, etching is significantly more pronounced on certain reflections, specifically visible for the (h00) "staggering" direction. The amorphization of (00l) planes remains limited, which is explained by the crystal morphology since in the corresponding facets the monomers expose their glycol tail to the surface shielding the coumarin motif from the solvent (Figure 5d-e).

2.4. Conclusion

In this study, we designed an amphiphilic monomer whose assembly is controlled by a pH-switchable coumarin motif. Characterising the switching behaviour in the resulting material we demonstrated that the activation of the pH switch is influenced by its state of assembly and, in the case of micro-crystallization, the rate of coumarin hydrolysis occurs at different rates depending on the crystal facet. Our conclusion at the end of this Chapter is that anisotropic etching, a

technique usually explored to control crystal morphology, can be reversely applied to influence the reactivity of monomers embedded in a supramolecular structure.

Indeed, rather than chasing other features inspired by bio-polymerization motors, such as dissipative operative regimes or processive behaviour, the focus of Chapter 2 was the quest for directionality, which is the starting point in the design of any molecular machine.[37] In a polymerisation motor, the relationship between supramolecular architecture and monomer activity is at the origin of chemical gating. Without distinguishing tubulin by its structural position—whether at the nanotube ends or within the bulk—there would be no asymmetry to sustain the bias in the chemo-mechanical cycle. In the search for similar features, we have found how the anisotropy of a crystal lattice can be imprinted into the reactivity of the coumarin switches to achieve a directional disassembly of microfibres. We envision that this mechanism if coupled with a multivalently bound cargo, has the potential to deliver a new energy transduction strategy mediated by self-assembly.

This idea will be explored in Chapter 4, which will delve into the mechanism of bias diffusion of polystyrene microspheres on the surface of these microfibres upon directional disassembly. We anticipate that the role of the crystal morphology in the biased diffusion of cargo goes beyond the modulation of monomer reactivity. The use of force spectroscopy techniques, besides the purpose of quantifying the mechanical work produced by this system, will be crucial to elucidate how energy is supplied during cargo transport and to investigate the close relationship between frictional forces and elements of the crystal surface.

2.5. Acknowledgements

I wish to thank M.C.A. Stuart for the acquisition of Cryo-EM images and for the useful discussions. I gratefully acknowledge J. Martinelli for the DFT simulations and the deviation-secant midpoint analysis. I wish to thank W.R. Browne for his help in the interpretation of Raman microspectroscopy data. I gratefully acknowledge E. Calicchia and G. Portale for the acquisition and the interpretation of the X-ray scattering data. I gratefully acknowledge J. Baas for the acquisition of the XRD data.

2.6. Experimental section

Supplementary Video 1: Anisotropic etching of microcrystalline fibres observed with epifluorescence microscopy (video speed 100X, scale bar 50 μm, λ_{ex}=330 – 380 nm and λ_{em}=420 nm). Disassembly of the fibres was induced by basic hydrolysis of the monomer (NaOH, 60 °C).

2.6.1 Materials

Chemicals and solvents were obtained from commercial sources and used without further purification unless stated otherwise.

General procedure for preparation of VsA microcrystalline fibres for TEM and Cryo-EM: a stock solution of monomer in acetonitrile ([VsA]=100 μM) was diluted and dispersed in MilliQ water (water/acetonitrile 80:20) to adjust the final concentration of monomer to 10 μM. The sample was annealed in a thermostated bath at 60°C which was left cooling at room temperature for 10 h. After ageing the samples for 24 hours, microcrystalline fibres flocculate and the sample can be concentrated up to 100 times by separating the precipitate from the supernatant and re-dispersing the fibres by mechanical agitation. The resulting solutions were cast on the desired surface and blotted shortly after deposition. TEM samples were stained with a 2% PTA solution (pH=7).

General procedure for preparation of VsA micro-crystalline fibres for DLS: All solvents were previously filtered through a 0.45 μm membrane, a stock solution of monomer in acetonitrile ([VsA]=100 μM) was diluted and dispersed in MilliQ water (water/acetonitrile 80:20) to adjust the final concentration of monomer to 5 μM. The sample was pre-heated at 60°C and measured in a DTS0012 cell thermostated at 20°C after 5 minutes of equilibration.

General procedure for preparation of drop casted films for GIWAXS, XRD, Raman and AFM analysis: a stock solution of monomer in acetonitrile ([VsA]=100 μM) was diluted and dispersed in MilliQ water (water/acetonitrile 80:20) to adjust the final concentration of monomer to 10 μM. The sample was annealed in a thermostated bath at 60°C which was left cooling at room

temperature for 10 hours. After ageing the samples for 24 hours, microcrystalline fibres flocculate and the sample can be concentrated up to 100 times by separating the precipitate from the supernatant and re-dispersing the fibres by mechanical agitation. The resulting solutions were cast on the desired surface (GIWAXS, XRD, AFM, silicon wafer; Raman, aluminium foil), blotted after deposition and the residual solvent was dried under reduced pressure.

General procedure for preparation of VsA micro-crystalline fibres for optical microscopy: a stock solution of monomer in acetonitrile ([VsA]=100 μM) was diluted and dispersed in MilliQ water (water/acetonitrile 80:20) to adjust the final concentration of monomer to 5 μM. The sample was annealed in a thermostated bath at 60°C which was left cooling at room temperature for 10 hours.

2.6.2 Methods

UV-Vis absorption spectroscopy: spectra were recorded on an Agilent Technologies 8453 UV-Vis Spectrophotometer. During the titration experiment the monomer was initially dissolved in a solution of 1 M sodium hydroxide which was gradually neutralized with hydrochloric acid solutions at different concentrations (1 M, 100 mM, 10 mM and 1 mM solutions) ([VsA]=2.5 μM, water). The pH reading was performed in between the spectroscopic measurements using a Mettler Toledo FiveEasy F-20 benchtop pH/mV meter equipped with a pH electrode inLab microprobe.

FTIR spectroscopy: Infrared spectra were recorded on an Agilent Cary 630 FTIR spectrometer. VsA and Na_4VsA solid samples were directly deposited on the crystal after drying the samples.

Fluorescence spectroscopy: fluorescence excitation and emission of the VsA monomer were recorded with an FS5 spectrofluorometer from Edinburgh Instruments. λ_{ex}= 320 nm λ_{em}436 nm ([VsA]=250 nM, water, pH=4.5)

Fluorescence and Cross-Polarized Optical Microscopy: Imaging with fluorescence microscopy was performed in a Nikon Eclipse LV100N POL microscope using filters of the following excitation and emission wavelengths cut-offs: λ_{ex}= 330-380 nm and long pass λ_{em}=420 nm for imaging the VsA fibres. In the disassembly experiments in the presence of base, the normalized fluorescence intensity and distance measurements were calculated by analysing the micrographs with the processing package Fiji. For the control experiments on temperature (Figure 5b), the fluorescence microscopy experiment was carried out under

constant irradiation power, five regions of interest (ROI) were selected from the micrographs where fibres were equilibrated on a 2D surface during the whole footage (See Supplementary Fig. 3b-e). After background subtraction, mean grey values from each ROI were normalized and averaged values were plotted against time. Error bars represent standard deviation for each timepoint.

DLS: Dynamic light scattering measurements were performed with a Zetasizer Ultra Red (ZSU3305) from Malvern Panalytical.

TEM and Cryo-EM: TEM images were recorded with a CM120 at 120keV acceleration voltage, samples were prepared using carbon-coated copper grids. Cryo-EM images were recorded with a Tecnai T20 TEM microscope (FEI) operating at 200 keV using a Gatan model 626 cryo-stage sample holder. Distance measurements were performed by analysing the micrographs with the processing package Fiji.

XRD: thin film X-ray diffraction measurements were carried out using a Bruker D8 Advance diffractometer equipped with a Cu-Kα source. The cell parameters were extracted from the diffraction pattern using N-TREOR09 from the software EXPO2014.[38]

GIWAXS: grazing incidence wide-angle X-ray scattering measurements were performed at the multipurpose instrument for nanostructure analysis (MINA) instrument at the University of Groningen. This instrument is built on a Cu rotating anode source providing an X-Ray beam with wavelength l=0.15413 nm. 2D patterns were collected using a Vantec500 detector (1024 x 1024 pixel array with pixel size 136 x 136 μm located at 89 mm away from the sample for GIWAXS. The samples were placed in reflection geometry at 0.4° incident angle (α) with respect to the direct beam using a Huber goniometer. The direct beam centre position on the detector and the sample to detector distance were calibrated using the diffraction rings from standard silver behenate and α-Al_2O_3 powders.

Polarized Raman Microspectroscopy: Solid-state Raman spectroscopy at 785 nm was performed with an Olympus BX51M microscope equipped with a fibre-coupled laser (BT785, ONDAX, 500 mW) and a fibre coupled Andor Shamrock SR-163 spectrograph and Andor iVac 316 DR-316B-LDC-DD CCD camera. Polarised Raman microspectroscopy were obtained at 785 nm using 50x long working distance objective on a BX-51 microscope. Excitation was provided by an ONDAX LM-785 freespace laser (75 mW at source), which was passed through a laser line clean up filter (Semrock LL01-785), a λ/2 retarder and polarising beamsplitter to control power followed by a second λ/2 retarder to

control polarisation. The laser was combined with the optical path of the spectrometer with a dichroic mirror (45°) (Semrock Di02-R785) and directed to the microscope with gold mirrors. The Raman scattering passed through the dichroic mirror and a Rayleigh line rejection filter (Semrock BLP01-785R) and was focused with a 35 mm focal length plano convex lens into an Andor Kymera-193i spectrograph with a 600 l/mm grating blazed at 750 nm and Andor idus-DU416A-LDC-DD CCD camera. Spectra were acquired with Andor Solis. Spectra were calibrated with polystyrene or cyclohexane (ASTM E 1840). The estimated spot size was less than 1 μm (diameter)

HRMS: high-resolution mass spectrometry was performed using a Thermo LTQ Orbitrap XL with the ESI method, or alternatively using a Voyager DE-Pro MALDI-TOF when matrix-assisted laser desorption is specified as the ionization method. Super DHB (dihydroxybenzoic acid) was used for matrix preparation.

Nuclear magnetic resonance (NMR): NMR spectra were recorded at room temperature on a Varian 400 or Agilent 400 spectrometer and were referenced against the residual non-deuterated solvent signal.

DFT methodology: All DFT calculations were carried out in the ORCA software.[39] Three isomers were optimized, corresponding to two symmetrical conformers and an asymmetrical one. Initial geometries were constructed in the Chemcraft software. The PEG moiety was replaced by a methoxy group for each structure. All calculations were carried out at the B3LYP(G)/def2-SVP level of theory.[40,41,42,43,44] The D3 dispersion correction with Becke-Johnson dumping was applied to account for geometrical dispersion.[45,46] The RIJCOSX approximation, in conjunction with the def2-J auxiliary basis set was used to speed up integral evaluation.[47,48] The exchange integral grid grid4 was used for all calculation. Increased accuracy was requested via the NoFinalGrid TightOpt VeryTightSCF keywords. For frequency calculation, hessian were calculated using numerical integration via the NumFreq keyword.

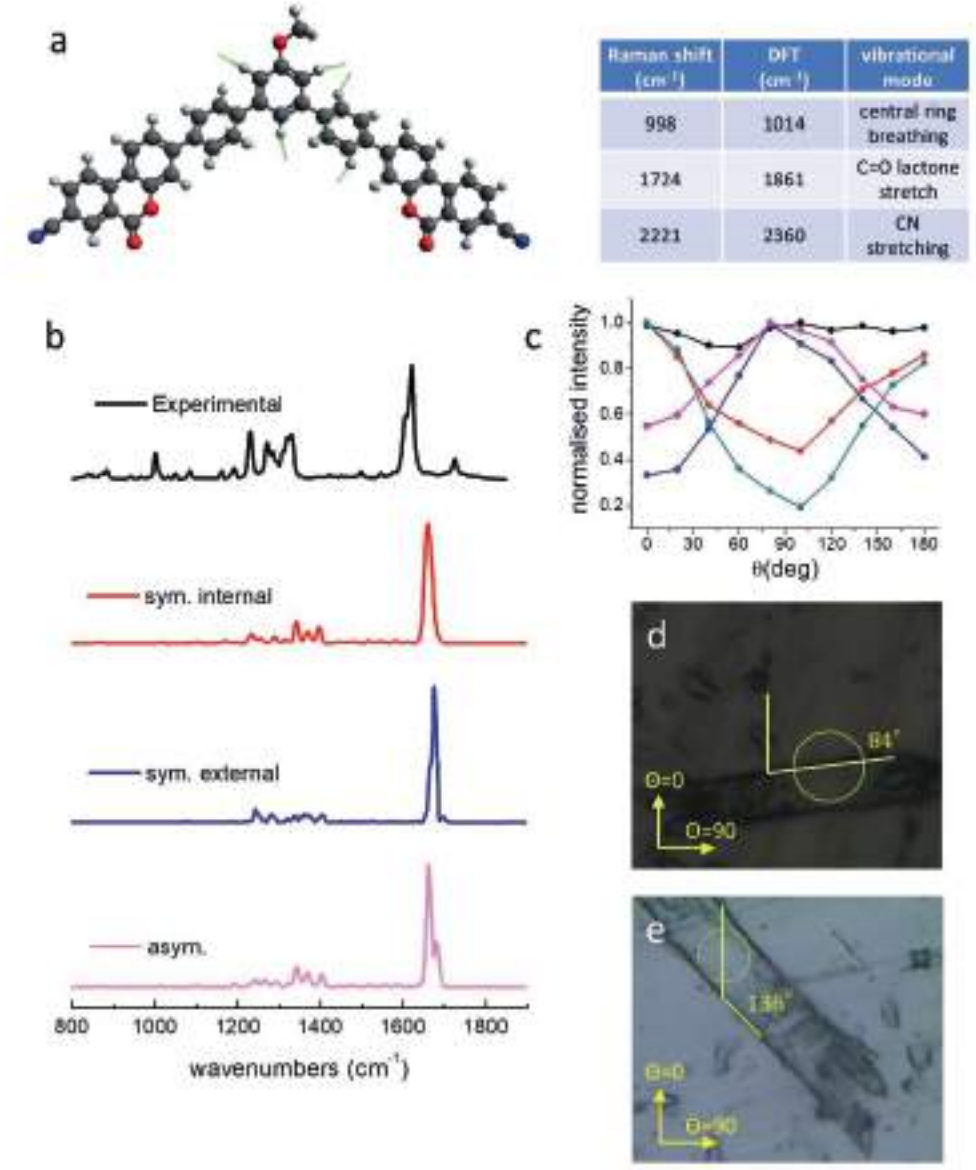

Raman shift (cm^{-1})	DFT (cm^{-1})	vibrational mode
998	1014	central ring breathing
1724	1861	C=O lactone stretch
2221	2360	CN stretching

Figure S1: Polarized Raman micro-spectroscopy. (a) DFT graphic representing the central ring breathing vibration in the symmetrical VSA conformer with internal lactone rings. (b) Comparison between experimental Raman spectra of VsA fibres and DFT simulation. Experimental (bulk) spectra was obtained by sampling a region where multiple deposited fibres were superimposed with random orientations to average the fibres' orientation and minimize the effects of polarization. (c) Normalized intensity of Raman scattering for different vibrations as a function of laser polarization (pink, υ_2=998 cm^{-1}; red υ_3=624 cm^{-1}; green, υ_4=784 cm^{-1}; black, υ_5=496cm^{-1}; blue, υ_6=678 cm^{-1}). (d)(e) Micrographs of single crystalline VsA fibres during spectral analysis, estimated laser spot size is <1µm, fibre orientation is reported with respect to the laser polarization.

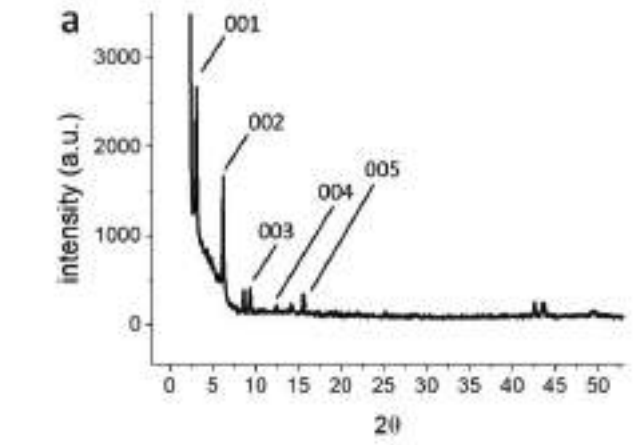

reflection	2θ	d (Å)
001	3.09227	28.57
002	6.21245	14.23
100	7.08876	12.44
	7.69411	11.49
	8.62174	10.26
003	9.35245	9.46
004	12.4514	7.11
200	14.1793	6.25
005	15.6076	5.68
	43.5728	2.08
	42.5172	2.13
	49.4609	1.84

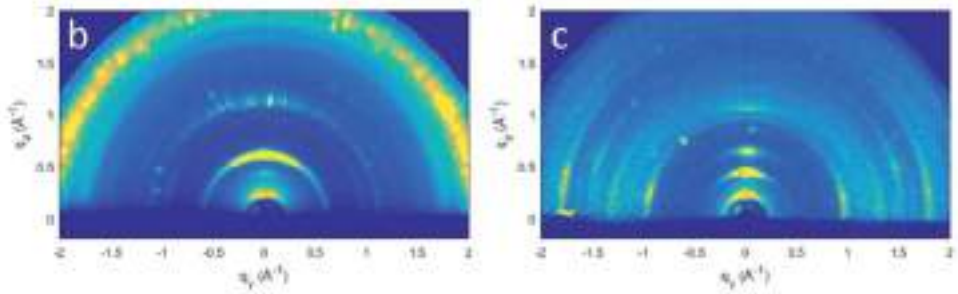

Figure S2: X-ray diffraction and scattering experiments. (a) Diffraction of VsA from a thin film deposition of microcrystalline fibres. (b)(c) GIWAXS pattern from a partially hydrolyzed sample before (b) and after (c) washing away the residues of NaOH and digested monomer.

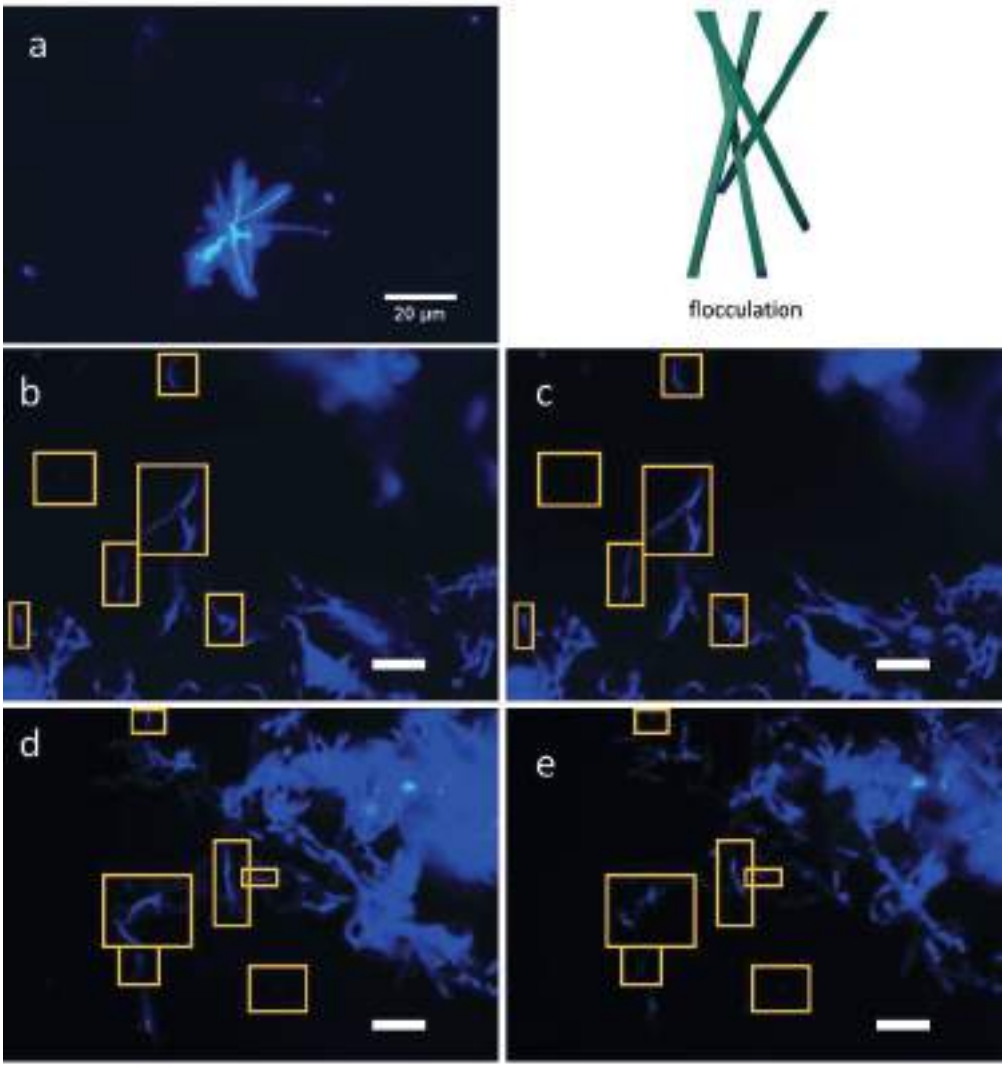

Figure S3: (a) Fibres formed after neutralization of an alkaline solution of hydrolyzed monomer ([VSA^{4-}]=2.5 µM). The increase in salt concentration caused by the switching cycle ([NaCl]~1mM) influences the self-assembly inducing the formation of smaller fibres and increasing the flocculation of aggregates. (b)(c) fibre disassembly, control experiment in the absence of base: initial (left) and final (right) frames with selected ROI, scale bar 100 µm. (d)(e) Fibre disassembly in the presence of base: initial (left) and final (right) frames with selected ROI; scale bar 100 µm.

2.6.3 Synthesis

Synthesis of methyl 4'-chloro-4-cyano-2'-methoxy-[1,1'-biphenyl]-2-carboxylate (1)

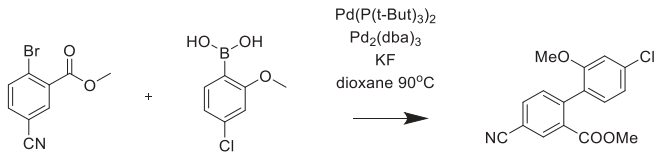

1

The aryl bromide 2.00 g (8.3 mmol, 1 eq), and KF 1.46 g (24,9 mmol, 3 eq) was added to a Schlenk tube under nitrogen. Next, the boronic acid 1.55 g (8.3 mmol, 1 eq) and 80 mL of dry dioxane were added, followed by a solution of 42 mg of $Pd(P(t\text{-}Bu)_3)_2$ (0.083 mmol, 1%) and 76 mg of $Pd_2(dba)_3$ (0.083 mmol, 1%) in dry dioxane. Three freeze-pump-thaw cycles were performed before the stirring the reaction mixture at 90°C for 48h. Once TLC analysis confirmed the full conversion of the starting material, the reaction mixture was diluted with Et_2O, filtered through a pad of celite with copious washings and concentrated, yielding after purification by column chromatography on silica gel (pentane/diethyl ether 80:20) 1.76 g product **1** as a white solid (yield 70%).

^{1}H NMR (400 MHz, $CDCl_3$) δ 8.16 (dd, J = 1.8, 0.5 Hz, 1H), 7.80 (dd, J = 8.0, 1.8 Hz, 1H), 7.41 (dd, J = 8.0, 0.5 Hz, 1H), 7.15 (d, J = 8.1 Hz, 1H), 7.05 (dd, J = 8.1, 1.9 Hz, 1H), 6.91 (d, J = 1.9 Hz, 1H), 3.72 (s, 3H), 3.71 (s, 3H)

^{13}C NMR (101 MHz, $CDCl_3$) δ 166.40, 156.37, 142.45, 135.48, 134.62, 133.29, 132.67, 132.23, 130.27, 127.31, 121.10, 117.92, 111.56, 111.24, 55.52, 52.28.

HRMS-ESI Orbitrap (m/z): [M+H$^+$] calculated for $C_{16}H_{12}ClNO_3H$, 302.05786; found 302.05806

m.p.: 112.1-112.9 °C

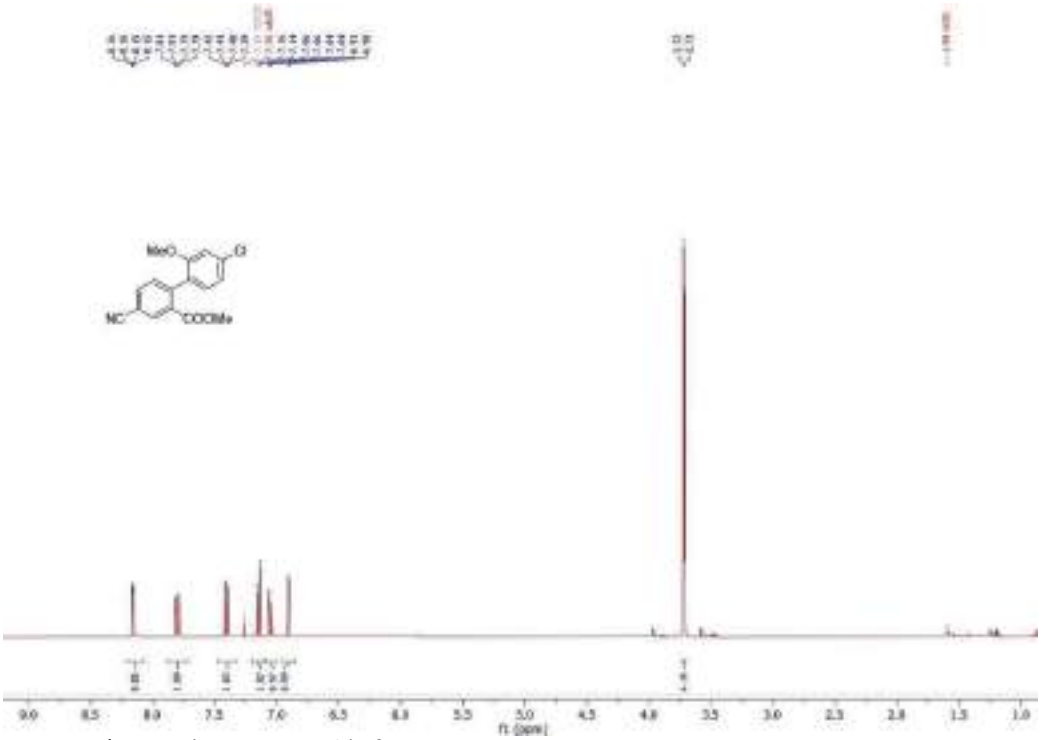

*Figure S4: ^{1}H NMR (400 MHz, $CDCl_3$) of **1***

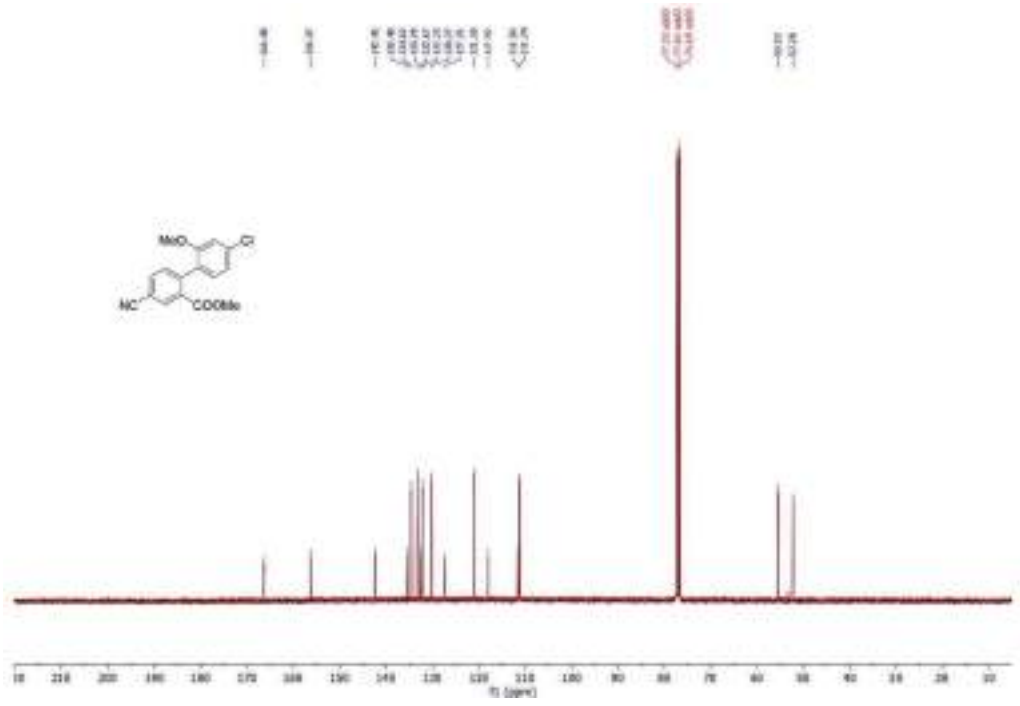

*Figure S5: ^{13}C NMR (101 MHz, $CDCl_3$) of **1***

Synthesis of 3-chloro-6-oxo-6H-benzo[c]chromene-8-carbonitrile (2)

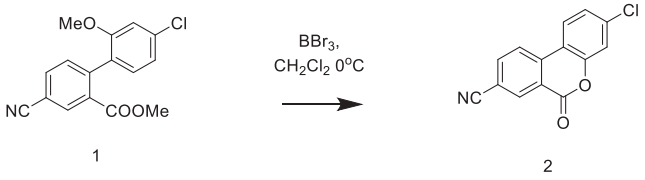

1 2

In a round bottom flask 143 mg of compound **1** (0.47 mmol, 1 eq) were dissolved in 5 mL of dry CH_2Cl_2. The reaction flask was chilled at 0°C while purging the solution with nitrogen. After 15 minutes 1.4 mL of 1M BBr_3 solution in CH_2Cl_2 (1.42 mmol, 3 eq) were injected dropwise in the reaction mixture under inert atmosphere. Once the addition was completed the reaction was stirred at 0 °C for 60 minutes. Subsequently, 3.5 mL of cold water were added to the reaction mixture and the organic layer was extracted with 3x5 mL CH_2Cl_2. The combined extracts were washed with 3x20 mL brine solution, dried over Na_2SO_4 and concentrated. The crude was then filtered over a pad of silica, washed with a mixture of pentane/ether (80:20) and eluted with CH_2Cl_2. The resulting solution was concentrated under reduced pressure to afford 85 mg of product **2** a**s** a white solid (yield 71%).

^{1}H NMR (400 MHz, $CDCl_3$) δ 8.70 (d, J = 1.7 Hz, 1H), 8.19 (d, J = 8.4 Hz, 1H), 8.10 – 8.04 (m, 1H), 8.01 (d, J = 8.5 Hz, 1H), 7.44 (s, 1H), 7.43 – 7.37 (m, 1H).

^{13}C NMR (101 MHz, $CDCl_3$) δ 158.68, 152.17, 138.25, 137.55, 137.18, 135.16, 125.74, 124.50, 122.90, 121.62, 118.45, 117.19, 115.23, 113.02,

MS-MALDI TOF (m/z): [M^+] calculated for $C_{14}H_6ClNO_2$, 255.0087; found 254.9703

m.p.: 311.8-312.7 °C

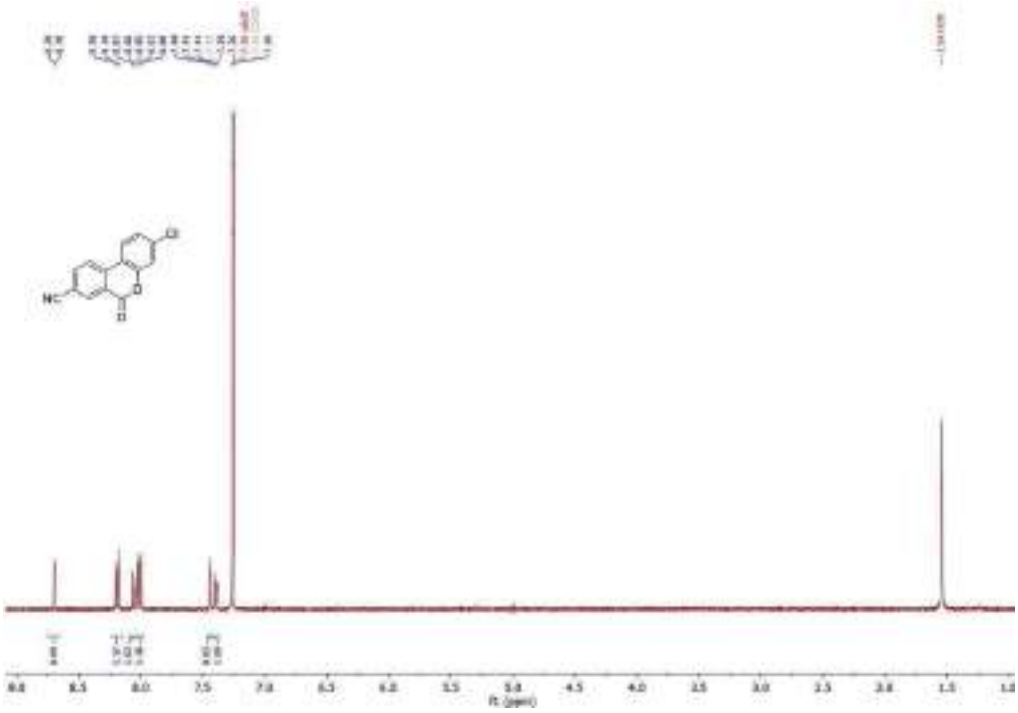

*Figure S6: ^{1}H NMR (400 MHz, $CDCl_3$) of **2***

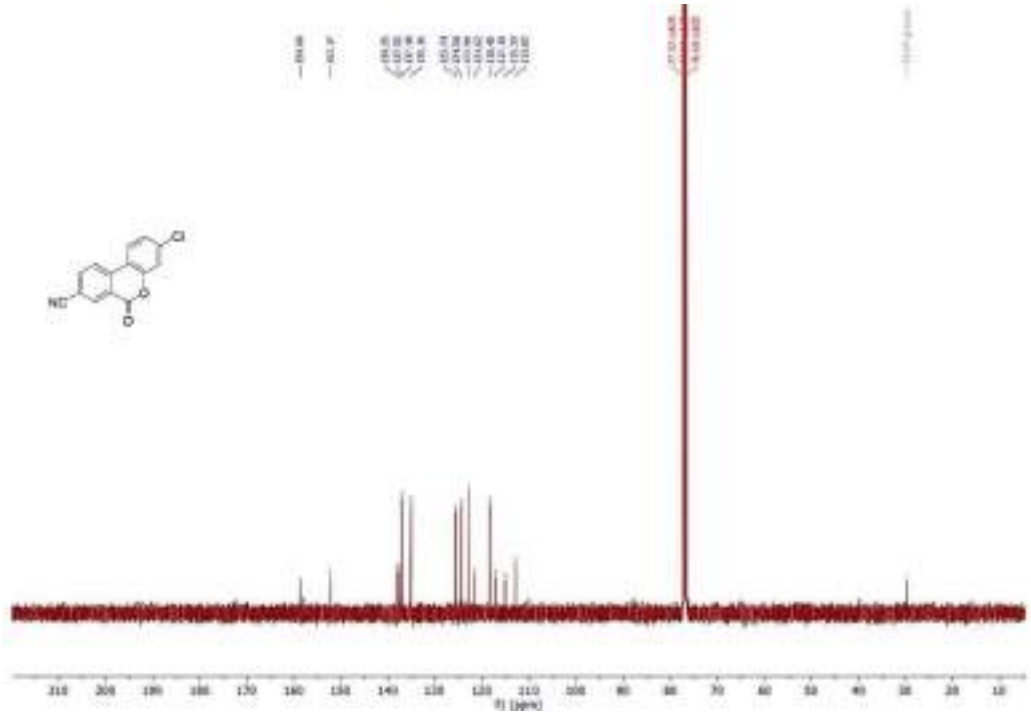

*Figure S7: ^{13}C NMR (101 MHz, $CDCl_3$) of **2***

Synthesis of 6-oxo-3-(4-(trimethylsilyl)phenyl)-6H-benzo[c]chromene-8-carbonitrile (3)

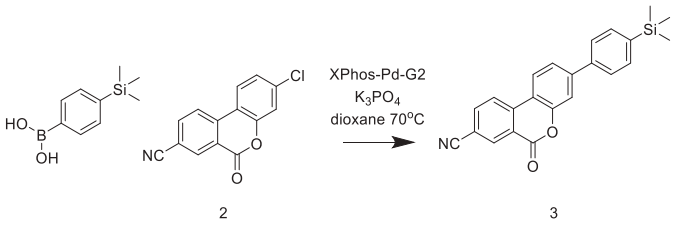

2 3

A three neck flask equipped with reflux condenser was loaded with 11 mg of XPhos-Pd-G2 (0.014 mmol, 3%), 467 mg of $K_3PO_4 \cdot 7H2O$ (1.4 mmol, 3eq), 90 mg of boronic acid (0.69 mmol, 1.5 eq) and dissolved in 8 mL of dry dioxane. The mixture was degassed for 10 minutes under nitrogen before adding 117 mg of **2** (0.46 mmol, 1 eq). The reaction mixture was stirred at 70 °C for 3 hours. The reaction mixture was diluted with 4 mL of ethyl acetate, filtered through a thin pad of celite and concentrated under reduced pressure. The crude obtained was purified via column chromatography on silica gel (CH_2Cl_2/pentane 80:20), yielding 148 mg of product **3** as a white solid (yield 87%).

^{1}H NMR (400 MHz, $CDCl_3$) δ 8.71 (d, *J* = 1.8 Hz, 1H), 8.24 (d, *J* = 8.4 Hz, 1H), 8.13 (d, *J* = 8.3 Hz, 1H), 8.05 (dd, *J* = 8.4, 1.8 Hz, 1H), 7.65 (dp, *J* = 5.4, 1.7 Hz, 6H), 0.32 (s, 9H).

^{13}C NMR (101 MHz, $CDCl_3$) δ 159.37, 152.33, 145.59, 141.52, 138.90, 138.22, 136.98, 135.11, 134.18, 126.35, 123.93, 123.89, 122.87, 121.71, 117.42, 116.11, 115.41, 112.48, -1.17.

HRMS-ESI Orbitrap (m/z): [M+H$^+$] calculated for $C_{23}H_{19}NO_2SiH$, 370.12568; found 370.12826

m.p.: 211.3-213.1 °C

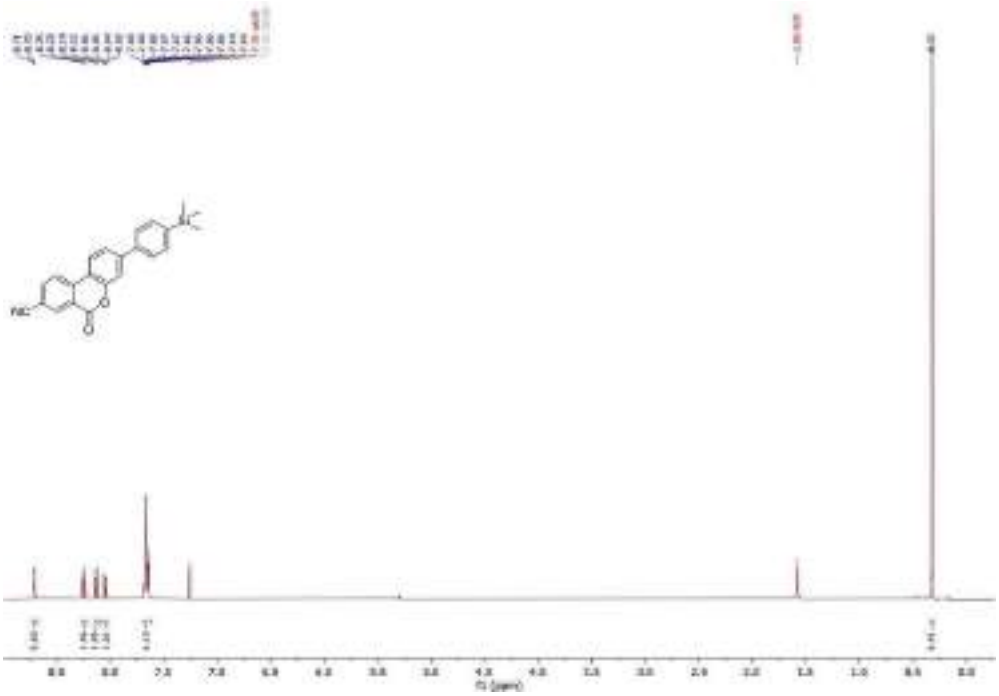

*Figure S8: ^{1}H NMR (400 MHz, $CDCl_3$) of **3***

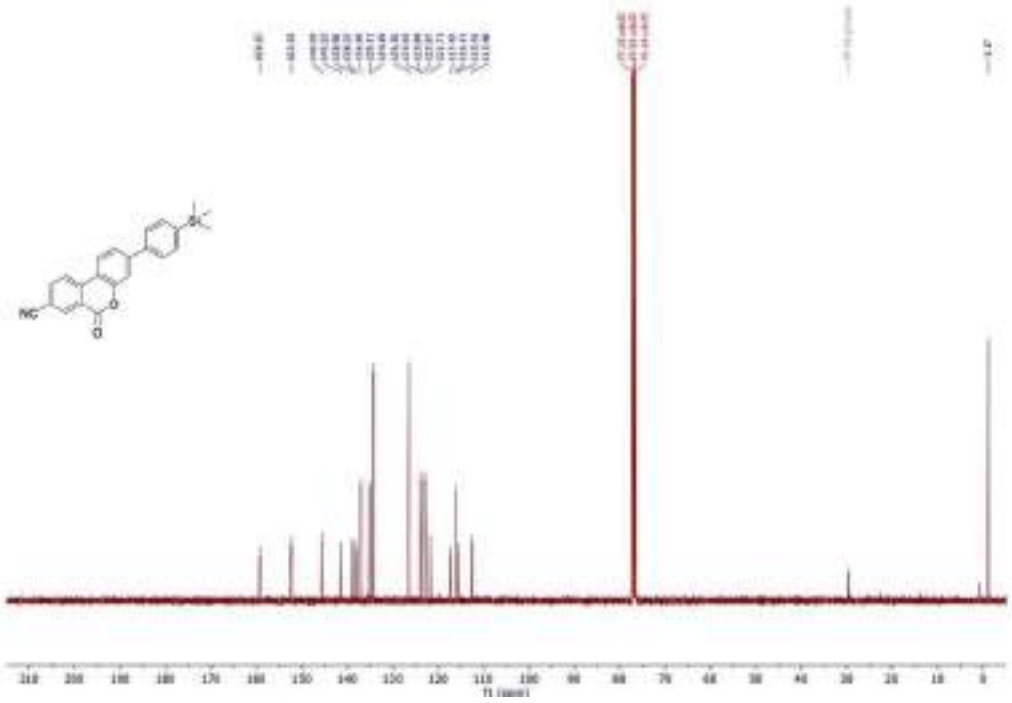

*Figure S9: ^{13}C NMR (101 MHz, $CDCl_3$) of **3***

Synthesis of 3-(4-iodophenyl)-6-oxo-6H-benzo[c]chromene-8-carbonitrile (4)

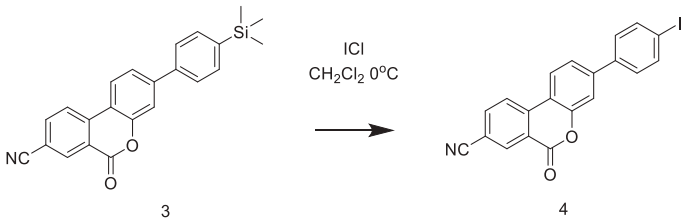

A round bottom flask was loaded with 154 mg of **3** (0.42 mmol, 1 eq) and dissolved in 15 mL of dry CH_2Cl_2. The flask was placed under nitrogen atmosphere and chilled for 10 minutes at 0 °C before adding dropwise 840 uL of 1 M solution of ICl in CH_2Cl_2 (0.84 mmol, 2 eq). The reaction mixture was kept in the dark, stirring at room temperature overnight. Once the reaction was completed, the reaction mixture was first washed with 30 mL of 0.1 M NaOH and, subsequently, with 3x20 mL of brine. After drying the organic phase with Na_2SO_4, the solvent was evaporated, and the crude was recrystallized by solvent diffusion ($CHCl_3$/Pentane), yielding 169 mg of product **4** as a white solid (yield 95%).

^{1}H NMR (400 MHz, CDC_3) δ 8.72 (d, *J* = 1.6 Hz, 1H), 8.25 (d, *J* = 8.5 Hz, 1H), 8.13 (d, *J* = 8.4 Hz, 1H), 8.06 (dd, *J* = 8.4, 1.8 Hz, 1H), 7.85 (d, *J* = 8.4 Hz, 2H), 7.64 – 7.58 (m, 2H), 7.43 – 7.36 (m, 2H).

^{13}C NMR (101 MHz, $CDCl_3$) δ 159.10, 152.34, 144.36, 138.27, 138.12, 137.96, 136.95, 135.08, 128.74, 124.03, 123.52, 122.83, 121.77, 117.26, 115.93, 115.71, 112.67, 94.83.

HRMS-ESI Orbitrap (m/z): [M+H$^+$] calculated for $C_{20}H_{10}INO_2H$, 423.98290; found 423.98250

m.p.: 300.6-302.1 °C

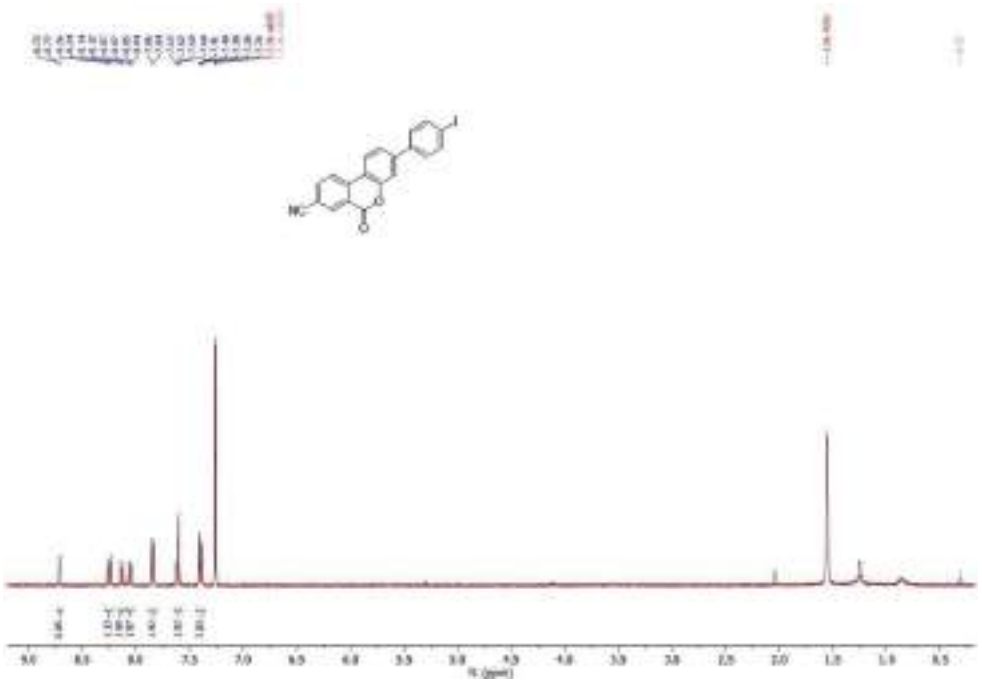

*Figure S10: ^{1}H NMR (400 MHz, $CDCl_3$) of **4***

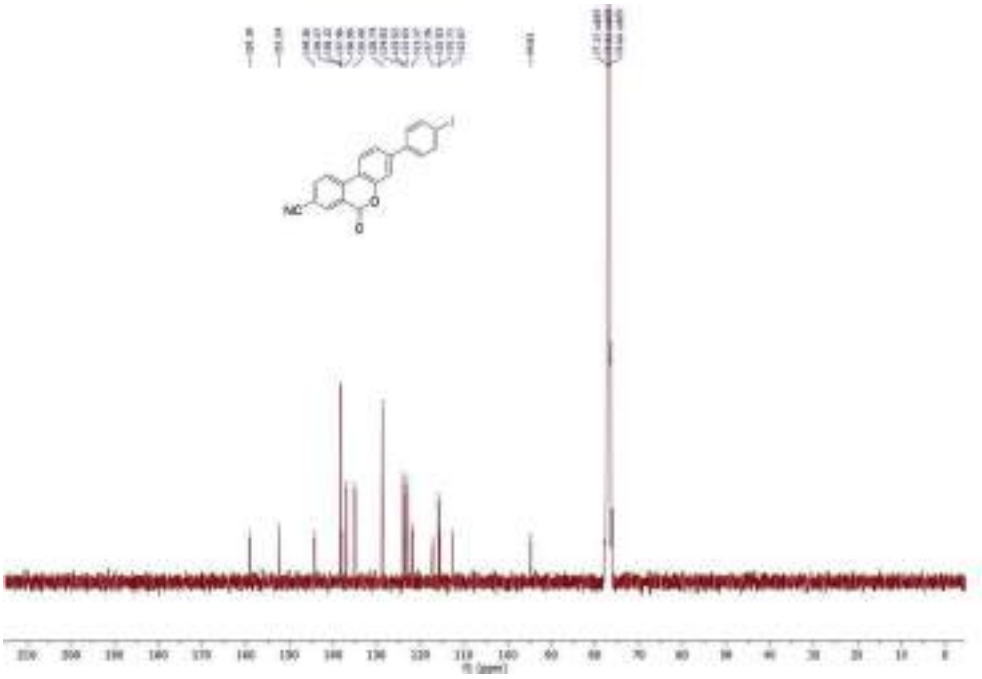

*Figure S11: ^{13}C NMR (101 MHz, $CDCl_3$) of **4***

Synthesis of 6-oxo-3-(4-(4,4,5,5-tetramethyl-1,3,2-dioxaborolan-2-yl)phenyl)-6H-benzo[c]chromene-8-carbonitrile (5)

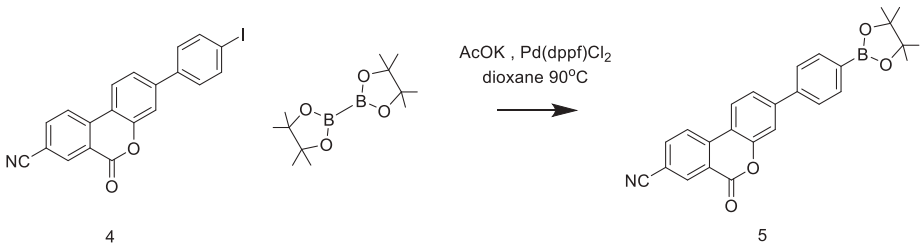

4 5

A three neck flask equipped with reflux condenser was loaded with 168 mg of **4** (0.40 mmol, 1 eq), 119 mg of KOAc (1.20 mmol, 3 eq.), 154 mg of bis(pinacolato)diboron (0.61 mmol, 1.5 eq.) and a catalytic amount of $Pd(dppf)Cl_2$ (11.7 mg, 16 μmol, 4%) under nitrogen atmosphere. After addition of 15 mL of dry and degassed dioxane, the reaction mixture was stirred at 90°C overnight. Next, the solution was cooled down, diluted with dichloromethane and washed with 3x15mL of water, then dried over Na_2SO_4, filtered and concentrated. To remove the excess of bis(pinacolato)diboron, the crude was first washed with pentane and subsequently purified by column chromatography on silica gel (CH_2Cl_2/Heptane 80:20) yielding 25 mg of product **5** as a white solid (yield 15 %).

^{1}H NMR (400 MHz, $CDCl_3$) δ 8.70 (d, *J* = 1.7 Hz, 1H), 8.24 (d, *J* = 8.4 Hz, 1H), 8.12 (d, *J* = 8.3 Hz, 1H), 8.04 (dd, *J* = 8.4, 1.8 Hz, 1H), 7.94 (d, *J* = 8.2 Hz, 2H), 7.69 – 7.63 (m, 4H), 1.37 (s, 12H).

^{13}C NMR (101 MHz, $CDCl_3$) δ 159.30, 152.33, 145.44, 141.17, 138.17, 136.98, 135.57, 135.13, 126.37, 123.99, 123.91, 122.91, 121.79, 117.41, 116.31, 115.61, 112.55, 84.04, 24.88.

HRMS-ESI Orbitrap (m/z): [M+H$^+$] calculated for $C_{26}H_{22}BNO_4H$, 424.17147; found 424.17054

m.p.: 229.5-231.2 °C

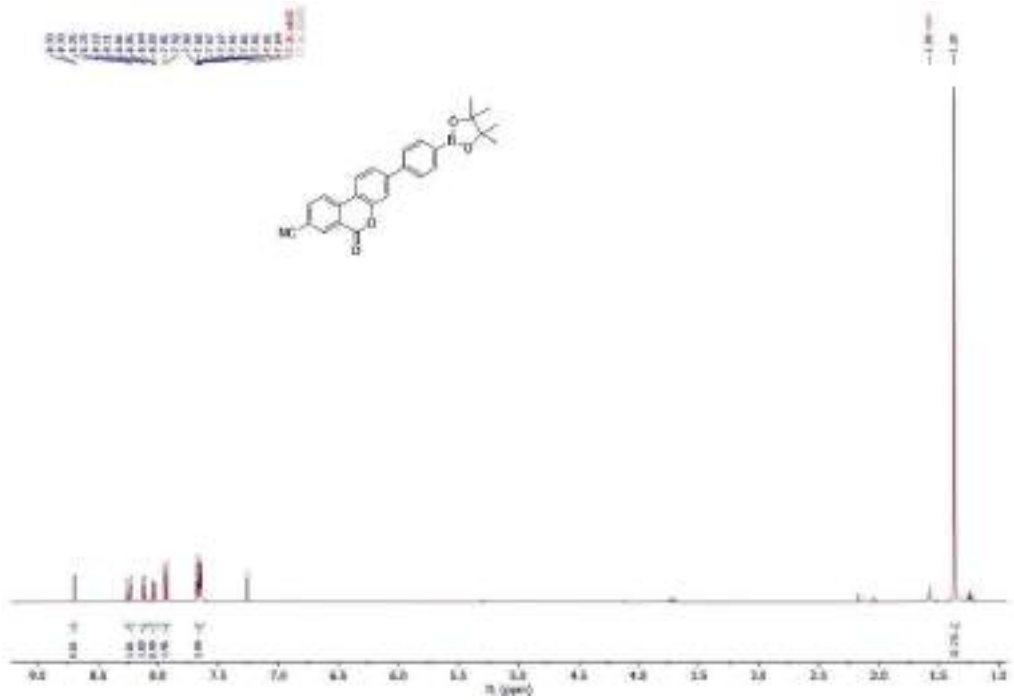

*Figure S12: ^{1}H NMR (400 MHz, $CDCl_3$) of **5***

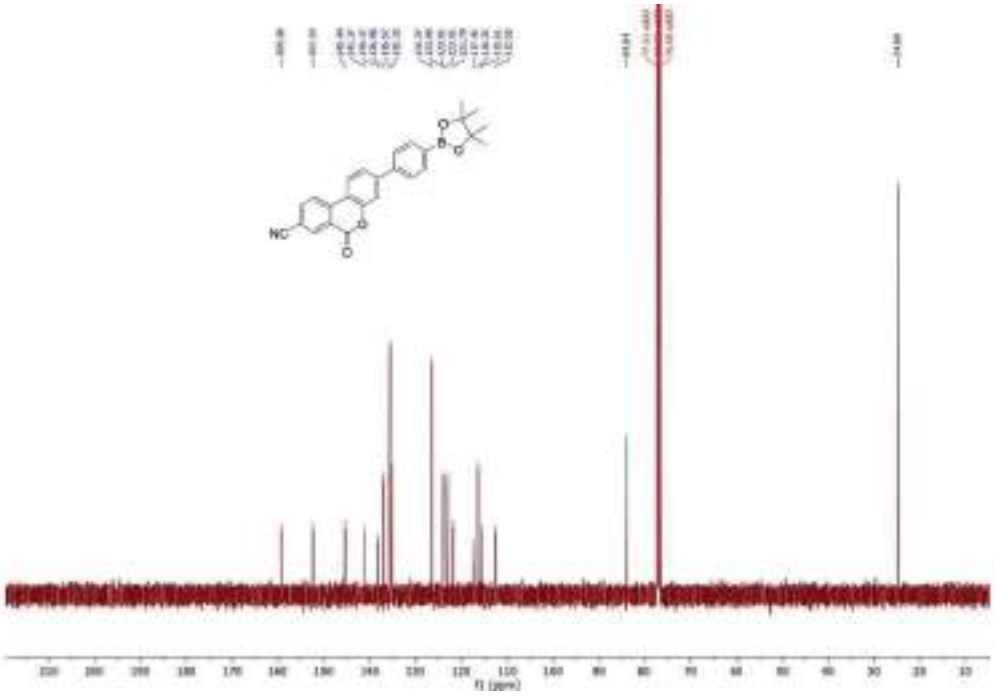

*Figure S13: ^{13}C NMR (101 MHz, $CDCl_3$) of **5***

Synthesis of dendron precursor (6)

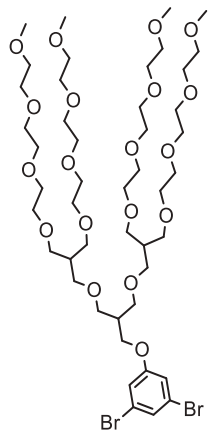

6

The procedure used for the synthesis of the dendron precursor **6** has been reported by Lee and co-workers.[49]

^{1}H NMR (400 MHz, $CDCl_3$) δ 7.22-7.13 (m, 1H), 7.06 – 6.88 (m, 2H), 3.97 (t, *J* = 5.4 Hz, 2H), 3.67 – 3.38 (m, 64H), 3.37 (d, *J* = 1.5 Hz, 13H), 2.32 (dd, *J* = 7.4, 4.0 Hz, 1H), 2.21 – 2.09 (m, 2H).

HRMS-ESI Orbitrap (m/z): [M+H$^+$] calculated for $C_{46}H_{84}Br_2O_{19}H$, 1101.40259; found 1101.40437

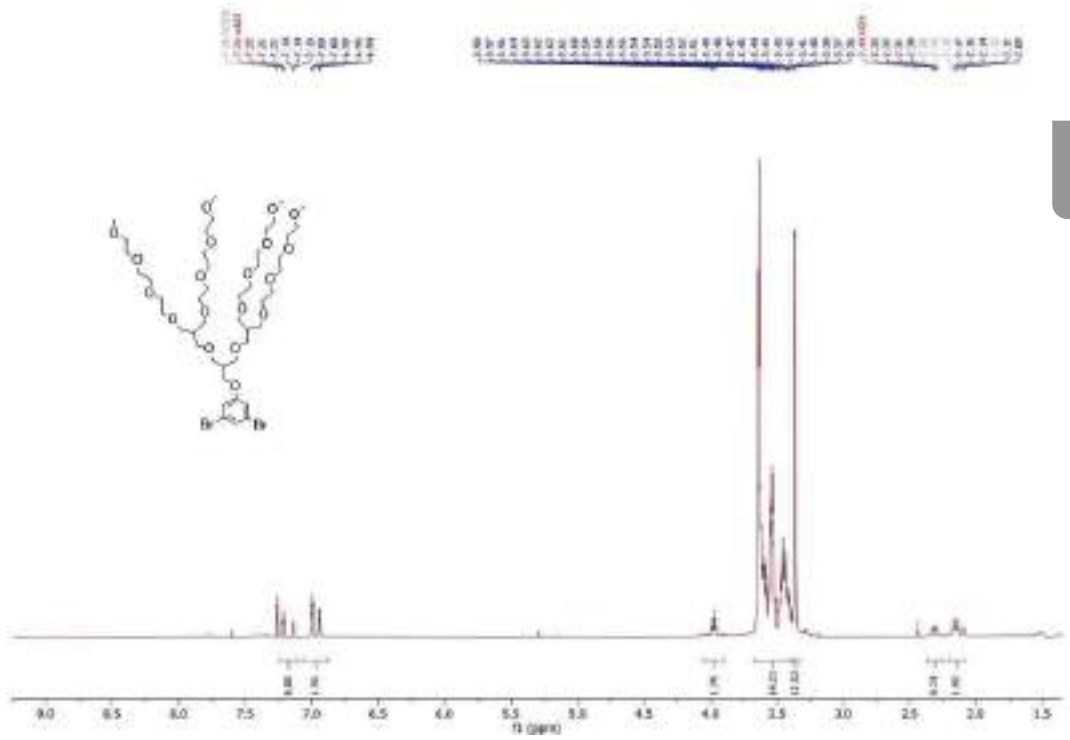

*Figure S14: ^{1}H NMR (400 MHz, $CDCl_3$) of **6***

Synthesis of VsA monomer

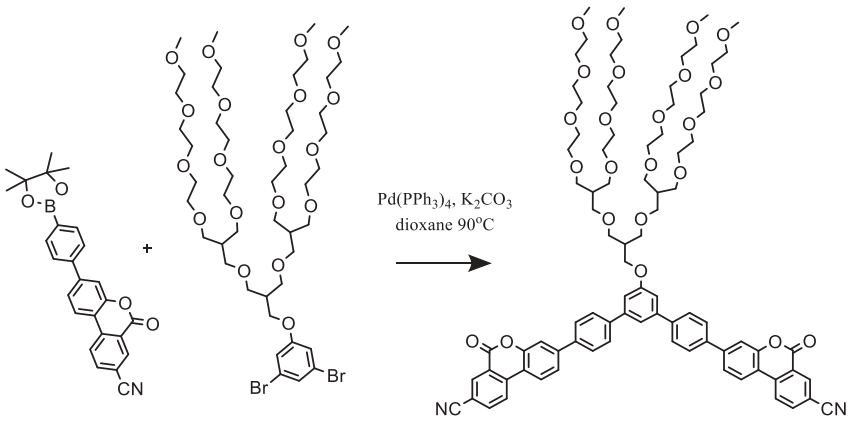

5 6 VsA

In a three neck flask equipped with reflux condenser was loaded with 25 mg of **5** (0.06 mmol, 3 eq.), 22 mg of **6** (0.02 mmol, 1 eq), $Pd(PPh_3)_4$ (2.5 mg, 10%), 2 mL of a 2M aqueous solution of K_2CO_3 and 5 mL of dioxane. The reaction mixture was stirred vigorously while degassing under nitrogen for 15 minutes. Next, the reaction mixture was kept under inert atmosphere, stirring for 30 hours at 90°C. After checking product formation by TLC chromatography, the flask was cooled to room temperature, the two phases were separated and the aqueous phase was extracted with ethyl acetate. The combined organic layers were washed with water, dried over Na_2SO_4, filtered and concentrated. The crude was purified by preparative TLC chromatography (silica, ethyl acetate/methanol 95:5). Yield: 9 mg (29%) of **VsA** as a pale yellow solid.

^{1}H NMR (400 MHz, $CDCl_3$) δ 8.72 (d, *J* = 1.8 Hz, 2H), 8.27 (d, *J* = 8.5 Hz, 2H), 8.16 (d, *J* = 8.4 Hz, 2H), 8.06 (dd, *J* = 8.4, 1.8 Hz, 2H), 7.85 – 7.75 (m, 8H), 7.75 – 7.69 (m, 4H), 7.49 (t, *J* = 1.5 Hz, 1H), 7.21 (d, *J* = 1.5 Hz, 2H), 4.17 (d, *J* = 5.7 Hz, 2H), 3.67 – 3.44 (m, 64H), 3.35 (s, 12H), 2.51 – 2.38 (m, 1H), 2.24 – 2.17 (m, 2H).

^{13}C NMR (101 MHz, $CDCl_3$) δ 159.37, 152.33, 145.62, 138.66, 138.22, 136.98, 135.12, 129.19, 128.93, 128.81, 127.87, 127.12, 127.07, 123.92, 122.88, 121.73, 117.42, 116.16, 115.37, 112.48.

HSQC

δ (ppm)

70.68	3.63
122.97	8.26
124.14	8.14
127.29	7.67
129.12	7.51
135.26	8.71
137.25	8.04

HRMS-ESI Orbitrap (m/z): [M+Na^+] calculated for C86H104N2O23Na, 1555.6920; found 1555.6922

UV-VIS: (CH_3CN) λ_{max}=284 nm ($\log_{10}\varepsilon$ 4.5); 357 nm ($\log_{10}\varepsilon$ 4.3)

FTIR: ν (CO) 1727 cm^{-1} (sh, s); ν (CN) 2233 cm^{-1}(sh, w)

m.p.: 149.4-151.2 °C

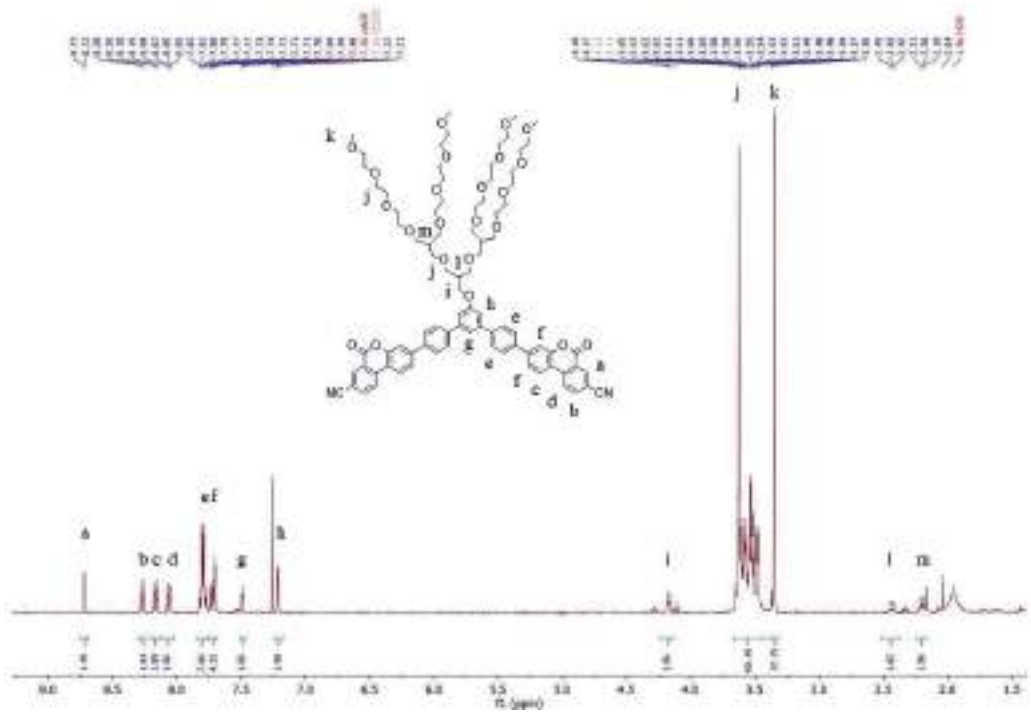

*Figure S15: ^{1}H NMR (400 MHz, $CDCl_3$) of **VsA***

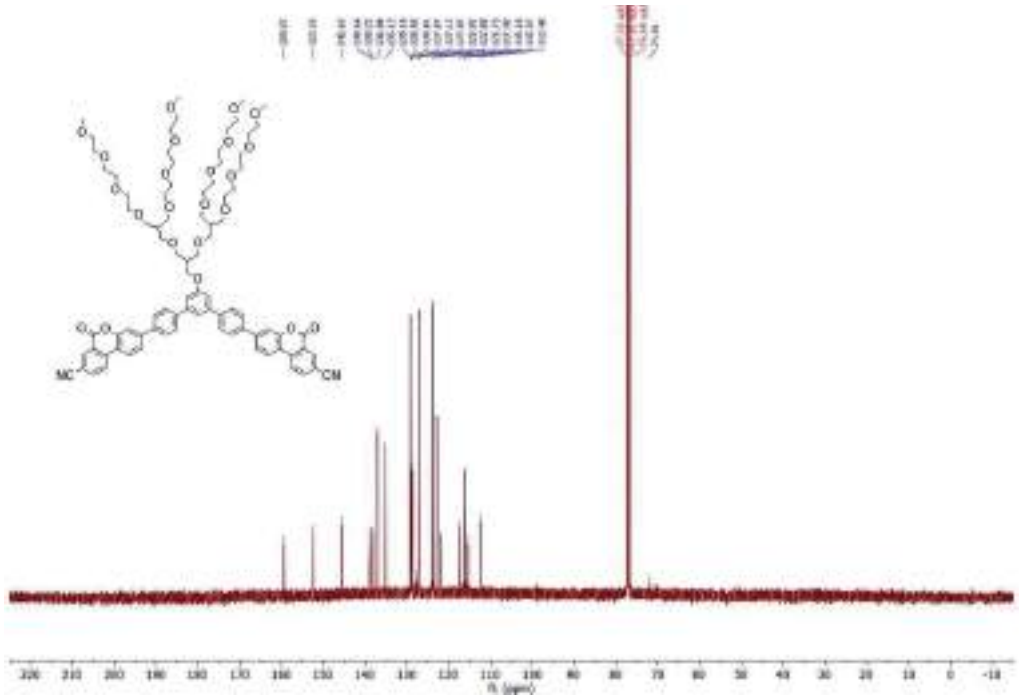

*Figure S16: ^{13}C NMR (101 MHz, $CDCl_3$) of **VsA***

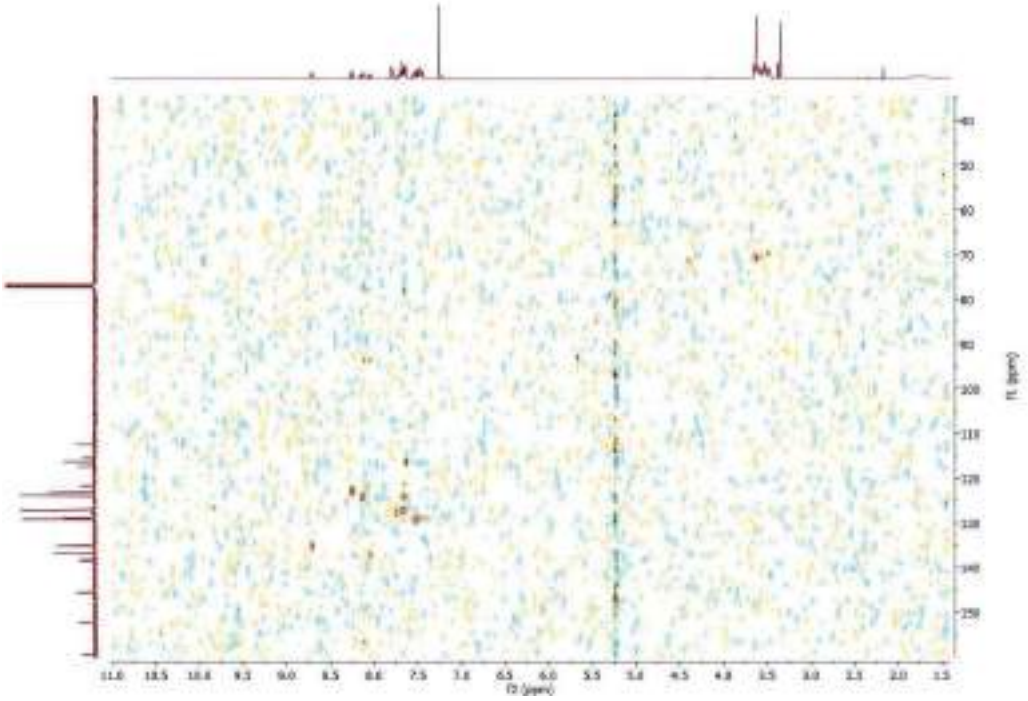

*Figure S17:HSQC ($CDCl_3$) of **VsA***

2.7. References

2.7.1 Front page illustration (Chapter 2)

Goodsell, D. S. *Biosites: Muscle.* (PDB-101, 2005).

2.7.2 References (Chapter 2)

1 van der Zwaag, D. & Meijer, E. W. Self-organization. Fueling connections between chemistry and biology. *Science* **349**, 1056-1057, doi:10.1126/science.aad0194 (2015).

2 Howard, J. & Hyman, A. A. Dynamics and mechanics of the microtubule plus end. *Nature* **422**, 753-758, doi:10.1038/nature01600 (2003).

3 Hurtgen, D., Vogel, S. K. & Schwille, P. Cytoskeletal and Actin-Based Polymerization Motors and Their Role in Minimal Cell Design. *Adv Biosyst* **3**, e1800311, doi:10.1002/adbi.201800311 (2019).

4 Lubbe, A. S., Wezenberg, S. J. & Feringa, B. L. Artificial microtubules burst with energy. *Proc Natl Acad Sci U S A* **114**, 11804-11805, doi:10.1073/pnas.1716868114 (2017).

5 Fredy, J. W. *et al.* Molecular photoswitches mediating the strain-driven disassembly of supramolecular tubules. *Proc Natl Acad Sci U S A* **114**, 11850-11855, doi:10.1073/pnas.1711184114 (2017).

6 Krieg, E., Bastings, M. M., Besenius, P. & Rybtchinski, B. Supramolecular Polymers in Aqueous Media. *Chem Rev* **116**, 2414-2477, doi:10.1021/acs.chemrev.5b00369 (2016).

7 Cleary, J. M. & Hancock, W. O. Molecular mechanisms underlying microtubule growth dynamics. *Curr Biol* **31**, R560-R573, doi:10.1016/j.cub.2021.02.035 (2021).

8 Akhmanova, A., Stehbens, S. J. & Yap, A. S. Touch, grasp, deliver and control: functional cross-talk between microtubules and cell adhesions. *Traffic* **10**, 268-274, doi:10.1111/j.1600-0854.2008.00869.x (2009).

9 van der Zwaag, D., de Greef, T. F. & Meijer, E. W. Programmable Supramolecular Polymerizations. *Angew Chem Int Ed Engl* **54**, 8334-8336, doi:10.1002/anie.201503104 (2015).

10 Levin, A. *et al.* Elastic instability-mediated actuation by a supra-molecular polymer. *Nature Physics* **12**, 926-930, doi:10.1038/nphys3808 (2016).

11 Fu, M. *et al.* Disassembly of Dipeptide Single Crystals Can Transform the Lipid Membrane into a Network. *ACS Nano* **11**, 7349-7354, doi:10.1021/acsnano.7b03468 (2017).

12 Cera, L. *et al.* PolyWhips: Directional Particle Transport by Gradient-Directed Growth and Stiffening of Supramolecular Assemblies. *Adv Mater* **29**, doi:10.1002/adma.201604430 (2017).

13 Theriot, J. A. The polymerization motor. *Traffic* **1**, 19-28, doi:10.1034/j.1600-0854.2000.010104.x (2000).

14 Asbury, C. L., Gestaut, D. R., Powers, A. F., Franck, A. D. & Davis, T. N. The Dam1 kinetochore complex harnesses microtubule dynamics to produce force and movement. *Proc Natl Acad Sci U S A* **103**, 9873-9878, doi:10.1073/pnas.0602249103 (2006).

15 Powers, A. F. *et al.* The Ndc80 kinetochore complex forms load-bearing attachments to dynamic microtubule tips via biased diffusion. *Cell* **136**, 865-875, doi:10.1016/j.cell.2008.12.045 (2009).

16 Footer, M. J., Kerssemakers, J. W., Theriot, J. A. & Dogterom, M. Direct measurement of force generation by actin filament polymerization using an optical trap. *Proc Natl Acad Sci U S A* **104**, 2181-2186, doi:10.1073/pnas.0607052104 (2007).

17 Hill, T. L. Theoretical problems related to the attachment of microtubules to kinetochores. *Proc Natl Acad Sci U S A* **82**, 4404-4408, doi:10.1073/pnas.82.13.4404 (1985).

18 Asbury, C. L., Tien, J. F. & Davis, T. N. Kinetochores' gripping feat: conformational wave or biased diffusion? *Trends Cell Biol* **21**, 38-46, doi:10.1016/j.tcb.2010.09.003 (2011).

19 Huang, Z. *et al.* Pulsating tubules from noncovalent macrocycles. *Science* **337**, 1521-1526, doi:10.1126/science.1224741 (2012).

20 Ryu, J. H., Oh, N. K. & Lee, M. Tubular assembly of amphiphilic rigid macrocycle with flexible dendrons. *Chem Commun (Camb)*, 1770-1772, doi:10.1039/b419213c (2005).

21 Kim, H. J. *et al.* Self-dissociating tubules from helical stacking of noncovalent macrocycles. *Angew Chem Int Ed Engl* **49**, 8471-8475, doi:10.1002/anie.201003779 (2010).

22 Frisch, H. & Besenius, P. pH-switchable self-assembled materials. *Macromol Rapid Commun* **36**, 346-363, doi:10.1002/marc.201400623 (2015).

23 Wang, G. & Liu, S. Strategies to Construct a Chemical-Fuel-Driven Self-Assembly. *ChemSystemsChem* **2**, doi:10.1002/syst.201900046 (2020).

24 Boekhoven, J., Hendriksen, W. E., Koper, G. J., Eelkema, R. & van Esch, J. H. Transient assembly of active materials fueled by a chemical reaction. *Science* **349**, 1075-1079, doi:10.1126/science.aac6103 (2015).

25 van Ravensteijn, B. G. P., Hendriksen, W. E., Eelkema, R., van Esch, J. H. & Kegel, W. K. Fuel-Mediated Transient Clustering of Colloidal Building Blocks. *J Am Chem Soc* **139**, 9763-9766, doi:10.1021/jacs.7b03263 (2017).

26 Tena-Solsona, M. *et al.* Non-equilibrium dissipative supramolecular materials with a tunable lifetime. *Nat Commun* **8**, 15895, doi:10.1038/ncomms15895 (2017).

27 Grotsch, R. K. *et al.* Pathway Dependence in the Fuel-Driven Dissipative Self-Assembly of Nanoparticles. *J Am Chem Soc* **141**, 9872-9878, doi:10.1021/jacs.9b02004 (2019).

28 Grotsch, R. K. *et al.* Dissipative Self-Assembly of Photoluminescent Silicon Nanocrystals. *Angew Chem Int Ed Engl* **57**, 14608-14612, doi:10.1002/anie.201807937 (2018).

29 Heuser, T., Steppert, A. K., Lopez, C. M., Zhu, B. & Walther, A. Generic concept to program the time domain of self-assemblies with a self-regulation mechanism. *Nano Lett* **15**, 2213-2219, doi:10.1021/nl5039506 (2015).

30 Carlson, E. J., Riel, A. M. S. & Dahl, B. J. Donor–acceptor biaryl lactones: pH induced molecular switches with intramolecular charge transfer modulation. *Tetrahedron Letters* **53**, 6245-6249, doi:10.1016/j.tetlet.2012.09.016 (2012).

31 Sorrenti, A., Leira-Iglesias, J., Markvoort, A. J., de Greef, T. F. A. & Hermans, T. M. Non-equilibrium supramolecular polymerization. *Chem Soc Rev* **46**, 5476-5490, doi:10.1039/c7cs00121e (2017).

32 Wang, Y., Huang, Z., Kim, Y., He, Y. & Lee, M. Guest-driven inflation of self-assembled nanofibers through hollow channel formation. *J Am Chem Soc* **136**, 16152-16155, doi:10.1021/ja510182x (2014).

33 Vogel, E. & Kiefer, W. Investigation of the metal adsorbate interface of the system silver coumarin and silver hydrocoumarin by means of surface enhanced Raman spectroscopy. *Fresenius' Journal of Analytical Chemistry* **361**, 628-630, doi:10.1007/s002160050972 (1998).

34 Moriyama, T. *et al.* Polarization Raman Imaging of Organic Monolayer Islands for Crystal Orientation Analysis. *ACS Omega* **6**, 9520-9527, doi:10.1021/acsomega.0c06313 (2021).

35 Ji, X. *et al.* Reactivity triggered by an organic microcrystal interface: a case study involving an environmentally benign, aromatic boric acid reaction. *Chem Commun (Camb)* **56**, 11114-11117, doi:10.1039/d0cc04805d (2020).

36 Kumar, D., Thipparaboina, R., Sreedhar, B. & Shastri, N. R. The role of surface chemistry in crystal morphology and its associated properties. *CrystEngComm* **17**, 6646-6650, doi:10.1039/c5ce01182e (2015).

37 Borsley, S., Leigh, D. A. & Roberts, B. M. W. Molecular Ratchets and Kinetic Asymmetry: Giving Chemistry Direction. *Angew Chem Int Ed Engl* **63**, e202400495, doi:10.1002/anie.202400495 (2024).

38 Altomare, A. *et al.* EXPO2013: a kit of tools for phasing crystal structures from powder data. *Journal of Applied Crystallography* **46**, 1231-1235 (2013).

39 Neese, F. The ORCA program system. *Wiley Interdisciplinary Reviews: Computational Molecular Science* **2**, 73-78 (2012).

40 Becke, A. D. Densityfunctional thermochemistry. III. the role of exact exchange. 98 (7): 5648–5652. *The Journal of Chemical Physics. doi: https://doi.org/10.1063/1.464913* (1993).

41 Lee, C., Yang, W. & Parr, R. G. Development of the Colle-Salvetti correlation-energy formula into a functional of the electron density. *Physical review B* **37**, 785 (1988).

42 Vosko, S. H., Wilk, L. & Nusair, M. Accurate spin-dependent electron liquid correlation energies for local spin density calculations: a critical analysis. *Canadian Journal of physics* **58**, 1200-1211 (1980).

43 Stephens, P. J., Devlin, F. J., Chabalowski, C. F. & Frisch, M. J. Ab initio calculation of vibrational absorption and circular dichroism spectra using density functional force fields. *The Journal of physical chemistry* **98**, 11623-11627 (1994).

44 Weigend, F. & Ahlrichs, R. Balanced basis sets of split valence, triple zeta valence and quadruple zeta valence quality for H to Rn: Design and assessment of accuracy. *Physical Chemistry Chemical Physics* **7**, 3297-3305 (2005).

45 Grimme, S., Ehrlich, S. & Goerigk, L. Effect of the damping function in dispersion corrected density functional theory. *Journal of computational chemistry* **32**, 1456-1465 (2011).

46 Grimme, S., Antony, J., Ehrlich, S. & Krieg, H. A consistent and accurate ab initio parametrization of density functional dispersion correction (DFT-D) for the 94 elements H-Pu. *The Journal of chemical physics* **132** (2010).

47 Neese, F., Wennmohs, F., Hansen, A. & Becker, U. Efficient, approximate and parallel Hartree–Fock and hybrid DFT calculations. A 'chain-of-spheres' algorithm for the Hartree–Fock exchange. *Chemical Physics* **356**, 98-109 (2009).

48 Weigend, F. Accurate Coulomb-fitting basis sets for H to Rn. *Physical chemistry chemical physics* **8**, 1057-1065 (2006).

49 Kim, H.-J., Zin, W.-C. & Lee, M. Anion-directed self-assembly of coordination polymer into tunable secondary structure. *Journal of the American Chemical Society* **126**, 7009-7014 (2004).

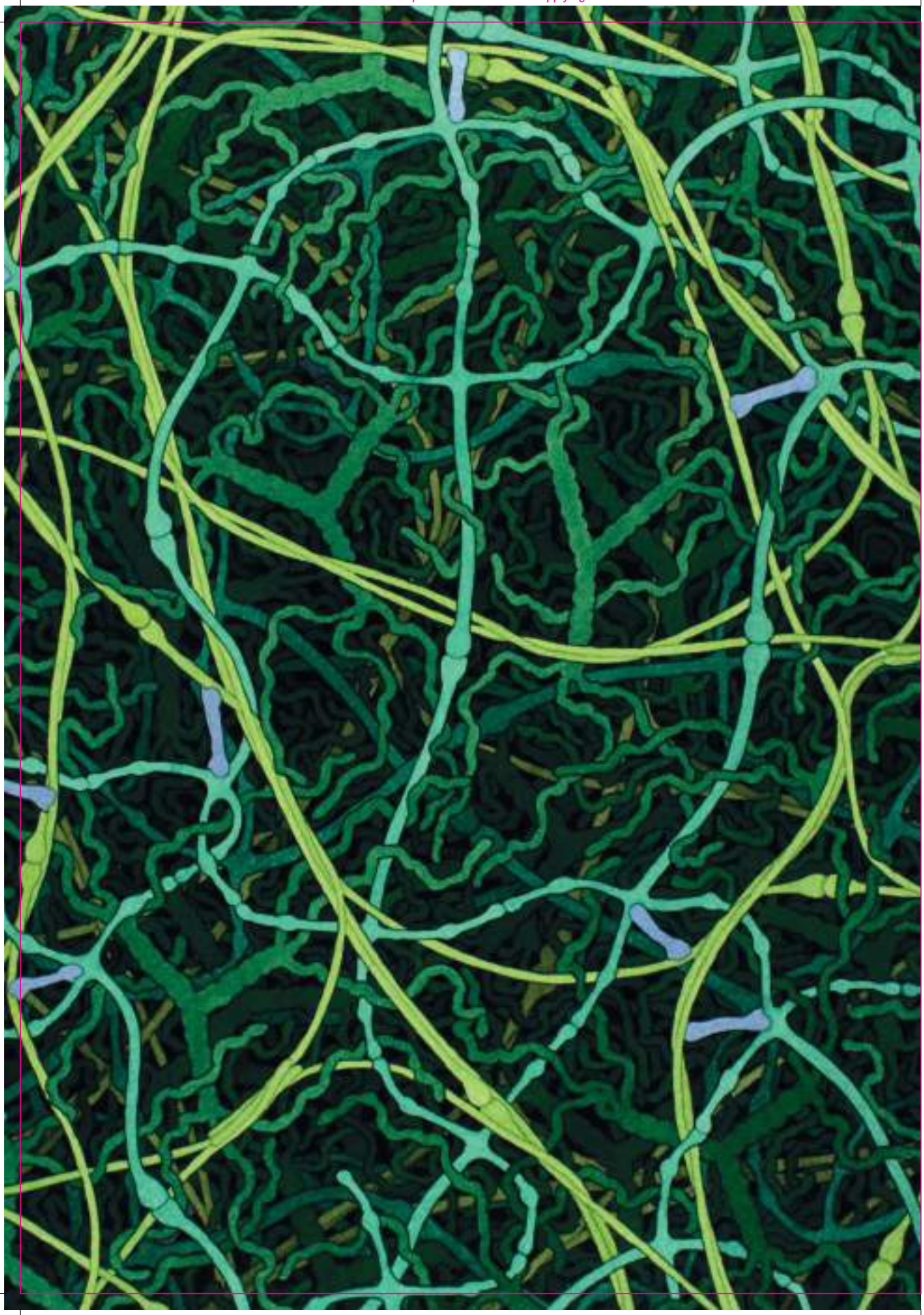

3

Pre-organization effect on photoacids in supramolecular confinement

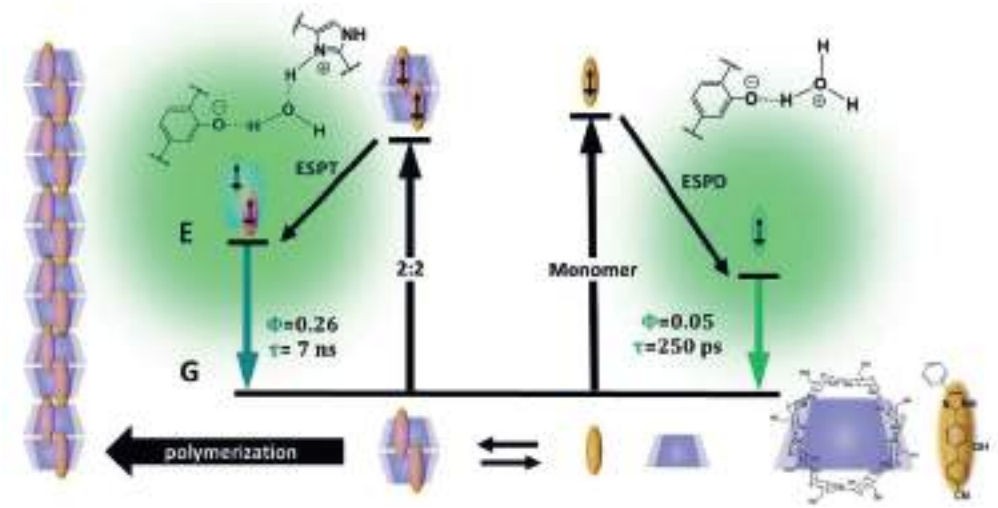

ABSTRACT:

The photoluminescence of photoacids in supramolecular assemblies provides essential information for studying proton transfer processes in biologically relevant confinement. In this chapter, we propose a new strategy to activate intermolecular excited state proton transfer in the hydrophobic cavities of cyclodextrin based nanotubes. This was achieved by designing an amphoteric probe with photo-acidic properties which undergoes a pKa inversion in the excited state. Despite this photophysical behaviour, intramolecular proton transfer does not occur because of the separation between proton donor and acceptor sites in the molecular design. However, in the presence of γ-cyclodextrin, the probe assembles into guest pairs, pre-organizing the transfer between neighbouring molecules. The anomalous effect of confinement on quantum yield and lifetime indicates a mechanistic transition from an excited state protolytic dissociation to intermolecular excited state proton transfer. A detailed spectroscopic investigation of the assembly mechanism and solvent isotope substitution experiments support the role of a pre-organization effect reminiscent of enzymatic activation influencing the adiabatic reaction in the excited state.

L.C. Pantaleone†, R. Hutchings, J. Martinelli, W.R. Browne, T. Kudernac*; *manuscript in preparation.*

3.1. Introduction

Proton transfer (PT) is ubiquitous in biochemical processes, as shown by studies underpinning the importance of this phenomenon in a wide variety of contexts, from bio-catalysis and transport channels to genetic replication.[1,2] An approach to investigate these processes in biologically relevant confinements is using spectroscopic probes based on excited state proton transfer (ESPT).[3] The proton transfer in the excited state can occur intramolecularly (ESIPT), generally followed by tautomer/isomer formation, or bimolecularly, in the case of acids (or bases) that undergo a significant increase of their dissociation constants upon electronic excitation (ESPD).[4] The photoluminescence of these probes offers a fast and sensitive physical method to observe the influence of the microenvironment on proton transfer and shows that the effects of confinement largely depend upon the molecularity of these mechanisms. The ESIPT, which does not depend upon an external proton donor or acceptor, was reported in the cavities of inclusion complexes, micelles and nanotubes, where it benefits from the absence of competing structured hydrogen bond networks and even in organic solvents and soft condensed matter.[5-8] By contrast, ESPD of photoacids is generally deactivated in the same conditions since interfacial water in hydrophobic confinements hardly engages in the proton transfer, and when it does, the viscosity of these water nanopools promotes the geminal recombination in the excited state.[9-11] Several approaches have been proposed to promote intermolecular proton transfer, for example, by transferring the proton to an external base or by self-aggregation of amphoteric compounds.[12-15] However, the possibility of activating this mechanism by supramolecular confinement has been received less attention despite tailored structured microenvironments being highly exploited to direct the PT in biological examples, e.g., protonation of proximal residues in protein binding pockets or multiple proton conduction between DNA base pairs.[16-18] Therefore, gathering proton donor and acceptor sites in hydrophobic cavities represents a new strategy to revert the ESPT deactivation trend observed in the confinement of photoacids.

With this idea in mind, we designed an amphoteric fluorescent probe (G_1) with photoacidic properties. This chapter will explore the effects of pre-organization and confinement on PT by studying how the co-assembly with γ-cyclodextrin (γ-CD) impacts the photophysical behaviour of G_1 in water. Besides the biological relevance, successful confinement of bimolecular ESPT emitters would allow combining the properties that favoured the diffusion of ESIPT-based materials

(e.g., aggregation-induced emission, photostability, anisotropic luminescence) with new effects that may emerge from molecular recognition in supramolecular assemblies.[19-21] In this context of research, exploring ESPT in nanotubes channels not only provides a framework for studying fundamental biochemical processes but learning to influence the photochemical pathway of this class of emitters may lead to novel strategies to direct chemical reactivity using tailored structured microenvironments.

3.2. Results and Discussion

3.2.1 Spectroscopic pH titrations

Spectroscopic titrations were used to investigate the photophysical behaviour of G_1 in water and estimate the pK_a of the probe in the ground and excited state. The dependence of the electronic absorption of G_1 in pH (Figure 1a-b) shows two distinct acid/base equilibria, corresponding to the titration of the basic imidazole site and the acidic phenol. The acid/base equilibrium of imidazole is consistent with a $pKa_1=4.1\pm0.1$, whereas the titration indicates a pKa_2 of 9.7 ± 0.2 for the phenolic proton (Figure 1b). These transitions were respectively identified by a hypsochromic shift upon formation of the imidazolium cation (C) ($\lambda_{max}=314$ nm), and by the coalescence of the absorption bands at $\lambda=307$ nm and $\lambda=358$ nm upon the protonation of the phenolate anion (A) (Figure 1a-b,d). The appearance of the neutral form (N), which absorbs with $\lambda_{max}=338$ nm, resulted in both titrations in an increase in light scattering due to the low solubility of this species.

The spectroscopic titration in the presence of γ-CD showed little or no influence on the acid/base chemistry ($pKa_1=4.4\pm0.3$, $pKa_2=9.7\pm0.2$), despite the neutral form of the G_1 showing increased solubility and changes in its absorption spectrum upon addition of the cyclodextrin (Supplementary Figure 1).

The pH dependence of fluorescence reflects the acid base chemistry of the excited state (Figure 1a,c-d). Comparing emission spectra at pH 8 and pH 11, a similar spectrum is observed upon photoexcitation of the neutral and anionic forms of G_1 (Figure 1d). Indeed, both emissions originate from the radiative relaxation of the same species (A*), indicating a proton transfer in the excited state upon photoexcitation of neutral G_1. Upon protonation of the imidazole ring in the ground state the quantum yield of emission increases significantly ($\phi_N=0.05$, $\phi_C=0.23$) (Figure 1c,d).

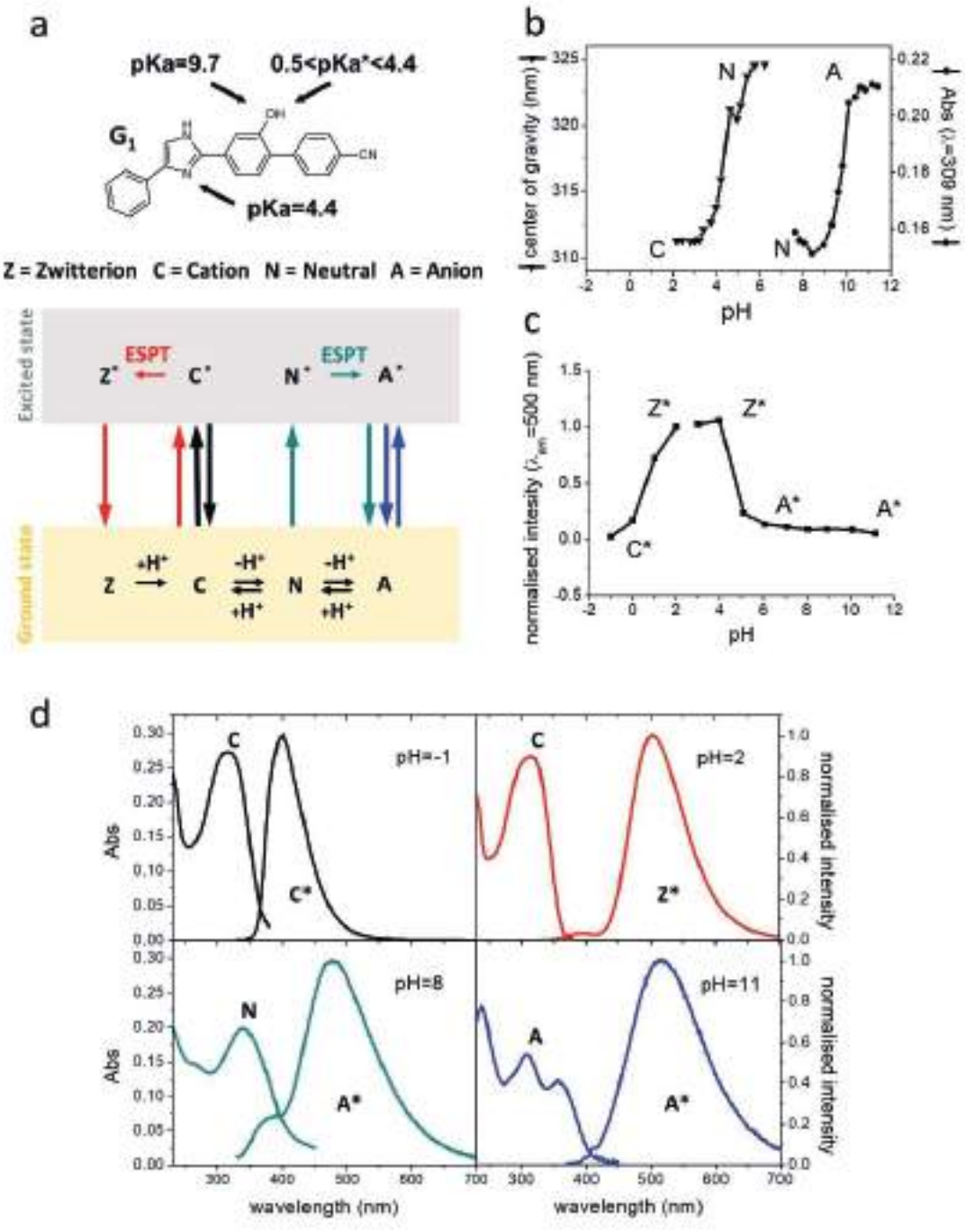

Figure 1: (a) The photophysical behaviour of G_1 in water is characterized by a pKa inversion between ground and excited states. (b) pH titration of G_1 in the excited state. (c) pH titration of G_1 in the ground state. (d) Absorption and emission spectra of G_1 at selected pHs.

The positive charge developed on the cation increases the acidity of the phenol group in the excited state, ESPT is promoted, and the emission occurs from the stabilised zwitterion (Z*).

Titration of the phenolic proton in the excited state was observed around pKa*~0.5 (Figure 1c). In this pH range, the band corresponding to the emission from the zwitterion was suppressed and a new emission was formed characterized by a reduced Stokes shift, which was assigned to the relaxation from the cationic form of G_1 (C*)(Figure 1d). The latter spectral transition occurred without changes in the electronic absorption.

Besides confirming the photoacidic properties of G_1, these experimental results show a pKa inversion between the ground and excited states. The fact that the absorption of the neutral form and the emission of the zwitterion were detected without observing the formation of the corresponding species in the excited (N*) and ground states (Z) means that the phenol is less acidic than the imidazolium ion in the ground state but roles are inverted upon photoexcitation (Figure 1d). Determination of ΔpKa between ground and excited states using direct titration or the Förster cycle was not possible, since both methods require the spectroscopic observation of the transient species (N*).[22] However, considering the pKa(s) of titrated species as bounds of an interval for the transient one, we can confirm that upon photoexcitation of the neutral form of G_1, the phenol undergoes a significant increase in acidity estimated between 5.6 and 9.2 units of pKa.

3.2.2 Excimer formation by aggregation in water

During the spectroscopic titrations we observed the presence of a shoulder in the emission spectra (λ_{max}=368 nm) over the pH range dominated by the N species (5<pH<9)(Figure 1d). The fact that the ratio between these two bands is not significantly affected in this range of acidity excluded an additional acid/base equilibrium. The hypothesis of a double emission from the excitation of N, which is possible in some ESPT emitters, was also discarded because the photoluminescence of G_1 was found to be dependent on the excitation wavelength (Figure 2a). This behaviour means that G_1 must exist in two distinct forms in the ground state, which can be usually explained by the presence of a conformational equilibrium or by self-aggregation.[23] The latter option proved to be the case since it was found that the ratio of intensities of the two bands was affected by the fluorophore concentration and by the ionic strength of buffered solutions, suggesting that the lack of charge and the aromatic structure of G_1 make the N form prone to assemble in water (Figure 2b). Promoting the

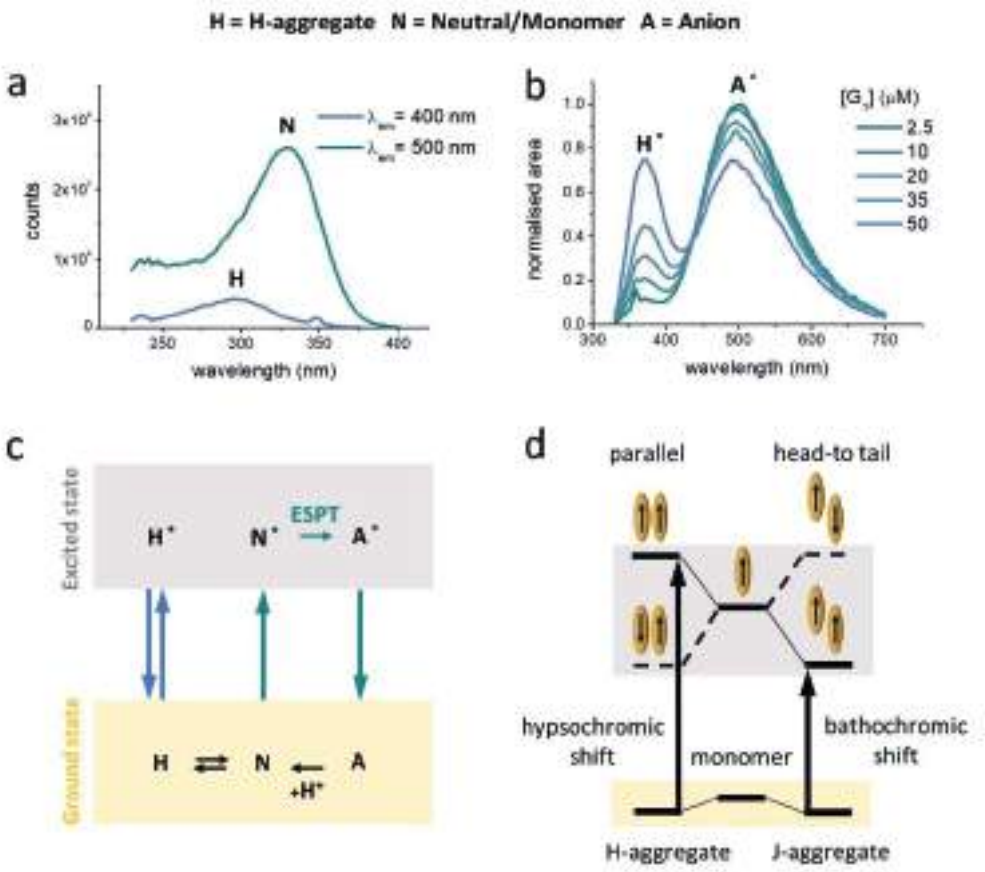

Figure 2: (a) Photoexcitation of G_1, at neutral pH shows double emission as the result of an equilibrium between monomers and H-type aggregates. (b) Kasha's exciton theory. (c) Excitation spectra for each of the emission bands. (d) Changes in the emission spectra as a function of G_1 concentration.

aggregation enhances the intensity of the shoulder emission at λ_{max}=368 nm and therefore, we attributed this band to the photoluminescence of an exciton species (H*)(Fig. 2c).

Comparing the excitation spectra from the monomer emission (λ_{max}=328nm) and from H-aggregate emission (λ_{max}=295nm), the absorption is shifted to shorter wavelengths upon aggregation (Figure 2a). As explained by Kasha's exciton theory, Coulomb coupling between neighbouring chromophores can induce such a hypsochromic shift when the transition dipole moment of π-conjugated molecules assumes a side-by-side relative orientation (Figure 2d).[24] In these systems, H* emission is usually weak or quenched because radiative relaxation is forbidden by symmetry rules, which rationalises the monomer's ESPT band appears as the dominant emission.

3.2.3 The role of the solvent.

The next step was to identify which kind of PT mechanism occurs in the excited state. The fact that the transfer of a proton from phenol to imidazole would be thermodynamically favoured in the excited state does not imply that the ESPT process occurs intramolecularly since the molecular structure was specifically chosen to avoid ESIPT, placing proton donor and acceptor site at distal positions. A simple but effective method for discriminating ESIPT from ESPD mechanisms consists of analysing the effects of solvent on the Stokes shift of the fluorophore. For ESPD emitters, in a solvent that cannot accept or mediate proton transfer, we expect a decrease in the Stokes shift compared to in protic solvents.[13] By contrast, the ESIPT mechanism is promoted by organic solvents that do not compete with the internal hydrogen bond that pre-organizes proton donor and acceptor sites.[7] Based on these considerations, the significant decrease of the

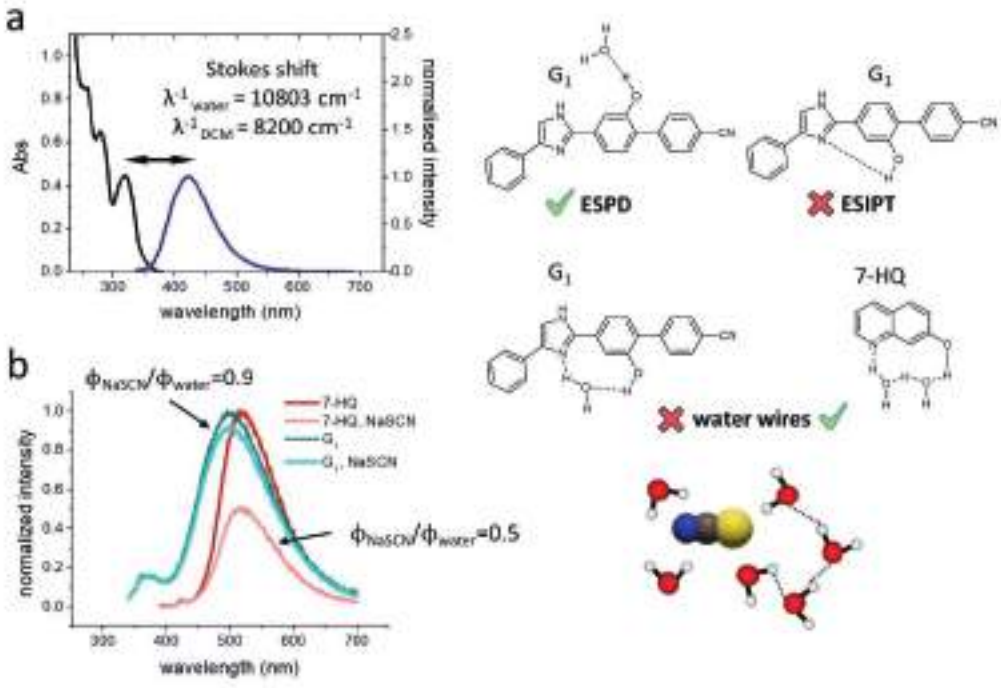

Figure 3: (a) Absorption and emission spectra of G_1 in dichloromethane. (b) Effect of sodium thiocyanate on the quantum yield of emission of G_1 and 7-HQ

Stokes shift observed in dichloromethane suggests that water molecules participate in the PT process, excluding an intramolecular mechanism (Figure 3a).

The role of water was also investigated by comparing the effects of hydrogen bond-breaking salts on the quantum yield of emission of G_1 and 7-hydroxy quinoline (7-HQ). This experiment aimed to assess if water is the final recipient of the PT or if it is instead bridging donor and acceptor sites. It has been reported that 7-HQ and similar photoacids can transfer a proton to distant sites thanks to the formation of extended proton wires around the molecule.[25,26] Although all ESPT processes require a pre-organized hydrogen bond, unlike protolytic dissociation (ESPD), water wires necessitate not just a single bond but a well-structured water network connecting the two sites of the solute molecule. Upon addition of sodium thiocyanate, a chaotropic salt known for weakening the hydrogen bond of water,[27] 7HQ emission was significantly quenched, whereas the effect on G_1 emission was minimal (Figure 3b). Thus, we concluded that the photoluminescence of G_1 in water proceeds via ESPD mechanism, and that despite being thermodynamically favoured, the PT between acidic and basic sites of the amphoteric molecule does not occur in the excited state.

3.2.4 Supramolecular polymerization

Despite the amphoteric nature of the probe, self-aggregation did not increase ESPT emission but instead provided a distinct pathway for relaxation through the formation of an exciton. The lack of intermolecular ESPT is likely due to the fact that the optimal configuration for the π-stacking of H-aggregates is not compatible with a pre-organizing hydrogen bond between phenol and imidazole. In the attempt to shift the assembly equilibrium towards a more suitable configuration of the probe that could activate intermolecular ESPT, we investigated the co-assembly of G_1 with cyclodextrins.

The absorption spectrum of G_1 changes in the presence of γ-CD. A fast spectral transition, characterized by the rapid appearance of a shoulder band at λ=280 nm, suggests the formation of an inclusion complex (Figure 4a). This pre-equilibrium, which happens a few seconds after sugar addition, is followed by a slower drift of the main absorption band: a bathochromic shift that occurs in conjunction with an increase in the Tindal effect (Figure 4a, 4c). Following the exciton theory again, a red shift in the absorption band indicates that, while π-stacking in water results in a parallel orientation, the cyclodextrin cavities favour a head-to-tail configuration of the chromophores. Aggregates with such configuration are

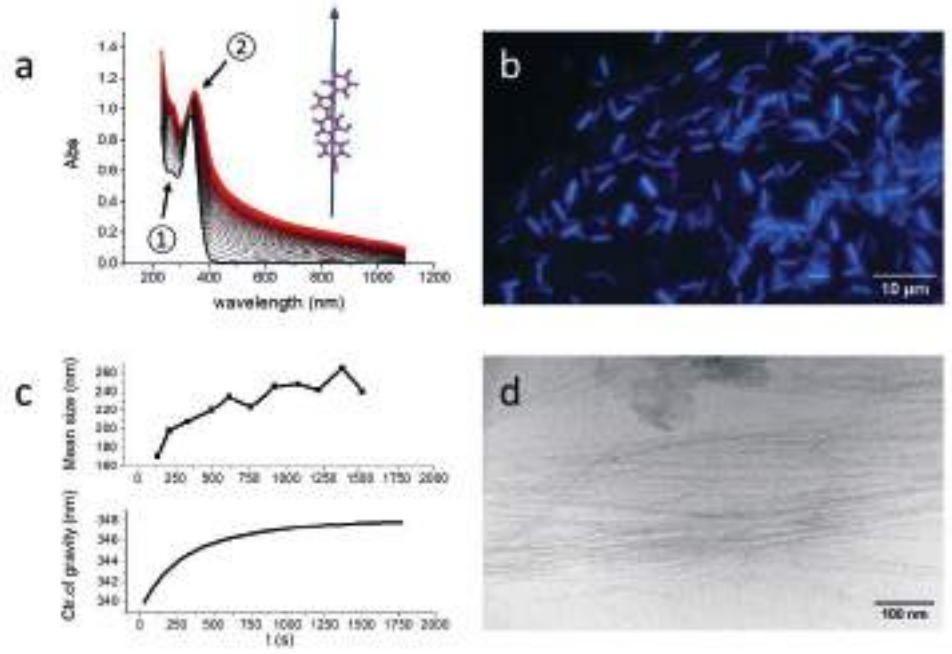

Figure 4: (a) Spectral changes of absorption during supramolecular polymerization (shoulder band at 280 nm ①, bathocromic shift ②) and representation of G_1 transition dipole moment. (b) Epifluorescence microscopy of rod shaped microcrystals. (c) Polymerization of nanotubes followed by dynamic light scattering (top) and bathochromic shift of absorption (bottom). (d) Cryo-EM shows that the microscopic rods are formed by bundling of individual nanotubes

usually referred to as J-type. The transition dipole moment ($\vec{\mu}$) of the main electronic absorption band of G_1 was calculated for an accurate structural representation of these aggregates (Figure 4a).

Regarding the change in turbidity, dynamic light scattering (DLS) showed the formation of objects with a mean size in the dimensional range of visible light (Figure 4c). According to the evolution of the kinetic profile, 90% of the supramolecular polymerization occurs within 15 minutes from mixing time.

Cyclodextrins are prone to form stacked assemblies since the hydroxy groups in the outer rims of the macrocycle can hydrogen bond other sugar units. It has been reported that when the formation of an inclusion complex stabilises the interaction between cyclodextrins, the host-guest binding can result in the supramolecular polymerization of γ-CD nanotubes.[28,29]

A linear version of the probe (G_2) was synthesised to explore the role of design in the formation of the assembling complex, with the only structural difference being the absence of the phenyl substituent on the imidazole ring. The lack of this

structural element prevents supramolecular polymerization in γ-CD solutions. Therefore, the extension of the aromatic scaffold and its non-sequential design is necessary for the arrangement of the guest inside the cavities to promote the contacts between cyclodextrin units.

In addition to the stacking of the cyclodextrins, the secondary assembly of these nanotubes, driven by their bundling, often forms hierarchically structured microscopic materials. In this case, when concentrated samples were analysed with epifluorescence microscopy, a suspension of rod-shaped objects of regular size (2-3 μm) was observed in solution (Figure 4b). The microscopic rods were also imaged with cross-polarized optical microscopy (POM), making use of their birefringence, and Cryo-electron microscopy (Cryo-EM). In the Cryo-EM micrographs, it is possible to identify individual γ-CD nanotubes bundling together to constitute the semi-crystalline rods (Figure 4d). Drop-casting a suspension of rods on mica enables the bundle thickness to be estimated between d=80-160 nm by means of AFM topography (Supplementary Figure 2).

3.2.5 Stoichiometry and assembly mechanism

Investigating the stoichiometry of the inclusion complex responsible for the polymerization required determination of its critical aggregation concentration (CAC), which is a function of $[\gamma\text{-CD}]_0$ and $[G_1]_0$. This phenomenon was investigated using the scattering of the samples. The scattering increases as the concentration of G_1 increases in the presence of an excess of the cyclodextrin (Fig. 5a-b). The DLS data shows that addition of $[G_1]$=10 μM in $[\gamma\text{-CD}]_0$=5 mM reaches the threshold for supramolecular polymerization (Figure 5b). This information was then used to design two experimental scenarios where the system could be studied at fixed $[G_1]_0$, varying the [γ-CD] below or across the CAC of the assembling complex (Figure 5a).

In the first experimental scenario ($[G_1]_0$=2.5 μM), which excludes the effects of supramolecular polymerization, a two-fold increase in A* emission was observed during the titration with $2{\cdot}10^3$ equivalents of γ-CD (Figure 5c). The change in fluorescence anisotropy (r_N=0.10, $r_{1:1}$=0.14), compatible with the formation of an inclusion complex, confirmed that spectral changes were due to supramolecular binding. Indeed, the spectroscopic data fit a binding isotherm model for a 1:1 inclusion complex with K_1=180 (Figure 5e).[30]

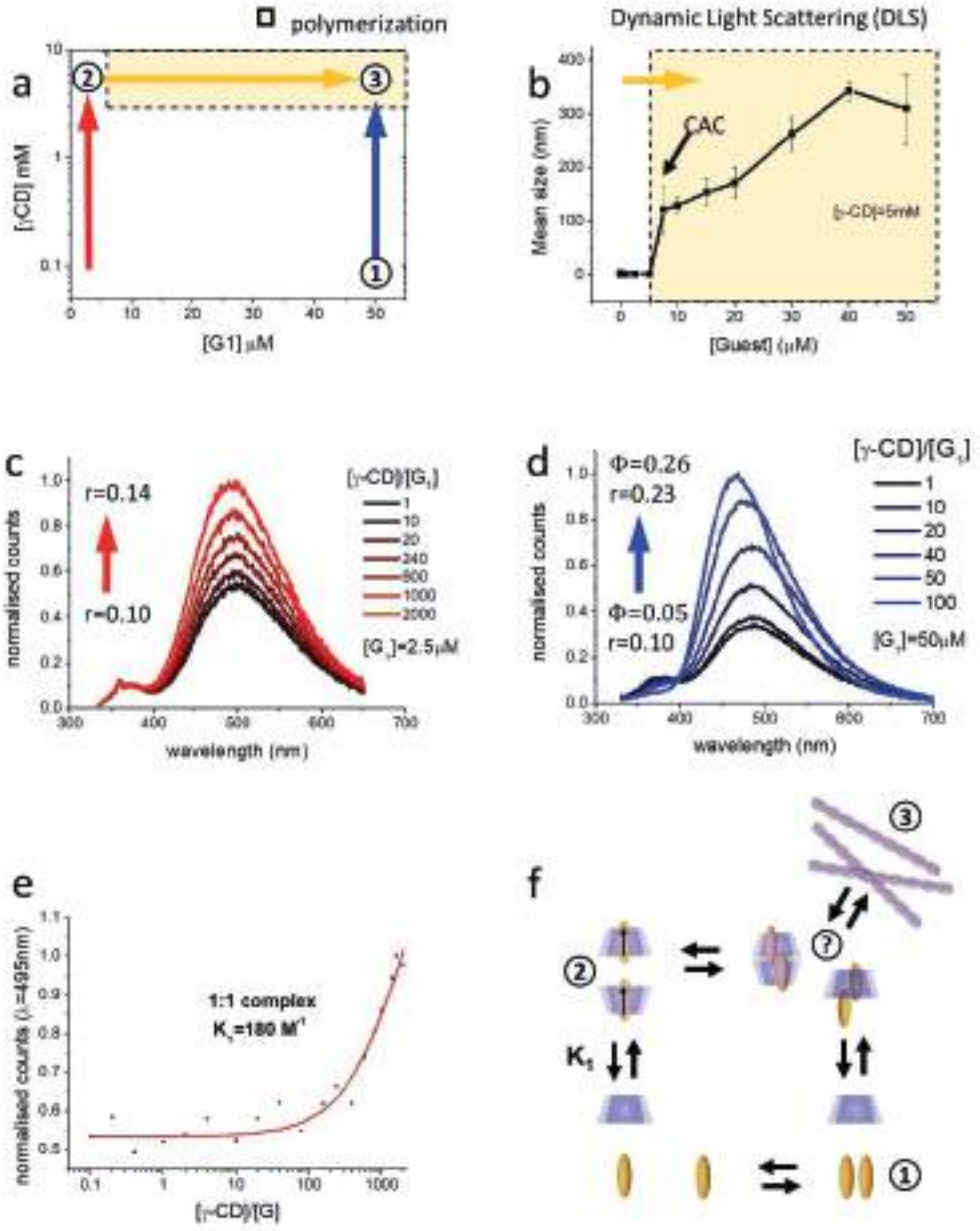

Figure 5: (a) Self-assembly landscape with identified species: ① H-aggregates; ② 1:1 complexes, head and tail ③ nanotubes. Arrows represent the experimental conditions screened during G_1 (yellow) and γ-CD (red and blue) titrations. (b) G_1 titration: critical aggregation concentration (CAC) defined by DLS at increasing concentrations of G_1 and fixed $[γ\text{-CD}]_0$=5mM. (c) γ-CD titration below CAC: fluorescence at increasing concentrations of γ-CD and fixed $[G_1]$=2.5μM. (d) γ-CD titration across CAC: fluorescence at increasing concentrations of γ-CD and fixed $[G_1]$=50 μM. (e) Fitting of the binding isotherm from the sugar titration below CAC. (f) Identified species in the self-assembly landscape.

Our interpretation, based on the low binding constant, is that at low concentrations of G_1 and excess of γ-CD a loose complex is formed with 1:1 stoichiometry. The phenol is still hydrated in this complex, and proton transfer to solvent can occur with an ESPD mechanism. The modest increase in emission without a change in the Stokes shift is caused by the partial suppression of non-radiative mechanisms that are restricted by the γ-CD binding, such as solvent-assisted vibrational relaxation or TICT quenching.[31]

In the second experimental scenario, in the abundance of guest ($[G_1]_0$= 50 μM), the increase in sugar concentration results in the accumulation of inclusion complex above the CAC (Fig. 5d). Upon the formation of nanotubes, tumbling of the fluorophore was considerably restricted resulting in a large fluorescence polarisation anisotropy ($r_{2:2}$=0.23). In addition, the emission of the H-aggregates was completely suppressed, whereas monomer emission experienced a five-fold increase (ϕA^*=0.05, ϕA^*_{nano}=0.26) and a small but measurable shift of the emission band (Figure 5d).

Given the larger effects of cyclodextrin addition on the photoluminescence of G_1 upon formation of nanotubes, we envisioned that the polymerization mechanism occurs through the formation of a complex with different stoichiometry from 1:1. We hypothesised that this species has a stoichiometry that must be favoured by the higher $[G_1]_0$ and that the new configuration of chromophores favours the ESPT emission even in the viscous confinement of the nanotube cavity. Although it was not possible to fit the spectral changes with a simple binding or polymerization models, judging from the disappearance of H-aggregate emission, we knew that the formation of this new complex and its polymerization drain the G_1 from the assembling equilibrium. Taking into account these aspects and the changes in the absorption spectrum of G_1 during polymerization, we hypothesised two plausible mechanisms: in the abundance of G_1, the addition of γ-CD could either result in the formation of a 2:1 complex by addition of sugar to an H-type aggregate, followed by a change in the chromophores' configuration from parallel to head to tail (Figure 5f). Alternatively, G_1 could initially assemble with γ-CD into two kinds of spectroscopically indistinguishable 1:1 complexes, namely head and tail, and later dimerize into a 2:2 complex, directly falling into a J-type configuration (Figure 5f).[32]

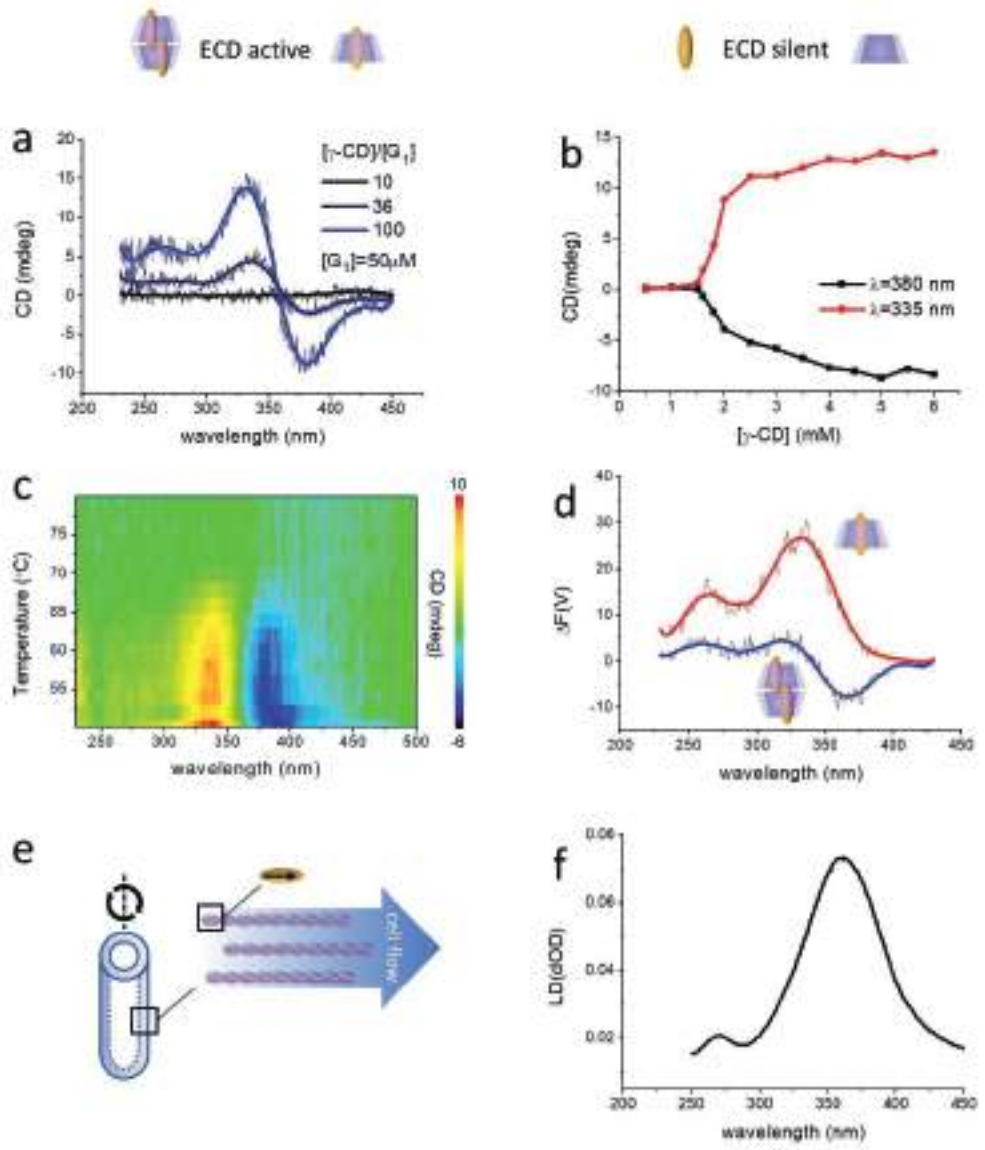

Figure 6: (a) Sugar titration across polymerization zone: electronic circular dichroic (EDC) spectra at increasing concentrations of γ-CD and fixed [G_1]=50 μM. (b) Evolution of the Cotton bands during sugar titration across polymerization zone. (c) Temperature map of the EDC spectra, [G_1]=50 μM, [γ-CD]=5mM. (d) Pathway complexity experiment: fluorescence detected circular dichroism (FDCD) of 1:1 and 2:2 complex, spectra were obtained at the same final concentration ([G1]=2.5 μM, [γ-CD]=5mM) but using different methods for sample preparation. (e) Linear dichroic (LD) spectra [G_1]=50 μM, [γ-CD]=5mM. (f) experimental setup and nanotube alignment in the LD spinning probe.

Electronic circular dichroism (ECD) was employed to discriminate between the assembly mechanisms (Figure 6a-b). This technique allows for monitoring the formation of inclusion complexes during the sugar titration across the CAC. When analysed separately neither host nor guest shows circular dichroism, but their inclusion complexes provides the chromophore (G_1) with a chiral environment (γ-CD) which results in an induced Cotton effect. Analysing the spectroscopic data, the absence of an isodichroic point during the titration confirmed the presence of more than one CD active species, and following the spectral bands at λ=335 nm and λ=380 nm, it was possible to identify two inter-dependent but asynchronous events (Fig. 6b). Initially, the CD spectra was dominated by a positive Cotton band associated with the presence of the 1:1 inclusion complex. Spectral interpretation, according to Kodaka's rule, places the $\vec{\mu}$ parallel with respect to the axis of the cyclodextrin.[33] Following the initial binding, the same electronic band turned into a negative couplet. This transition often occurs when two chromophores constitute an exciton within the γ-CD cavity, in excellent agreement with the hypothesised pairing of G_1 into J-type aggregates during supramolecular polymerization.[33] The accumulation of the 1:1 complex and the inter-dependence of the two bands suggest that dimerization is the assembly mechanism. In addition, considering the dimensions of the G_1 (V_{G1}=395 Å^3) and host's cavity ($V_{\gamma\text{-CD}}$=427 Å^3), a guest pair (2G1) would better fit the nanotube channel in a 2:2 stoichiometric ratio. Furthermore, despite the low binding constant found for the 1:1 complex, temperature scans have shown that the exciton is stable up to T=68°C, indicating that the dimerization of the complex is likely to improve the fit and strengthen binding with the γ-CD cavities (Figure 6c).

This interpretation of the assembly mechanism and the ECD spectral assignments were verified by fluorescence-detected circular dichroism (FDCD). This technique allowed recording the CD spectra of both complexes isolated in diluted conditions, at concentrations that are usually inaccessible because of the sensitivity of ECD analysis (Figure 6d). Taking advantage of pathway complexity, it was possible to direct the system toward the formation of the desired stoichiometry by changing the sample preparation method. Specifically, the dimerized species can be obtained in the concentration range usually dominated by 1:1 complex through dilution of pre-aggregated samples. The FDCD spectra of the individual complexes confirmed our assignment of the Cotton bands in the ECD titration experiment. In addition, the stability of the 2:2 complex upon dilution implies that dimerization represents the thermodynamic sink of the chemical equilibrium, and this process is essentially limited by the encounter probability of the 1:1 complex.

Lastly, the orientation of G_1 inside the nanotube cavity was probed using linear dichroism (LD). Under a shear flow, the alignment of the nanotubes and the chromophores in their cavities induced anisotropic absorption (Figure 6e). The positive LD spectrum indicates the $\vec{\mu}$ being oriented along the nanofibers (Figure 6f).

Together the spectroscopic information indicate the most probable assembly mechanism proceeds through an intermediate 1:1 complex characterized by a loose binding constant, where G_1 can assume two interconverting orientations, head or tail. At higher concentrations of G_1, the accumulation of the 1:1 complexes lead to their dimerization, forming a 2:2 inclusion complex with a pre-organized pair with head-to-tail configuration ($2G_1$). The formation of this dimer is favoured by an optimization of the binding and by the stabilization of the sugar-sugar interactions, shifting the equilibrium towards the supramolecular polymerization of the complex into nanotubes.

3.2.6 Solvent isotope effects.

The guest has previously been observed to act as an ESPD emitter in water. However, the anomalous increase in emission upon confinement indicates a change in the relaxation mechanism within the nanotube cavities. Structural characterization revealed the formation of a guest pair in these cavities, suggesting that the new relaxation pathway may involve intermolecular ESPT.

This hypothesis was tested by determining the solvent isotope effect induced by hydrogen/deuterium exchange on the quantum yield and fluorescence lifetime of the G_1. The interpretation of the data is not trivial since isotope exchange can have several and often contrasting effects on photoluminescence. Specifically, two opposing mechanisms can alter the relaxation of the guest through solvent deuteration (Figure 7a). The first is attenuation of the vibrational relaxation.[34] This effect is caused by a lower efficiency of energy transfer between the electronically excited compound and solvent through dipole-dipole coupling.[35,36] Compared to H_2O, the vibrational overlap with the stretching mode of D_2O is lower, which means that the mechanism of dissipation of energy to the surrounding solvation shell is diminished, increasing the quantum yield and extending the fluorescence lifetime.[35] In addition, for exchangeable protons, the lower frequency of vibration makes N-D oscillators less efficient at deactivating the excited state through internal conversion.

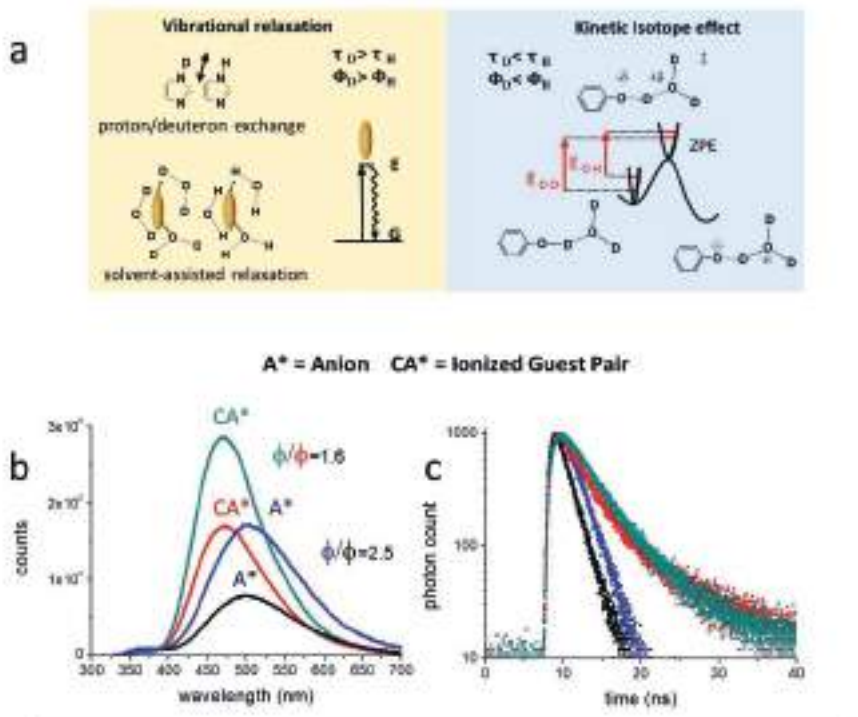

emitter	solvent	$\tau_{\Delta y}$	τ_1	%	τ_2	%	χ^2	ϕ
A*	H_2O	-	<1 ns	-	-	-	2.00	0.06
A*	D_2O	-	<1 ns	-	-	-	1.12	0.15
CA*	H_2O	3.3 ns	<1 ns	62	7.2 ns	38	1.19	0.09
CA*	D_2O	2.9 ns	1.0 ns	47	4.4 ns	53	1.04	0.15

Figure 7: (a) Competing effects caused by solvent isotope substitution on fluorescence quantum yield and lifetime of G_1. (b) emission spectra and (c) corresponding fluorescence decays were compared in H_2O (black, orange and red) and in D_2O (blue, purple and green). The isotope effects were determined in the absence of γ-CD (black, orange, blue and purple) and in the presence of polymerized inclusion complexes (red and green). Emission lifetimes determined by TCSPC are summarized in the (bottom) table together with relative amplitudes and fitting parameters.

On the other hand, for an emissive process resulting from ESPT, a primary kinetic isotope effect is expected to decrease quantum yield and lifetimes by retarding proton transfer (Figure 7a).[37] In fact, disfavouring the ESPT pathway means that non-radiative processes will take over the relaxation of the excited state. That said, it is expected that both mechanisms, vibrational relaxation and kinetic isotope effect, will contribute to the changes in photoluminescence of the G_1 in deuterated water, and it will be shown how confinement will play a role in determining which effect dominates.

The double emission of G_1 in H_2O shows distinct lifetimes for emission from G_1 monomers (A*) (τ<1 ns) and H-aggregates (H*) (τ=1.2 ns), as expected in the

case of excimers formed from ground state aggregation (Figure 7b, Supplementary Figure 3). In D_2O, the quantum yield for the main band of emission (A*) was more than double (ϕ_D/ϕ_H=2.5) and, despite it remained in the sub-nanosecond regime, the fluorescence lifetime τ_{A^*} increased also, manifested in a change in slope of the fluorescence decay (Figure 7b-c). These results indicate that when the probe is well solvated in solution, the attenuation of vibrational relaxation is the dominant isotope effect, causing an increase in the emission.

Upon γ-CD addition and supramolecular polymerization of the inclusion complex, the fluorescence decay of the main band (CA*) becomes biexponential, presenting a sub-nanosecond component associated with a relaxation of free-G_1 monomers in solution, and a long-lived component (τ=7.2 ns), assigned to the relaxation of G_1 confined in the nanotubes (Figure 7 b-c). Opposite isotope effects were observed on the two components of the decay. While the lifetime of emission from free-G_1 increased, as observed in the previous experiment, the lifetime of confined fluorophore nearly halved (τ=4.5 ns) in deuterated water. This reversed trend is reflected in the quantum yield of emission, which overall increases (ϕ_D/ϕ_H=1.6) because of the contribution of free-G1 to the biexponential decay, though to a lesser extent (-36%) with respect to that observed in the absence of γ-CD. Our interpretation is that the opposite isotope effect on the two components of the decay occurs because, in the microenvironment of the nanotube cavities, the guest is poorly hydrated. Thus, the effect of deuteration on solvent-assisted vibrational relaxation becomes less important compared to the primary kinetic isotope effect. These results confirm that ESPT occurs within the confinement of nanotubes. Additionally, the observed increase in emission upon confinement, which is incompatible with the protolytic dissociation mechanism (ESPD) seen for G1 in the absence of γ-CD, suggests that ESPT must occur intermolecularly within the guest pair.[9,10] This supports our hypothesis of a mechanistic transition in the adiabatic process of proton transfer upon self-assembly.

3.2.7 Photophysical properties of an ESPT material.

The confinement of G_1 in the nanotube micro-environment not only sustains ESPT but favours it at the expense of other photochemical pathways, such as those that lead to photo-degradation.[5] This mechanism prevents photo-bleaching of the fluorophore, as demonstrated in the epifluorescence micrographs after prolonged UV exposure comparing solid samples of assembled micro-rods and amorphous material obtained from dried G_1 solutions (Figure 8a). In addition, the organisation of G_1 in a semi-crystalline state results in interesting photophysical properties. For example, even with unpolarised excitation light, the anisotropy due to the supramolecular architecture results in the fluorescence emanating from the rods showing polarisation along the axis of the micro-rods (Figure 8b-c).
These effects on the photoluminescence are not the focus of this chapter and will not be discussed further. Nevertheless, we envision that with respect to ESIPT-based materials, intermolecular ESPT emitters could feature properties not yet explored for optoelectronics, for example, in terms of proton conductivity.

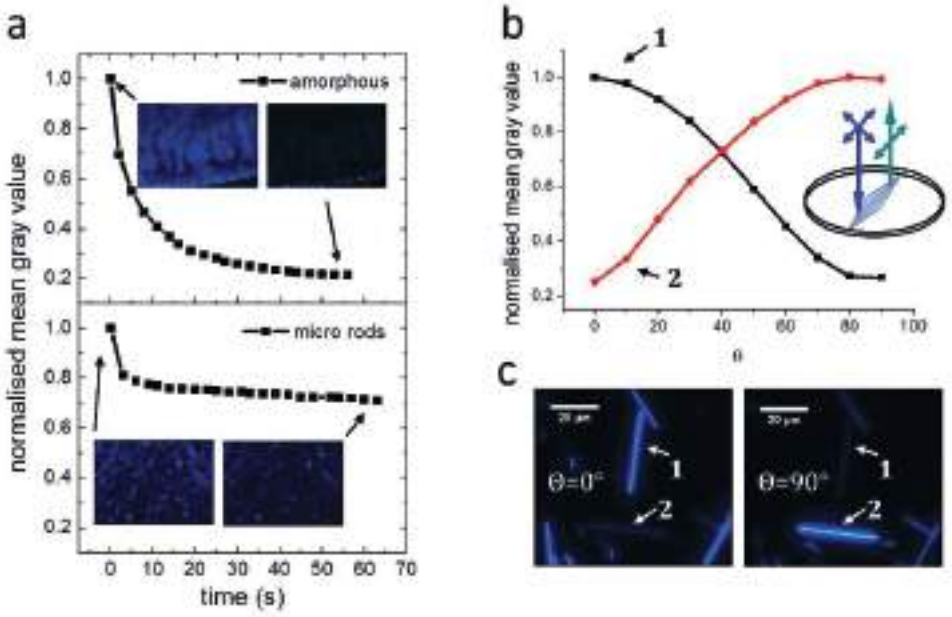

Figure 8: (a) Image analysis comparing the photobleaching of an amorphous sample with micro-crystalline rods under sustained illumination in the epifluorescence microscope. (b)(c) Image analysis of fluorescence micrographs shows that when excited with unpolarized radiation the intensity of emission captured from the crystals (1)(2) is maximised when the rod axis is aligned with the analyser.

3.3. Conclusion

In this study, we developed an ESPT fluorescent probe and characterized its photo-physical properties. Despite its amphoterism, our results indicate that in water the emitter undergoes ESPD, with the solvent being the sole acceptor in the proton transfer. It was also found that the fluorescent probe co-assembles with γ-CD forming inclusion complexes that polymerize into supramolecular nanotubes. During this process, the anomalous increase of ESPT photoluminescence of G_1 was the first indication that the nanotube microenvironment induced a shift in the mechanism of the adiabatic reaction since ESPD-type emission would usually be suppressed upon confinement. A spectroscopic investigation of the aggregates revealed that in the nanotube cavities fluorophores sit in proximity of each other, organized in a J-type configuration forming a guest pair ($2G_1$). This characterization indicates that pre-organization in the inclusion complex opens a new pathway for intermolecular proton transfer within the guest pair. More evidence mounted in support of this mechanism, as the kinetic isotope effect confirmed that the emission from confined G_1 is still associated with an ESPT process despite the poor hydration of G_1 in the nanotubes' cavities.

Although confined water may still mediate intermolecular proton transfer, it is evident that the solvent is not the ultimate proton acceptor. In fact, if that were the case, the viscosity of the microenvironment would promote geminal recombination and quench ESPD emission,[9,10] which is contrary to the observed trend upon nanotubes formation. Conversely, preorganization of proton transfer with a stronger base, such as a neighbouring imidazole unit, can explain how confinement promotes intermolecular ESPT emission.

Pre-organization of residues is the cornerstone of enzymatic catalysis. This effect can turn a simple combination of acid, base, and nucleophile into an effective catalytic triad, due entirely to the ordered microenvironment of the enzymatic pocket. Applying the same principles, we have shown that adding an external host can pre-organize pairs of ESPT emitters and shift the mechanism of their adiabatic reaction from ESPD to intermolecular ESPT. In other words, we have shown how confinement in supramolecular polymers can direct PT. If this approach proves to be effective in activating chemical conversion, it could represent a novel strategy for developing general acid-catalysed reactions.

3.4. Acknowledgements

I wish to thank R. Hutchings for helping me start this project during his master internship. I gratefully acknowledge him for the synthesis of the guest and the initial characterisation of its photophysical properties. I gratefully acknowledge J. Martinelli for the calculation of the transition dipole moment of the guest. I gratefully acknowledge I. F. Leach for the calculation of the volume of the guest. I gratefully acknowledge Y.Y. Lopatina for the AFM measurements. I gratefully acknowledge M.C.A. Stuart for the Cryo-EM. I wish to thank A. Ryabchun for his help with advanced spectroscopic techniques such as FDCD and LD, as well as for his advice and many useful discussions on this project. I wish to thank W.R. Browne for supervising this research along with T. Kudernac.

3.5. Experimental Section

3.5.1 Materials

Chemicals and solvents were obtained from commercial sources and used without further purification unless stated otherwise.

The guest (G_1) was synthesised in a two-step linear synthesis consisting of a Suzuki-Miyaura cross-coupling reaction between 3-hydroxy-4-iodobenaldehyde (R_1) and 4-cyanophenyl boronic acid (R_2), followed by a Debus-Radziszewski imidazole synthesis. The final product was characterized by ^{1}H NMR, ^{13}C NMR, HRMS, UV-Vis absorption, FTIR and Raman spectroscopy. Detailed experimental procedures and final product characterization are reported in the extended supporting information.

General procedure for the preparation of nanotube fibres was based on the solvent processing method: a stock solution of guest in methanol ($[G_1]_0$=5 mM) was dispersed in an aqueous solution of γ-cyclodextrin ($[\gamma\text{-CD}]_0$=5 mM) adjusting the final concentration of G_1 to 50 μM (water/methanol 99:1). After the addition, samples were stirred using a vortex mixer for a few seconds and stored at room temperature for 30 minutes while supramolecular polymerization proceeded. Stock solutions were freshly prepared for each experiment to avoid pre-aggregation of G_1.

Sample preparation of microcrystalline rods followed the same experimental procedure. The concentration of the stock solutions used were ($[G_1]_0$=5 mM) and ($[\gamma\text{-CD}]_0$=10 mM), the final concentration of G_1 was 0.5 mM (water/methanol 9:1).

Kinetic isotope effect experiments: deuteration of the G_1 acidic protons was obtained by $^{1}H/^{2}H$ exchange with deuterated water (isotropic purity ≥99.9%), which was used in the preparation of stock solutions of γ-cyclodextrin.

3.5.2 Methods

UV-Vis absorption spectra were recorded with an Analytik Jena-Specord 210 Plus Spectrophotometer.

Fluorescence spectra were recorded with an FS5 Spectrofluorometer from Edinburgh Instruments. In a typical fluorescence titration measurement the

excitation wavelength used was λ_{ex}=320 nm and the absorption of the sample was maintained between 0.2-0.3 to avoid inner filter effects.

The quantum yield of emission was determined by Williams' method using $[Ru(bpy)_3](PF_6)_2$ as a comparative standard.[38] For determining the quantum yield the excitation wavelength used was λ_{ex}=360 nm to avoid the overlap of absorption of the N species of G_1 with the H aggregates.

In the experiment with chaotropic salt the samples were measured at pH=7±0.5 with a concertation of [NaSCN]=100mM.

Spectroscopic pH-titrations were carried out using small additions of HCl or NaOH solutions to gradually adjust the pH of the samples; the pH was determined between the spectroscopic measurements using a Mettler Toledo FiveEasy F-20 benchtop pH/mV meter equipped with a pH electrode inLab microprobe. For the fluorescence titrations outside the calibration range (pH<2) the pH was calculated from the [HCl]. The absorption data were processed using the optical spectroscopy software Specragryph. For the determination of the pKa values the spectral changes were analysed with the Origin software for the sigmoidal fitting (DoseResp) and the analysis of inflection points ($\log_{x0}$).

Binding isotherm titrations were fitted with the open-source software bindfit, which used the Nelder–Mead algorithm for the global fitting method.[39]

Circular dichroism (CD) spectra of aqueous solutions were recorded with a JASCO J-815 spectropolarimeter at room temperature in 1 cm quartz cuvette.

Fluorescence-detected Circular Dichroism (FDCD) measurements were performed on a JASCO J-815 spectropolarimeter equipped with accessory JASCO FDCD-405. The PMT detector was attached perpendicularly in respect to probe beam in order to collect the total fluorescence. The long-pass filter ($l \leq$ 380 nm) was placed before PMT detector unit to eliminate effect of scattering of excitation light. The signal was collected at fixed HT (400V) and 50 nm/min scanning speed. The measurements were performed in 1 cm quartz cuvette at room temperature.

Linear dichroism (LD) study was performed on a JASCO J-815 spectropolarimeter equipped with micro-volume flow LD cell (Dioptica Scientific Ltd.) The cell consists of coaxially aligned stationary quartz rod (D = 2.5 mm) and rotating quartz cylinder (ID = 3 mm). The revolution speed was set up at 3000 rpm and kept constant. The measurements were performed at 20°C, using pure water as a reference.

Fluorescence decay lifetimes were measured using a Picoquant 300 TCSPC: a PicoQuant PDL 800-B diode laser driver was connected to a PicoQuant PLS 255 nm led-head equipped with 250-350 nm bandpass filter. A PicoQuant Tau-SPAD-100 single photon counting module equipped with a 400 or 450 nm bandpass filter was connected with a PicoQuant PicoHarp 300 TC-SPC module. The Tau SPAD was powered by a DSN 102 dual SPAD power supply. The internal trigger from the PDL was used as input for time stamping on the PicoHarp. Samples were held in a Thorlabs cuvette holder CVH100 with CVH100-CV lid. Data were fit using a FluoFit, the IRF used was generated by scattering from water, and Rh6G was used as a standard for validation of the method.

Dynamic light scattering measurements were carried out with a Zetasizer Ultra Red (ZSU3305) from Malvern Panalytical.

Epifluorescence and cross-polarized optical microscopy were performed in a Nikon Eclipse LV100N POL microscope equipped with a 12V-50W halogen lamp for diascopic illumination as well as a 120V-130W C-LHGFI HG lamp mounted on intenselight C-HGFI fibre illumination system for episcopic illumination. For the epifluorescence measurements the microscope was equipped with a UV-2A filter (bandpass excitation λ_{exc}=330-380 nm, long pass λ_{em}=420 nm).

Cryo-electron microscopy images were recorded with a Tecnai T20 TEM microscope (FEI) operating at 200 keV using a Gatan model 626 cryo-stage sample holder. Both optical and electron micrographs were analysed using the processing package Fiji.

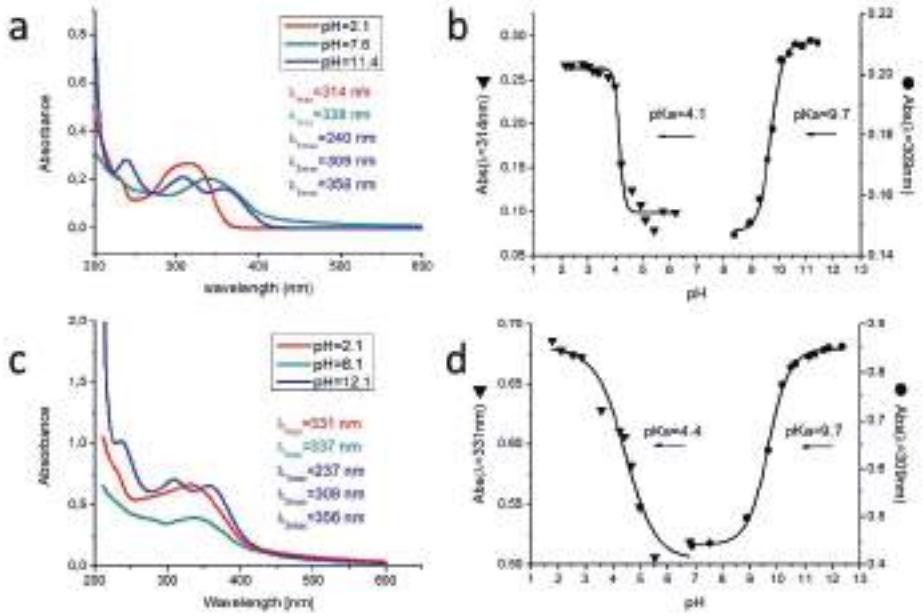

Figure S1: (a)(b) Spectroscopic titration of G_1.(c)(d) Spectroscopic titration of G_1 in the presence of γCD

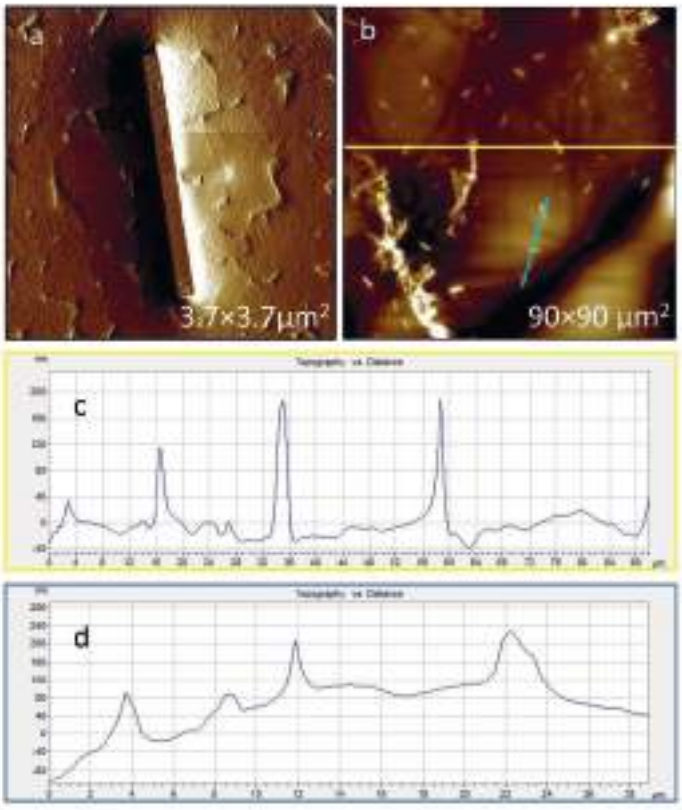

Figure S2: (a)(b) AFM topography of microscopic rods. (c)(d) Corresponding z profile of micrographs

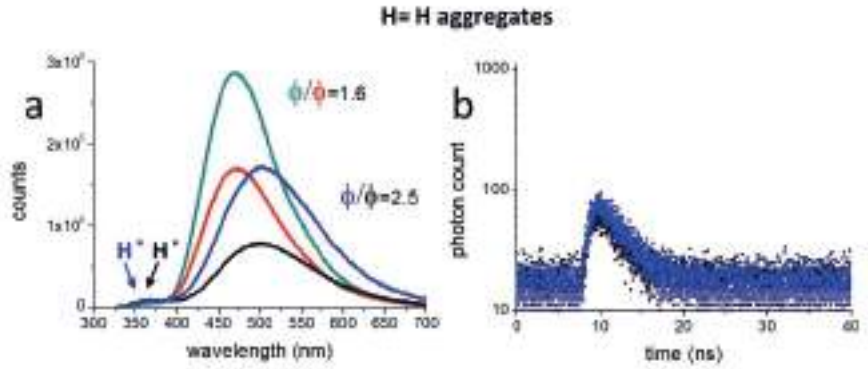

emitter	solvent	τ_{Av}	τ_1	%	τ_2	%	χ^2	ϕ
H*	H_2O	-	1.2 ns	-	-	-	0.97	-
H*	D_2O	-	1.5 ns	-	-	-	0.92	-

Figure S3: Isotope effect on the emission of H-aggregates: (a) emission spectra and (b) fluorescence decay of H-band recorded using TCSPC.

3.5.3 Synthesis

Synthesis of 4'-formyl-2'-hydroxy-[1,1'-biphenyl]-4-carbonitrile

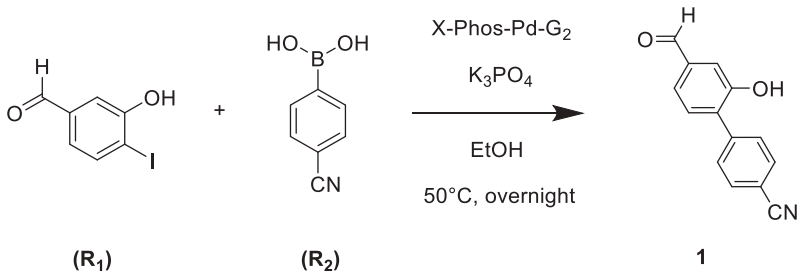

(R_1) **(R_2)** **1**

A solution of 3-hydroxy-4-iodobenzaldehyde (**R_1**) (500 mg, 2.02 mmol) in ethanol (6 mL) was added to a stirred solution of 4-cyanophenyl boronic acid (**R_2**)(350 mg, 2.38 mmol), X-Phos-Pd-G2 (64 mg) and potassium phosphate (880 mg) in ethanol (7 mL) under a nitrogen atmosphere. The reaction mixture was degassed by three freeze-pump-thaw cycles, and stirred at 50°C for 16 hours. The crude product was eluted with ethyl acetate over a pad of celite, dried over magnesium sulphate and the solvent was removed under reduced pressure. The crude was purified by column chromatography (silica, MeOH/DCM 1%) to afford **1** with 83 % yield.

^{1}H NMR (400 MHz, CD_3OD) δ 9.89 (s, 1H), 7.77 – 7.68 (m, 4H), 7.47 – 7.36 (m, 3H), 5.45 (s, 1H).

^{13}C NMR (101 MHz, CD_3OD) δ 193.6, 156.4, 143.9, 139.0, 134.0, 132.9, 132.3, 131.3, 123.1, 119.8, 116.4, 111.9.

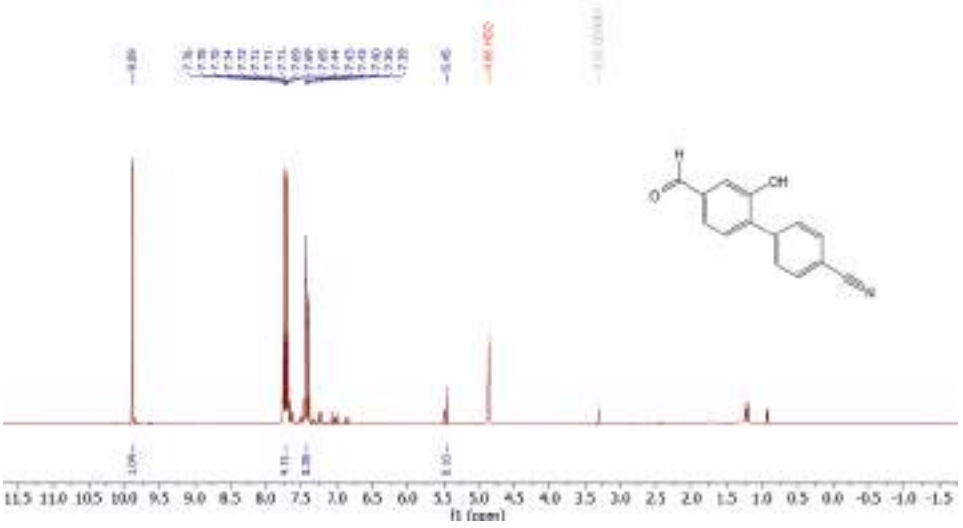

Figure S4: ^{1}H NMR (400 MHz, CD_3OD) spectrum of 4'-formyl-2'-hydroxy-[1,1'-biphenyl]-4-carbonitrile

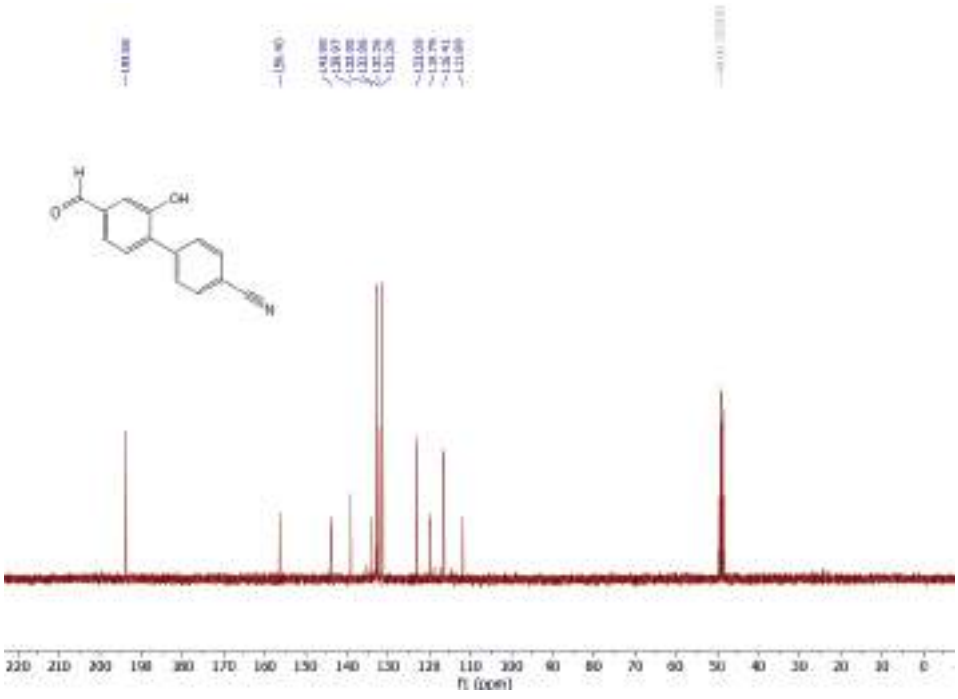

Figure S5: ^{13}C NMR (101 MHz, CD_3OD) spectrum of 4'-formyl-2'-hydroxy-[1,1'-biphenyl]-4-carbonitrile

Synthesis of G_1 and G_2

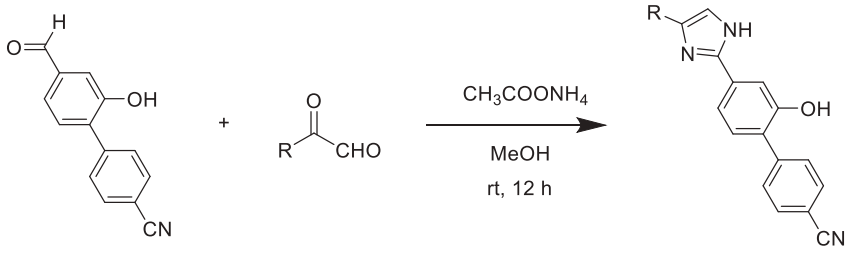

1 | **R = Ph (R_3)** **R = H (R_4)** | **R = Ph (G_1)** **R = H (G_2)**

A solution of **1** (350 mg, 1.57 mmol) and ammonium acetate (590 mg, 7.65 mmol) in methanol (10 mL) was added, over a period of 10 minutes, to a solution of phenylglyoxal monohydrate (**R_3**) (250 mg, 1.64 mmol) or glyoxal oxalaldehyde (**R_4**) 40 wt % water (189 µL, 1.65 mmol) in methanol (12 mL), for **G_1** and **G_2**, respectively. The reaction mixtures were stirred overnight at room temperature, after which the crude mixture was evaporated under reduced pressure, re-dissolved ethyl acetate and washed with 3 x 50 mL water. The combined organic layers were dried over magnesium sulphate and the solvent was evaporated under reduced pressure. The crude product was purified by column chromatography (**G_1**, silica, MeOH/DCM 1%→MeOH/DCM 3%)(**G_2**, silica, MeOH/DCM 3% → MeOH/DCM 5%) to afford the final products with 29 %(**G_1**) and 47 %(**G_2**) yields, respectively.

Characterization of G_1

^{1}H NMR (400 MHz, CD_3OD) δ 7.78 (t, *J* = 9.0 Hz, 4H), 7.71 (d, *J* = 8.1 Hz, 2H), 7.52 (s, 1H), 7.45 (d, *J* = 8.6 Hz, 2H), 7.39 (t, *J* = 7.2 Hz, 3H), 7.26 (t, *J* = 7.4 Hz, 1H), 5.47 (s, 1H).

^{13}C NMR (101 MHz, CD_3OD) δ 156.2, 148.3, 144.7, 132.8, 132.8, 132.0, 131.2, 129.8, 128.3, 128.1, 126.1, 120.0, 118.3, 114.4, 111.1.

HRMS-ESI Orbitrap (m/z): [M+H$^+$] calculated for $C_{22}H_{15}N_3O$, 338.12879; found 338.12860

UV-VIS: λ_{max} (MeOH) = 331 nm ($\log_{10}$ ε 4.5)

FTIR: ν (C=C) 1601 cm^{-1} (sh, m); ν (C≡N) 2233 cm^{-1}(sh, m)

Raman spectrum: ν (C-N) 1474 cm^{-1} (sh, m); ν (C=C) 1608 cm^{-1} (sh, s); ν (C≡N) 2233 cm^{-1}(sh, w)

Characterization of G_2

^{1}H NMR (400 MHz, CD_3OD) δ 7.75 (dd, 4H), 7.44 (s, 1H), 7.38 (d, J = 1.1 Hz, 2H), 7.16 (s, 2H), 5.47 (s, 1H), 1.98 (s, 1H).

^{13}C NMR (101 MHz, CD_3OD) δ 156.2, 147.4, 144.6, 132.8, 132.5, 132.1, 131.2, 128.4, 124.0, 120.0, 118.0, 114.2, 111.2.

HRMS-ESI Orbitrap (m/z): $[M+H^+]$ calculated for $C_{16}H_{11}N_3O$, 262.09749; found 262.09739

UV-VIS: λ_{max} (MeOH) = 297 nm ($\log_{10}$ ε 4.3), λ_{max} (MeOH) = 323 nm ($\log_{10}$ ε 4.3)

FTIR: ν (C=C) 1604 cm^{-1} (sh, s); ν (C≡N) 2225 cm^{-1}(sh, s)

Raman spectrum: ν (C-N) 1464 cm^{-1} (br, w); ν (C=C) 1608 cm^{-1} (sh, s); ν (C≡N) 2233 cm^{-1}(sh, w)

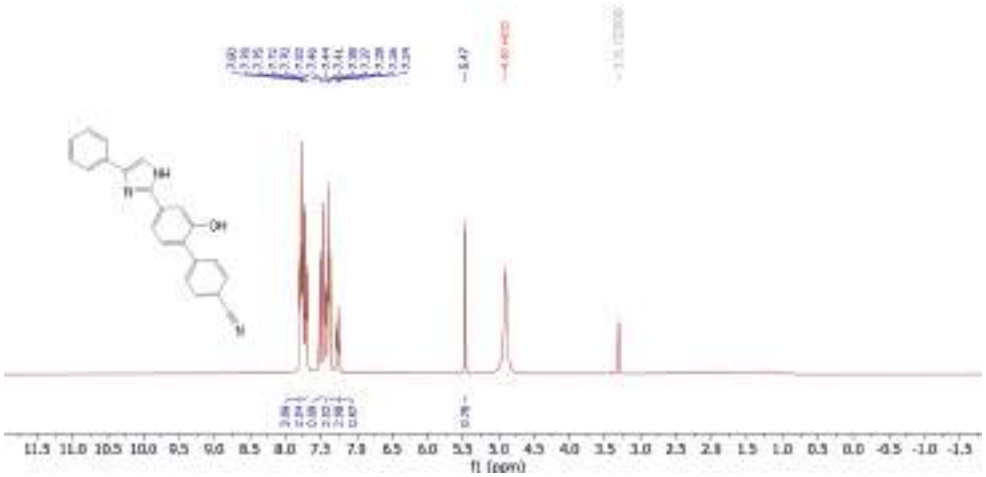

Figure S6: ^{1}H NMR (400 MHz, CD_3OD) spectrum of G_1

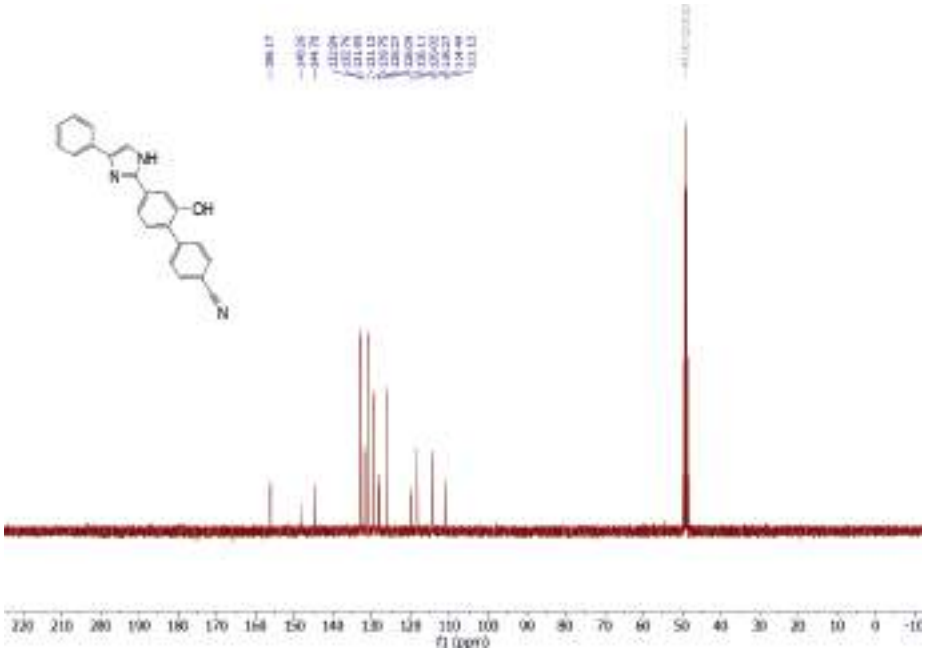

Figure S7: ^{13}C NMR (101 MHz, CD_3OD) spectrum of G_1

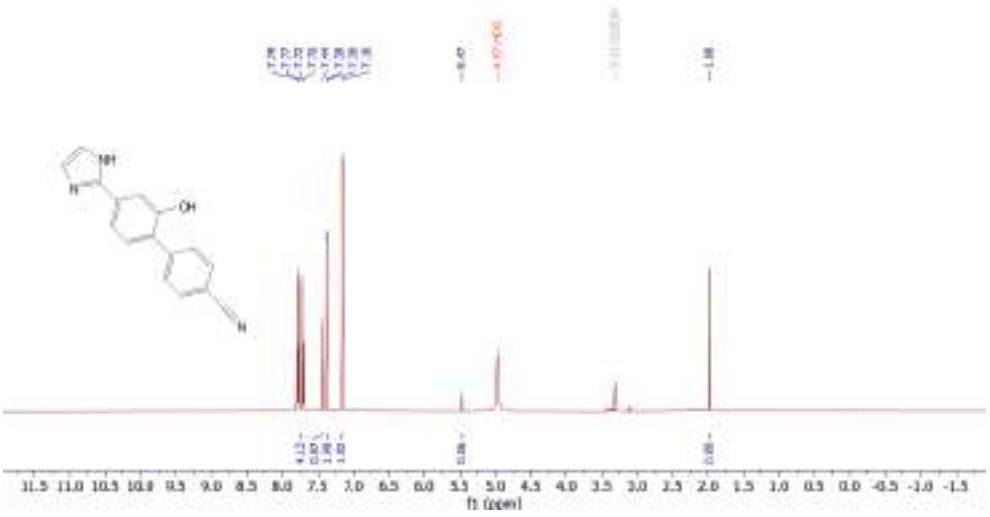

Figure S8: ^{1}H NMR (400 MHz, CD_3OD) spectrum of G_2

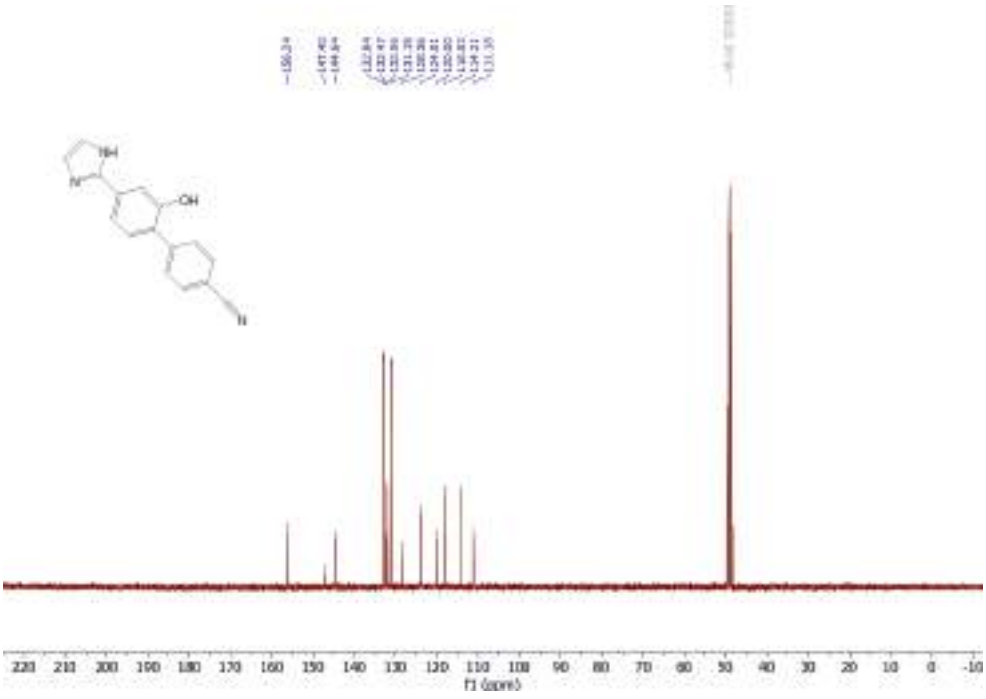

Figure S9: ^{13}C NMR (101 MHz, CD_3OD) spectrum of G_2

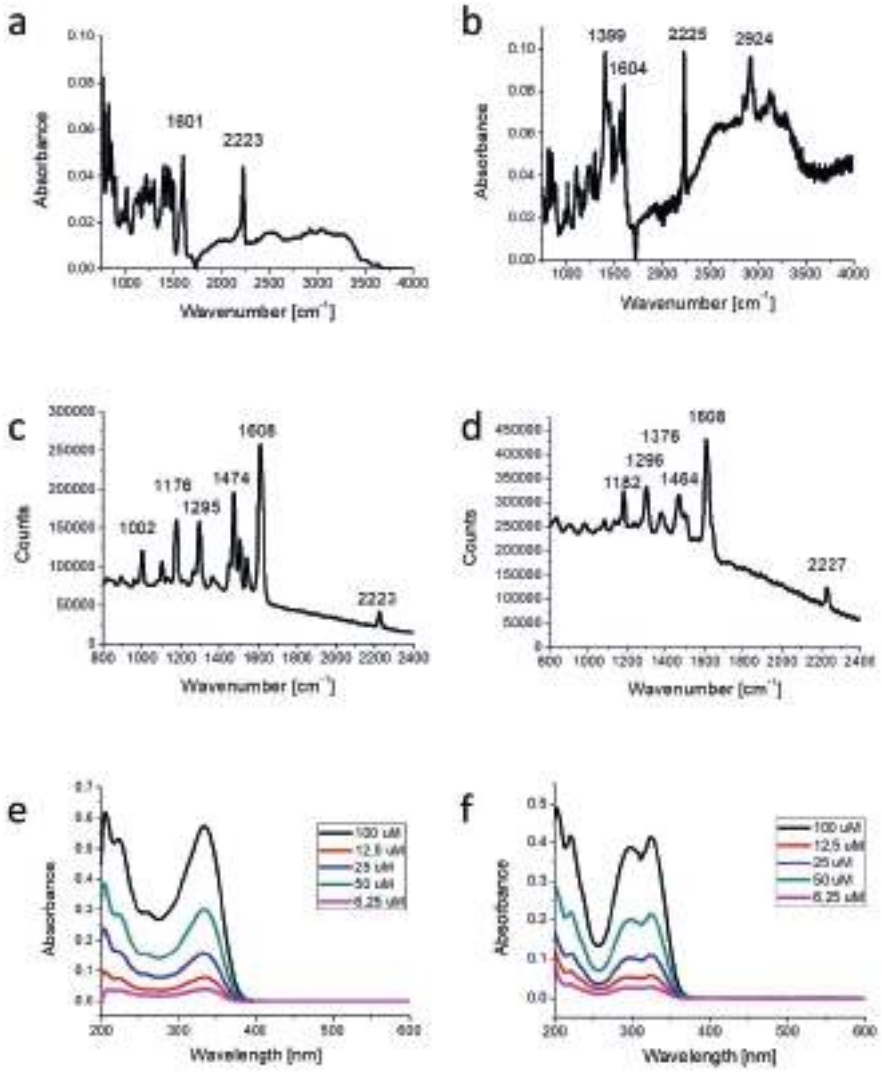

Figure S10: FTIR spectra of (a) G_1 and (b) G_2; Raman spectra of (c) G_1 and (d) G_2; UV-Vis absorption in methanol of (c) G_1 and (b) G_2

3.6. References

3.6.1 Front page illustration (Chapter 3)

Goodsell, D. S. *Biosites: Basement Membrane.* (PDB-101, 2005).

3.6.2 References (Chapter 3)

1 Slocombe, L., Winokan, M., Al-Khalili, J. & Sacchi, M. Proton transfer during DNA strand separation as a source of mutagenic guanine-cytosine tautomers. *Commun Chem* **5**, 144, doi:10.1038/s42004-022-00760-x (2022).

2 Demchenko, A. P. Proton transfer reactions: From photochemistry to biochemistry and bioenergetics. *BBA Adv* **3**, 100085, doi:10.1016/j.bbadva.2023.100085 (2023).

3 Sahu, K., Nandi, N., Dolai, S. & Bera, A. A Ratio-Analysis Method for the Dynamics of Excited State Proton Transfer: Pyranine in Water and Micelles. *J Phys Chem B* **122**, 6610-6615, doi:10.1021/acs.jpcb.8b04271 (2018).

4 Toldo, J. M., do Casal, M. T., Ventura, E., do Monte, S. A. & Barbatti, M. Surface hopping modeling of charge and energy transfer in active environments. *Phys Chem Chem Phys* **25**, 8293-8316, doi:10.1039/d3cp00247k (2023).

5 Zhang, W. *et al.* Highly Fluorescent Liquid Crystals from Excited-State Intramolecular Proton Transfer Molecules. *Advanced Optical Materials* **7**, doi:10.1002/adom.201801349 (2019).

6 Maity, S., Ray, S. S., Chatterjee, A., Chakraborty, N. & Ganguly, J. Sugar-Based Self-Assembly of Hydrogel Nanotubes Manifesting ESIPT: Theoretical Insight and Application in Live Cell Imaging. *ChemistrySelect* **3**, 6575-6580, doi:10.1002/slct.201800604 (2018).

7 Santos, F. S., Ramasamy, E., Ramamurthy, V. & Rodembusch, F. S. Confinement effect on the photophysics of ESIPT fluorophores. *Journal of Materials Chemistry C* **4**, 2820-2827, doi:10.1039/c5tc03245h (2016).

8 Sarkar, N. *et al.* Excited-State Intramolecular Proton Transfer of 2-(2'-Hydroxyphenyl)benzimidazole in Micelles. *The Journal of Physical Chemistry* **99**, 17711-17714, doi:10.1021/j100050a007 (2002).

9 Hossen, T. & Sahu, K. Contrasting pKa shift and fluorescence modulation of 6-cyano-2-naphthol within α- and β-cyclodextrin. *Journal of Photochemistry and Photobiology A: Chemistry* **412**, doi:10.1016/j.jphotochem.2021.113254 (2021).

10 Park, S.-Y., Jeong, H., Kim, H., Lee, J. Y. & Jang, D.-J. Excited-State Proton Transfer and Geminate Recombination in Hydrogels Based on Self-Assembled Peptide Nanotubes. *The Journal of Physical Chemistry C* **115**, 24763-24770, doi:10.1021/jp207245q (2011).

11 Hossen, T. & Sahu, K. Effect of Photoacid Strength on Fluorescence Modulation of 2-Naphthol Derivatives inside beta-Cyclodextrin Cavity: Insights from Fluorescence, Isothermal Calorimetry, and Molecular Dynamics

Simulations. *J Phys Chem B* **123**, 9291-9301, doi:10.1021/acs.jpcb.9b05457 (2019).

12 Chou, H. C. *et al.* Multiple hydrogen bonds tuning guest/host excited-state proton transfer reaction: its application in molecular recognition. *J Am Chem Soc* **126**, 1650-1651, doi:10.1021/ja039240f (2004).

13 Amoruso, G., Taylor, V. C. A., Duchi, M., Goodband, E. & Oliver, T. A. A. Following Bimolecular Excited-State Proton Transfer between Hydroxycoumarin and Imidazole Derivatives. *J Phys Chem B* **123**, 4745-4756, doi:10.1021/acs.jpcb.9b01475 (2019).

14 Kwon, O. H. & Zewail, A. H. Double proton transfer dynamics of model DNA base pairs in the condensed phase. *Proc Natl Acad Sci U S A* **104**, 8703-8708, doi:10.1073/pnas.0702944104 (2007).

15 Qin, X. *et al.* Nano aggregates of amphiphilic phenanthridine dyes for reversible intermolecular excited state proton transfer. *Dyes and Pigments* **145**, 538-541, doi:10.1016/j.dyepig.2017.06.055 (2017).

16 Jacquemin, D., Zuniga, J., Requena, A. & Ceron-Carrasco, J. P. Assessing the importance of proton transfer reactions in DNA. *Acc Chem Res* **47**, 2467-2474, doi:10.1021/ar500148c (2014).

17 Stoner-Ma, D. *et al.* Observation of excited-state proton transfer in green fluorescent protein using ultrafast vibrational spectroscopy. *J Am Chem Soc* **127**, 2864-2865, doi:10.1021/ja042466d (2005).

18 Carroll, E. C. *et al.* Subpicosecond Excited-State Proton Transfer Preceding Isomerization During the Photorecovery of Photoactive Yellow Protein. *J Phys Chem Lett* **1**, 2793-2799, doi:10.1021/jz101049v (2010).

19 Chen, L., Fu, P. Y., Wang, H. P. & Pan, M. Excited-State Intramolecular Proton Transfer (ESIPT) for Optical Sensing in Solid State. *Advanced Optical Materials* **9**, doi:10.1002/adom.202001952 (2021).

20 Dong, H., Yang, H., Zhao, J., Liu, X. & Zheng, Y. Modulation of excited state proton transfer. *Journal of Luminescence* **231**, doi:10.1016/j.jlumin.2020.117840 (2021).

21 Silberbush, O., Engel, M., Sivron, I., Roy, S. & Ashkenasy, N. Self-Assembled Peptide Nanotube Films with High Proton Conductivity. *J Phys Chem B* **123**, 9882-9888, doi:10.1021/acs.jpcb.9b07555 (2019).

22 Szczepanik, B. Protolytic dissociation of cyano derivatives of naphthol, biphenyl and phenol in the excited state: A review. *Journal of Molecular Structure* **1099**, 209-214, doi:10.1016/j.molstruc.2015.05.062 (2015).

23 Behera, S. K., Park, S. Y. & Gierschner, J. Dual Emission: Classes, Mechanisms, and Conditions. *Angew Chem Int Ed Engl* **60**, 22624-22638, doi:10.1002/anie.202009789 (2021).

24 Hestand, N. J. & Spano, F. C. Expanded Theory of H- and J-Molecular Aggregates: The Effects of Vibronic Coupling and Intermolecular Charge Transfer. *Chem Rev* **118**, 7069-7163, doi:10.1021/acs.chemrev.7b00581 (2018).

25 Kwon, O. H. & Mohammed, O. F. Water-wire catalysis in photoinduced acid-base reactions. *Phys Chem Chem Phys* **14**, 8974-8980, doi:10.1039/c2cp23796b (2012).

26 Kwon, O. H., Lee, Y. S., Yoo, B. K. & Jang, D. J. Excited-state triple proton transfer of 7-hydroxyquinoline along a hydrogen-bonded alcohol chain:

vibrationally assisted proton tunneling. *Angew Chem Int Ed Engl* **45**, 415-419, doi:10.1002/anie.200503209 (2006).

27 Assaf, K. I. & Nau, W. M. The Chaotropic Effect as an Assembly Motif in Chemistry. *Angew Chem Int Ed Engl* **57**, 13968-13981, doi:10.1002/anie.201804597 (2018).

28 Wenz, G., Han, B. H. & Muller, A. Cyclodextrin rotaxanes and polyrotaxanes. *Chem Rev* **106**, 782-817, doi:10.1021/cr970027+ (2006).

29 Liu, Y., Zhao, Y. L., Chen, Y. & Guo, D. S. Assembly behavior of inclusion complexes of beta-cyclodextrin with 4-hydroxyazobenzene and 4-aminoazobenzene. *Org Biomol Chem* **3**, 584-591, doi:10.1039/b415946b (2005).

30 Thordarson, P. Determining association constants from titration experiments in supramolecular chemistry. *Chem Soc Rev* **40**, 1305-1323, doi:10.1039/c0cs00062k (2011).

31 Ma, S. *et al.* Organic molecular aggregates: From aggregation structure to emission property. *Aggregate* **2**, doi:10.1002/agt2.96 (2021).

32 Park, J. W. in *Cyclodextrin Materials Photochemistry, Photophysics and Photobiology* 1-26 (2006).

33 Pescitelli, G., Di Bari, L. & Berova, N. Application of electronic circular dichroism in the study of supramolecular systems. *Chem Soc Rev* **43**, 5211-5233, doi:10.1039/c4cs00104d (2014).

34 Browne, W. R. & Vos, J. G. The effect of deuteriation on the emission lifetime of inorganic compounds. *Coordination Chemistry Reviews* **219**, 761-787 (2001).

35 Kučera, J. *et al.* Enhancement of luminescence signal by deuterated water – Practical implications. *Sensors and Actuators B: Chemical* **352**, doi:10.1016/j.snb.2021.131029 (2022).

36 Filer, C. N. Luminescence enhancement by deuterium. *J Labelled Comp Radiopharm* **66**, 372-383, doi:10.1002/jlcr.4056 (2023).

37 Stryer, L. Excited-State Proton-Transfer Reactions. A Deuterium Isotope Effect on Fluorescence. *Journal of the American Chemical Society* **88**, 5708-5712, doi:10.1021/ja00976a004 (2002).

38 Williams, A. T. R., Winfield, S. A. & Miller, J. N. Relative fluorescence quantum yields using a computer-controlled luminescence spectrometer. *The Analyst* **108**, doi:10.1039/an9830801067 (1983).

39 Brynn Hibbert, D. & Thordarson, P. The death of the Job plot, transparency, open science and online tools, uncertainty estimation methods and other developments in supramolecular chemistry data analysis. *Chem Commun (Camb)* **52**, 12792-12805, doi:10.1039/c6cc03888c (2016).

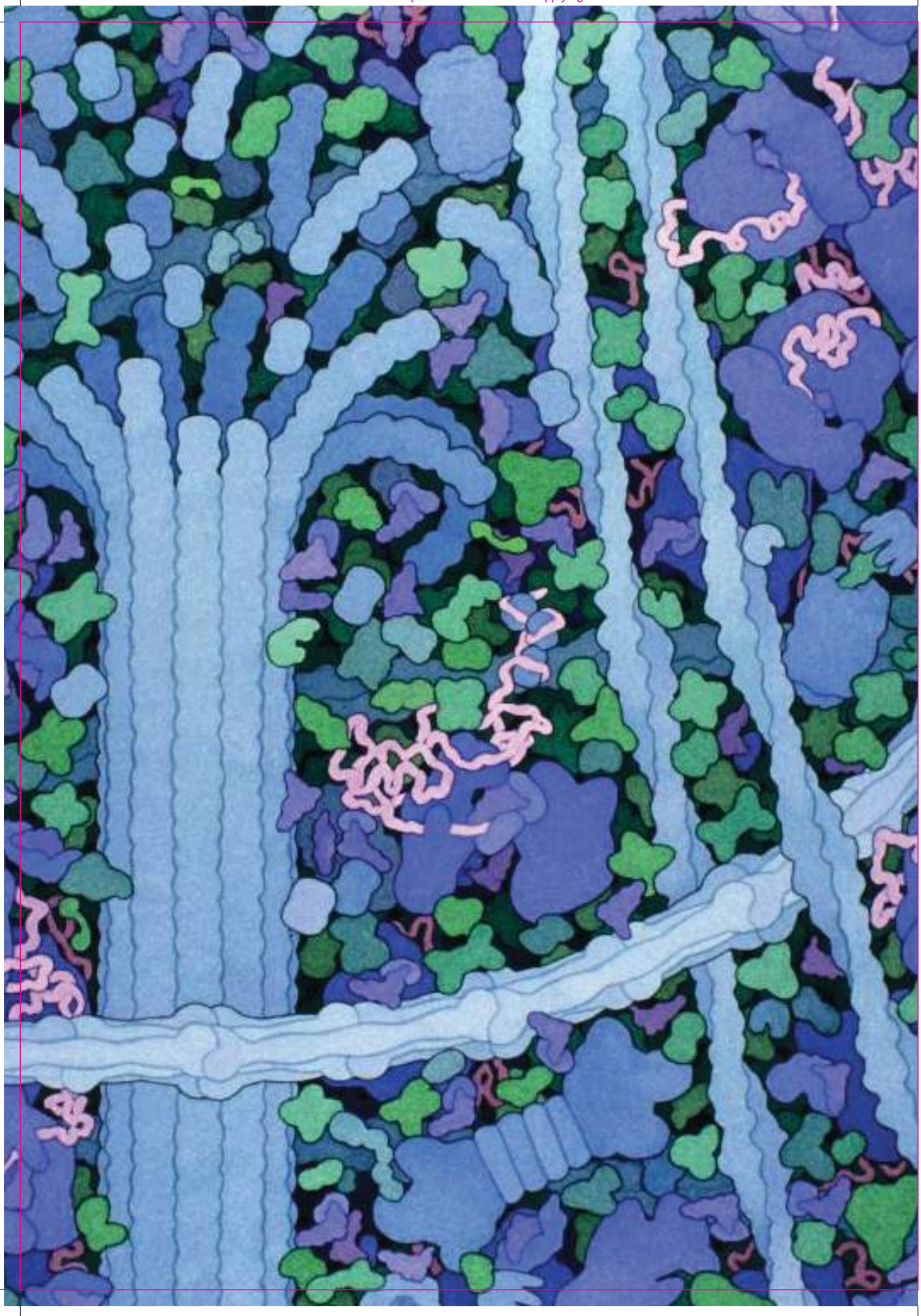

4

Exerting mechanical forces through supramolecular self-assembly

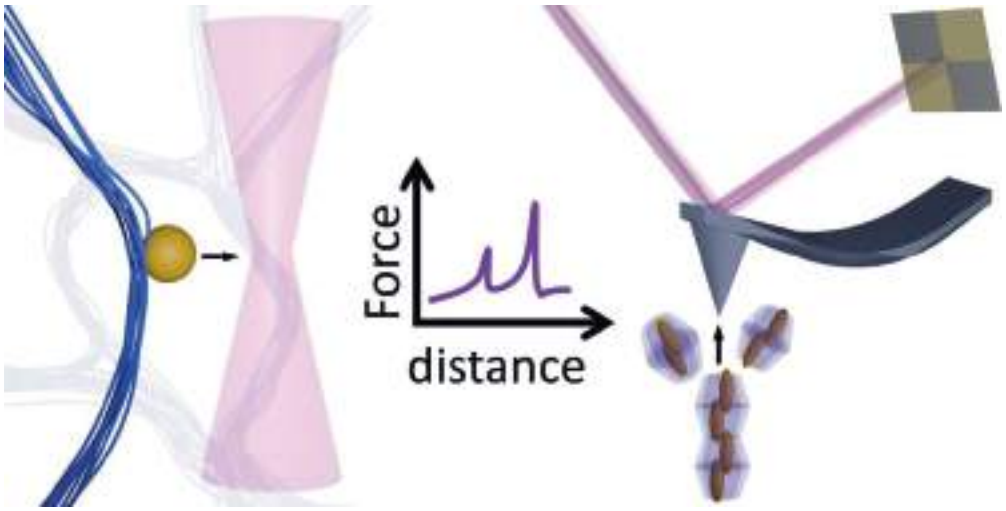

ABSTRACT:

Measuring forces at the micro- and nanoscale has significantly advanced our understanding of biomechanics and nanomachinery. Despite optical tweezers and atomic force microscopy having revolutionized this field of study, only recently has force spectroscopy gained attention for characterizing mechanically active synthetic systems inspired by the self-assembly of bio-polymerization motors. These advanced techniques combine the precision of quantitative analysis with real-time observation and non-invasive micromanipulation, enabling detailed investigation of how supramolecular structures respond to or exert mechanical forces via self-assembly. This chapter explores the application of these methods in hierarchically structured materials, emphasizing the critical role of structure-function relationships in harnessing molecular events while maintaining directionality across length scales.

Part of this Chapter is based on a publication: L. C. Pantaleone†, E. Calicchia, J. Martinelli, M. C. A. Stuart, Y. Y. Lopatina, W. R. Browne, G. Portale, K. M. Tych*, T. Kudernac*; Nature Nanotechnology (2024)

4.1. Outline

This Chapter explores the application of force spectroscopy in studying mechanical transduction in hierarchically structured materials. It is divided into three sections, each section is based on a distinct synthetic system (Figure 1).

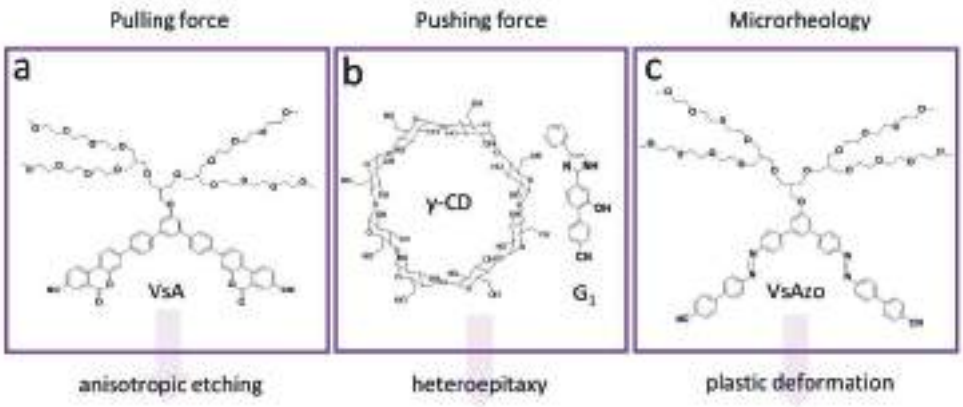

*Figure 1: Synthetic designs used in this Chapter to study distinct properties of hierarchically structured materials resulting from their self-assembly. (**a**) Coumarin-based amphiphile. (**b**) Inclusion complexes of γ-cyclodextrin and G_1. (**c**) Azobenzene-based amphiphile.*

In the first section, we leveraged the anisotropic effects observed during the etching of microcrystalline fibers, as discussed in Chapter 2, to exert pulling forces on microscopic loads (Figure 1a). This subchapter, along with the structural characterization and reactivity studies presented in Chapter 2, constitutes a comprehensive work detailing how the biased diffusion mechanism originates from the anisotropy of the material. The study of the pulling forces produced by disassembly highlights the role of fiber morphology in controlling the diffusion of cargo on the crystal surface through frictional and adhesive forces.

The second section introduces a templating strategy to orient supramolecular polymerization on a surface, adapting the system introduced in Chapter 3 for AFM measurements of pushing forces (Figure 1b). Although force measurements remain a future goal of this project, in this subchapter we addressed one of the key challenges in developing Brownian ratcheting from self-assembling systems: controlling the spatial growth of supramolecular structures. Various surface characterization techniques were used to demonstrate the value of heteroepitaxy as a strategy to direct the polymerization of cyclodextrin complexes from a barrier (Au surface) toward the load (AFM probe).

In the third and final section of this Chapter, optical tweezers were used to investigate the plastic deformation of a synthetic hydrogel, revealing a mechanism of mechanical energy dissipation based on interfiber sliding (Figure 1c). By combining the technical capabilities of optical tweezers for micromanipulation, force spectroscopy, and confocal imaging, we demonstrated how the secondary interactions responsible for the bundling of nanofibers enable the mesh to adapt under tensile forces, resembling the plastic behavior of collagen networks. The synthetic system introduced in this subchapter will also be studied in Chapter 5, where we will explore the mechano-chemistry of this hydrogel in microcompartments.

4.2

4.2. Pulling forces

4.2.1 Exerting pulling forces in fluids by directional disassembly of microcrystalline fibres

In Chapter 2 we introduced a self-assembling system based on a pH-switchable amphiphile (VsA)(Figure 2a). After characterizing the pH actuation mechanism based on the reversible hydrolysis of the coumarin motif embedded in the aromatic scaffold, we studied the effects of self-assembly on monomer reactivity. The main conclusion from this first part of the study was that upon assembling into microcrystalline fibres, the monomer is stabilized against hydrolysis in the bulk of this structured material. Moreover, due to the anisotropic properties of these crystalline fibres, the morphology influences the reactivity of VsA at the interface, with the rate of coumarin hydrolysis being dependent on the crystal facet. Specifically, the 00l facet, covering the largest surface of the crystal, shields the coumarin switch from the solvent by exposing the glycol tail of the amphiphilic monomers. Etching the crystalline material in alkaline solutions results in the directional disassembly along the fibre axis, with the crystal edge at the fibre ends exposing the most reactive facets in the [0k0] crystallographic direction.

Controlling the directional disassembly of microfibres is the starting point for exerting pulling forces. In this second part of the project, we will focus on introducing a cargo that could be mechanically displaced by the disassembly of the crystal. The cargo should be bound to the surface with a multivalent interaction to develop biased diffusion, as shown in Figure 2a. As anticipated, force spectroscopy will play a central role in investigating how crystal morphology and surface chemistry control the motion of cargo through adhesion and frictional forces. Most importantly, the main goal of this section will be to prove chemo-mechanical transduction in fluids and provide a quantitative measure of the mechanical work that this synthetic system can eventually produce.

This subchapter is based on a publication: L. C. Pantaleone†, E. Calicchia, J. Martinelli, M. C. A. Stuart, Y. Y. Lopatina, W. R. Browne, G. Portale, K. M. Tych*, T. Kudernac*; Nature Nanotechnology (2024)

4.2.2 Main

To explore whether the shortening of the fibres can effectively exert mechanical pulling forces, the fibres were decorated with multivalently bound microscopic cargo. Specifically, amino-functionalized polystyrene beads were chosen to adsorb to the crystal surface by hydrogen bonding with the dendron tails of the glycol-rich monomers.[1] These interactions result in the strong adhesion of beads to the surface of the fibres and allow incorporation of beads in the fibre network after pre-incubation of the former with assembling monomer, or to decorate individual fibres with beads using the optical tweezers as micro-manipulators (Supplementary Figure 1a-c, 1d-f). A strong but dynamic multivalent interaction is required to prevent the detachment of cargo, while allowing its surface diffusion.[2] As shown in Figure 2c, the latter process implies a lower activation energy due to simultaneous loosening and formation of dynamic fibre-bead contacts. By contrast, AFM measurements confirmed that desorption of microspheres from the crystal surface only occurs upon application of large forces, in the nano-newtons range (Figure 3a-b). Despite the strong adsorption, in biased diffusion models the dynamic nature of the contacts implies that the cargo is capable of randomly exploring the fibre surface by thermal activation, albeit diffusion on a scale relevant to optical-microscopy only occurs under the drive of fibre disassembly (See Supplementary Video 1, and 2). Etching of the decorated fibre networks was first imaged with bright field and epifluorescence microscopy (See Supplementary Video 3, and 4). Directional motion was detected when beads were interconnected by disassembling fibres, pulling the cargo over micrometre distances (Figure 2b).

Optical tweezers (OTs) force measurements were employed to gain more quantitative insight into the directional forces exerted during the anisotropic etching. This pulling experiment was performed by trapping a pair of beads connected by a bridging fibre (Figure 4a) (See Supplementary Video 5). Following the successful trapping of the pair of beads in two laser beams the hydrolysis of the fibre was initiated. Force traces corresponding to the individual beads were perfectly anticorrelated, as expected from two trapped objects connected by a rigid element (Figure 4b, Supplementary Figure 1g). As the crystal edge reached the contact area the distance between the beads decreased. The corresponding displacement from the trap centre was confirmed by a proportional increase in the F_x force traces, while significant fluctuations of force were not detected along its orthogonal component (Fig. 4b-c, 4d-e). The beads were displaced until the system reached a stall force of 2.3 pN ($\pm$ 0.1 pN), producing an estimated mechanical work of 85 kT. These figures are in the same range of tensions

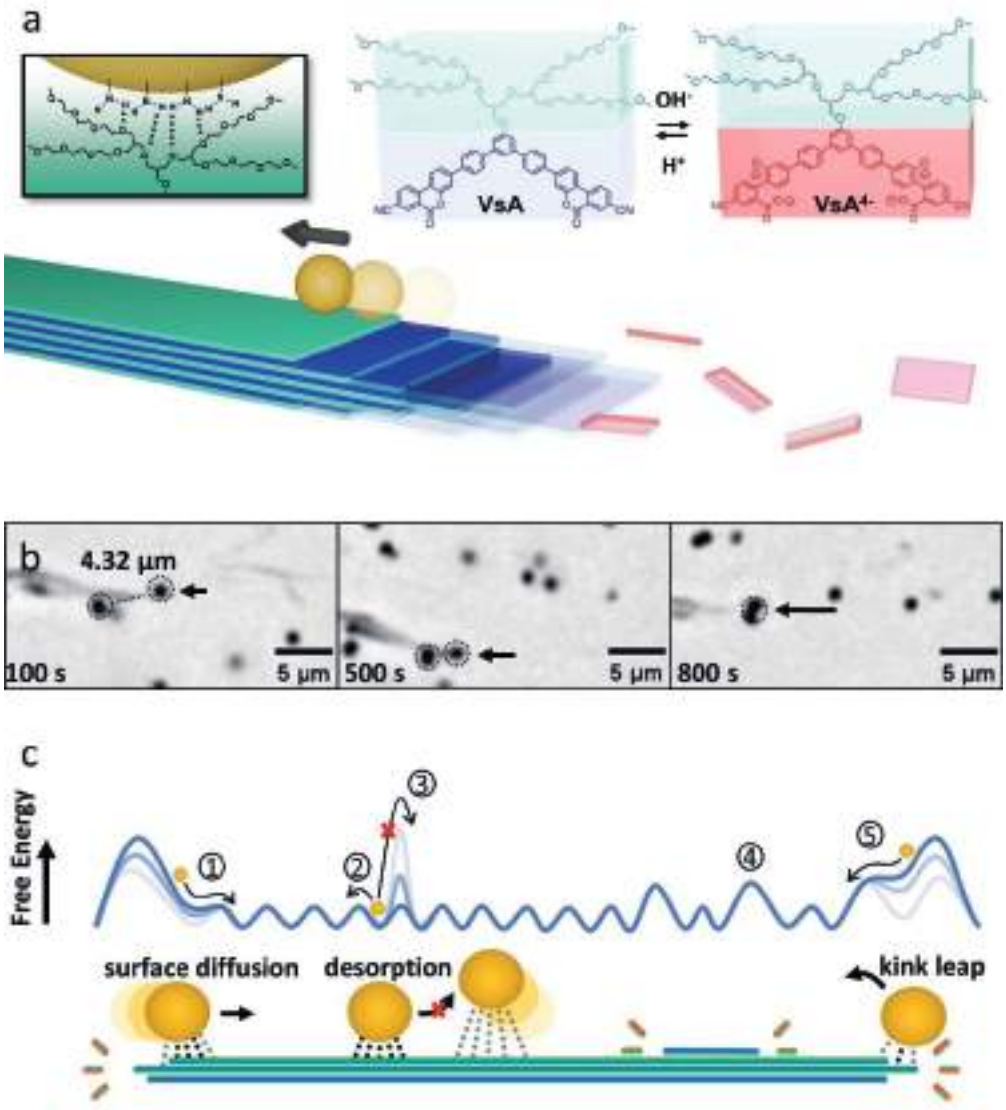

*Figure 2: (**a**) Mechanism of force exertion by disassembling microcrystalline fibres. Amino functionalized 1µm polystyrene beads are pulled along the fibre axis during the anisotropic etching at the crystal interface to maintain the multivalent interactions with the crystal surface. The disassembly is controlled by the pH-switchable coumarin motif as part of the aromatic scaffold of the monomer. (**b**) Pulling motion in a connected pair of beads was observed with microscopy during fibre disassembly. (**c**) The scheme correlates the dynamics of a multivalently bound cargo with a free energy landscape showing the effect of anisotropic etching on surface diffusion. ① Biased and ② thermal diffusion, ③ desorption, and ④⑤ effect of asperities caused by crystal morphology on corrugation height.*

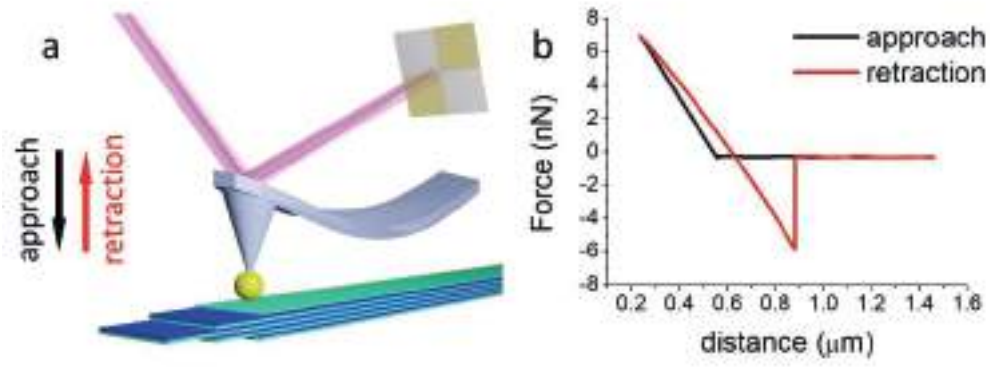

*Figure 3: (**a**) Representation of the experimental setup for adhesion force measurement between AFM colloidal probe and crystal surface. The cantilever is equipped with a spherical colloidal probe of amino functionalized polystyrene (d=1µm). (**b**) Adhesion force measurement. The force required to desorb the AFM colloidal probe from the crystal surface is 5.85 nN.*

(0.5 – 3 pN) supported by microtubules during in vitro motility assays.[11] The fact that the movement observed was associated with concerted pulling events spanning hundreds of nanometres, as shown by the distribution of the histograms in Figure 4c and Figure 4e, suggests that crystal kinks, which possess a similar spacing according to AFM topography of the crystal edge (Figure 5a-b), may play a role in limiting diffusion along the fibre surface generating sliding or rolling friction.[3] These kinks, with a step size between 10-30 nm of height, constitute the main element of asperity of a relatively flat terracing morphology. Therefore, based on how work is supplied according to the force traces, one could speculate that these elements of surface morphology may affect the shape of the energy landscape in the same way corrugation height is considered in the biased diffusion model of kinetochores (Figure 2c).[4,5]

Comparing optical microscopy and force spectroscopy pulling experiments we observed that the restriction of microbeads' motion has implications on the extent of the disassembly of the fibres. In the absence of external forces applied on the beads, the disassembly of the crystal pulls the beads across µm distances, fully hydrolysing the fibres at an approximate rate of 200-300 nm per minute. In contrast, when the beads are subjected to the force field of the OTs, the disassembly initially proceeds at a comparable pace but ceases after reaching the stall force. Because the etching mechanism is halted once the cargo is unable to move and the fibre-bead contact is retained even after 30 minutes of digestion

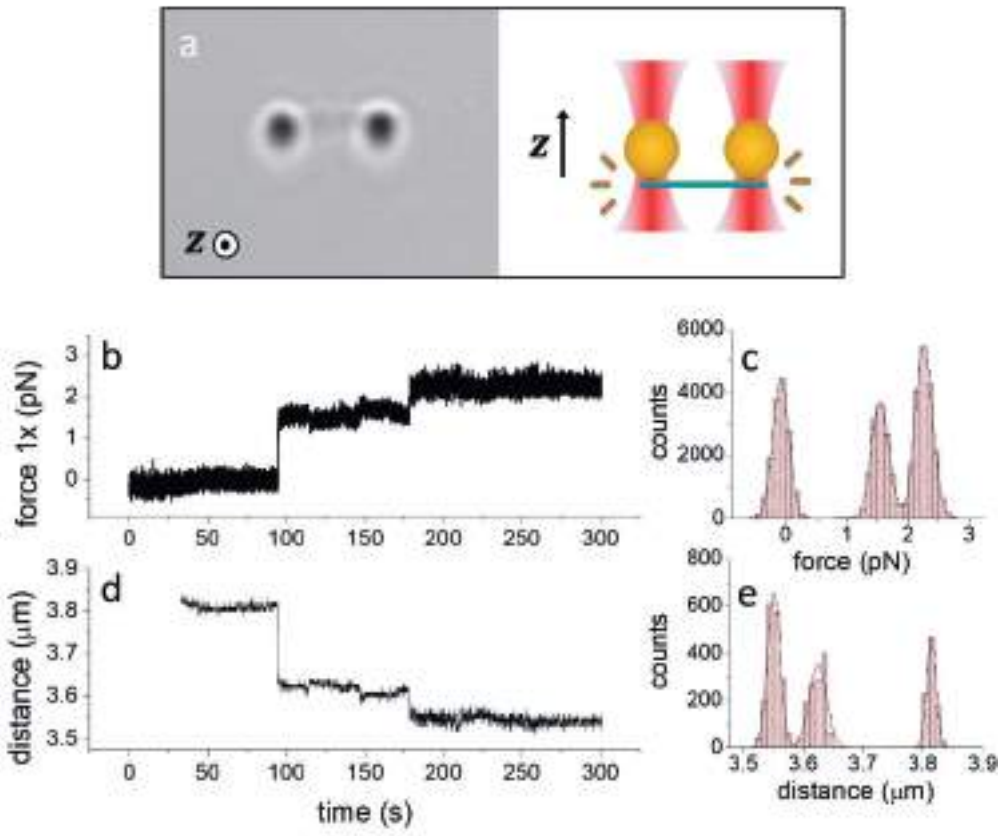

*Figure 4: (**a**) Bright-field microscopy of beads connected by a bridging fibre in the OT setup. A side view of the setup with the configuration of the OT is outlined next to the micrograph. (**b**)(**c**) The pulling force generated by the disassembly of a fibre was measured using two optically trapped beads (1μm). The spring constant of the trap k=18.3 fN/nm, sampling frequency of the force 150Hz. (**d**)(**e**) Inter-beads distance sampling frequency 15Hz. Work done during the pulling events (W= $F_{1x}\Delta x$) was calculated assuming the beads experience anticorrelated forces (F_{1x}=-F_{2x}).*

with base, we suspect that the polystyrene surface may stabilize adsorbed monomers in the contact area.

Once again, to understand what lies behind this mechanism, it is useful to think in terms of free energy as the maximization of the fibre-bead contacts. The optimal binding site for the beads is the 00l facet, constituted by the peg-rich, flat surface of the crystal. However, if an external force does not allow the cargo to reconfigure and diffuse along the disassembling axis, then beads in proximity of a crystal kink can adsorb onto the 0k0 facet, while resting at the crystal edge. Unable to move, the bead is effectively "capping" the most reactive crystal facets,

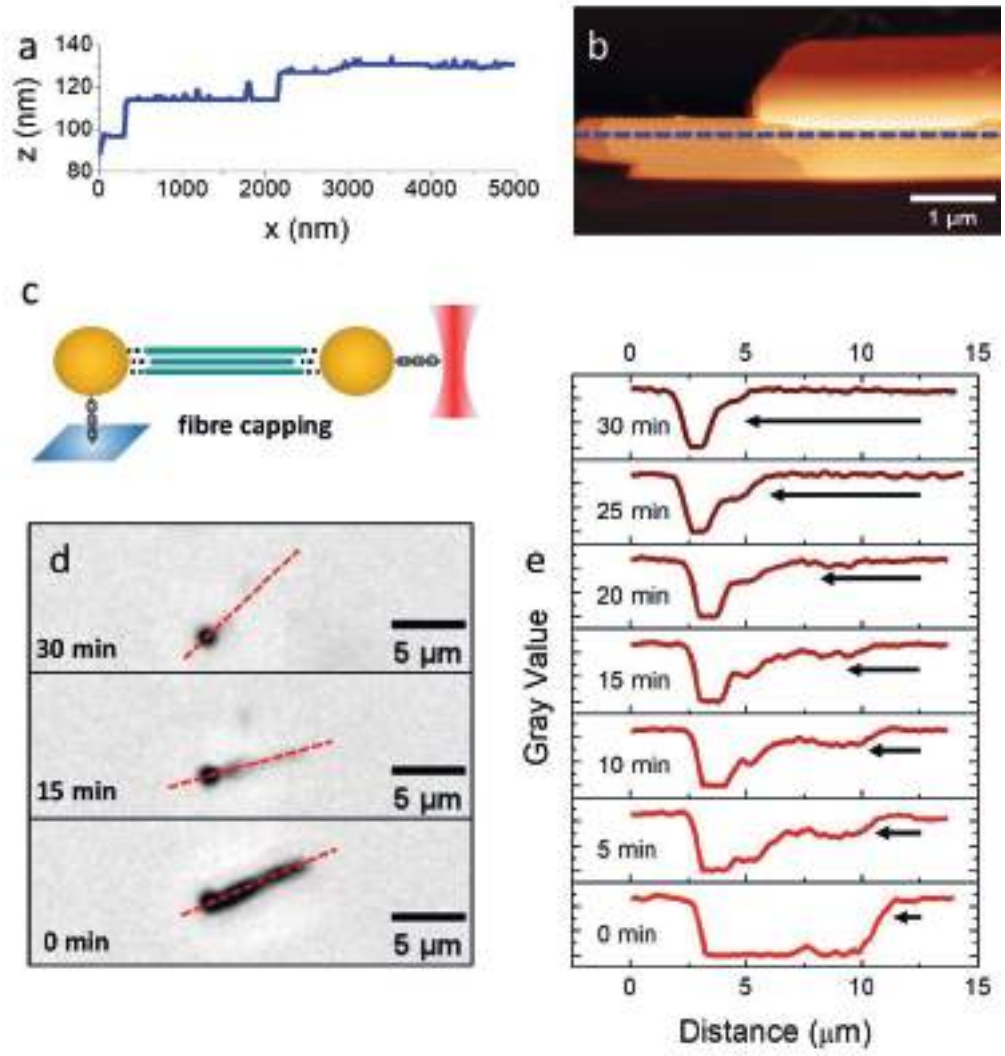

*Figure 5. (**a**) z-profile of the crystal edge and (**b**) corresponding AFM topography imaging, blue dashed line is the plotted profile. Topography reveals that the crystal edge is characterized by a flat terracing morphology, where smooth surfaces extending hundreds of nanometres are spaced by crystal steps of 10-30 nm height. . (**c**) Beads can stabilize the fibre edge by adsorbing hydrolysis-sensitive crystal facets. This mechanism holds as long as the cargo is unable to move, immobilized by the force field of the optical tweezers or by a strong interaction with the glass surface. (**d**)(**e**) Micrographs from Video S-6 and corresponding image analysis show that the disassembly along the fibre axis occurs asymmetrically, with the capped end of the crystal showing greater etching resistance.*

and the result is an increased resistance towards hydrolysis (Figure 5c). In other words, the stabilization of the fibre bridge is caused by an observer effect since the measurement restricts the movement of cargo.

The stabilization effect in "capped" crystal edges was also observed when adsorbed beads were occasionally immobilized by interaction with the glass surface of microscopy chambers (See Supplementary Video 6). Analysis of the micrographs shows that the anisotropic etching of such anchored crystals occurs asymmetrically, starting from the exposed edge of the fibre towards its capped end (Figure 5d-e). This experiment confirms that, besides the optical trap, any external constrain that immobilizes the cargo can result in the stabilization of monomers the contact area.

Regarding the inertness of monomers in the contact area, stabilization of crystal facets by the addition of adsorbing polymeric additives has been widely reported.[6,7] The effectiveness of polystyrene adsorption in preventing monomer hydrolysis is also supported by the coumarin emission from the surface of the beads, which was detected long after the complete disassembly of fibre networks in pulling experiments monitored with epifluorescence microscopy (See Supplementary Video 4).

4.2.3 Conclusions

In conclusion, we demonstrated that anisotropic etching of microcrystals suspended in fluid can result in an effective chemo-mechanical transduction. Albeit distant from the sophistication of biological depolymerization machinery, the present system is the first synthetic example of mechanical work generation in fluids by crystal disassembly, where the equilibration of the system is driven by complex chemical conversion. The generation of mechanical force in our system can be understood by Hill's diffusion model which considers diffusion of multivalently bound cargo in the direction of the disassembling tracks.[5] The measured mechanical force of 2.3 pN is similar to the forces exerted by disassembling cellular microtubules.[11] The active area of the disassembling crystal that solely contributes to the produced mechanical force is its topmost layer. Consequently, self-assembling architectures as thin as a single layer could in principle exert equally large mechanical forces while benefitting from a more efficient atom economy and energy conversion. The same ratcheting mechanism stands for any supramolecular polymer that can transfer its directionality to a multivalently bound cargo when disassembling. The diversification of monomer

reactivity at the crystal interface provides such a mechanism, imprinting the anisotropy of the lattice into the movement of cargo.

Biased diffusion, which we have demonstrated can operate at the mesoscale, represents a promising strategy to develop new methods for active transport and chemical actuators based on fibre disassembly.[8] Further advances in these directions, will require exploring nanofabrication techniques to achieve macroscopic fibre alignment.[9,10] Indeed, scaling the anisotropic properties of microcrystals will be crucial, both for investigating cargo diffusion in fibre networks and for developing novel bulk rheological properties emerging from the energy transduction process.

4.2.4 Acknowledgements

I wish to thank K. M. Tych for her support and guidance in the OTs experiments. I gratefully acknowledge Y. Y. Lopatina for the AFM measurements. I wish to thank Victor Verduijn for his contribution to processing force spectroscopy data using the Pylake Python package.

4.2.5 Supplementary information

Supplementary Video 1: Thermal diffusion of beads in the absence of hydrolysis, bright field microscopy (video speed 100X, scale bar 10 μm) (60°C). This control experiment shows that the thermal diffusion of cargo adsorbed on the crystal surface is very limited compared with biased diffusion. The strength of the adhesion force is also evident as beads transported by the flow often adsorb on the crystal surface.

Supplementary Video 2: Biased diffusion of bead induced by fibre disassembly, bright field microscopy (video speed 100X, scale bar 10 μm) (NaOH, 60°C). During the hydrolysis of fibres, the movement of adsorbed beads remains minimal if the fibre edge does not reach the contact area.

Supplementary Video 3: Biased diffusion of bead induced by fibre disassembly, bright field microscopy (video speed 100X, scale bar 10 μm) (NaOH, 60°C). In this video both bead and fibre are visible during the pulling event. The directions of cargo diffusion and crystal etching coincide. By serendipity, the movement observed counters the chamber's flow.

Supplementary Video 4: Disassembly of fibres exerts enough pulling force to drag a connected triplet of beads close together. Pulling of beads was observed with epifluorescence microscopy (video speed 100X, beads diameter = 1 μm, λ_{ex}= 330 – 380 nm and λ_{em} =420 nm for imaging fibres, λ_{ex}= 510 – 560 nm and

λ_{em}=580 nm for imaging beads). Directional and coupled motion of connected beads was detected during pulling. Disassembly of the fibres was induced by basic hydrolysis of the monomer (NaOH, 35 °C).

Supplementary Video 5: Bright-field microscopy of a pair of beads connected by a bridging fibre in the OT setup. Disassembly of the fibres was induced by basic hydrolysis of the monomer (NaOH, 35 °C). At the end of the experiment, one of the beads was released from the optical trap to show that the fibre was still connecting the pair.

Supplementary Video 6: Asymmetric etching of fibre axis caused by the stabilization of the crystal edge by anchored polystyrene bead, bright field microscopy (video speed 100X, scale bar 10 μm) (NaOH, 60°C).

General procedure for preparation of VsA micro-crystalline fibres for optical microscopy: a stock solution of monomer in acetonitrile ([VsA]=100 μM) was diluted and dispersed in MilliQ water (water/acetonitrile 80:20) to adjust the final concentration of monomer to 5 μM. The sample was annealed in a thermostated bath at 60°C which was left cooling at room temperature for 10 hours.

Fluorescence and Cross-Polarized Optical Microscopy: Imaging with fluorescence microscopy was performed in a Nikon Eclipse LV100N POL microscope using filters of the following excitation and emission wavelengths cut-offs: λ_{ex}= 330-380 nm; λ_{em} =420 nm - for imaging the VsA fibres; λ_{ex}=510-560

nm; λ_{em}580 nm - for imaging polystyrene microsphere labelled with fluorescent red.

Atomic force microscopy (AFM): topography imaging and AFM-based force-spectroscopy (AFM-FS) were performed on an Agilent PicoLE system in air. Images of microcrystalline fibers were obtained in AC-mode using standard silicon nitride probes (PPP-NCHR, Nanosensors) with resonance frequency ~330 kHz. The error in measuring height was within 6%. Data leveling and background subtraction were performed with Gwyddion software. The force-spectroscopy measurements were carried out using NH_3-functionalized polystyrene microspherical probes (diameter d=1.0 μm) with spring constant k=0.03 N/m (PT.PS.NH 3,Novascan). The estimate of adhesion force range was based on fifty spectra acquisitions, conducted with different tips and varying sampling locations.

General procedure for preparation of VsA micro-crystalline fibres for OTs experiment: a stock solution of monomer in acetonitrile ([VsA]=100 μM) was diluted and dispersed in MilliQ water (water/acetonitrile 80:20) to adjust the final concentration of monomer to 5 μM. The sample was annealed in a thermostated bath at 60˚C which was left cooling at room temperature for 10 hours. The fibre suspension was loaded in a custom-made microscopy chip with a 40 μL capacity and 0.3 mm thickness. The chip was constituted by three communicating chambers designed to minimize mixing their content by diffusion. After loading the fibre solution in the first compartment, the two other chambers were loaded with a solution of 1M NaOH and a suspension of 1μm amino-functionalized polystyrene microspheres respectively. After immobilizing a single crystalline fibre using two optically trapped microspheres (See Supplementary Figure 1d-f), the fibre was moved into the chamber filled with the alkaline solution and the temperature of the objective and condenser was increased to 35˚C to induce the hydrolyzation of the fibres. The effect of temperature change on the trap stiffness was assessed by comparison of the spring constant with the value extrapolated from a trap calibration; the offset at 35˚C was found negligible (Δk=0.4%) and no correction was applied (See Supplementary Figure 1h).

Optical Tweezers: Force spectroscopy measurements were performed with optical tweezers using a commercial setup (C-Trap) from Lumicks operated in dual-trap regime. The force was measured by a position-sensitive detector (PSD) in two dimensions on both beads with an acquisition rate of 78 kHz. The measurement of the inter-bead distance was performed by bright-field optical tracking with a resolution of 10 nm at 15 Hz. The acquisition was controlled by Bluelake software (Lumicks). To analyze and store the force trace data the force

acquisition frequency was down-sampled to 150 Hz using the Pylake Python package.[11] The trap stiffness was calibrated using the thermal noise method.[12] The force resolution of this calibration was estimated to be 100 fN at 150Hz, with a theoretical limit of 0.4 fN for a typical trap stiffness of 16.5 fN/nm at room temperature.

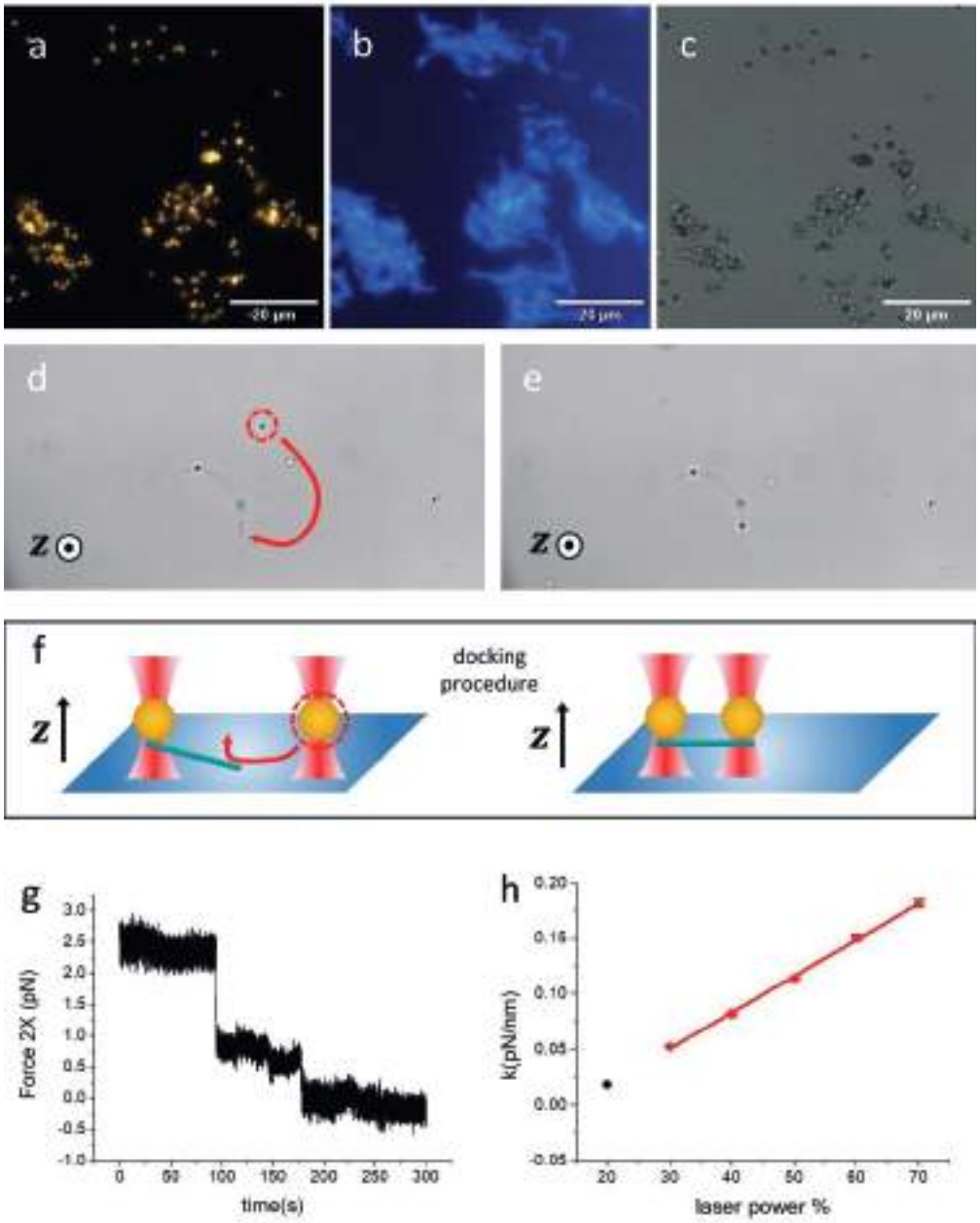

*Figure S1: (**a**)(**b**)(**c**) Fluorescence and bright field micrographs of beads pre-incubated with assembling monomer. (**d**)(**e**)(**f**) Bead docking procedure for the preparation of a fibre bridge in the OT setup. (**g**) Force measurement from the second trapped bead. The comparison of force traces from the two traps shows that pulling events are anti-correlated, as expected for motions on this timescale for a fibre that is not attached to any other surfaces. (**h**) Calibration of spring constant values at 35°C (red, Adj. R-Square 0.99834, Intercept -0.047, Slope 0.00326), spring constant used during force spectroscopy measurements (black, k=18.2665 fN/nm), measured operative laser power $P_{100\%}$=14 mW.*

4.3. Pushing forces

4.3.1 Templating the self-assembly: towards polymerization motors operating by the mechanism of Brownian ratcheting

Precise coordination of molecular events at the correct location is necessary for ensuring proper function in all living systems. The operation of bio-polymerization machinery represents no exception. Unlike biased diffusion or conformational wave mechanisms, that rely on coupling devices for spatial control, Brownian ratcheting requires specialized nucleation proteins to ensure that the growth of the polymerization motor is directed toward the load. Microtubule organizing centres (MTOCs) are an example of such nucleation sites used to initiate the outgrowth of microtubules, stabilize their minus end, and anchor the fibre to the centrosome.[13,14]

The interest in direct force measurements for studying polymerization motors encouraged researchers to develop similar nucleation strategies to control fibre growth. In the one of the first successful attempts to observe the assembly dynamics of microtubules with optical tweezers, Kerssemakers et al. used an axoneme, a stabilized axial filament, to nucleate and direct the polymer growth against a microfabricated barrier.[15] A later study by Schmidt et al. reported a direct measurement of pushing force exerted by the growth of actin gels on an AFM colloidal probe functionalized with Wiskott–Aldrich Syndrome protein (WASp).[16] When associated with the Arp2/3 actin-regulatory complex, this protein is known to induce the branching and local formation of new actin filaments.[17]

With the perspective of studying the pushing force exerted by the supramolecular polymerization of synthetic systems, in the second part of this chapter, we will focus on developing nucleation strategies to direct the polymerization of cyclodextrin nanotubes in an AFM experimental setup (Figure 6). The formation of these nanotubes is

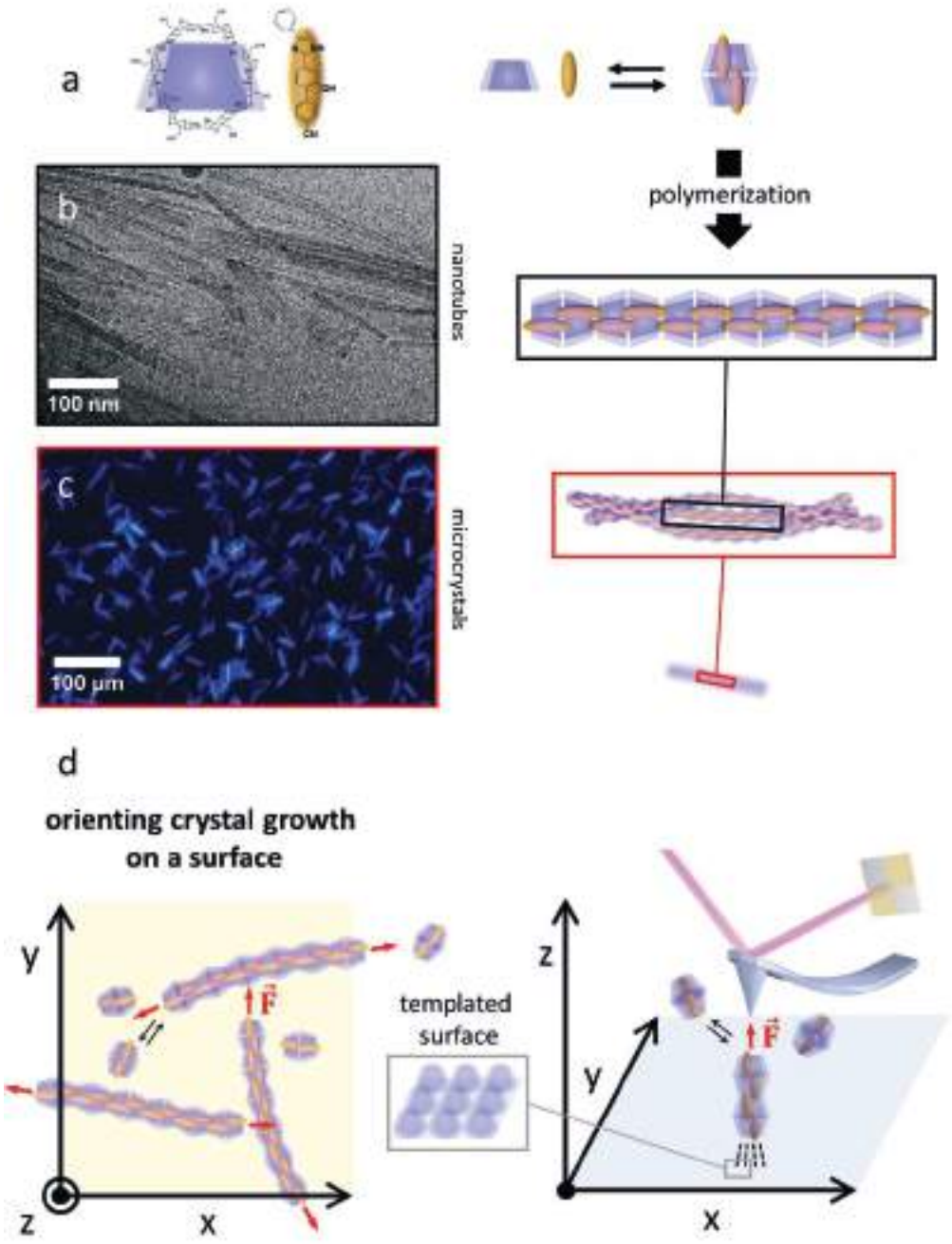

*Figure 6. (**a**) Self-assembly of the inclusion complex formed between γ-cyclodextrins and aromatic guest molecule into crystalline bundles (**b**) Cryo-EM of nanotubes (**c**) Epifluorescence micrograph of crystalline rods. (**d**) Orienting crystal growth using a templated surface for AFM force spectroscopy experiments*

mediated by the formation of an inclusion complex between γ-cyclodextrin and an aromatic guest (G_1), as was previously discussed in Chapter 3. Among other advantages, the formation of the inclusion complex can be time-controlled by pH activation since both protonation or deprotonation equilibria of the amphoteric G_1 can reverse the supramolecular binding with cyclodextrin and depolymerize the hierarchical structure. The supramolecular polymerization, summarized in Figure 6a, matches the essential requirements for harvesting mechanical work via Brownian ratcheting. Tubular-shaped aggregates naturally possess a defined growing direction and display an inherent rigidity due to their morphology (Figure 6b). Moreover, we observed that these nanotubes arranged into bundles when concentrated, forming microscopic crystalline rods of very regular shape and size (Figure 6c). This secondary hierarchical organization orients the polymerization of individual nanofibres in one direction, which coincides with the long axis of the crystalline rods. Aligning this growing axis perpendicular to the surface in a liquid chamber would enable the observation of polymerization through the pushing force exerted on the AFM colloidal probe (Figure 6d). Thanks to the possibility of imaging with atomic resolution in a fluid environment and coupling this measurement with force spectroscopy information, AFM has proven to be a powerful method for gaining insights into the dynamics of macromolecules, supramolecular binding, and details of biological processes in real time.[18-21]

Inspired by the possibility to apply such a technique to study polymerization of artificial systems, we focused our efforts in developing a self-assembled monolayer (SAM) that could template the growth of our synthetic fibres and impart the desired orientation to the crystal-bundles. We envision that heteroepitaxy will not only enable us to harness the mechanical potential of polymerization, but also improve the predictability of molecular events during uniaxial growth. This increased directionality will enhance our ability to resolve individual steps of the chemo-mechanical cycle during force spectroscopy measurements.

4.3.2 Main

The template effect is a versatile tool in supramolecular chemistry which has been largely employed to control self-assembly and molecular orientation on surfaces.[22,23] For a templating surface to bind the cyclodextrin units with a precise configuration the structure of the SAM should match the packing mode of the crystalline bundles. Besides for anchoring and orienting the nanotubes, this

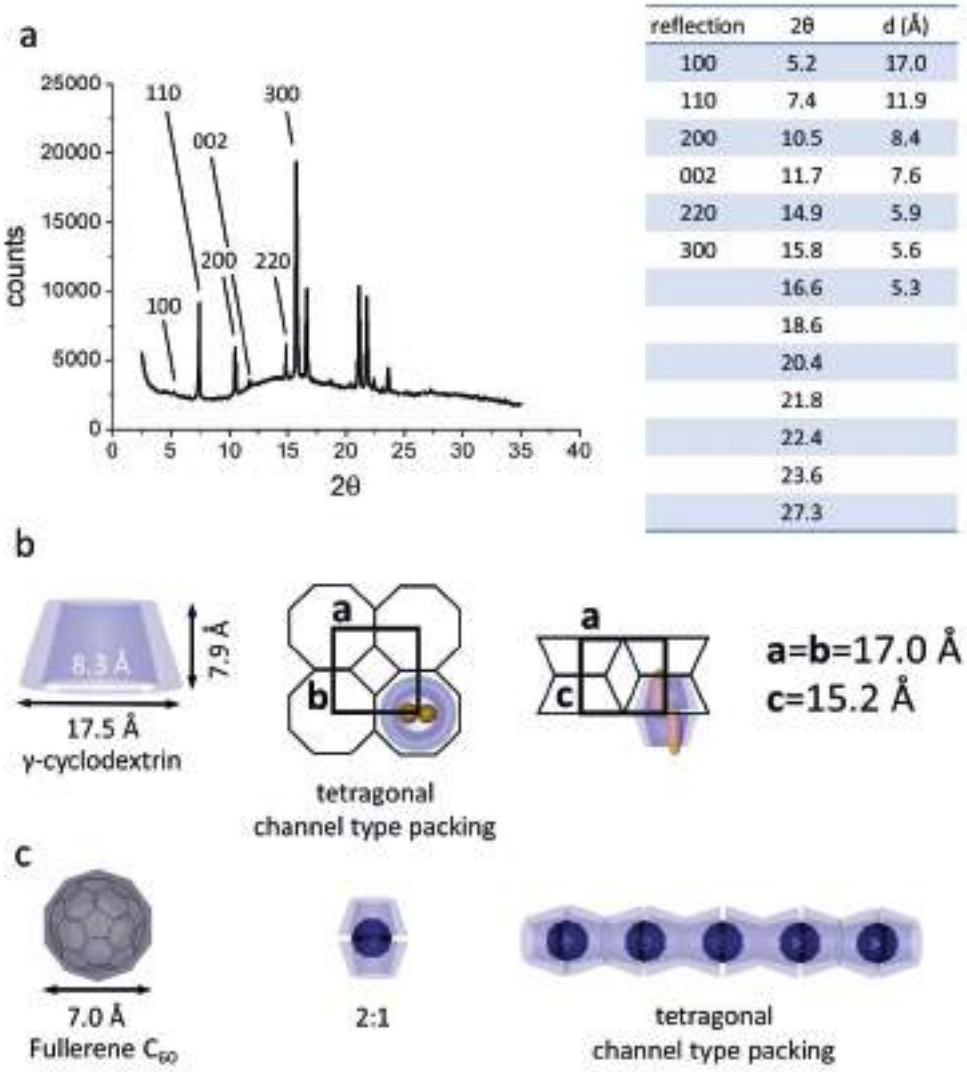

reflection	2θ	d (Å)
100	5.2	17.0
110	7.4	11.9
200	10.5	8.4
002	11.7	7.6
220	14.9	5.9
300	15.8	5.6
	16.6	5.3
	18.6	
	20.4	
	21.8	
	22.4	
	23.6	
	27.3	

*Figure 7: (**a**) PXRD spectrum of deposition of microcrystalline rods. The diffraction pattern shows that both the γ-cyclodextrin-G1 2:2 complex (**b**) and γ-cyclodextrin-fullerene 2:1 complex (**c**) crystallize with the same packing mode and type of lattice.*

requirement is meant to preserve the same hierarchical organization and crystal morphology observed for the material polymerized in solution.

The packing mode of our crystalline bundles was analysed using X-ray powder diffraction (PXRD). Despite the organic guest being crucial in determining the packing mode of inclusion complexes, its reflections typically disappear upon crystallization, and the pattern is mainly represented by the diffraction of

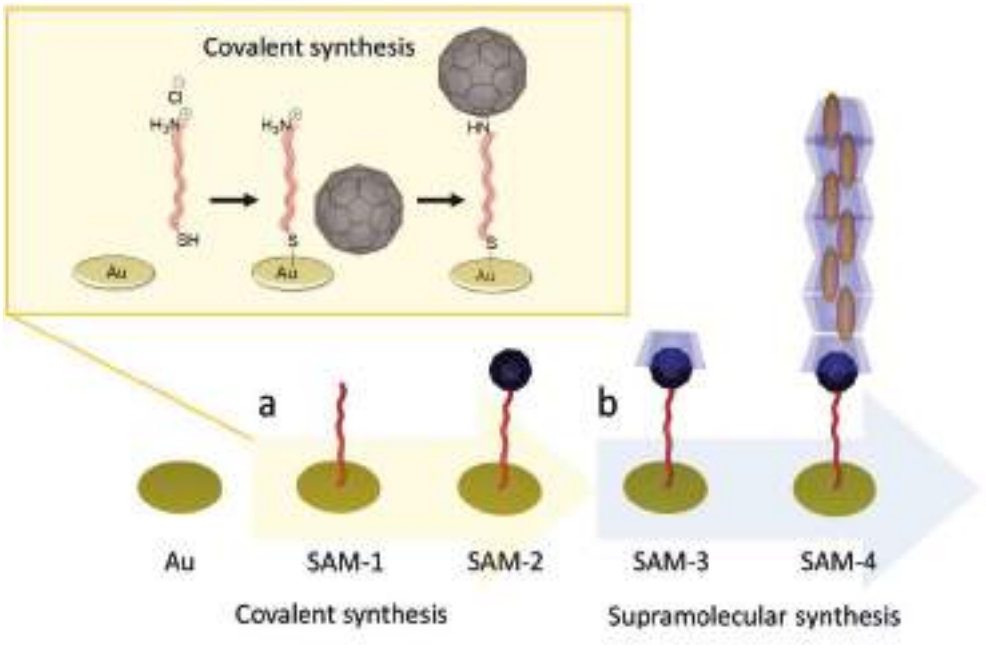

*Figure 8: (**a**) Covalent and (**b**) Supramolecular synthesis of SAMs for templating crystal growth on surface*

cyclodextrin molecules.[24] This phenomenon allows the comparison of our diffraction data with those of other cyclodextrin inclusion complexes to identify suitable guests for constructing the SAM template.

The PXRD spectrum obtained from the deposition of a suspension of crystalline rods on a silicon wafer shows a clear diffraction pattern characterized by a dozen sharp and intense reflections (Figure 7a). Analysing the diffraction, we found that the pattern is consistent with a tetragonal cell with axis a=b=17 Å, c= 15.2 Å. Confronting the cell parameters with the molecular dimensions of a γ-cyclodextrin unit, we assigned the [00l] crystallographic direction to be the main axis of growth of the tubular-shaped nanofibres (Fig. 7b).[25] Cyclodextrin complexes are usually classified into three packing modes: cage mode, layer mode, and channel mode. As expected in the case of crystalline bundles formed upon aggregation of nanotubes, the reflexes found at 2θ values 7.4 and 10.5° are a typical of a channel packing mode (Figure 7a). Identical reflections were found in the diffraction of polymers-cyclodextrin complexes, where linear aliphatic chains such as polypropylene glycol and polyethylene oxide thread through the cavities of many γ-cyclodextrin molecules.[26,27] However, the best matching spectrum was found to be from PXRD of the 2:1 inclusion complex between γ-cyclodextrin and fullerene C_{60}. The main peaks in this spectrum appear at 2θ values of 7.7, 10.6,

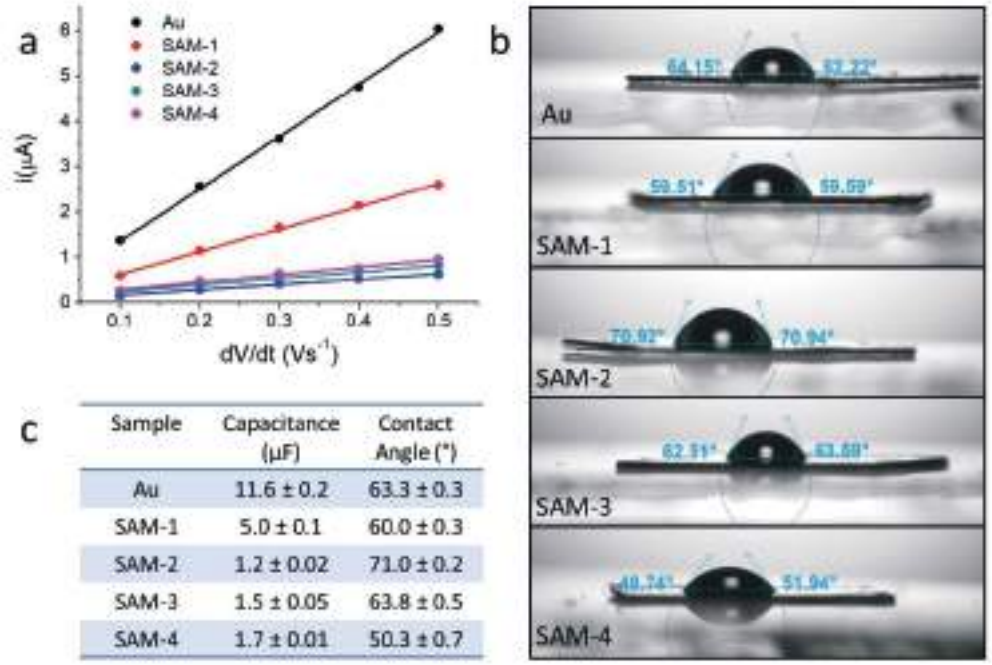

c

Sample	Capacitance (μF)	Contact Angle (°)
Au	11.6 ± 0.2	63.3 ± 0.3
SAM-1	5.0 ± 0.1	60.0 ± 0.3
SAM-2	1.2 ± 0.02	71.0 ± 0.2
SAM-3	1.5 ± 0.05	63.8 ± 0.5
SAM-4	1.7 ± 0.01	50.3 ± 0.7

*Figure 9: (**a**) Characterization of SAMs with cyclic voltammetry and (**b**) wettability measurement. (**c**) Summary of capacitance and contact angle for different SAMs.*

and 16.0°, similarly to the intense reflexes found in our samples and identified with the Miller indices 110, 200, and 300, respectively.[28]

In summary, according to PXRD analysis, γ-cyclodextrin-fullerene 2:1 complex is a suitable template for our system due to the shared channel packing mode and a similar tetragonal lattice. In addition, fullerene C_{60} presents the advantage of being a bulky, highly symmetric molecule, meaning that the packing structure and density of resulting SAMs will have little impact on the optimal binding configuration with cyclodextrin. In our final design (SAM-2), fullerene was functionalized with an alkane thiol chain to adsorb the monolayer on Au (111) and orient the [00l] growing crystal axis perpendicular to the surface.

The synthesis of this monolayer is represented in Figure 8a and consists of two covalent steps: the first intermediate (SAM-1) was formed by chemisorption of an amine-terminated thiol (8-AOT) on a gold surface followed by the amine addition to fullerene. Two additional supramolecular steps were required to grow the crystalline bundles on the template (Figure 8b). Firstly, the SAM-2 was loaded with a γ-cyclodextrin solution, and cyclodextrin-fullerene supramolecular binding led to the formation of SAM-3, which exposes the cyclodextrin's narrow face at

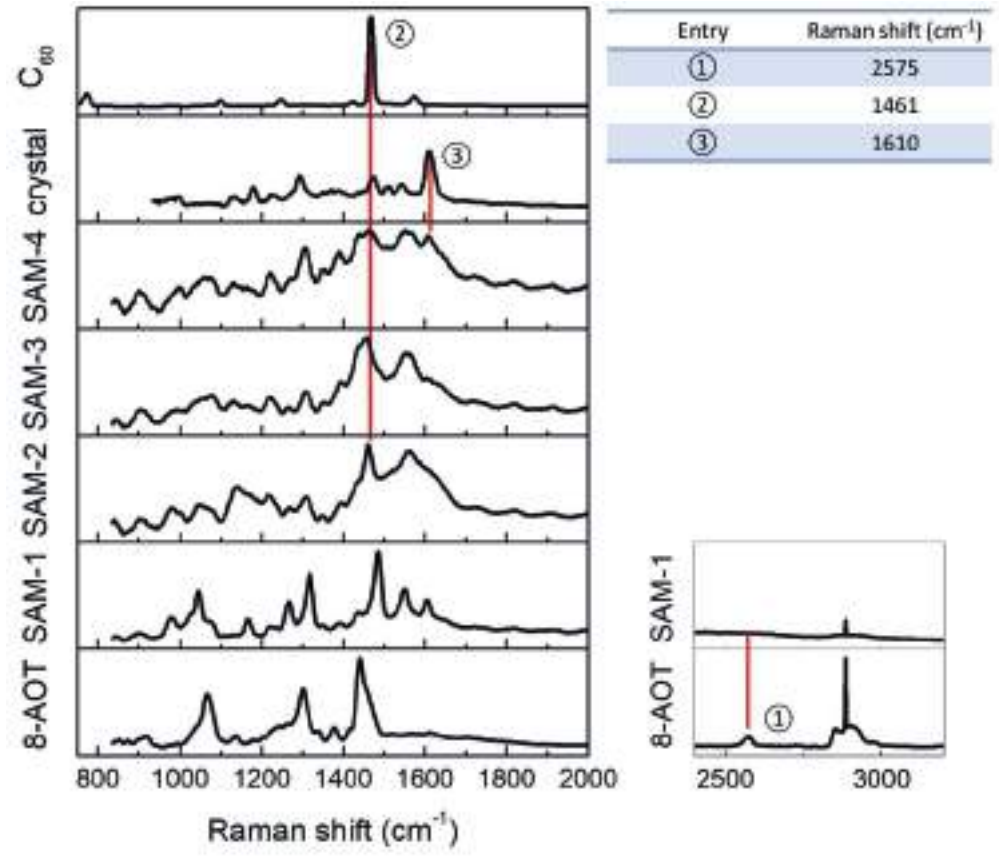

Figure 10: SERS spectra of SAMs compared to the Raman spectra of reactants. The main diagnostic vibrational bands are reported in the table (top right).

the solid-liquid interface. The addition of G_1 to the γ-cyclodextrin solution in the liquid phase initiates the supramolecular polymerization and the growth of crystalline material from the oriented surface (SAM-4). The characterization of SAM-4 and all of the intermediate SAMs was carried out by cyclic voltammetry, contact angle, and surface-enhanced Raman spectroscopy (SERS).

In cyclic voltammetry measurements, the capacitance of the SAMs was obtained from the changes in non-faradic current as a function of the voltage scanning rates (eq. 1). Changes in capacitance reflect how the dielectric constant and the thickness of the SAM affect the accumulation of charge at the gold electrode interface once a voltage is applied (eq. 2). After thiols chemisorb onto gold, the capacitance decreases from 11.6 to 5.0 μF (Figure 9a). Subsequently, upon functionalization with bulky fullerene units, it decreases even further to 1.2 μF. By contrast, the non-covalent synthetic steps have shown, in comparison, little

influence on the capacitance of SAMs (Figure 9a, 9c). Our interpretation is that after the addition of fullerene, further increasing the thickness of the monolayer does not impact on the capacitance because, at that distance from the electrode, the electric potential is too low to observe the effects of a change in permittivity.[29] In addition, from the observation of this saturation effect, one could infer that a total surface coverage of the electrode occurred during the covalent functionalization steps.

$$i = C\frac{dV}{dt} \qquad \text{eq. 1}$$

$$C = \frac{\varepsilon_0 \varepsilon_r A}{d} \qquad \text{eq. 2}$$

The effectiveness of supramolecular synthetic steps was more evident by analysing the changes in surface wettability. Specifically, the sequence of contact angles (θ_C) evidenced that the hydrophobic nature of the surface, observed after fullerene functionalization, was completely reversed once the SAM-2 had been exposed to a concentrated solution of γ-cyclodextrin for 30 minutes (Figure 9b-c). In the last step, consisting in the seeded supramolecular polymerization, the chemical composition of the surface is not significantly altered. Thus, the corresponding increase in wettability was attributed to an increase of roughness of the surface caused by the growth of the crystallites, in accordance with the Wenzel model.[30]

The synthesis of the monolayers was also replicated on a roughened gold electrode, and each synthetic step was investigated by SERS. Comparing the SERS spectra with the Raman scattering of the reagents, it was possible to follow spectroscopically the functionalization of the surface (Figure 10). After the first step, the absence of the S-H stretching band (ν_1=2575 cm^{-1}) in the spectra of SAM-1 confirmed the chemisorption of the thiol group on Au. Next, the addition of fullerene, results in the appearance of a new band in the spectrum of SAM-2 at ν_2=1461 cm^{-1}. In spite of the partial loss of symmetry in the functionalization, this vibration is characteristic of Ag(2) "pentagonal pinch" of fullerene C_{60}. In the following non-covalent synthetic steps, the molecular vibrations of γ-cyclodextrin, being more active in IR spectroscopy rather than Raman (See Supplementary Figure 2a-b), do not significantly alter the SERS spectra upon cyclodextrin binding. On the other hand, the last step of supramolecular polymerization was marked by the appearance of a new vibrational band at ν_3=1610 cm^{-1}, which was assigned to the C=N stretching in the imidazole ring of G_1.

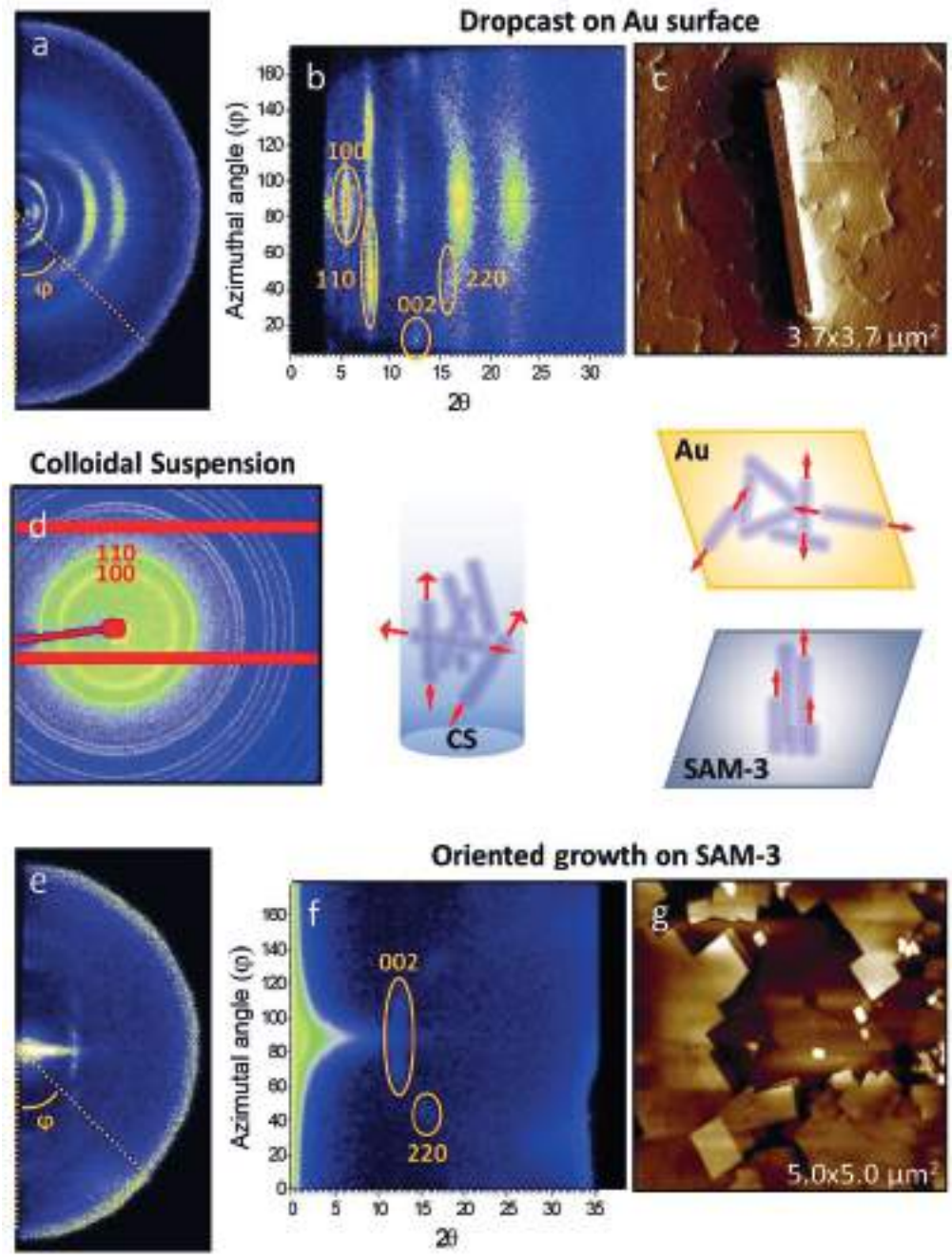

*Figure 11: (**a**) GIWAXS pattern, (**b**) azimuthal dispersion, and (**c**) AFM micrograph of microcrystalline rods deposition on a gold surface. (**d**) WAXS pattern from colloidal suspension of microcrystalline rods. (**e**) GIWAXS pattern, (**f**) azimuthal dispersion, and (**g**) AFM micrograph of crystallites grown on gold surface templated with SAM-3.*

Once it was confirmed that SAM-4 can support the growth of the supramolecular polymer we investigated if the template effect introduces the desired directionality while preserving the structure of the hierarchical assembly. The AFM scans showed that the surface of SAM-4 was studded with squared shaped crystallites formed after the polymerization of the cyclodextrin inclusion complex (Figure 11g). The morphology and size of the microscopic material conforms to a reorientation of rod-shaped microcrystals grown from non-templated solutions. The topographical analysis of these crystallites shows that their surface has relief areas, forming a patchy pattern with corrugation of approximately 1-2 nm. This feature is compatible with the height of the supramolecular complex in the unit cell (See Supplementary Figure 2c-d).

Taking advantage of the fluorescent emission of G_1, the molecular orientation in squared crystallites was studied with epifluorescence microscopy. In Chapter 3 we have shown that upon photoexcitation of microcrystalline rods with unpolarized radiation G_1 emission is polarized along the main axis of the crystalline rods as a result of molecular alignment (See Supplementary Figure 3a-b, 3e). With the same experimental setup we observed no polarization in the fluorescence of template-grown crystallites, as expected if the emission dipole moment of the fluorophore would have been reoriented perpendicularly to the analyser and, therefore, to the surface (See Supplementary Figure 3c-d, 3f).

More insights on how microscopic structures orient on surface were provided by analysing the substrates by grazing incidence wide angle X-ray scattering (GIWAXS). When polymerization and bundling occur in solution, the axis of microcrystalline rods is randomly oriented in these colloidal suspensions. The isotropic orientation is reflected in the absence of a preferential angular position around the detector (φ) in the scattering of these samples, which is characterized by a series of well-defined concentric rings (Figure 11d). By contrast, when drop casted and blotted on a surface the depositions of microcrystalline rods scattered with anisotropic alignment (Figure 11a). According to the AFM imaging of these depositions, the alignment occurs because the long axis of the rods always lays on the plane of the surface (Figure 11c). Crossing the information of the GIWAXS pattern with PXRD data, we found that the position of the (002) scattered plane is parallel (φ=0°) with respect to the azimuth (Figure 11b). This information is in agreement with our previous interpretation of the crystal habit, which identified the long axis of the rod as the nanotubes' growing direction [00l]. The GIWAXS pattern obtained from the crystallites polymerized on the SAM-3 template exhibited narrow scattering features but a pronounced anisotropy (Fig.11e). The difference in scattering intensity, compared to casted samples of crystalline rods, can be attributed to smaller coverage area of the thinner depositions achieved

through the templated-growth preparation method. Despite that, it was possible to identify two reflexes, namely (200) and (220), oriented respectively at φ=90 and 45° from the detector plane (Figure 11f). The change in azimuthal distribution of this reflexes with respect to GIWAXS pattern of microcrystalline rods depositions proved that the template directed the growth the crystal axis perpendicular to the surface.

4.3.3 Conclusions

In principle, isotropic growth can exert a pushing force when polymers are confined between a barrier and a cargo.[31] However, the control of nucleation and directionality of the assembly mechanism are key elements that enhance the mass/energy efficiency of the process and ensure the predictable mechanical output that characterizes bio-polymerization machinery.

In this second section of Chapter 4, we explored the use of the template effect to orient the supramolecular polymerization on a self-assembled monolayer. Our proposed approach is based on the structural analysis of the assembling system to tailor-design a substrate that can support the polymerization of nanotubes from the surface. After investigating the synthesized monolayers with the standard techniques for surface characterization, we also proved, by combining the information from X-ray scattering and AFM imaging of templated grown crystallites, the effectiveness of this method for orienting the growth of the nanotubes' bundles.

These results will pave the way for a mechanistic investigation of synthetic systems with AFM force spectroscopy. In future research, we wish to study polymerization in real time, and, in our opinion, this goal can only be matched with increased predictability of ordered synthetic structures. The scope of this research is broad. This technique could provide fundamental information on the Brownian ratcheting of synthetic systems, such as the dynamics of monomer insertion or the relationship between growth velocity and loading history.[21,32]

4.3.4 Acknowledgements

I wish to thank Y. Y. Lopatina for contributing in the design of the project and for the AFM measurements. I wish to thank G. Pacella and G. Portale for the useful discussions and for the X-ray scattering measurements. I wish to thank J. Baas for the acquisition of XRD data.

4.3.5 Supplementary Information

Chemicals and solvents were obtained from commercial sources and used without further purification unless stated otherwise.

The synthesis of the aromatic guest G_1 was previously described in Chapter III, along with the general procedure for the preparation of colloidal suspensions of nanotube fibres in solution.

Four distinct Au-coated substrates were used for the preparation of the monolayers: mica sheets, silicon wafer, Au roughened beads, and Au electrodes. Au-coated mica sheets were purchased from Phasis (layer thickness 210^3 Å, Au 99.99%). The procedure for the fabrication of Au-coated silicon wafer is described in the GIWAXS section. The roughening of Au beads is reported in the SERS section. The treatment of gold electrodes is described in the section on cyclic voltammetry.

Covalent synthesis was realized by adapting a procedure for the chemisorption of thiols on gold reported by Patnaik et al. and the amine addition to fullerene described by Sahoo et al..[33,34]

SAM-1: The gold-coated substrates (mica sheets, silicon wafer, gold bead) were annealed at 200 °C for three hours. After cooling, the substrates were immersed in a 1 mM solution of 8-Amino-1-octanethiol hydrochloride **(**8-AOT**)** in toluene at room temperature for 24 hours. Thus, the amino thiolate **(**SAM-1**)** formed was exhaustively cleaned with ethanol to get rid of the physisorbed moieties and dried under nitrogen.

SAM-2: The substrates functionalized with SAM-1 were immersed in a 1 mM fullerene C_{60} solution in toluene and kept for 24 hours under reflux. The SAM-2 thus formed was washed with toluene, ethanol, and dichloromethane and used for respective experimental investigations after drying in air.

SAM-3: The substrates functionalized with SAM-2 were immersed in a 5mM aqueous solution of γ-cyclodextrin. The wetting solution was blotted after 30 minutes of dwell time. The SAM-3 thus formed was rinsed three times with Milli-Q water before blotting again and drying the substrate in air.

SAM-4: The substrate functionalized with SAM-3 was immobilized on a tweezer and this support was loaded in a vial with the substrate plate standing upright. The chamber was loaded first with a 10 mM aqueous solution of γ-cyclodextrin, followed by the addition of a 5mM stock solution of G_1 in methanol, adjusting

652563-L-bw-Pataleone
Processed on: 5-9-2024

the final concentration of G_1 to 0.5 mM (water/methanol 9:1). The resulting colloidal suspension of microcrystals was decanted overnight and after collecting the substrate, the SAM-4 was rinsed three times with Milli-Q water, blotted and dried in air.

Colloidal liquid crystal: was prepared by dispersing a 5mM stock solution of G_1 in methanol in 10 mM aqueous solution of γ-cyclodextrin, adjusting the final concentration of G_1 to 0.5 mM (water/methanol 9:1). Once a colloidal suspension was formed, the microcrystals were repeatedly concentrated by centrifugation (20°C, 10^4 rcf, 15 minutes) and washed with Milli-Q water for three times, and freeze-dried. The obtained lyophilized powder was mixed with an equal amount of water (50% w/w) and sealed in a capillary or in between two glass slides.

Cyclic voltammetry. The capacitance was determined by cycling the potential between 50 mV and -50 mv using a standard three-electrode arrangement consisting of a platinum wire counter electrode, an Ag/AgCl reference electrode, and a gold electrode modified with the corresponding monolayer as the working electrode. An aqueous solution of 100 mM KNO_3 was used as electrolyte. The scan rate was varied between 0.1 and 0.5 $mV \cdot s^{-1}$, and the resulting non-faradaic current values were plotted against the scan rate. The data was fitted to a linear model and the corresponding slope gave the capacitance in μF.

Contact angle measurements were performed at 20°C with an optical tensiometer Theta Lite Biolin Scientifc, using the static sessile drop method, Milli-Q water as the liquid phase, and glass as a calibrant.

SERS measurements were performed on roughened Au beads, which were functionalized according to the synthetic procedures previously described for SAMs. Raman spectra were recorded using a Perkin Elmer Raman station with an Olympus BX-51 microscope equipped with a 785 nm laser operated typically at 20mW through a 50X magnification objective, estimated laser spot size 1μm (diameter). Spectra were acquired with Andor Solis. Spectra were calibrated with polystyrene or cyclohexane (ASTM E 1840).

Electrochemical cleaning and roughening of Au surface: A gold bead was heated on a butane flame until it glowed. After cooling, the bead was immersed in H_2SO_4 (aq, 0.5 M) and kept against a Pt-wire at 9 V (battery) until it colored orange. Subsequently, the bead was immersed in HCl (aq. 0.1 M) until its surface turned golden again. After rinsing the bead with Milli-Q water and then ethanol, the surface was dried in air. In the next cleaning step, the bead was immersed again in a solution of H_2SO_4 (aq, 0.5 M) against Pt-wire as counter electrode and SCE as reference electrode, cycling the potential five times between -0.2 and 1.2 V (potentiostat).

After rinsing with water, the Au bead was immersed in a solution of 0.1 M KCl against a Pt wire as a counter electrode and SCE as a reference electrode. The surface was roughened using a sweep-step function: the potential was varied from -0.3 to 1.2 V at 1 $V \cdot s^{-1}$, held at 1.2 V for 30 seconds, then cycled back to -0.3 V at 0.5 $V \cdot s^{-1}$, and kept at -0.3 V for 1.2 seconds (potentiostat). The surface was roughened by cycling the sweep step function 24 times.

WAXS/GIWAXS: wide-angle X-ray scattering measurements were performed at the multipurpose instrument for nanostructure analysis (MINA) instrument at the University of Groningen. This instrument is built on a Cu rotating anode source providing an X-ray beam with wavelength l=0.15413 nm. 2D patterns were collected using a Vantec500 detector (1024 x 1024 pixel array with pixel size 136 x 136 μm located at 89 mm away from the sample for GIWAXS. The samples were placed in reflection geometry at 0.4° incident angle (α) with respect to the direct beam using a Huber goniometer. The direct beam centre position on the detector and the sample-to-detector distance was calibrated using the diffraction rings from standard silver behenate and α-Al_2O_3 powders.

Au-coated silicon wafers were prepared by adapting a procedure reported by Weiss et al. for the fabrication of template-stripped metal substrates.[35]

Before loading into the vacuum chamber, a Si wafer was rinsed with ethanol and acetone and blown dried with N_2. 99.99% Au (obtained from Umicore) was used for metal deposition. A 100 or 200 nm layer of the metal was then deposited on the Si/SiO_2 wafer using the thermal evaporation method. The metal was initially evaporated at a rate of about 0.2-0.4 Å s^{-1} for the first 10 nm, after which the rate was gradually ramped up to rates of 0.5 Å-0.8 Å s^{-1}. After deposition and annealing, the resulting Au thin films were analysed with AFM before and after preparation of SAMs for GIWAXS experiments. Comparing the samples grown on Au-coated silicon wafers with those prepared on Au-coated mica sheets, we found that the crystallites exhibit the same morphology and dimensions in both cases. The only notable difference is the higher surface coverage of crystallites observed on the Au-coated mica substrates.

AFM: topography imaging were performed on an Agilent PicoLE system in air. Images of microcrystalline rods and SAM-4 were obtained in AC-mode using standard silicon nitride probes (PPP-NCHR, Nanosensors) with resonance frequency ~330 kHz. The error in measuring height was within 6%. Data leveling and background subtraction were performed with PicoView software.

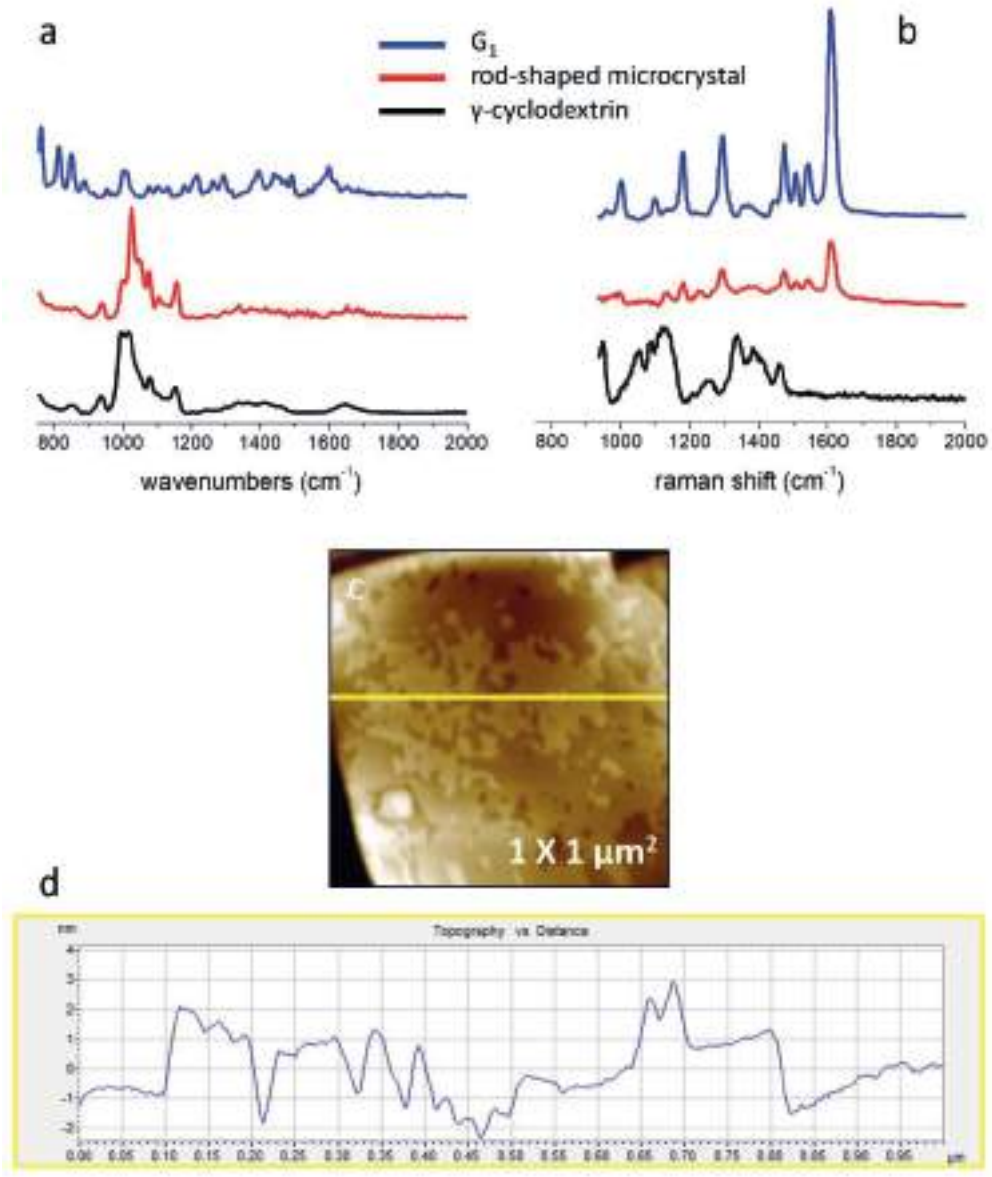

Figure S2: (**a**) FTIR absorbance and (**b**) Raman spectra of G_1, microcrystalline material and γ-cyclodextrin. (**c**) AFM topography imaging of the crystallite surface grown on SAM-4 and (**d**) corresponding z-profile, yellow line is the plotted profile.

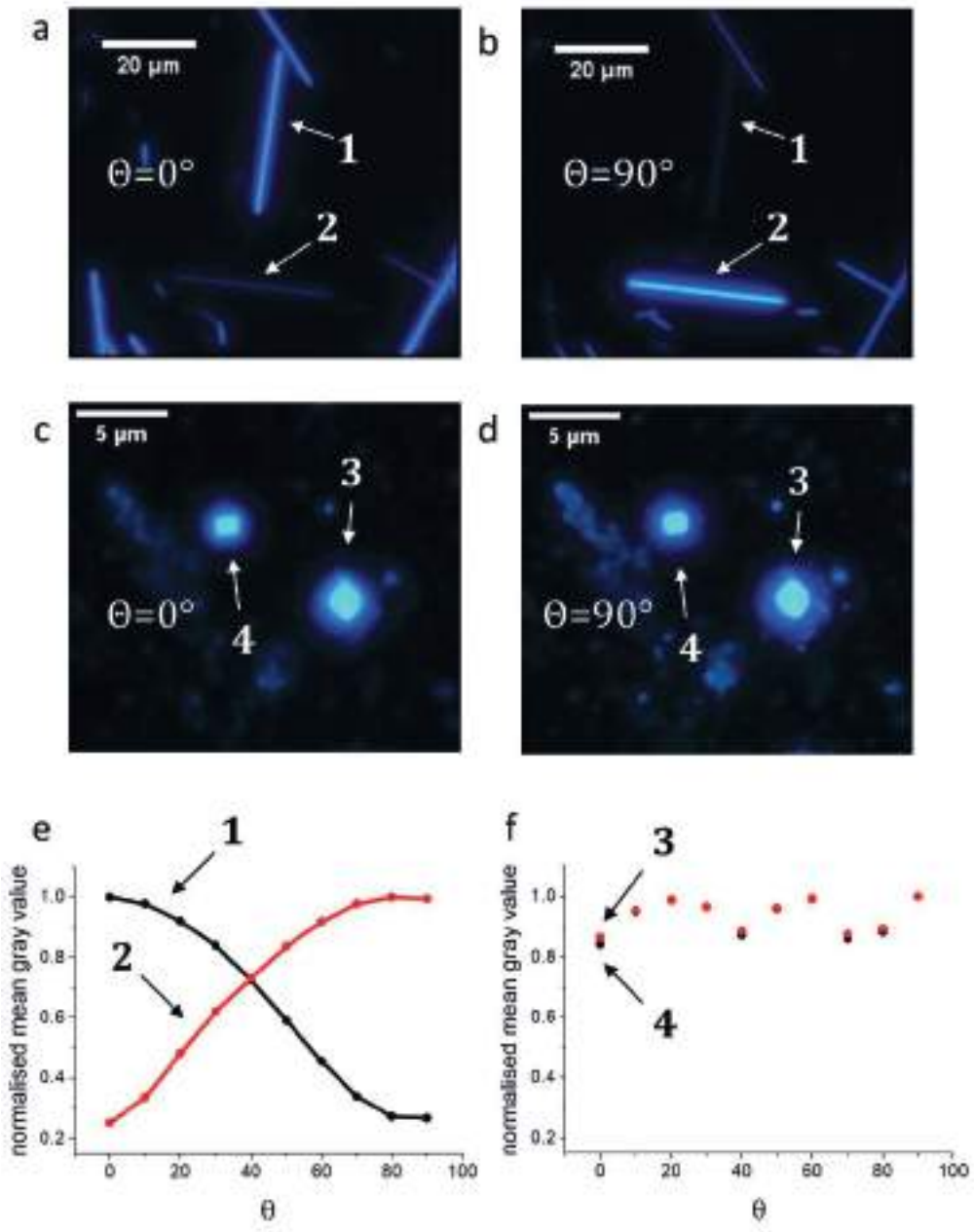

Figure S3: (**a**)(**b**) Epifluorescence micrographs of microcrystalline rods with analyser rotation at (**a**) θ=0° and (**b**) θ=90°. (**c**)(**d**) Epifluorescence micrographs of crystallites grown on SAM-4 with analyser rotation at (**c**) θ=0° and (**d**) θ=90°. (**e**)(**f**) Image analysis of the micrographs: normalized intensity of emission from the crystals as a function of the rotation angle (θ) of the analyser.

4.4. Microrheology

4.4.1 Imaging plastic deformations in a synthetic hydrogel network

Adaptation is one of the most iconic yet elusive properties of living materials,[36] allowing them to evolve with their environment.[37] In particular, structural plasticity is used in Nature to survive large mechanical stresses and learn from them.[38] The scientific community has been steadily discovering how to engineer plastic synthetic materials,[39] first with the advent of self-healing,[40,41] and now with controlled mechanical evolution,[42] often by co-assembly of two monomers with complementary properties.[43] Here we harness the intrinsic reversibility of supramolecular bonds to craft fully self-assembled and mechanically adaptive strain-stiffening materials, based on a single monomer (VsAzo). Through inter-fibre sliding inside bundles or through bundle merging, this material undergo structural reconfiguration to withstand large strains. The properties of the assemblies can be controlled by varying KCl and monomer concentrations, generating fibre networks at physiologically relevant temperatures. To the best of our knowledge, this is the first example of plasticity in synthetic supramolecular hydrogels. Our results show how extracting the fundamental principles governing the assembly of the extracellular matrix allows the reengineering of its properties in artificial materials. This process gives new tools for the creation of bioinspired supramolecular materials with novel and useful properties, with impact in regenerative medicine[44] or tissue engineering.[45-48]

J. W. Smith†, F. Lancia†, V. Verduijn†, L.C. Pantaleone, K. M. Tych, T. Kudernac*; *manuscript in preparation*

4.4.2 Main

Our single building block (VsAzo) associates two moieties to combine a strong (core) and a weaker (lateral) interaction (Figure 12a). The V-shaped aromatic core directs self-assembly into hexameric ring units that stack until they form micrometre-long tubules with an external diameter of 12 nm. Water solubility is ensured by outward-facing branched oligoethylene glycol (OEG) groups, the second half of our building blocks (Figure 12a).[49] Nanotubes formation is immediate upon dissolution of the monomer in water. The second interaction is revealed upon KCl addition and heating, which triggers the OEG's low critical solution temperature (LCST) transition toward hydrophobic coils. This transition has two effects, namely bundling of the nanotubes by weak lateral OEG-OEG interactions, and crosslinking of the fibres present in the system to form a percolating gel (Figure 12d-e). This weak lateral interaction is what enables the network plasticity observed during shear rheology experiments in bulk (Figure 12b).

The goal of this project was to confirm the that the dissipation of mechanical energy in the hydrogel network is based on a fibre sliding mechanism within bundles (Figure 12c). Observing such effects at the network level requires precise micromanipulation of the sample coupled with microscopy techniques for imaging the structure of the mesh before and after the plastic deformation. With this idea in mind we designed an experiment to investigate how the morphology of the hydrogel responds to mechanical stress using an optical tweezer setup integrated with confocal microscopy.

For achieving a controlled stimulation and delivering mechanical stress to bundles the hydrogel was decorated with polystyrene microspheres. The integration of these condensed particles in the network has a multiple advantages. The large difference in refractive index between these objects and the medium improves optical trapping at low laser power. In addition, using anchored beads as "handles" for exerting pulling force on the network minimizes the radiation dose absorbed by the soft material.

The decoration of the network was achieved by incubating a colloidal suspension of nanofibres with microspheres prior the formation of the hydrogel. The LCTS transition was triggered in the optical tweezer setup by increasing the temperature of the stage above the gelation temperature (37°C).

The adsorption of oligoethylene glycol sidechains to the amine-coated surface of the polystyrene microspheres anchored the latter to the network's mesh. The effectiveness of the adhesive contacts was demonstrated with bright field microscopy of the pulling experiments (Figure 13a). Pulling the bead in the optical trap clearly results in the propagation of tension across the network.

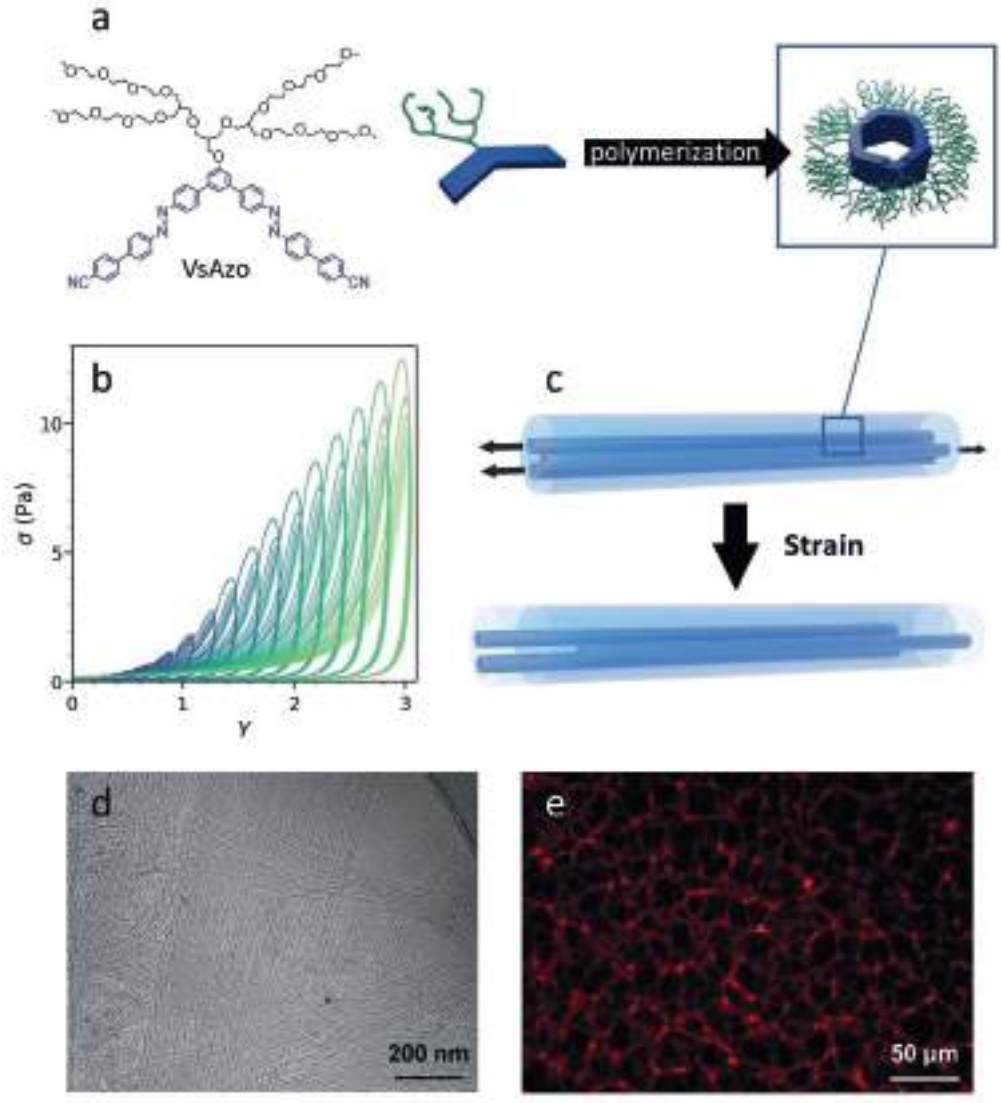

*Figure 12: (**a**) Monomer design and self-assembly mechanism into tubular-shaped nanofibres. (**b**) Shear rheology of hydrogel: stress(σ)-strain(γ) curves show that increasing the strain amplitude after every cycle the system dissipates part of the mechanical energy in plastic deformations.(**c**) Mechanism of interfibre sliding within the bundles of the hydrogel. (**d**) Cryo-EM of the hydrogel reveals its hierarchical structure composed of large bundles of individual nanofibres.(**d**) Epifluorescence micrograph of the cellular network formed by the hydrogel.*

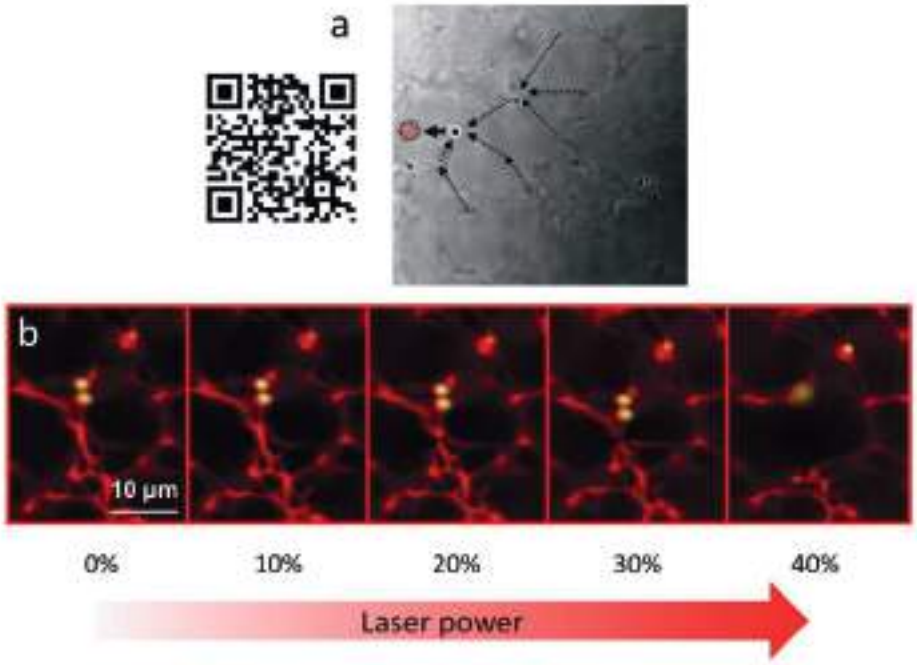

*Figure 13: (**a**) Bright field video showing how tensile forces propagate across the hydrogel network upon micromanipulation with the optical tweezers. (**b**) Confocal microscopy: control experiment to assess the radiation damage produced by the IR laser on the hydrogel in the optical tweezer setup.*

Before analysing structural changes in the mesh caused by the mechanical stress we wanted to assess the range of trap stiffness where it is possible to manipulate the sample without observing radiation damage. The trapping laser was focused on a bundle and its intensity was gradually increased, imaging the sample with a confocal fluorescence scan every 30 seconds of exposure (Figure 13b). Appreciable radiation damage was not observed below 20% of the maximum laser power.

The effect of mechanical stress on the network was observed by positioning the centre of the optical trap at 1 µm distance (Δx=1 µm) from one of the anchored microspheres. In this conditions the bead is located in the close proximity of an optical trap but misaligned with respect to the position of the laser (Figure 14a). Consequently, once the laser power is ramped up to 10%, the microsphere experiences a force field generated by radiation pressure. The force exerted on the bead is proportional to its displacement from the trap centre (Δx) and can be calculated using Hook's law, with the trap centre acting like a spring characterized by a spring constant (***k***). In response to the force, the network is deformed in such a way that the microsphere is progressively moved towards the centre of the

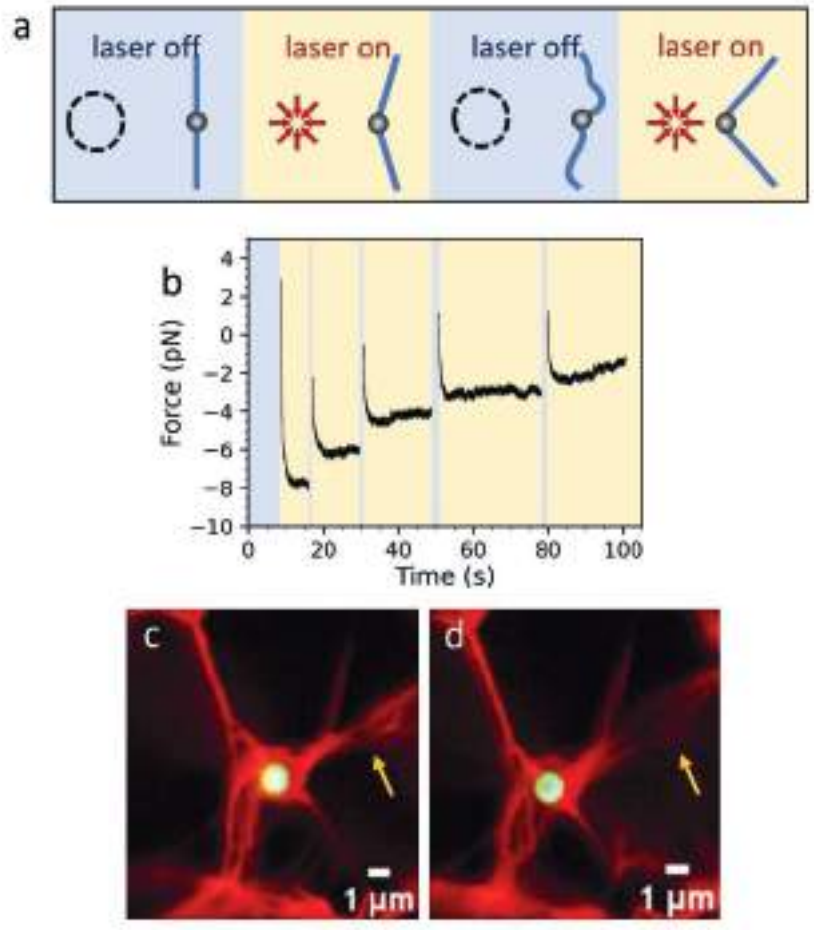

*Figure 14: (**a**) Design of microrheology measurement. Trap centre is placed at 1µm distance from the polystyrene microsphere. (**b**) Force trace recorded during the micromanipulation. During the measurement the laser shutter was repeatedly opened (yellow) and closed (blue). (**c**)(**d**) Confocal scans of the hydrogel network before (**c**) and after (**d**) micromanipulation. The loosening of a bundle confirms the mechanism of interfibre sliding.*

optical trap. During the pulling experiment the laser shutter was repeatedly opened and closed to observe the relaxation of the network back to its resting position (Figure 14a).

Although the immobilization of microspheres in the hydrogel prevents an accurate calibration of ***k*** at the gelation temperature, the changes in the force trace upon deformation of the network are still indicative of its mechanical response under tension. The force trace in Figure 14b shows how the network opposes less and less resistance as the microsphere is repeatedly pulled in the trap centre. Interestingly, turning the trap off and on again doesn't reset the progress made.

On the contrary, the bead regains its position and takes up where it left off, progressively loosening the bundle it is attached to in order to fall towards the trap. This behaviour is a clear sign of plasticity at the bundle level.

Confocal microscopy, performed before and after the manipulation, shows how a bundle of tubes becomes looser and seemingly longer under the tension applied (Figure 14c-d). Specifically, the second image (Figure 14d) echoes cryo-TEM observations of a hierarchical architecture (Figure 12d): individual tubules bundle into intermediate bundles, which then bundle again to form the large fibres. Imaging the deformations of the material at the network level confirmed that the pulling force loosens the mesh and reveals the intermediate bundles that compose it. Such morphological changes in the secondary structure constitute convincing evidence that the dissipation of mechanical energy is based on the mechanism of inter-fibre sliding.

4.4.3 Conclusions

In this study, we demonstrated how optical tweezers can be used to characterize the rheological properties emerging from the secondary structure of a synthetic hydrogel. By combining force spectroscopy data with confocal imaging of the network, we gained mechanistic insights into the plastic deformation process, which mirrors the adaptive strategies of hierarchically structured materials that support the cellular mechanics. Specifically, the secondary OEG-OEG interactions governing fibre bundling play a crucial role in dissipating mechanical energy within the hydrogel network, allowing fibres to slide and form new contacts, thereby adapting the morphology of the mesh under tensile forces. This findings confirm that the hierarchical organization of supramolecular polymers into anisotropic structures effectively scale molecular interactions into material properties. Understanding the role of self-assembly in mediating these structure-function relationships is essential for developing biomimetic, mechanically active systems.

4.4.4 Acknowledgements

I wish to thank J. W. Smith and F. Lancia for designing the project and for the bulk rheology experiments. I wish to thank M. C. A. Stuart for Cryo-EM and K. M. Tych for her support and guidance in the OT experiments. I gratefully acknowledge V. Verduijn for the useful discussions and for developing the fluorescence staining procedure described in the supplementary information. I wish to thank Q. Huang for providing the $AzoN_3$ compound required for fluorescence staining of the hydrogel.

4.4.5 Supplementary Information

Chemicals and solvents were obtained from commercial sources and used without further purification unless stated otherwise.

For confocal microscopy of the hydrogel, the **VsAzo** nanotubes solutions were stained with 2% **VsAzo-DBCO-Cy5** labelled monomer. The labelling reaction was performed in situ, reacting **AzoN$_3$** monomers with **DBCO-Cy5**, as described in the sample preparation method.

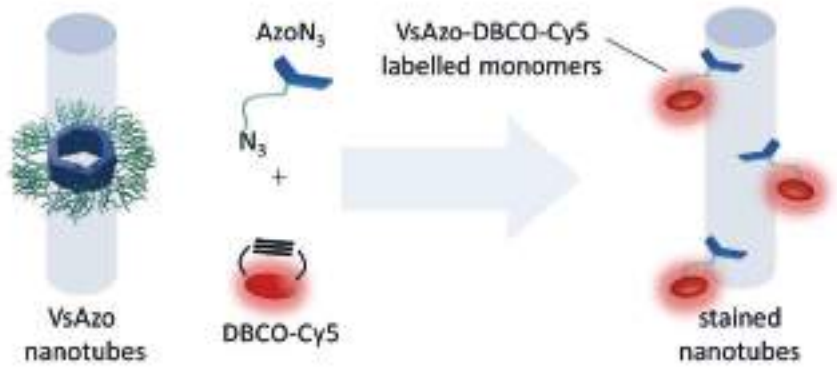

Figure S4: Click reaction and staining of VsAzo nanotubes.

Optical Tweezers: Force spectroscopy measurements were performed with optical tweezers using a commercial setup (C-Trap) from Lumicks operated in single-trap regime. The force was measured by a position-sensitive detector (PSD) in two dimensions on both beads with an acquisition rate of 78 kHz. The measurement of the inter-bead distance was performed by bright-field optical tracking with a resolution of 10 nm at 15 Hz. The acquisition was controlled by Bluelake software (Lumicks). To analyze and store the force trace data the force acquisition frequency was down-sampled to 160 Hz using the Pylake Python package.[11] The trap stiffness was calibrated prior gelation of the sample (k=0.39 pN/nm at 25°C) using the thermal noise method.[12] The micro rheology experiment was performed at 37°C using 10% of the operative laser power ($P_{100\%}$=14mW, λ=1064nm).

Confocal Microscopy:

The lasers used in the confocal scans had excitation wavelength of λ_{ex}=561 nm for imaging the microspheres with a band pass filter APD2 (575-625 nm), and λ_{ex}=639 nm for imaging the hydrogel using a band pass filter ADP3 (635-835nm).

The excitation end emission wavelengths of the fluorophores were λ_{ex}=505-585 nm/λ_{em}=550-645nm fluorescent red, and λ_{ex}=646nm/λ_{em}=670 nm for DBCO-Cy5for.

General procedure for preparation of VsAzo hydrogel network for OTs experiment:

To a vial containing VsAzo (1mg, 1 eq.) was added a stock solution of $AzoN_3$ in acetonitrile (66.4µL, [$AzoN_3$]=200µM) and additional acetonitrile was added until complete dissolution. Subsequently, the solution was dried under nitrogen at room temperature. The resulting thin film of azide (12.5µg, 0.02 eq.) and VsAzo (1mg, 1 eq.) was re-dissolved in 664µL of MilliQ water ([VsAzo]=1 mM [azide]=0.02mM) by vortexing on a low setting until optically clear, and stored overnight at room temperature in the dark. The next day, aqueous DBCO-Cy5 (14µL, [DBCO-Cy5]=0.833mM, 0.9 eq. to azide) was added and incubated for at least 1 hour before use. The resulting solution of VsAzo-DBCO-Cy5 stained nanotubes was diluted with a solution of KCl ([KCl=3M]) to obtain the final concentration of [VsAzo]=0.5 mM and [KCl]=1M.

The sample was subsequently incubated with a 1µm amine-functionalized polystyrene microspheres (labelled with Fluorescent Red) for 30 minutes before loading the solution in a custom-made microscopy chip with a 40 µL capacity and 0.3 mm thickness. After using polystyrene microspheres to calibrate the optical trap in the solution, the temperature of the micro stage was increased to 37°C. This allowed for the formation of the gel and the creation of a network decorated with the microspheres trapped in its mesh.

Synthesis of VsAzo:

The synthesis of **VsAzo** was reported by Fredy et al.[50] The last synthetic step of this procedure was adapted to optimize the reaction conditions of the double Suzuki coupling and the purification of the final product:

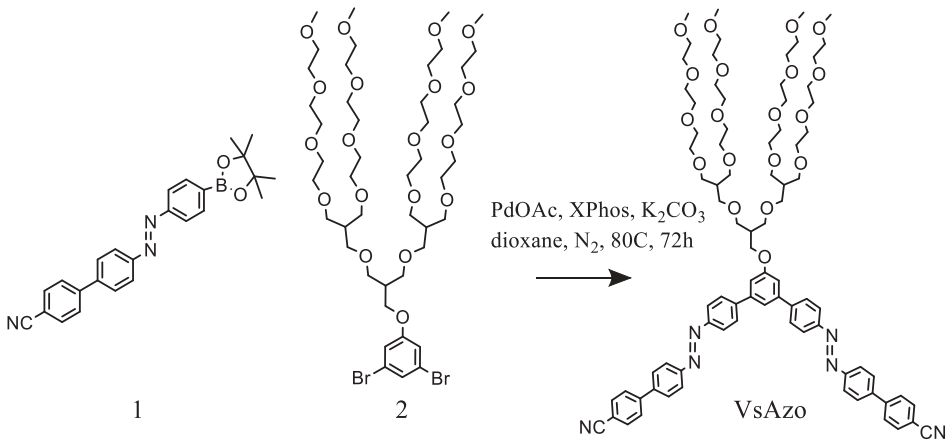

A solution of 170 mg of boronic ester **1** (0.41 mmol, 3eq.), 150 mg of haloarene **2** (0.14 mmol, 1eq.), 3.14 mg of $Pd(OAc)_2$, 23 mg of Xphos, and 140 mg of K_2CO_3 in 20 mL of dioxane/water (4:1) was degassed and stirred under nitrogen atmosphere at 80°C for 72h. After cooling to room temperature, reaction mixture was extracted three times with ethyl acetate and the combined organic layers were dried ($MgSO_4$), filtered and concentrated. The resulting crude product was purified by flash column chromatography (silica, MeOH/DCM, 3%→5%) to yield 145 mg of **VsAzo** as an orange solid (yield 69%).

^{1}H NMR (400 MHz, $CDCl_3$) δ 8.12 – 8.01 (m, 8H), 7.88 – 7.81 (m, 4H), 7.80 – 7.73 (m, 12H), 7.53 (t, J = 1.5 Hz, 1H), 7.25 (d, J = 1.5 Hz, 2H), 4.19 (d, J = 5.6 Hz, 2H), 3.69 – 3.41 (m, 64H), 3.36 (d, J = 8.3 Hz, 12H), 2.43 (d, J = 5.3 Hz, 1H), 2.20 (dt, J = 12.2, 6.0 Hz, 2H).

HRMS-ESI Orbitrap (m/z): [M+H$^+$] calculated for $C_{84}H_{108}N_6O_{19}H$, 1505.77741; found 1505.77420

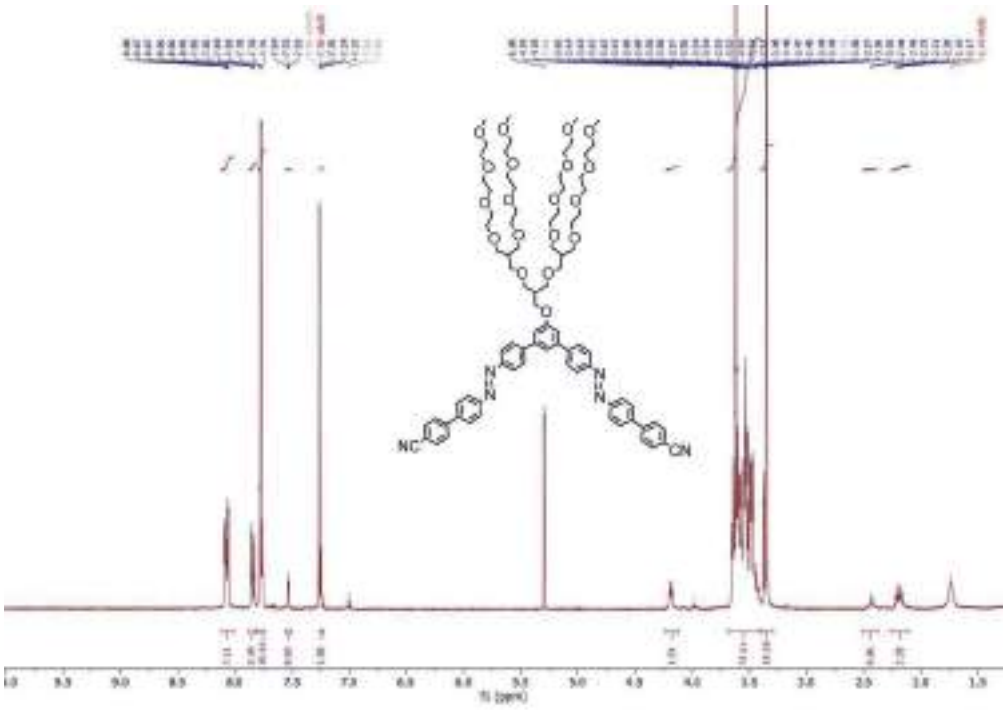

*Figure S5: ^{1}H NMR (400 MHz, $CDCl_3$) of **VsAzo***

Synthesis of AzoN$_3$

The starting material (**3**) for the synthesis of **AzoN$_3$** was prepared according to a procedure previously reported by Xiu et al.[51]

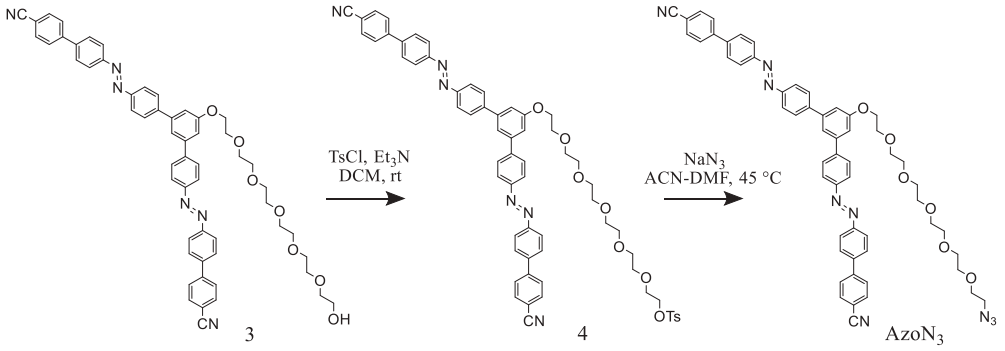

Compound **3** (29 mg, 0.03 mmol, 1 eq.) and tosyl chloride (19 mg, 0.10 mmol, 3 eq.) were dissolved in DCM (4 mL). Triethylamine (20 µL, 0.14 mmol, 5 eq.) was added to the solution and the reaction mixture was stirred at room temperature overnight. The solvent was evaporated under reduced pressure and the residue was purified using flash column chromatography (silica, MeOH/DCM 3%) to obtain **4** (31 mg, 93%) as an orange paste which was immediately used in the next synthetic step.

Compound **4** (31 mg, 0.03 mmol, 1 eq.) was dissolved in a mixture of acetonitrile (4 mL) and DMF (1mL). Sodium azide (10 mg, 0.15 mmol, 5 eq.) was added to the solution and the reaction mixture was stirred at 45 °C overnight. The solvent was evaporated under reduced pressure and the residue was purified using flash column chromatography (silica, MeOH/DCM 2%) to obtain product **AzoN$_3$** (24 mg, 89%) as an orange paste.

^{1}H NMR (600 MHz, $CDCl_3$) δ 8.13 – 8.00 (m, 8H), 7.83 (dd, J = 8.5, 2.1 Hz, 4H), 7.78 (t, J = 1.5 Hz, 12H), 7.66 (d, J = 8.4 Hz, 2H), 7.55 (s, 1H), 4.36 – 4.24 (m, 2H), 4.01 – 3.89 (m, 2H), 3.78 (dt, J = 5.5, 3.0 Hz, 2H), 3.72 (q, J = 4.6, 3.4 Hz, 2H), 3.70 – 3.58 (m, 14H), 3.37 (t, J = 4.5 Hz, 2H).

^{13}C NMR (101 MHz, $CDCl_3$) δ 159.78, 152.60, 152.02, 144.62, 143.70, 142.19, 141.46, 132.72, 128.04, 128.00, 127.79, 123.66, 123.58, 121.36, 111.50, 70.92, 70.68, 70.62, 70.59, 70.02, 67.81, 50.67.

ESI-TOF m/z, ($[M+Na]^+$): calculated for $C_{56}H_{51}N_9O_6Na$: 968.386, found: 967.969.

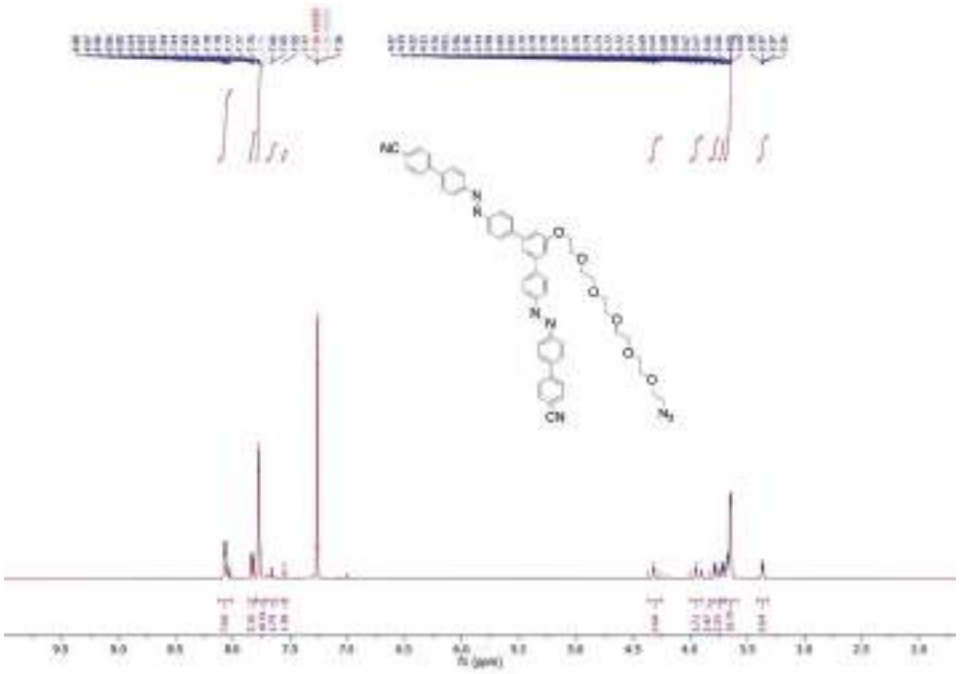

*Figure S6: ^{1}H NMR (600 MHz, $CDCl_3$) of **$AzoN_3$***

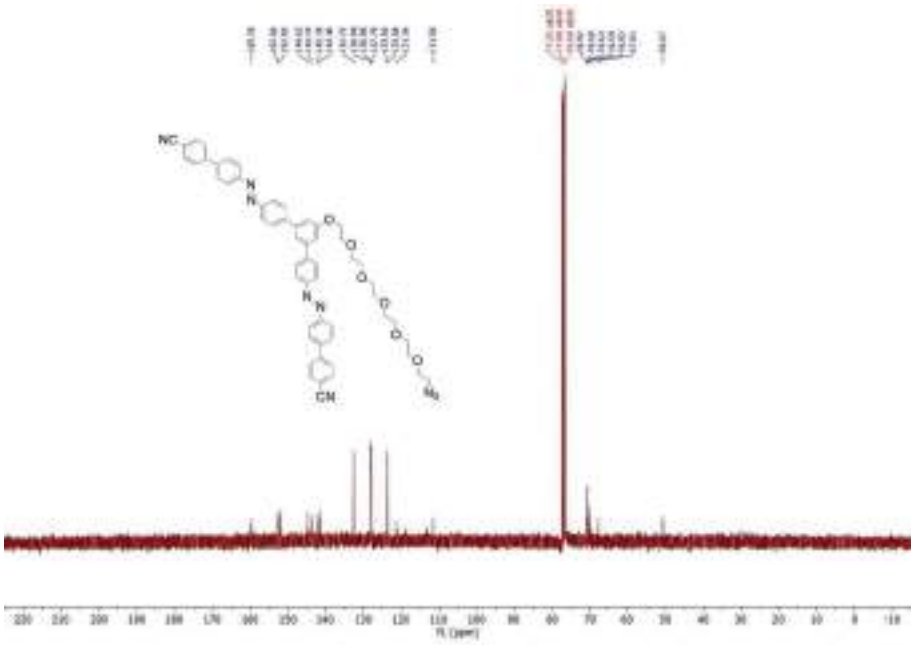

*Figure S7: ^{13}C NMR (101 MHz, $CDCl_3$) of **$AzoN_3$***

4.5. References

4.5.1 Front page illustration (Chapter 4)

Goodsell, D. S. *Cytoplasm*. (PDB-101, 2005).

4.5.2 References (Chapter 4)

1 Miller, D. D. & Chuang, S. S. C. Control of CO2 Adsorption and Desorption Using Polyethylene Glycol in a Tetraethylenepentamine Thin Film: An In Situ ATR and Theoretical Study. *The Journal of Physical Chemistry C* **120**, 25489-25504, doi:10.1021/acs.jpcc.6b09506 (2016).

2 Perl, A. *et al.* Gradient-driven motion of multivalent ligand molecules along a surface functionalized with multiple receptors. *Nat Chem* **3**, 317-322, doi:10.1038/nchem.1005 (2011).

3 Vanossi, A., Manini, N., Urbakh, M., Zapperi, S. & Tosatti, E. Colloquium: Modeling friction: From nanoscale to mesoscale. *Reviews of Modern Physics* **85**, 529-552, doi:10.1103/RevModPhys.85.529 (2013).

4 Bormuth, V., Varga, V., Howard, J. & Schaffer, E. Protein friction limits diffusive and directed movements of kinesin motors on microtubules. *Science* **325**, 870-873, doi:10.1126/science.1174923 (2009).

5 Hill, T. L. Theoretical problems related to the attachment of microtubules to kinetochores. *Proc Natl Acad Sci U S A* **82**, 4404-4408, doi:10.1073/pnas.82.13.4404 (1985).

6 Wen, H., Morris, K. R. & Park, K. Hydrogen bonding interactions between adsorbed polymer molecules and crystal surface of acetaminophen. *J Colloid Interface Sci* **290**, 325-335, doi:10.1016/j.jcis.2005.04.049 (2005).

7 Poornachary, S. K. *et al.* Anisotropic Crystal Growth Inhibition by Polymeric Additives: Impact on Modulation of Naproxen Crystal Shape and Size. *Crystal Growth & Design* **17**, 4844-4854, doi:10.1021/acs.cgd.7b00802 (2017).

8 Li, Z., Fan, Q. & Yin, Y. Colloidal Self-Assembly Approaches to Smart Nanostructured Materials. *Chem Rev* **122**, 4976-5067, doi:10.1021/acs.chemrev.1c00482 (2022).

9 Sather, N. A. *et al.* 3D Printing of Supramolecular Polymer Hydrogels with Hierarchical Structure. *Small* **17**, e2005743, doi:10.1002/smll.202005743 (2021).

10 Xi, Y. & Pozzo, L. D. Electric field directed formation of aligned conjugated polymer fibers. *Soft Matter* **13**, 3894-3908, doi:10.1039/c7sm00485k (2017).

11 Joep Vanlier, R. P., Dean Moldovan, Tobias Jachowski, Aafke van den Berg, Onno Broekmans, Agostino Mirone, Robert Moerland, Michael Hasselmann, Abel Moyo, & Steven Lamerton. lumicks/pylake: v1.4.0 (v1.4.0). . doi:https://doi.org/10.5281/zenodo.10723300 (2024).

12 Florin, E. L., Pralle, A., Stelzer, E. H. K. & Horber, J. K. H. Photonic force microscope calibration by thermal noise analysis. *Appl Phys a-Mater* **66**, S75-S78, doi:DOI 10.1007/s003390051103 (1998).

13 Paz, J. & Luders, J. Microtubule-Organizing Centers: Towards a Minimal Parts List. *Trends Cell Biol* **28**, 176-187, doi:10.1016/j.tcb.2017.10.005 (2018).
14 Martin, M. & Akhmanova, A. Coming into Focus: Mechanisms of Microtubule Minus-End Organization. *Trends Cell Biol* **28**, 574-588, doi:10.1016/j.tcb.2018.02.011 (2018).
15 Kerssemakers, J. W. *et al.* Assembly dynamics of microtubules at molecular resolution. *Nature* **442**, 709-712, doi:10.1038/nature04928 (2006).
16 Schmidt, S., Helfer, E., Carlier, M. F. & Fery, A. Force generation of curved actin gels characterized by combined AFM-epifluorescence measurements. *Biophys J* **98**, 2246-2253, doi:10.1016/j.bpj.2010.01.055 (2010).
17 Marcy, Y., Prost, J., Carlier, M. F. & Sykes, C. Forces generated during actin-based propulsion: a direct measurement by micromanipulation. *Proc Natl Acad Sci U S A* **101**, 5992-5997, doi:10.1073/pnas.0307704101 (2004).
18 Bacharouche, J. *et al.* Multivalency: influence of the residence time and the retraction rate on rupture forces measured by AFM. *J Mater Chem B* **3**, 1801-1812, doi:10.1039/c4tb01261e (2015).
19 Drake, B. *et al.* Imaging crystals, polymers, and processes in water with the atomic force microscope. *Science* **243**, 1586-1589, doi:10.1126/science.2928794 (1989).
20 Song, Y., Ma, Z. & Zhang, W. Manipulation of a Single Polymer Chain: From the Nanomechanical Properties to Dynamic Structure Evolution. *Macromolecules* **55**, 4177-4199, doi:10.1021/acs.macromol.2c00076 (2022).
21 Parekh, S. H., Chaudhuri, O., Theriot, J. A. & Fletcher, D. A. Loading history determines the velocity of actin-network growth. *Nat Cell Biol* **7**, 1219-1223, doi:10.1038/ncb1336 (2005).
22 Goronzy, D. P. *et al.* Supramolecular Assemblies on Surfaces: Nanopatterning, Functionality, and Reactivity. *ACS Nano* **12**, 7445-7481, doi:10.1021/acsnano.8b03513 (2018).
23 Baris, B. *et al.* Robust and open tailored supramolecular networks controlled by the template effect of a silicon surface. *Angew Chem Int Ed Engl* **50**, 4094-4098, doi:10.1002/anie.201100332 (2011).
24 Dang, Z. *et al.* Applications of powder X-ray diffraction to inclusion complexes of cyclodextrins. *Current Organic Chemistry* **15**, 848-861 (2011).
25 Li, Z. *et al.* gamma-Cyclodextrin: a review on enzymatic production and applications. *Appl Microbiol Biotechnol* **77**, 245-255, doi:10.1007/s00253-007-1166-7 (2007).
26 Kawaguchi, Y., Nishiyama, T., Okada, M., Kamachi, M. & Harada, A. Complex formation of poly (ε-caprolactone) with cyclodextrins. *Macromolecules* **33**, 4472-4477 (2000).
27 Jiao, H., Goh, S. & Valiyaveettil, S. Inclusion complexes of single-C60-end-capped poly (ethylene oxide) with cyclodextrins. *Macromolecules* **35**, 1399-1402 (2002).
28 Priyadarsini, K., Mohan, H., Tyagi, A. & Mittal, J. Inclusion complex of. gamma.-cyclodextrin-C60: formation, characterization, and photophysical properties in aqueous solutions. *The Journal of Physical Chemistry* **98**, 4756-4759 (1994).
29 Bard, A. J., Faulkner, L. R. & White, H. S. *Electrochemical methods: fundamentals and applications*. (John Wiley & Sons, 2022).

30 Bell, M. S. & Borhan, A. A Volume-Corrected Wenzel Model. *ACS Omega* **5**, 8875-8884, doi:10.1021/acsomega.0c00495 (2020).
31 Fygenson, D. K., Marko, J. F. & Libchaber, A. Mechanics of microtubule-based membrane extension. *Physical review letters* **79**, 4497 (1997).
32 Thomson, N. H. *et al.* Large fluctuations in the disassembly rate of microtubules revealed by atomic force microscopy. *Ultramicroscopy* **97**, 239-247, doi:10.1016/S0304-3991(03)00048-2 (2003).
33 Patnaik, A., Setoyama, H. & Ueno, N. Surface/interface electronic structure in C 60 anchored aminothiolate self-assembled monolayer: An approach to molecular electronics. *The Journal of chemical physics* **120**, 6214-6221 (2004).
34 Sahoo, R. R. & Patnaik, A. Binding of fullerene C60 to gold surface functionalized by self-assembled monolayers of 8-amino-1-octane thiol: a structure elucidation. *Journal of colloid and interface science* **268**, 43-49 (2003).
35 Weiss, E. A. *et al.* Si/SiO2-templated formation of ultraflat metal surfaces on glass, polymer, and solder supports: Their use as substrates for self-assembled monolayers. *Langmuir* **23**, 9686-9694 (2007).
36 Weinkamer, R. & Fratzl, P. Mechanical adaptation of biological materials — The examples of bone and wood. *Materials Science and Engineering: C* **31**, 1164-1173, doi:10.1016/j.msec.2010.12.002 (2011).
37 Walther, A. Viewpoint: From Responsive to Adaptive and Interactive Materials and Materials Systems: A Roadmap. *Adv Mater* **32**, e1905111, doi:10.1002/adma.201905111 (2020).
38 Burla, F. *et al.* Connectivity and plasticity determine collagen network fracture. *Proc Natl Acad Sci U S A* **117**, 8326-8334, doi:10.1073/pnas.1920062117 (2020).
39 Rajagopal, K. R. & Srinivasa, A. R. On the thermomechanics of materials that have multiple natural configurations Part I: Viscoelasticity and classical plasticity. *Zeitschrift fur angewandte Mathematik und Physik* **55**, 861-893, doi:10.1007/s00033-004-4019-6 (2004).
40 Roy, N., Bruchmann, B. & Lehn, J. M. DYNAMERS: dynamic polymers as self-healing materials. *Chem Soc Rev* **44**, 3786-3807, doi:10.1039/c5cs00194c (2015).
41 Ding, Q. *et al.* Nanocellulose-Mediated Electroconductive Self-Healing Hydrogels with High Strength, Plasticity, Viscoelasticity, Stretchability, and Biocompatibility toward Multifunctional Applications. *ACS Appl Mater Interfaces* **10**, 27987-28002, doi:10.1021/acsami.8b09656 (2018).
42 Wang, Z. *et al.* Bio-inspired mechanically adaptive materials through vibration-induced crosslinking. *Nat Mater* **20**, 869-874, doi:10.1038/s41563-021-00932-5 (2021).
43 Tong, C. *et al.* Spatial and Temporal Modulation of Cell Instructive Cues in a Filamentous Supramolecular Biomaterial. *ACS Appl Mater Interfaces* **14**, 17042-17054, doi:10.1021/acsami.1c24114 (2022).
44 Stupp, S. I. Biomaterials for Regenerative Medicine. *Mrs Bulletin* **30**, 546-553, doi:10.1557/mrs2005.148 (2005).
45 Shin, H., Jo, S. & Mikos, A. G. Biomimetic materials for tissue engineering. *Biomaterials* **24**, 4353–4364, doi:10.1016/S0142-9612(03)00339-9 (2003).
46 Das, R. K., Gocheva, V., Hammink, R., Zouani, O. F. & Rowan, A. E. Stress-stiffening-mediated stem-cell commitment switch in soft responsive hydrogels. *Nat Mater* **15**, 318-325, doi:10.1038/nmat4483 (2016).

47 Prince, E. & Kumacheva, E. Design and applications of man-made biomimetic fibrillar hydrogels. *Nature Reviews Materials* **4**, 99-115, doi:10.1038/s41578-018-0077-9 (2019).

48 Nam, S., Lee, J., Brownfield, D. G. & Chaudhuri, O. Viscoplasticity Enables Mechanical Remodeling of Matrix by Cells. *Biophys J* **111**, 2296-2308, doi:10.1016/j.bpj.2016.10.002 (2016).

49 Fredy, J. W. *et al.* Molecular photoswitches mediating the strain-driven disassembly of supramolecular tubules. *Proc Natl Acad Sci U S A* **114**, 11850-11855, doi:10.1073/pnas.1711184114 (2017).

50 Fredy, J. W. *et al.* Molecular photoswitches mediating the strain-driven disassembly of supramolecular tubules. *Proceedings of the National Academy of Sciences* **114**, 11850-11855 (2017).

51 Xiu, F. *et al.* Multivalent noncovalent interfacing and cross-linking of supramolecular tubes. *Advanced materials* **34**, 2105926 (2022).

5

Mechanochemistry in motile compartments

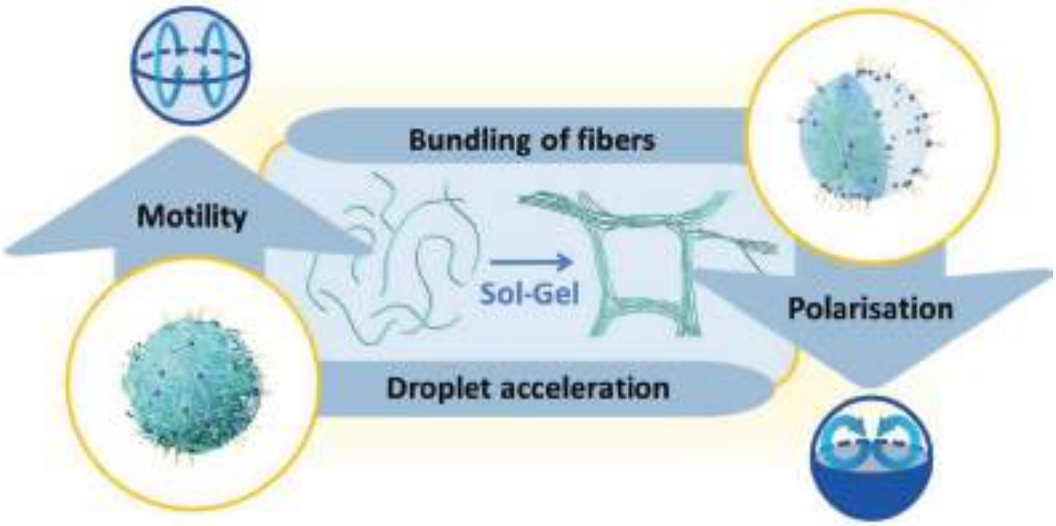

ABSTRACT:

The bottom-up approach has demonstrated that complex biomimetic behaviour can emerge from the interaction of simple molecular building blocks that can alter the physical properties of chemical systems. Exploring this strategy, it became increasingly clear that, rather than the number of elements added to a chemical system, synergistic effects are pivotal to achieving complex functionalities. This study unveils a novel *mechano-chemical feedback observed in water-in-oil droplets with compartmentalised fibrillar networks, resulting in an accelerated Marangoni propulsion* of *motile micro-objects. The Marangoni mechanism induces internal convectional flows within the droplets, generating sufficient mechanical shear to accelerate the bundling of supramolecular fibres. This, in turn, promotes a Sol-Gel transition that breaks the symmetry of the homogenous aqueous compartment and consequently amplifies the Marangoni effect. This study shows how mechanically responsive supramolecular polymers can mediate the reciprocal coupling of complex biomimetic functions, such as (proto)cell polarisation and motion.*

L.C. Pantaleone†, B. Marincioni†, V.B. Verduijn†, N. Katsonis*, T. Kudernac*; *manuscript in preparation.*

5.1. Introduction

Compartmentalisation is one of the hallmarks of living systems, a biological strategy that facilitates efficient regulation and spatial organisation within the cell and tissues. Membranes create the optimal physiological conditions by concentrating chemicals, isolating potentially damaging substances or preventing interference between incompatible reactions.[1] Similarly, the presence of dynamic networks of protein assemblies in the cytoplasm is a ubiquitous component of biological systems that has been long preserved throughout evolution.[2] Even in rudimentary cytoskeleton systems, in vitro studies have demonstrated that these filamentous networks inherently exhibit the non-linear elastic properties essential for the adaptation and structural support of cells.[3] Despite the importance of these essential tasks, complex biological functions can only emerge in the cell by integrating its multiple components.[4] Cell migration, differentiation, and morphogenesis require the interplay between membranes, extracellular matrix and the cytoskeleton. In other words, developing complex mechanisms requires active communication between cellular components. This idea stirred our interest in exploring the reciprocal impact of mechanically active systems and compartmentalising elements, e.g. liquid droplets and giant unilamellar vesicles.

One of the best examples of integration between cellular elements, is represented by the translation of mechanical stress into biochemical signals. This mechanism, also known as mechanosensing, enables the cytoskeleton to adapt to environmental cues.[5] Communication between fibre networks and membrane is granted by positive feedback loops, which are a widespread strategy of amplification in signal transduction.[6,7]

Recently, the growing interest in the field of system chemistry brought synergistic effects to the spotlight.[8,9] A few recent studies recognized that amplification pathways can often mediate, or even emerge from, the reciprocal coupling between cellular functions. Insua and Montenegro showed that supramolecular polymerization of amphiphilic peptides, when confined in microcompartments, can induce functional environmental responses mediating the coalescence of water droplets (Figure 1a).[10] A second demonstration that synergic effects arise from the interplay between cellular (or protocellular) elements was reported by Babu et al., who coupled physical autocatalysis of lipid surfactants with chemotactic Marangoni propulsion of oil droplets, observing the emergence of motile behaviour in active emulsions (Figure 1c).[11]

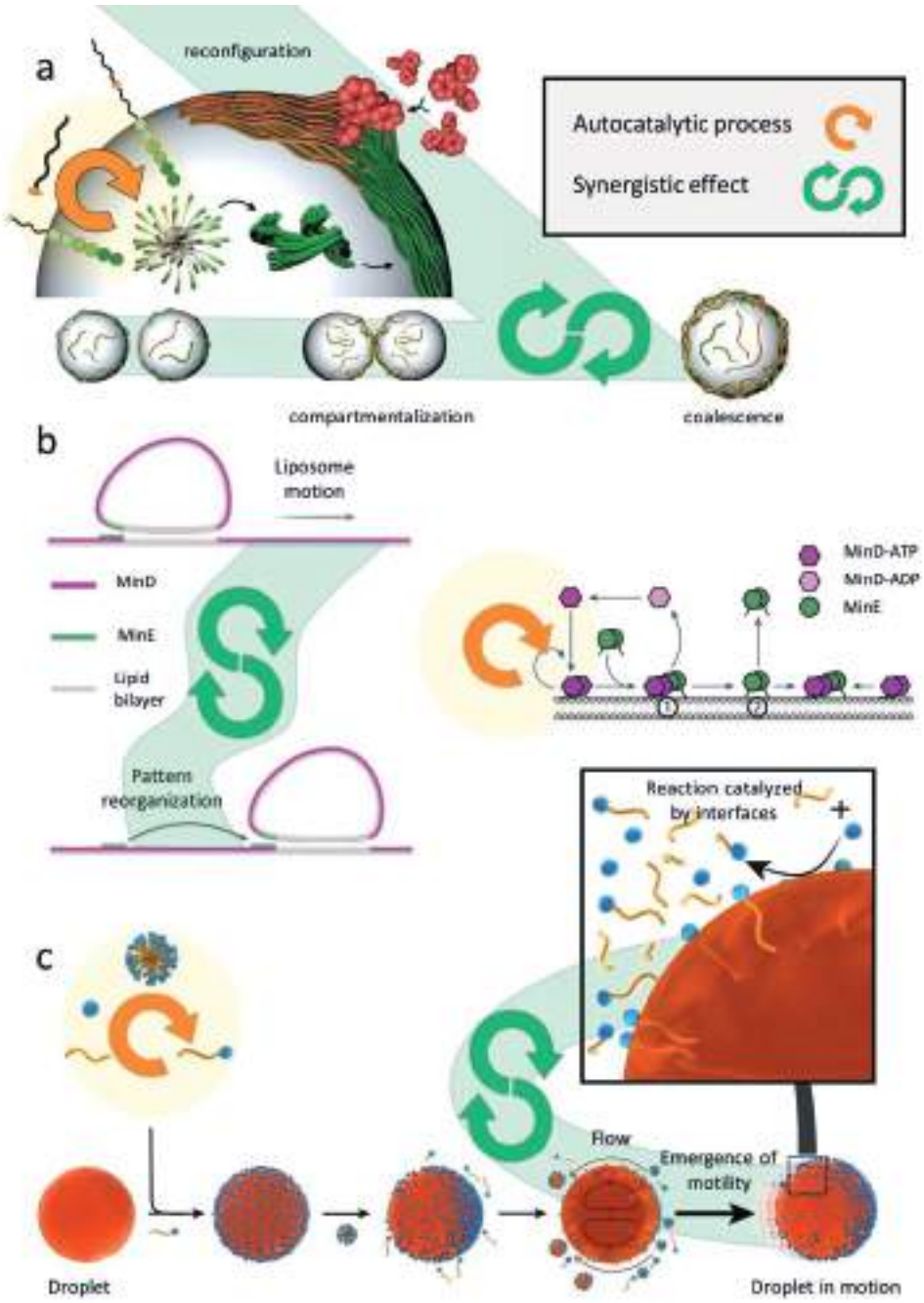

*Figure 1: (**a**) Autocatalytic formation of assembling peptides and spatial reorganization of their resulting fibres triggers a cascade of physical and chemical events resulting in droplet coalescence and cargo exchange (adapted with permission from ref. [10]). (**b**) Autocatalytic protein binding induces shape deformations in the liposome membrane, which generates a mechanical force gradient and consequently motion. Motion of the liposome drives the reorganization of the protein pattern (adapted with permission from ref. [12]). (**c**) The self-reproduction of lipid surfactants, catalyzed by micelles and oil droplets interfaces, generates an asymmetric surfactant distribution that initiates Marangoni flow. Chemotactic motion, in turn, enhances the reactant supply at the droplet interface (adapted with permission from ref. [11]).*

Lastly, it is worth mentioning the work of Fu et al. on a mechanochemical feedback loop which enables a persistent motion of cell-sized liposomes on Turin protein patterns (Figure 1b).[12]

The last two examples, introduce feedback mechanisms that can transduce information from environmental cues (e.g. reactant gradient, protein patterns) into motile behaviours, representing a further step towards life-like properties. Motion is not only an intrinsic feature of living systems, but it also represents a powerful method for promoting the "communication" between synthetic cellular elements.[13] In fact, motility is tightly connected with cell mechanics. For example, cytoplasmic streaming enhances intracellular transport, and micro-organisms adapt the movement of flagella mechanosensing fluid viscosity.[14-16]

The similarities among the aforementioned systems suggest two fundamental principles for the emergence of complex biomimetic behaviours: two or more elements must engage in mutual interactions, possibly through a feedback loop; secondly, the system must operate out of equilibrium. In this Chapter we will show how the latter condition could be matched taking advantage of the Marangoni effect. The energy supplied from the hydrodynamic instability of active emulsions can be channelled into a mechanical response of compartmentalised supramolecular networks. The mechanical response of the network leads to a phase separation within the micro-compartment and the formation of Janus droplet. This effect, in turn, has the potential to provide or enhance the asymmetry in surfactant distribution/activity at the core of Marangoni flows. The reciprocal coupling between Marangoni motion and droplet polarisation, mediated by the mechanical transformation of fibrillar networks, establishes the conditions for a novel feedback mechanism.

5.1.1 System design

The motile system chosen for compartmentalising the fibre networks was first reported by Dauchot and coworkers.[17] It consists of a biphasic system of water and squalane oil, with water being the dispersed phase. Upon emulsification of the system, the droplets are stabilised by monoolein (MO), a lipid surfactant previously dissolved in squalane. At high concentrations of monoolein, the lipid surfactant forms inverted micelles that can uptake water from the interface and progressively solubilise the droplets (Figure 2a). When the concentration of monoolein is higher than the critical propulsion concentration (CPC) ([MO]>25mM), this phenomenon causes an inhomogeneous distribution of surfactant on the droplet surface, at the base of Marangoni propulsion. The local gradients sustain the transport of lipids toward regions of high surface tension, and the resulting advection is matched by a net flow outside the droplets that causes the phoretic mobility of these microscopic objects.

Regarding the second component of this system, the fibre network, the choice of VsAzo hydrogelator, previously encountered in Chapter 4, was influenced by its sensitivity to mechanical stimulation. We recall from the previous Chapter that VsAzo is a V-shaped amphiphile composed of an aromatic scaffold and a hydrophilic oligoethylene glycol (OEG) side chain. The aromatic scaffold is equipped with two azobenzene actuator motifs whose photo-switching behaviour will not be at the centre of this study. The hierarchical assembly of monomers is depicted in Figure 2b.

While π-stacking of the aromatic core initiates the formation of nanofibres, secondary interactions between side chains govern the crosslinking and bundling of the fibre network, leading to gelation.[18,19] The entropic drive of this process explains why gelation occurs upon heating the colloidal suspension of nanofibres. Specifically, the entanglement of the side chains results from the dehydration of the OEG tails, and the addition of salt (KCl) can lower the sol-gel transition temperature (Figure 2c). In this chapter, it will be demonstrated how hydrogel formation can also be promoted using mechanical shear. Shear-induced phase separation of polymer solutions is known to depend on the internal dynamics of the materials. If interpolymer attractive interactions are restricted by the conformational freedom of sidechains, or limited by the kinetics of encounter, shear can accelerate the bundling process of fibres.[20,21] Knowing the phase diagram of VsAzo (Figure 2c), it is possible to design the ideal experimental conditions for the compartmentalisation of a meta-stable sol ([KCl]=1.2 M, 25°C), whose gelation can be promptly activated by mechanical shear.

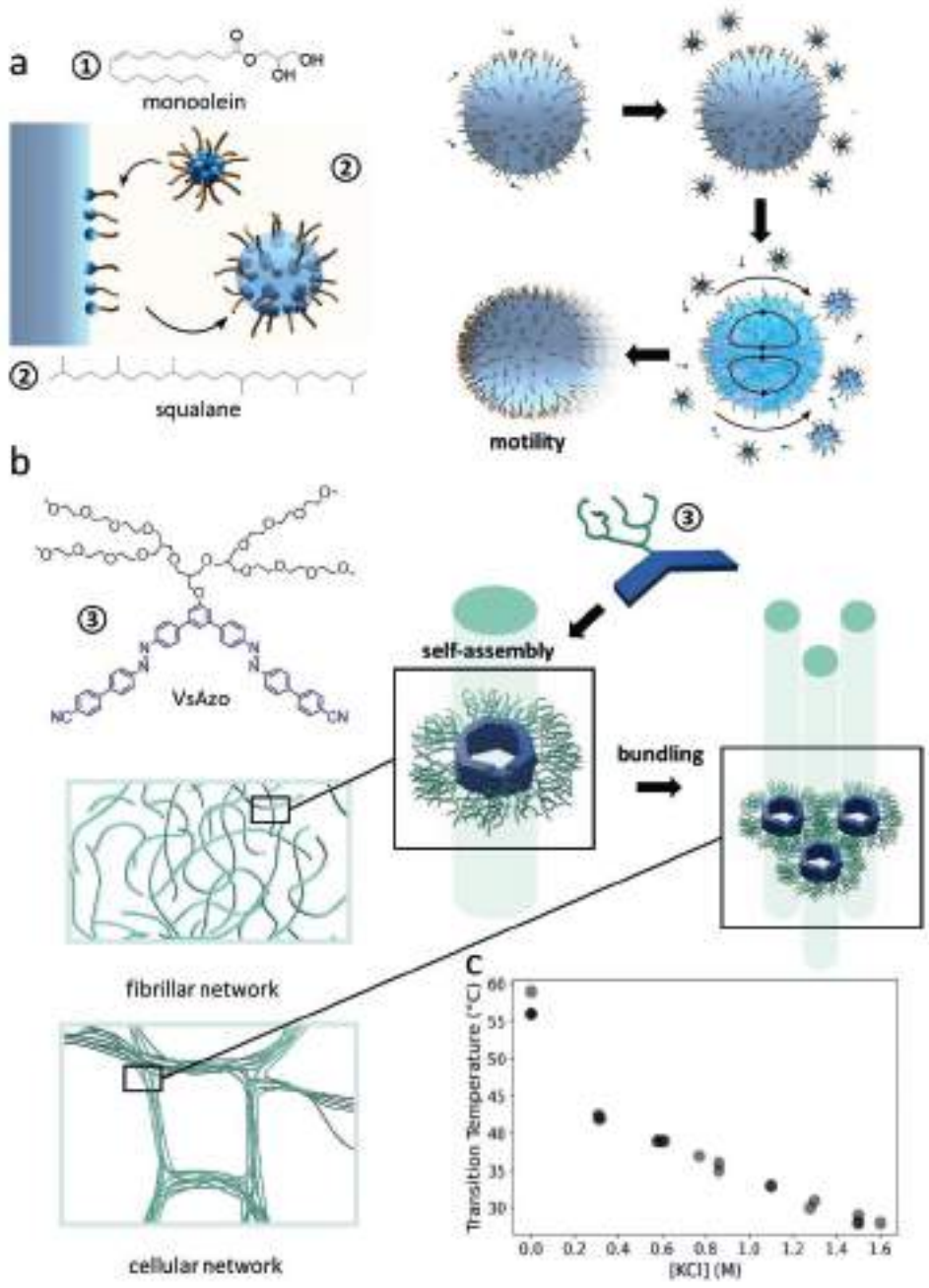

*Figure 2: (**a**) Water droplets stabilized by ① monoolein. Active emulsions show autonomous motile behaviour in ② squalane by Marangoni propulsion mechanism. (**b**) VsAzo hydrogelator ③ (**VsAzo**) and its hierarchical assembling mechanism: from monomer to individual nanotube fibres and fibres bundling mechanism. (**c**) Sol-Gel phase transition diagram of VsAzo colloidal suspensions as a function of salt concentration. and temperature.*

5.2. Results and Discussion

5.2.1 Motile behaviour in the presence of hydrogelators

The first step to study the effects of compartmentalization on motile behaviour was to establish a suitable method for preparing the active emulsions containing VsA hydrogelator. When droplets were prepared by mechanical agitation (Figure 1a), bright field (BF) microscopy analysis of the dispersed phase revealed that the aqueous compartment exhibited internal phase separation. We hypothesized that the mechanical stress during the emulsification process immediately induces hydrogelation in colloidal suspensions of VsA nanofibers. This results in the formation of a Janus droplet with two sub-compartments: a dense hydrogel phase and the excluded volume of saline solution dehydrated from the OEGs, as depicted in Figure 1a.

Interestingly, from the BF videos it seems that droplets with internal phase separation not only exhibit a motile behaviour but also swim faster compared to active emulsions without the hydrogelator. This effect was assessed through a competition experiment tracking the motion of both types of droplets, with and without VsAzo, with identical saline concentrations and within the same chamber. This experimental design ensured that the only variable influencing Marangoni propulsion was the presence of the hydrogel compartment formed by the mechanical agitation. The tracking analysis revealed that the phase-separated droplets moved at an average speed five times greater than that of droplets containing only saline solutions of KCl (Figure 1c).

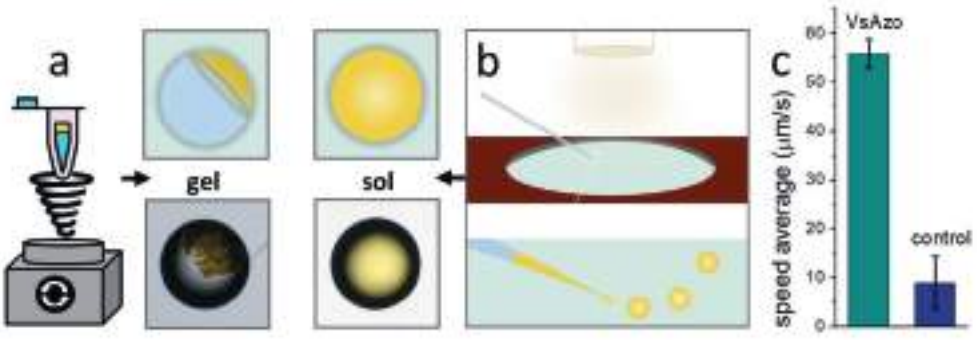

*Figure 3: Sample preparation and effect of hydrogel on motile behaviour. (**a**) Mechanical agitation during the emulsification process induces the immediate gelation of VsAzo in the droplets. (**b**) Droplets of metastable colloidal suspensions of VsAzo nanofibres can be prepared with a microinjector. (**c**) Speed average of motile droplets in competition experiments, number of tracked droplets for each experiment n=1 (fastest), plotted values are averaged from triplicated experiments.*

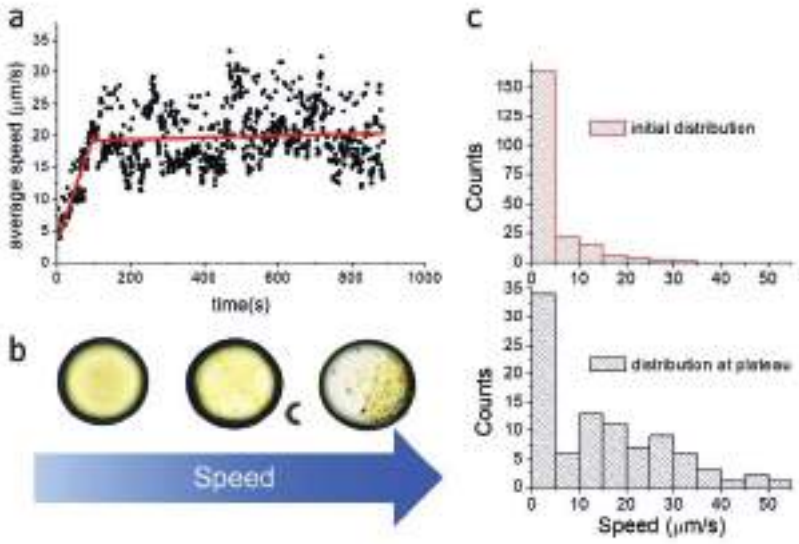

*Figure 4: (**a**) Motility assay of active emulsions containing the VsAzo hydrogelator. The speed values are averaged from instant speed values from the entire tracked population of droplets (n=18) throughout Δt=1s (moving average). Two distinct motile phases, acceleration and plateau, are fit linearly (red lines). (**b**) Phase transition within droplet compartment observed during the acceleration phase (**c**) Distribution of instant speed values in the droplet ensemble during acceleration phase (t=10s, Δt=10s) and plateau (t=600s, Δt=10s).*

Next, we sought to investigate whether Marangoni flow could activate the transition from colloidal suspension of nanofibers to a phase-separated hydrogel within the microcompartment, and the effect of this transition on the motile behaviour. The active emulsions were prepared by micro-injection of colloidal suspensions of VsAzo nanofibres in a microscopy chamber containing the oil dispersant (Figure 3b). This protocol was developed to avoid the destabilisation of fibrillar networks and untimely activation of the bundling process caused by mechanical agitation during the preparation of the sample. Tracking a large population of droplets (n=18) over 15 minutes, we obtained 109 tracks which were used to describe the motile behaviour of the ensemble over time. Each track provided instant speed values at an acquisition rate of r=1fps (Supplementary Figure 1). This information was then combined in Figure 4a, plotting the moving average (Δt=1s) of the instant speed values collected from the entire ensemble over time.

From the shift in the moving average of speed values we found that the droplets containing hydrogelator are characterised by an initial acceleration phase followed by a plateau (Figure 4a). The microscopy images of the swimming droplets indicate that the bundling process in the colloidal suspensions of nanofibres starts

during the accelleration phase, and that the formation of a subcompartment of phase separated hydrogel occurs in conjunction with the transition to the plateau region (Figure 4b). These observations were the first indication of a reciprocal coupling mechanism between Marangoni flow and the mechanically active fibre network. The linear fits of the two motile phases, acceleration and plateau, intersect at 95 seconds. The extension of this acceleration phase and the low initial speed values suggest that the presence of VsAzo nanofibers initially delays the onset of advective Marangoni flows. However, at a later stage, after the phase transition, the presence of the sub-compartment reinforces the propulsion mechanism. In comparison, the acceleration phase in active emulsions of saline droplets is difficult to observe experimentally as it occurs within seconds after emulsification. This is consistent with mathematical simulations of similar systems, which predict the emergence of advective flows in a time span an order of magnitude shorter than that observed in droplets containing the VsAzo hydrogelator.[22]

The diverse distribution of speed values (Figure 4c) reflects a coefficient of variation (CV) in the moving average ranging from 70% during the acceleration phase to 100% in the plateau region (See Supplementary Figure 1a). This significant fluctuation is indicative of the stochastic nature of the Marangoni effect. However, the ample dataset enabled us to extrapolate the general trend in the motility behaviour of the ensemble. Indeed, the acceleration of the system is clearly evidenced by the shift in speed distribution towards higher values in the plateau region.

5.2.2 Sol-gel transition and symmetry-breaking effects

To confirm that the phase separation observed within the droplet compartment was due to sol-gel transition and exclude a liquid-liquid phase separation mechanism, the relative motion of fluorescent trackers within the droplet compartment was studied at different surfactant concentrations. Comparing how inter-tracker distance changes over a short correlation time provides information on the micro-rheological properties of the droplet content (Figure 5a). Precisely, when suspended in a fluid environment, the relative position of these trackers (polystyrene microspheres, d=1μm) follow the random motion of Brownian particles. By contrast, if gelation occurs, the internal network formed by the hydrogel restricts particle motion, and the inter-tracker distance remains essentially frozen. The analysis of the tracker's motion (Figure 5c-d) confirmed

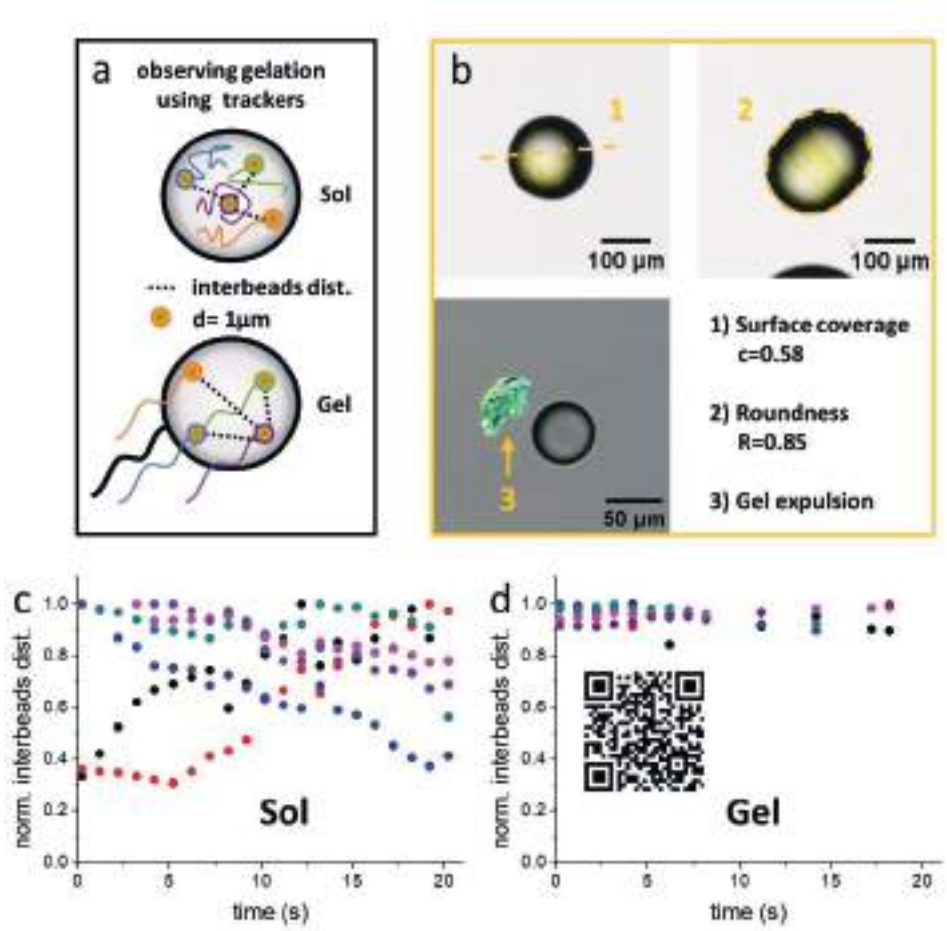

*Figure 5: (**a**) The transition of the aqueous compartment from colloidal suspension of fibres to crosslinked gel can be inferred by observing the change of intertracker distance over a short correlation time. (**b**) Polarising deformations (① asymmetric surface coverage, ② budding) and ③ gel expulsion caused by sol-gel phase transition in the aqueous compartment. (**c**) Normalised interbead distance in colloidal suspension, each colour represents a distinct tracker (**d**) Normalised inter bead distance after hydrogel formation. Small differences in the inter bead distance are present, this occurs because the droplet rotational motion can still affect the optical projection of beads positions. Tracker motion during Marangoni-promoted sol-gel transition was imaged by fluorescence microscopy, video accessible scanning the quick-response code.*

that, after 30 minutes from dispersion, the colloidal suspensions of nanofibres are stable when the concentration of monoolein surfactant was kept below CPC and that gelation only occurs in motile droplets. Video recordings of the bundling process in motile droplets show that trackers, before being trapped in the hydrogel matrix, are transported by advective Marangoni flow (Figure 5d).

Once the role of Marangoni flows in the mechanical activation of the hydrogelator was established, we focused on the mechanism of acceleration in phase separated droplets. The gelation of the fibre suspension in the microcompartment leads to

morphological changes that deform the droplets with two distinct mechanisms. Budding is the most common form of shape deformation observed, often resulting in droplets with an evident loss of roundness (Figure 5b). This mechanism implies that adhesion forces can transfer mechanical stress from the bundling network to the droplet interface. The other most common shape transition takes place when the hydrogel phase separates within the water compartment, creating an asymmetric distribution of material in the droplet (Figure 5b). The hydrogel always retains contact with the interface, confirming again the effectiveness of adhesion, and surface coverage usually spans from 30-70%. Lastly, it is worth mentioning that in a few cases, the phase transition was followed by the expulsion of gel (Figure 5b).

These shape deformations, culminating in the formation of a Janus droplet, result in in a loss of symmetry of the micro-compartment. Symmetry breaking is a key component of interfacial mechanisms, such as Marangoni, that lead to the autonomous locomotion of active emulsion.[23] Asymmetry, in the form of interfacial tension gradients, is achieved through the balance between surfactant advection and diffusion, summarised by the Péclet number. We envision that the dynamic behaviour of the lipid at the interface is influenced by both surface coverage and inhomogeneous droplet curvature, as the interfacial tension in the area in contact with the hydrogel will differ significantly from the rest of the interface.[24]

5.2.3 Polymer dynamic at the droplet interface

Symmetry breaking effects explain the acceleration of droplets. Nevertheless, other anomalies in the motile behaviour remain unanswered. For example, initial speed values in the early stages of motility, dominated by the sol presence, are significantly below the speed average when compared with droplets in the absence of a hydrogelator. In other words, it seems that before the phase transition occurs, the colloidal suspension of supramolecular fibres has a retarding effect on the onset of Marangoni flow. To understand this phenomenon, we focused our attention on the interplay between supramolecular polymers and the droplet interface.

The pendant droplet experiment was used to assess the presence of the monomer at the water-squalane interface. Conforming with the amphiphilic nature of VsAzo, the interfacial tension of a fibre colloidal suspension was significantly lower than water's (Figure 6a-b). Then, interfacial tension was used to compare

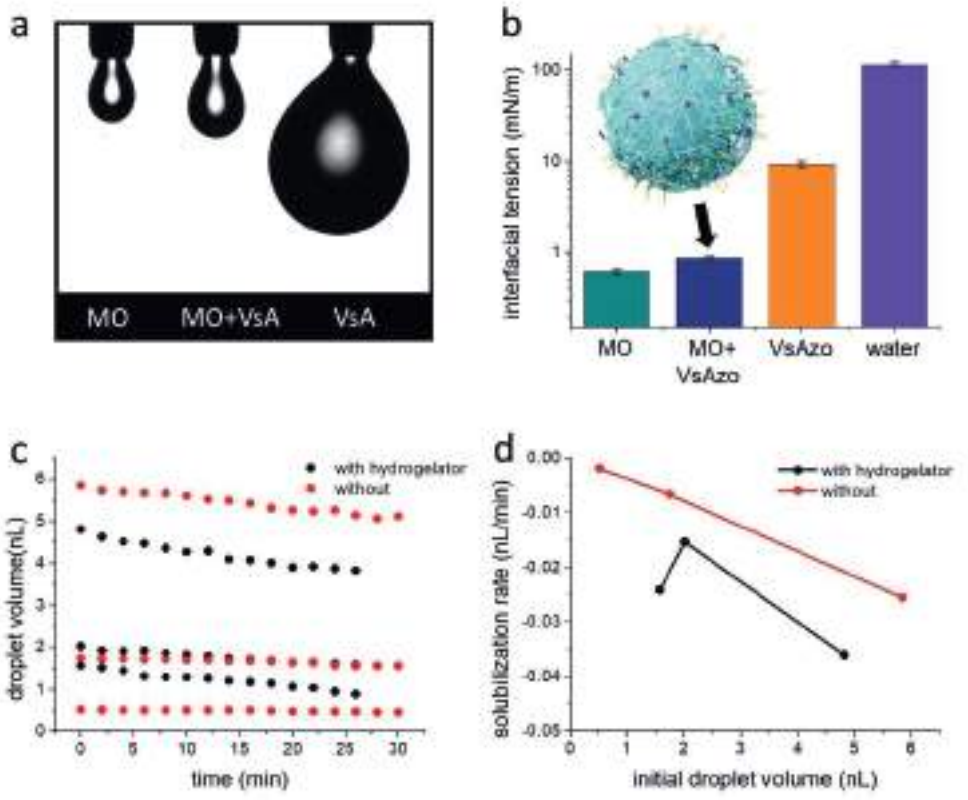

*Figure 6: (**a**) Comparison between pendant droplet experiments. The interphase is stabilized by the presence of monoolein (**MO**) dissolved in the squalane phase, by the VsAzo (**VsA**) monomer in the aqueous phase, or by both surfactants (**MO+VsA**). (**b**) Interfacial tension values from pendant droplet experiments. Average from triplicated measure, error bar is St. dev. (**c**) Effect of micellar solubilization on the droplet diameter over time, comparison between active emulsions in the presence (black) or absence (red) of hydrogelator, each trace corresponds to one droplet. (**d**) Micellar solubilization rate as a function of initial droplet volume, rate values were obtained from the slope (dV/dt) of the linear regression obtained from the volume over time traces.*

the effectiveness of monomer and monoolein at stabilising the interface. Both concentrations of VsAzo and MO were lowered with respect to the experimental conditions for motility assays, to overcome instrumental limitations. Nevertheless, a comparable molar ratio between monomer and lipid was used in these measurements (x_{MO}:x_{VsAzo}=6:1). The data show that the droplets are mainly stabilised by monoolein (γ_{MO}=0.62 mN/m; γ_{VsAzo}=9.22 mN/m) and that the interfacial tension measured for the combination of the two surfactants results in an intermediate value (γ=0.87 mN/m). This small but measurable shift of the interfacial tension confirms the presence of polymer fibres at the interface, indicating that VsAzo monomer competes with monoolein for the active surface of the droplets.

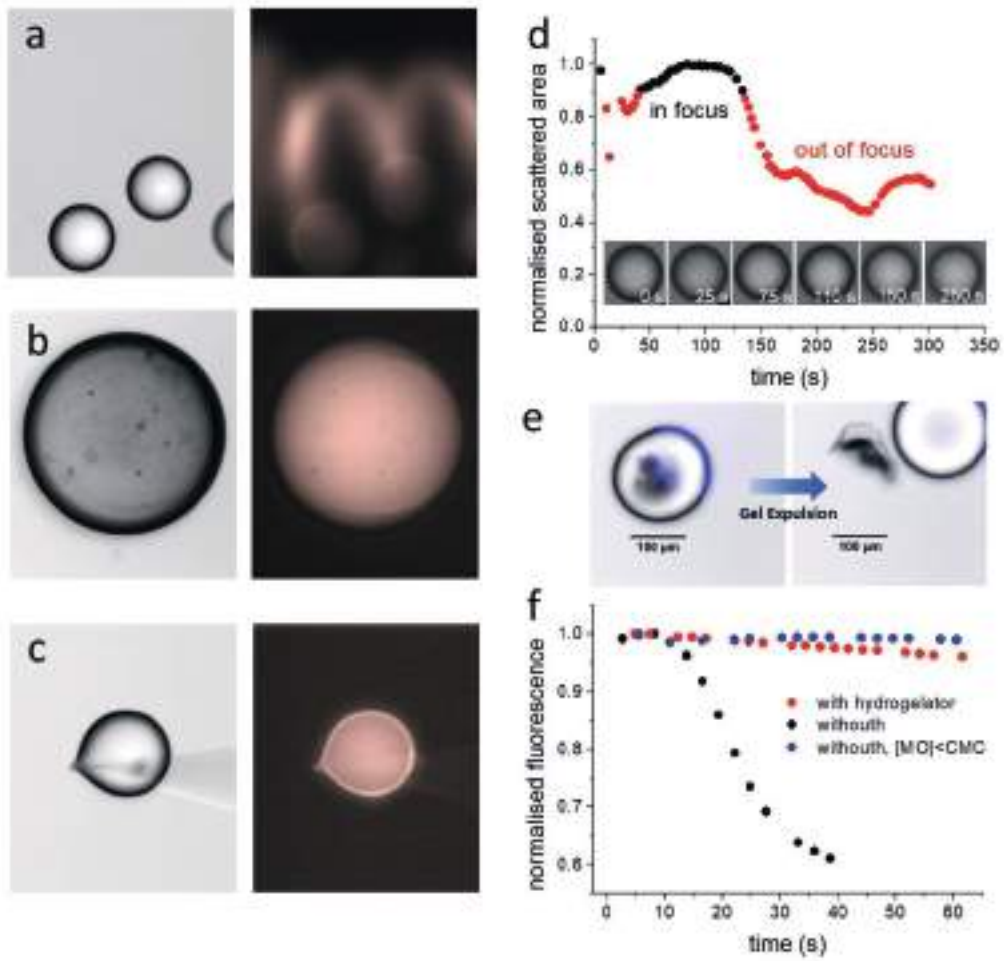

*Figure 7: (**a**) Motile droplets loaded with fluorescein in the absence of VsAzo hydrogelator. Bright field (left) and fluorescence (right) micrographs. (**b**) Motile droplets loaded with fluorescein from colloidal suspension of VsAzo fibres. (**c**) Water droplet loaded with fluorescein in the absence of monoolein surfactant. In this conditions, high interfacial tension causes the adhesion of water droplet to the surface of the microinjector, the glass needle is visible in the bright field micrograph. (**d**) Changes in normalised scattered area (nsa) reflect the position of droplets with respect to the focal plane. Scattered area was defined based on a greyscale threshold of bright field micrographs. Droplets with nsa<0.9 were considered out of focus. (**e**) Superposition of bright field (grayscale) and fluorescence (blue) micrographs during the expulsion of gel cap, consecutive frames (frame rate f=1.25s). (**f**) Normalised intensity from droplet fluorescence shows the rate of fluorescein leak in the oil phase caused by micellar solubilization.*

Another possibility for assessing the effect of the hydrogelator on the interfacial dynamics is to monitor the changes in micellar solubilisation. Autonomous Marangoni motion is sustained by the micellar uptake of water from the interface, causing the volume of the droplets to shrink. Measuring the variation in the droplet diameter over extended periods of time, we can obtain a solubilisation

rate. The experimental results show that the volume of the hydrogel droplets decreases steadily, with no evidence of accelerating behaviour. At first glance, these data may appear conflicting with droplet tracking experiments; however, in the previous motility assays, the accelerating motile behaviour occurred within the first two minutes, which is a prohibitive time frame for observing significant variations in the droplet volume. Therefore, we anticipate that the micellar solubilisation rate during the acceleration phase will be studied with a different method; namely, fluorophore leakage assay. Nonetheless, the changes in the droplet volume still provide information about the mechanism of propulsion in the plateau region.

Using a linear fit to extrapolate the solubilization rates we observed that, in the absence of hydrogelator, there is a good correlation between the droplet size and the micellar solubilisation rate (Figure 6d). This linear dependence of rate from the initial volume is lost in Janus droplets, generally displaying faster, but erratic, solubilization. Our interpretation is that in the latter case, in addition to the droplet volume, the solubilization rate also depends on the desymmetrization effects caused by the phase separation.

The interest in studying the micellar solubilization rate during acceleration phase was prompted by the evidence of polymer presence at the interface. If micellar solubilisation is disrupted by the presence of nanotube fibres, this would explain the initial inhibition of Marangoni propulsion in droplets containing the colloidal suspensions.

The solubilisation process at the early stages of droplet formation, preceding sol-gel transition, was analysed by measuring the leak of a fluorescent dye from the aqueous phase (Figure 7a-c). Imaging motile objects of this size with adequate time resolution presented some technical challenges. Reducing the time gap between injection of the droplets in the chamber and image acquisition required the use of an electronic microinjector. Objectives with low numerical apertures were preferred, since larger depth of field allows to monitor the motile objects over a longer time range. Bright field images were acquired alongside fluorescence to confirm that during measurements droplets were imaged within the focal volume. Specifically, the normalised scattered area (NSA) from the droplet surface was used to reconstruct the information about the droplet position with respect to the focus (Figure 7d). Excluding the datapoints where the droplet trajectories deviated from the focal volume allowed a quantitative analysis of fluorescence intensity.

Comparing the intensity decays, it was found that micellar solubilisation was significantly slowed down by the presence of the colloidal fibre suspension

(Figure 7f). In the absence of hydrogelator, fluorescein was rapidly solubilised, as shown by the sigmoidal profile of the fluorescence intensity of the droplets. Fluorophore leakage was so pronounced that it produced the fluorescent trail imaged in some of the micrographs (Figure 7a). By contrast, the fluorescence intensity of droplets in the presence of nanofibres decreases slowly, following a linear decay. The absence of fluorescein in expelled gels indicated that the permeability of the polymer matrix does not prevent the release of the dye (Figure 7e). Moreover, control samples lacking lipid surfactant showed no intensity changes over the experimental time interval, excluding any relevant contribution from photobleaching nor spontaneous migration of dye in the oil phase in the absence of micellar solubilisation. Therefore, we concluded that the solubilization process in colloidal droplets occurs at lower rate because of the micellar uptake at the interface being hampered by the presence of the supramolecular polymer.

5.2.4 Mechanical activation of nanofibres bundling

Above we proposed that the phase transition from a colloidal suspension of nanofibres to a hydrogel network is exacerbated by the internal Marangoni flows. More specifically, we hypothesised that shear stress (τ) could accelerate the bundling and crosslinking of nanofibres.

Insights into the mechanical actuation process were obtained by analysing the internal flows within the liquid droplet using particle tracking velocimetry (PTV). PTV experiments were carried out in active emulsions of water in squalane, with the same lipid and saline concentrations used for the motility assays, but in the absence of the hydrogelator. As shown in our previous experiments the formation of the hydrogel mesh restricts the motion of the trackers, thus, it is not possible to use PTV for quantifying the Marangoni flow in the presence of VsAzo. Nevertheless, these experimental conditions are still representative of the hydrodynamic stress developed in the motile compartments.

The droplets were loaded with fluorescently labelled polystyrene microspheres, which were used to visualise Marangoni flow as a two-dimensional projection of particles trajectories. The choice of the tracker size (d = 1 μm) was based on the dimensional range of the fibre bundles (100 nm - 1 μm).

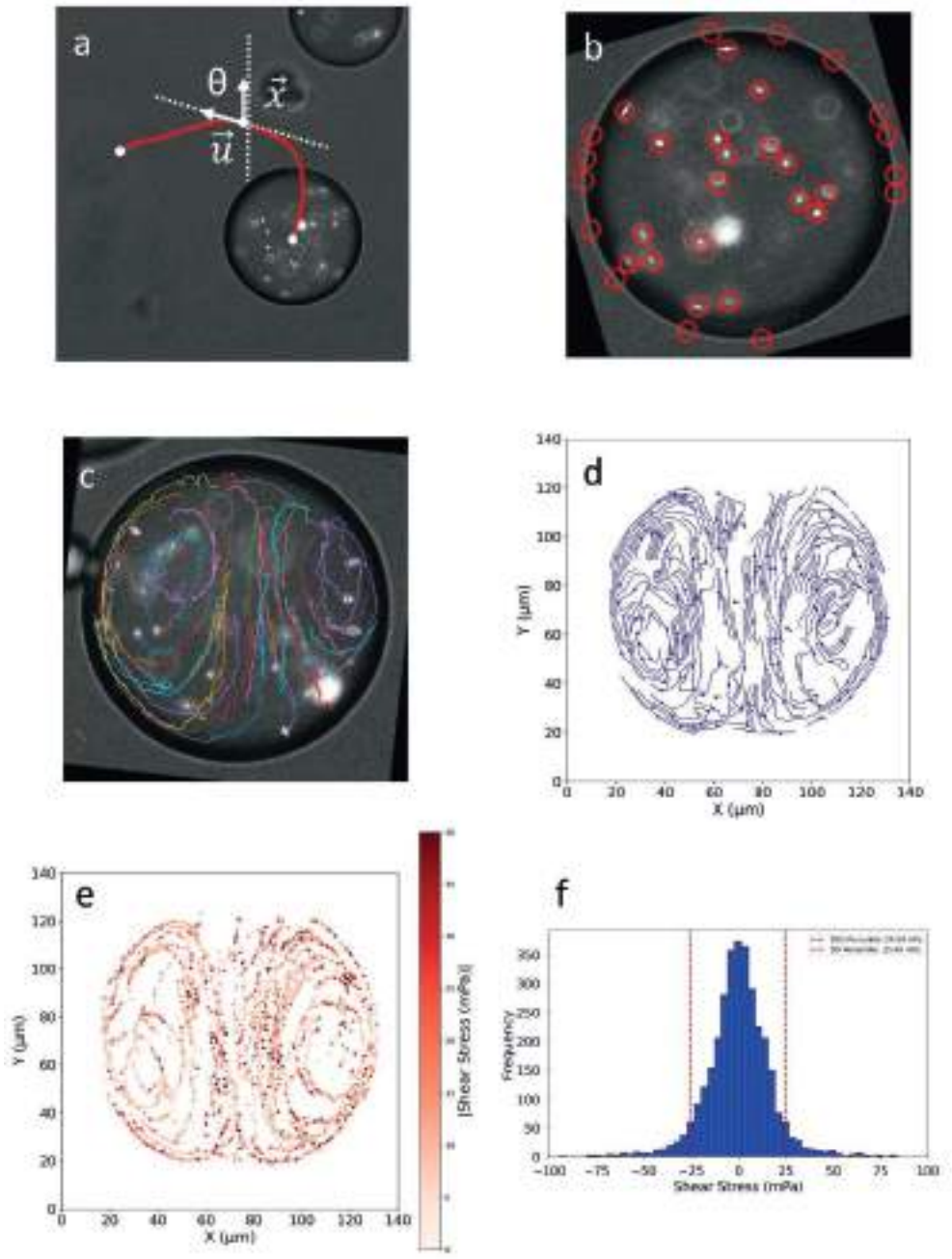

*Figure 8: (**a**) PTV analysis: correction of tracker motion based on the direction of droplet velocity vectors. (**b**) Image detection and tracking (**c**) of fluorescently labelled microspheres (d=1µm). (**d**) Velocity vector field and (**e**) the resulting shear stress scalar 2D map. (**f**) Distribution of shear stress values, 5th and 95th percentile thresholds are indicated with red dashed lines.*

The first step of PTV analysis consists of decoupling the motion of the droplet from particle tracking. Assuming that the internal flow is an axisymmetric convection, the direction of the droplet velocity vector coincides with this symmetry axis (Marangoni axis).[25] Thus, from the droplet trajectories, it is possible to calculate a rotation angle (θ) between the velocity vector and an arbitrary unit vector ($\vec{x}$) (Figure 8a). This θ angle is used to reorient the frames and have the Marangoni axis fixed with respect to a reference direction (x).

In the next step of the analysis, the fluorescence channel was used for tracking the microspheres (Figure 8b). Once corrected for the droplet motion, the new trajectories were used to calculate the velocity vectors ($\vec{u}$) of the trackers (Figure 8c). Summing the information from the entire stack of frames, a velocity vector field was obtained by spatially binning the $\vec{u}$ and averaging them (Figure 8d).

At low Raynolds numbers (Re), internal flows can be considered laminar, and the shear stress can be calculated from the velocity vector field (eq. 1). This assumption is commonly used to describe the fluid dynamics in microfluidics and biological systems where the flows are characterized by reduced velocities (u) and length scales (L)(eq.2).[26,27]

The presence of the hydrogelator, even after the sol-gel transition, does not alter significantly the viscosity (μ) of the solutions (μ_{gel}=1.12 mPa·s)*. Thus, the shear stress was calculated using the viscosity of water (μ_w=1.00 mPa·s).

eq.1 $$\tau_{xy} = \mu\left(\frac{\partial u_y}{\partial x} + \frac{\partial u_x}{\partial y}\right)$$

eq.2 $$Re = \frac{\rho u L}{\mu}$$ density of fluid (ρ)

Mapping the resulting shear stress values we observe that their distribution in the droplet follows the symmetrical circulation pattern expected for the internal Marangoni flows (Figure 8e). Interestingly, it seems that the mechanical stress is accentuated in the shear layers surrounding the two vortex cores, with maximum shear occurring along the Marangoni axis and in the regions around the poles. The 95th percentile threshold of shear stress is found to be τ=25mPa (Figure 8f).

*infinite rate viscosity value, extrapolated from shear rheology data

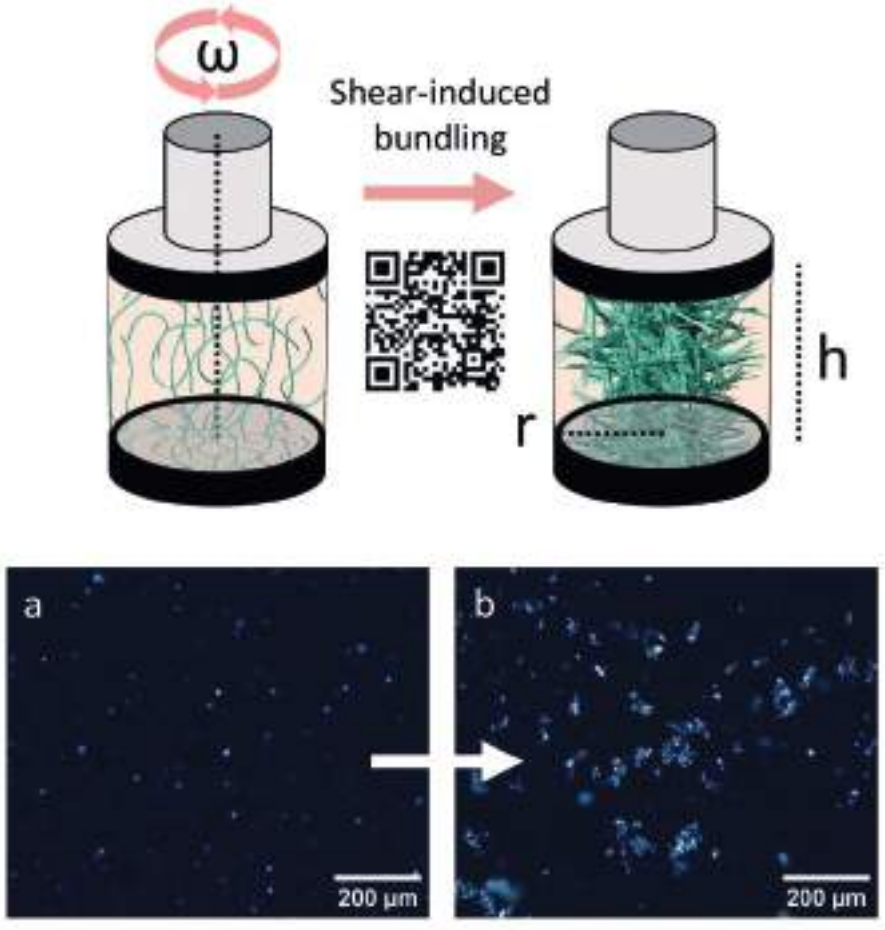

*Figure 9: Parallel plate geometry setting used for shear rheology experiment (r=20mm, h=300µm). Flocculation video accessible scanning the quick-response code. (**a**)(**b**) Cross-polarized microscopy shows the difference between non sheared (**a**) and sheared (**b**) samples.*

eq.3 $$\tau = \mu\dot{\gamma}$$

eq.4 $$\dot{\gamma}(r) = \frac{r}{h}\omega$$

radial distance (r)
gap between plates (h)

After characterizing the shear stress produced by Marangoni flows in the microcompartment, the mechanism of mechanical actuation was also demonstrated in the bulk material using shear rheology to induce the gelation of colloidal suspensions. In this experiment, a colloidal suspension of nanotubes was deposited in a setup consisting of a parallel plate geometry setting, with a

transparent lower plate (Figure 9). The transparent plate allowed a camera to record the sample from below while increasing the angular velocity (ω) of the upper plate. Once the angular velocity exceeded 5 rad/s, macroscopic flocculation of the suspensions began at the outer rim of the sample, and spread radially toward the centre of the plate as the velocity continued to increase. This behaviour is in good agreement with a mechanism of mechanical actuation of fibre bundling since the effective shear rate ($\dot{\gamma}$), and therefore the shear stress, varies across a parallel plate setting with the rotation of the plate at the edges exerting greater mechanical stress respect to the centre of the rotor. (eq.3, eq.4). The formation of fibre bundles in sheared samples was also confirmed by cross-polarized optical microscopy (Figure 9a-b). Indeed, the bundling process induces the anisotropic alignment of fibres, resulting in the presence of large domains of birefringent material in flocculated samples.

Micro and bulk rheology experiments demonstrated that the shear stress generated by internal Marangoni flows is fundamental to the hydrogel formation mechanism in motile droplets. Future work will explore whether confinement effects in the microcompartment can accelerate the phase transition. Preliminary results indicate that flocculation in bulk rheology experiments occurs at much higher shear stress (τ~720 mPa). However, a quantitative comparison of the efficiency of the mechanical actuation process in shear rheology and Marangoni flows requires more in-depth investigation of the shear stress distribution across the samples in bulk experiments.

5.3. Conclusions

In this study, we showed how the integration of mechanically responsive fibre networks with Marangoni flow enables the development a novel feedback mechanism, resulting in an accelerating motile behaviour in active water droplets. We demonstrated that the acceleration of motion originates from a sol-gel transition actuated in the aqueous compartment, with consequent formation of Janus droplets. This symmetry-breaking effect reverts the influence of the hydrogelator on motility; in fact, prior to phase transition, colloidal suspensions delay the onset of Marangoni flows because the homogeneous distribution of supramolecular polymer at the interface disrupts the micellar solubilisation. The hypothesized mechanism of mechanical actuation of supramolecular bundling was supported by micro- and bulk rheology measurements. Specifically, the shear stress produced by the internal Marangoni flow was quantified using particle

tracking velocimetry, while shear rheology experiments demonstrated that the phase transition in macroscopic colloidal suspensions can occur under similar mechanical stimulation.

The initiation of a sustained instability, especially in heterogenous systems, is an inherently stochastic event and the role of initial mechanical fluctuations in activating the cascade mechanism remains an aspect of particular interest and is worth future investigation. For instance, if the motion of neighbouring droplets would prove to be a sufficient stimulus to trigger feedback amplification, this research could pave the way to new communication strategies based on the transmission of mechanical signals between compartments and collective motile behaviour.

5.4. Acknowledgements

I gratefully acknowledge B. Marincioni and V. B. Verduijn for their contribution to this Chapter.

L.C.P., B.M. and V.B.V. contributed equally to this work. L.C.P. synthesized the VsAzo monomer. B.M. and L.C.P performed the experiments for motility assay and microrheology, L.C.P analysed the data. B.M. performed the micellar solubilisation and the pendant droplet experiments and analysed the data. L.C.P. and V.B.V. performed the fluorophore leakage assay and L.C.P analysed the data. B.M. performed the PTV experiments and V.B.V. analysed the data. L.C.P and V.B.V. performed the bulk rheology experiments and V.B.V. analysed the data. L.C.P. wrote the first draft of the manuscript. All authors contributed to the discussion, editing and revision of this chapter.

I wish to thank N. Katsonis for supervising this research along with T. Kudernac.

5.5. Experimental Section

5.5.1 Materials

Chemicals and solvents were obtained from commercial sources and used without further purification unless stated otherwise.

The synthesis of the VsAzo monomer was previously described in Chapter 4

General procedure for the preparation of the colloidal suspensions of VsAzo nanofibres.

VsAzo (5mg, 1 eq.) was transferred in a vial and dissolved in acetonitrile. Subsequently, the solution was dried under nitrogen at room temperature. The resulting thin film of VsAzo (5mg, 1 eq.) was re-dissolved in 650 µL of MilliQ water ([VsAzo]=5mM) by vortexing on a low setting until optically clear, and stored overnight at room temperature in the dark. The next day, the resulting solution of VsAzo nanotubes was diluted with a concentrated KCl solution ([KCl=4M]) to obtain the final concentration of [VsAzo]=3.5 mM and [KCl]=1.2M.

General procedure for the preparation of the active emulsions by mechanical agitation

A solution of dispersant was prepared by dissolving monoolain ([MO]=25mM) in squalane oil. After adding 2µL of colloidal suspension of VsAzo nanotubes to 200 µL solution of dispersant, the biphasic mixture was emulsified by vortexing on at high setting for 2 seconds. The final volume of the dispersed phase was adjusted by transferring 3 µL of the resulting emulsion along with 60 µL of dispersant solution into a silicon chamber (9 mm diameter, 1 mm width) mounted on a microscopy glass slide.

General procedure for the preparation of the active emulsions by injection

A solution of dispersant, prepared by dissolving monoolain ([MO]=25mM) in squalane oil, was transferred in a silicon chamber (9 mm diameter, 1 mm width) mounted on a microscopy glass slide. Next, the colloidal suspensions of VsAzo nanotubes were directly injected in the oil dispersant using a micropipette connected to a syringe pump. The micropipette was fabricated from a glass capillary pulled with a flaming micropipette puller P-1000 (Sutter Instruments) and cut with a Narishige MF-900 micro forge.

5.5.2 Methods

Wide field and fluorescence microscopy:

For the motility assay and micellar solubilization – Time-lapses of the motile droplets were recorded with an Eclipse Ti2 inverted microscope equipped with a LED lamphouse (Ti2-D-LHLED) for diascopic illumination. The droplets volume and the average speed values of motile droplets were measured with the software NIS Elements, while trajectories and the instant speed values were obtained by analyzing the videos with the software Fiji(ImageJ) using TrackMate.[28]

For particle tracking velocimetry – The colloidal suspensions of VsAzo nanofibres were loaded with amine coated polystyrene microspheres (d=1μm) labelled with fluorescent red (λ_{ex}=505-585 nm, λ_{em}=550-645nm). Time-lapses of the trackers in motile and non-motile droplets were recorded with a Nikon Eclipse LV100N POL microscope equipped with a 12V-50W halogen lamp for diascopic illumination as well as a 120V-130W C-LHGFI HG lamp mounted on intenselight C-HGFI fibre illumination system for episcopic illumination. For imaging the trackers the microscope was also equipped with an excitation wavelength filter (λ_{ex}=510-560 nm), and a band pass filter (λ_{ex}=580 nm). The microscopy data were processed with a combination of NIS Elements software, for tracking the motion of the droplets, and the python processing package TrackPy,[29] for tracking the motion of fluorescent microspheres.

For fluorophore leakage assay – The colloidal suspensions of VsAzo nanofibres were loaded with 2μL of concentrated fluorescein solution ([fluorescein]~1mM; λ_{ex}=498nm, λ_{em}=517nm). Time-lapses were acquired using a Zeiss Axio Observer Z1/7 wide-field microscope equipped with a EC Plan-Neofluar 20x 0.5 NA Air Objective. For each slice in the time-lapse the microscope acquired one brightfield image using a TL Halogen lamp at 1.6V and an exposure time of 50ms, as well as a fluorescence image using a 505 nm LED module at 100% intensity; equipped with a 488-512 nm excitation wavelength filter, and a 520-550 nm emission wavelength filter at an exposure time of 1s. For the fluorophore leakage assay the microscopy data were processed using the software Fiji(ImageJ).

Interfacial tension measurements

The interfacial tension values in squalane were determined using an optical tensiometer Theta Lite, BiolinScientific with the pendant drop method. At the high surfactant concentrations used for the motility assay, the interfacial tension

was below the detection limit. Therefore, the surfactant concentrations were reduced for the pendant drop experiment to [VsAzo] = 0.5 mM and [MO] = 3 mM.

Shear flow rheology

Shear flow rheology was performed using a DHR-3 Rheometer from TA Instruments equipped with a 40mm parallel plate geometry, optical plate accessory for videography, and Upper-Heated Plate for temperature control. After loading the sample ([VsAzo]=0.6mM, [KCl]=1.2M at a gap height of 300μm, the stage was equilibrated to 25°C. Subsequently, a linear flow ramp was performed from 0.15 rad/s to 100 rad/s over the course of 4000s while recording a video from below. Thereafter, the rheology data and the video were analyzed and overlaid using python and the software FFmpeg to determine the onset of shear flow induced gelation.

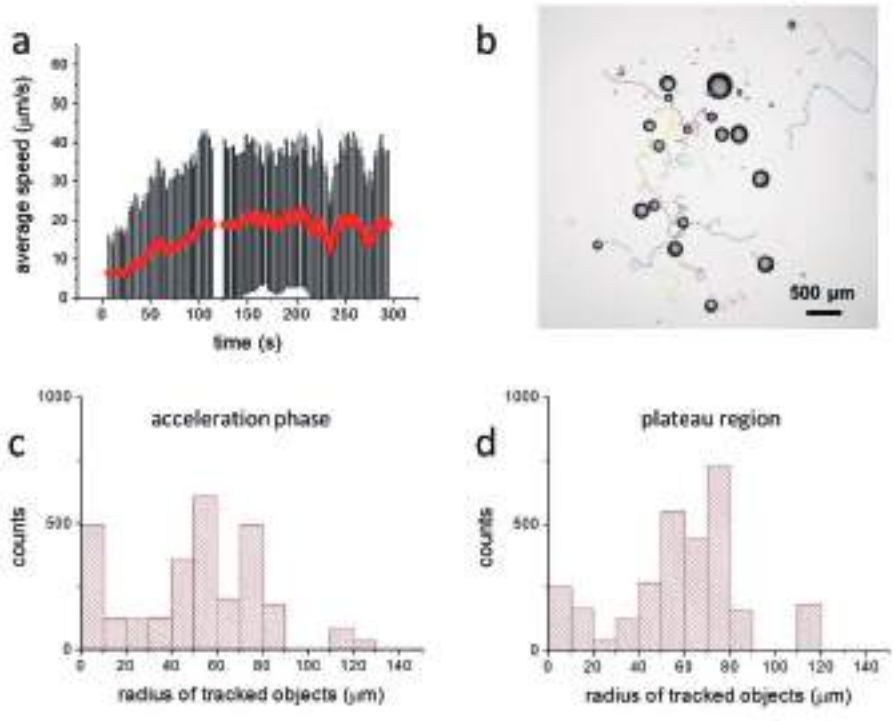

*Supplementary Figure 1: Droplet motility assay. (**a**) Moving average of instant speed values (Δt=5s) with standard deviation. (**b**) Motile droplets analysed with Trackmate, overlay of the tracks identified during the acceleration phase. (**c**)(**d**) Size distributions of the droplets recognised by Trackmate during acceleration and plateau phases.*

5.6. References

5.6.1 Front page illustration (Chapter 5)

Goodsell, D. S. *HIV maturation, HIV viral life cycle, illustration*. (Wellcome collection).

5.6.2 References (Chapter 5)

1 Wang, L. *et al.* Biomimicry of Cellular Motility and Communication Based on Synthetic Soft-Architectures. *Small* **16**, e1907680, doi:10.1002/smll.201907680 (2020).

2 Bashirzadeh, Y. & Liu, A. P. Encapsulation of the cytoskeleton: towards mimicking the mechanics of a cell. *Soft Matter* **15**, 8425-8436, doi:10.1039/c9sm01669d (2019).

3 Burla, F., Mulla, Y., Vos, B. E., Aufderhorst-Roberts, A. & Koenderink, G. H. From mechanical resilience to active material properties in biopolymer networks. *Nature Reviews Physics* **1**, 249-263, doi:10.1038/s42254-019-0036-4 (2019).

4 Tu, Y. *et al.* Mimicking the Cell: Bio-Inspired Functions of Supramolecular Assemblies. *Chem Rev* **116**, 2023-2078, doi:10.1021/acs.chemrev.5b00344 (2016).

5 Mohan, K., Luo, T., Robinson, D. N. & Iglesias, P. A. Cell shape regulation through mechanosensory feedback control. *J R Soc Interface* **12**, 20150512, doi:10.1098/rsif.2015.0512 (2015).

6 Stachowiak, M. R. *et al.* A mechanical-biochemical feedback loop regulates remodeling in the actin cytoskeleton. *Proc Natl Acad Sci U S A* **111**, 17528-17533, doi:10.1073/pnas.1417686111 (2014).

7 Zhang, H. *et al.* Feedback-controlled hydrogels with homeostatic oscillations and dissipative signal transduction. *Nat Nanotechnol* **17**, 1303-1310, doi:10.1038/s41565-022-01241-x (2022).

8 Insua, I. & Montenegro, J. Synthetic Supramolecular Systems in Life-like Materials and Protocell Models. *Chem* **6**, 1652-1682, doi:10.1016/j.chempr.2020.06.005 (2020).

9 Azevedo, H. S., Perry, S. L., Korevaar, P. A. & Das, D. Complexity emerges from chemistry. *Nat Chem* **12**, 793-794, doi:10.1038/s41557-020-0537-x (2020).

10 Booth, R., Insua, I., Ahmed, S., Rioboo, A. & Montenegro, J. Supramolecular fibrillation of peptide amphiphiles induces environmental responses in aqueous droplets. *Nat Commun* **12**, 6421, doi:10.1038/s41467-021-26681-2 (2021).

11 Babu, D. *et al.* Acceleration of lipid reproduction by emergence of microscopic motion. *Nat Commun* **12**, 2959, doi:10.1038/s41467-021-23022-1 (2021).

12 Fu, M. *et al.* Mechanochemical feedback loop drives persistent motion of liposomes. *Nature Physics* **19**, 1211-1218, doi:10.1038/s41567-023-02058-8 (2023).

13 Marincioni, B., Nakashima, K. K. & Katsonis, N. Motility of microscopic swimmers as protocells. *Chem* **9**, 3030-3044, doi:10.1016/j.chempr.2023.10.007 (2023).

14 Dufrene, Y. F. & Persat, A. Mechanomicrobiology: how bacteria sense and respond to forces. *Nat Rev Microbiol* **18**, 227-240, doi:10.1038/s41579-019-0314-2 (2020).
15 Sanchez, T., Chen, D. T., DeCamp, S. J., Heymann, M. & Dogic, Z. Spontaneous motion in hierarchically assembled active matter. *Nature* **491**, 431-434, doi:10.1038/nature11591 (2012).
16 Woodhouse, F. G. & Goldstein, R. E. Spontaneous circulation of confined active suspensions. *Phys Rev Lett* **109**, 168105, doi:10.1103/PhysRevLett.109.168105 (2012).
17 Izri, Z., van der Linden, M. N., Michelin, S. & Dauchot, O. Self-propulsion of pure water droplets by spontaneous Marangoni-stress-driven motion. *Phys Rev Lett* **113**, 248302, doi:10.1103/PhysRevLett.113.248302 (2014).
18 Xiu, F., Knežević, A., Huskens, J. & Kudernac, T. Interplay of Depletion Forces and Biomolecular Recognition in the Hierarchical Assembly of Supramolecular Tubes. *Small* **19**, doi:10.1002/smll.202207098 (2023).
19 Picu, R. C. & Sengab, A. Structural evolution and stability of non-crosslinked fiber networks with inter-fiber adhesion. *Soft Matter* **14**, 2254-2266, doi:10.1039/c7sm02555f (2018).
20 Tanaka, H. Viscoelastic phase separation. *Journal of Physics: Condensed Matter* **12**, R207-R264, doi:10.1088/0953-8984/12/15/201 (2000).
21 Xu, D., Hawk, J. L., Loveless, D. M., Jeon, S. L. & Craig, S. L. Mechanism of Shear Thickening in Reversibly Cross-linked Supramolecular Polymer Networks. *Macromolecules* **43**, 3556-3565, doi:10.1021/ma100093b (2010).
22 Yang, Q.-J., Mao, Q. & Cao, W. Numerical simulation of the Marangoni flow on mass transfer from single droplet with different Reynolds numbers. *Colloids and Surfaces A: Physicochemical and Engineering Aspects* **639**, doi:10.1016/j.colsurfa.2022.128385 (2022).
23 Herminghaus, S. *et al.* Interfacial mechanisms in active emulsions. *Soft Matter* **10**, 7008-7022, doi:10.1039/c4sm00550c (2014).
24 Dwivedi, P., Shrivastava, A., Pillai, D., Tiwari, N. & Mangal, R. Deforming active droplets in viscoelastic solutions. *Soft Matter* **19**, 3783-3793, doi:10.1039/d3sm00228d (2023).
25 Mao, Z.-S. & Chen, J. Numerical simulation of the Marangoni effect on mass transfer to single slowly moving drops in the liquid–liquid system. *Chemical Engineering Science* **59**, 1815-1828, doi:10.1016/j.ces.2004.01.035 (2004).
26 Purcell, E. M. in *Physics and our world: reissue of the proceedings of a symposium in honor of Victor F Weisskopf.* 47-67 (World Scientific).
27 Gande, V. V. *et al.* Engineering advancements in microfluidic systems for enhanced mixing at low Reynolds numbers. *Biomicrofluidics* **18** (2024).
28 Ershov, D. *et al.* TrackMate 7: integrating state-of-the-art segmentation algorithms into tracking pipelines. *Nature methods* **19**, 829-832 (2022).
29 Allan, D. B., Caswell, T., Keim, N. C., van der Wel, C. M., & Verweij, R. W. (Zenodo, 2024).

Sm

Summary

Biopolymerization motors are a class of cytoskeletal proteins that can convert chemical energy into useful mechanical work by using self-assembly to mediate the energy transduction process. One of the key challenges in replicating the function of such biological machinery, which operates in a fluid environment and at a scale dominated by Brownian motion, is to transfer the intrinsic directionality embedded in supramolecular architectures during the process of chemo-mechanical transduction. The main strategy explored in this thesis aims to differentiate the reactivity and dynamics of building blocks based on their supramolecular structure by using hierarchically structured materials with increased anisotropic properties compared to traditional supramolecular polymers. The central theme in this dissertation is the study of how self-assembly can influence chemical reactivity, photophysical, and mechanochemical properties of monomers.

Chapter 1

In the introductory chapter, we present a detailed description of the operational cycle in biopolymerization motors, with a specific focus on the main mechanistic models used to explain how the energy transduction process is mediated by self-assembly in microtubules and actin polymerization motors. In this review we wanted to highlight the central role of force spectroscopy techniques in biophysical studies, which have led to our current understanding of Brownian ratcheting, biased diffusion, and conformational wave models. The last section is dedicated to the analysis of the key steps toward reproducing the function of biopolymerization motors, reviewing recent advancements in synthetic systems that exhibit fueled processive behavior, nucleation strategies, and capabilities for processing mechanical work. Along these requirements we introduced the need to develop a relationship between supramolecular structure and monomer activity. In this context of research, we identified the potential of hierarchically structured materials with anisotropic properties to transfer directionality from the supramolecular structure to the mechanism of mechanical force exertion.

Chapter 2

In Chapter 2, we introduced a synthetic system based on a V-shaped amphiphile, whose self-assembly into micro-crystalline fibres is controlled by a coumarin-based pH switch embedded in the aromatic scaffold of the monomer. After a spectroscopic investigation of the pH actuation range and a structural characterization of the anisotropic material formed by the hierarchical self-assembly of the amphiphile, we explored the influence of the assembly state on the reactivity of monomers. The disassembly of these fibres in aqueous base occurs via a mechanism of anisotropic etching, with crystal facets at the edge of microfibers displaying faster rate of coumarin hydrolysis respect to the rest of the crystal interface. Microscopy and X-ray scattering experiments have demonstrated that the molecular orientation of the amphiphile within the lattice determines the relationship between fiber morphology and the directionality of its disassembly. The process of anisotropic etching will be exploited in Chapter 4 to transport microscopic objects adsorbed on the surface of the microfibers with a force exertion mechanism based on biased diffusion.

Chapter 3

In Chapter 3, we explore the effects of supramolecular confinement on the mechanism of excited state proton transfer (ESPT) of a novel fluorescent probe. The design of this probe includes a photoacidic phenolic group and a basic imidazole site, placed at distal positions. Spectroscopic titrations of both the ground and excited states indicated that in the ESPT mechanism the phenolic proton is transferred to water without the participation of the basic acceptor site. In the presence of γ-cyclodextrin, the fluorescent probe forms an inclusion complex that, upon supramolecular polymerization, leads to the formation of nanotubes. Changes in the photoluminescence of the probe, along with solvent isotope effects, suggested that within the cavities of the cyclodextrin nanotubes, the ESPT process occurs intermolecularly between phenol and imidazole. This mechanism was supported by a detailed characterization of the assembly process, which evidenced the formation of a guest pair capable of pre-organizing the proton transfer between the proton donor and acceptor sites of two neighboring probes. The mechanistic transition upon supramolecular confinement is also reflected in the photophysical properties of the material, resulting from the hierarchical organization of nanotubes into larger crystalline domains. The conclusions from this chapter show that self-assembly can direct chemical reactivity through pre-organization effects, even in a fundamental reaction like proton transfer.

Chapter 4

This technical Chapter explores the application of force spectroscopy techniques for studying mechanical transduction in hierarchically structured materials. The Chapter is divided into three projects based on different synthetic systems.

In the first project, the anisotropic etching of microcrystalline fibers, discussed in Chapter 2, was used to exert pulling forces on microscopic cargo multivalently bound to the surface of the crystals. In this subchapter, optical tweezers were employed for quantitative analysis of mechanical force produced by the disassembling fibres. Along with structural characterization and reactivity studies in Chapter 2, this comprehensive work details how the biased diffusion mechanism originates from material anisotropy. The study highlights how fiber morphology controls cargo diffusion on the crystal surface via frictional and adhesive forces.

In the second project we developed a templating strategy to orient supramolecular polymerization on a surface, with the aim of adapting the self-assembling system introduced in Chapter 3 for AFM measurements of pushing forces. While force measurements remain a future goal, this subchapter addresses the challenge of controlling the spatial growth of supramolecular structures, an essential requirement for quantitative measures of mechanical work produced by Brownian ratcheting. Using AFM imaging combined with X-ray scattering and diffraction, we demonstrated the effectiveness of heteroepitaxy in orienting the growth of crystallites formed by hierarchical assembly of cyclodextrin nanotubes. This approach for directing supramolecular polymerization from the surface towards the AFM probe paves the way for a mechanistic investigation of the mechanical transduction process in assembling synthetic systems with AFM force spectroscopy.

In the last section, we investigated the mechanism of plastic deformation of a synthetic hydrogel formed upon hierarchical assembly of third monomer with amphiphilic design. Using optical tweezers for micromanipulation, force spectroscopy, and confocal imaging, we showed how nanofiber bundling enables the mesh to adapt under tensile forces, resembling collagen network plasticity. The force spectroscopy data in this microrheology study confirmed a mechanism of mechanical energy dissipation based on interfiber sliding. This synthetic system will also be studied in Chapter 5 to explore the mechano-chemistry of this hydrogel in motile microcompartments.

Chapter 5

In Chapter 5, we explored a novel mechano-chemical feedback mechanism resulting from the compartmentalization of a hydrogelator in motile water droplets. In this study we found that the internal Marangoni flows propelling the droplets exacerbate nanofiber bundling and induce a sol-gel transition, leading to internal phase separation within the aqueous compartment. The formation of these Janus droplets results in accelerated motile behavior due to symmetry-breaking effects, which enhance the hydrodynamic instability fueling the Marangoni process. Insights into the acceleration mechanism were obtained by studying the micellar solubilization process in the presence of hydrogelator and its effects on interfacial tension. The role of mechanical force in promoting gelation was confirmed through bulk and microrheology experiments, using particle tracking velocimetry to estimate the shear stress produced by internal Marangoni flows. This chapter demonstrates how integrating complex biomimetic systems, such as mechanically active supramolecular materials and motile compartments, can lead to synergistic effects and complex functional responses.

Sv

Samenvatting

Biopolymerisatiemotoren zijn een klasse van cytoskeletale eiwitten die chemische energie kunnen omzetten in nuttig mechanische arbeid door zelforganisatie te gebruiken om het energietransductieproces te faciliteren. Een van de grootste uitdagingen bij het repliceren van de functie van dergelijke biologische machines, die in een vloeistof omgeving en op een schaal gedomineerd door Brownse beweging werken, is om de intrinsieke asymmetrie die is ingebed in supramoleculaire architecturen over te dragen tijdens het proces van chemomechanische transductie. De belangrijkste strategie die in dit proefschrift wordt onderzocht, is gericht op het differentiëren van de reactiviteit en dynamiek van bouwstenen op basis van hun supramoleculaire structuur door gebruik te maken van hiërarchisch gestructureerde materialen met meer anisotrope eigenschappen in vergelijking met traditionele supramoleculaire polymeren. Het centrale thema van dit proefschrift is de studie van hoe zelforganisatie chemische reactiviteit, fotofysische en mechanochemische eigenschappen van monomeren kan beïnvloeden.

Hoofdstuk 1

In het inleidende hoofdstuk presenteren we een gedetailleerde beschrijving van de operationele cyclus in biopolymerisatiemotoren, met speciale aandacht voor de belangrijkste mechanistische modellen die worden gebruikt om te verklaren hoe het energietransductieproces wordt gefaciliteerd door zelforganisatie in microtubuli en actine-polymerisatiemotoren. In deze review benadrukken we de centrale rol van krachtspectroscopietechnieken in biofysisch onderzoek , die hebben geleid tot ons huidige begrip van Brownse ratcheting, georiënteerde diffusie en conformationele golfmodellen. Het laatste deel is gewijd aan de analyse van de belangrijkste stappen om de functie van biopolymerisatiemotoren te reproduceren, waarbij recente vooruitgangen worden besproken in synthetische systemen die brandstofgedreven procesmatig gedrag, nucleatiestrategieën en mogelijkheden voor het uitvoeren van mechanische arbeid vertonen. Met behulp

van deze vereisten hebben we de noodzaak geïntroduceerd om een verband te ontwikkelen tussen supramoleculaire structuur en monomeeractiviteit. In decontext van dit onderzoek hebben we het potentieel van hiërarchisch gestructureerde materialen met anisotrope eigenschappen onderzocht om gerichtheid over te dragen van de supramoleculaire structuur naar het mechanisme van mechanische krachtsuitoefening.

Hoofdstuk 2

In Hoofdstuk 2 introduceren we een synthetisch systeem gebaseerd op een V-vormig amfifiel molecuul, waarvan de zelforganisatie in micro-kristallijne vezels wordt gecontroleerd door een coumarine-gebaseerde pH-schakelaar ingebed in het aromatische skelet van het monomeer. Na een spectroscopisch onderzoek van het pH-werkingsbereik en een structurele karakterisering van het anisotrope materiaal dat wordt gevormd door de hiërarchische zelforganisatie van het amfifiele molecuul, onderzoeken we de invloed van de organisatietoestand op de reactiviteit van monomeren. Het uiteenvallen van deze vezels in basisch water vindt plaats via een mechanisme van anisotrope etsing, waarbij kristalfacetten aan de rand van microvezels een snellere hydrolyse van coumarine vertonen in vergelijking met de rest van de kristaloppervlak. Microscopie- en röntgenkristallografieexperimenten hebben aangetoond dat de moleculaire oriëntatie van het amfifiel binnen het rooster de relatie bepaalt tussen vezelmorfologie en de gerichtheid van de desintegratie ervan. Het proces van anisotrope etsing zal in Hoofdstuk 4 worden benut om microscopische objecten die aan het oppervlak van de microvezels zijn geadsorbeerd te transporteren met een mechanisme gebaseerd op georiënteerde diffusie.

Hoofdstuk 3

In Hoofdstuk 3 onderzoeken we de effecten van supramoleculair opsluiting op het mechanisme van protonoverdracht in aangeslagen toestand (ESPT) van een nieuwe fluorescente probe. De probe bestaat uit een fotoacidische fenolgroep en een basische imidazoolsite die op afstand van elkaar worden gehouden. Spectroscopische titraties van zowel de grondtoestand als de aangeslagen toestand gaven aan dat in het ESPT-mechanisme de fenolproton wordt overgedragen aan water zonder deelname van de basische acceptorsite. In aanwezigheid van γ-cyclodextrine vormt de fluorescente probe een inclusiecomplex dat, bij supramoleculaire polymerisatie, leidt tot de vorming van nanotubes. Veranderingen in de fotoluminescentie van de probe, samen met isotoopeffecten van het oplosmiddel, suggereren dat het ESPT-proces in de holtes van de cyclodextrine-nanotubes intermoleculair plaatsvindt tussen fenol en imidazool. Dit mechanisme wordt ondersteund door een gedetailleerde karakterisering van

het organisatieproces, die de vorming van een gastpaar aantoont dat in staat is de protonoverdracht tussen de protondonor- en acceptorsites van twee aangrenzende probes te pre-organiseren. De mechanistische overgang bij supramoleculaire opsluiting wordt ook weerspiegeld in de fotofysische eigenschappen van het materiaal, resulterend uit de hiërarchische organisatie van nanotubes in grotere kristallijne domeinen. De conclusies uit dit hoofdstuk tonen aan dat zelforganisatie chemische reactiviteit kan sturen door pre-organisatie-effecten, zelfs in een fundamentele reactie zoals protonoverdracht.

Hoofdstuk 4

Dit technische hoofdstuk onderzoekt de toepassing van krachtspectroscopietechnieken voor het bestuderen van mechanische transductie in hiërarchisch gestructureerde materialen. Het hoofdstuk is onderverdeeld in drie projecten op basis van verschillende synthetische systemen.

In het eerste project wordt de anisotrope etsing van microkristallijne vezels, besproken in Hoofdstuk 2, gebruikt om trekkrachten uit te oefenen op microscopische ladingen die multivalent gebonden zijn aan het oppervlak van de kristallen. In dit subhoofdstuk worden optische pincetten gebruikt voor kwantitatieve analyse van de mechanische kracht die door de desintegrerende vezels wordt geproduceerd. Samen met structurele karakterisering en reactiviteitsstudies in Hoofdstuk 2, beschrijft dit uitgebreide werk hoe het georiënteerde diffusiemechanisme ontstaat uit materiaalanisotropie. De studie benadrukt hoe vezelmorfologie de ladingdiffusie op het kristaloppervlak reguleert via wrijvings- en adhesiekrachten.

In het tweede project ontwikkellen we een sjabloonvormingsstrategie om supramoleculaire polymerisatie op een oppervlak te oriënteren, met als doel het aanpassen van het zelforganiserende systeem geïntroduceerd in Hoofdstuk 3 voor AFM-metingen van duwkrachten. Hoewel krachtmetingen een toekomstig doel blijven, beschrijft dit subhoofdstuk de uitdaging van het sturen van de ruimtelijke groei van supramoleculaire structuren, een essentiële vereiste voor kwantitatieve metingen van mechanisch werk geproduceerd door Brownse ratcheting. Met behulp van AFM-beelden in combinatie met röntgenkristallografie en -diffractie, demonstreren we de effectiviteit van hetero-epitaxie bij het oriënteren van de groei van kristallieten gevormd door hiërarchische organisatie van cyclodextrine-nanotubes. Deze benadering voor het oriënteren van supramoleculaire polymerisatie van het oppervlak naar de AFM-probe opent de weg voor een mechanistisch onderzoek van het mechanische transductieproces in zelforganiserende synthetische systemen met AFM-krachtspectroscopie.

In het laatste deel onderzoeken we het mechanisme van plastische vervorming van een synthetische hydrogel gevormd door hiërarchische organisatie van een derde monomeer met amfifiel ontwerp. Met behulp van optische pincetten voor micromanipulatie, krachtspectroscopie en confocale fotografie tonen we aan hoe bundeling van nanovezels het net in staat stelt om zich aan te passen onder trekkrachten, wat lijkt op de plasticiteit van collageennetwerken. De informatie verkregen met krachtspectroscopie in deze microrheologiestudie bevestigt een mechanisme van mechanische energiedissipatie op basis van interfiber-glijden. Dit synthetische systeem zal ook worden bestudeerd in Hoofdstuk 5 om de mechanochemie van deze hydrogel in beweegbare microcompartimenten te verkennen.

Hoofdstuk 5

In Hoofdstuk 5 onderzoeken we een nieuw mechanochemisch feedbackmechanisme dat voortkomt uit de compartimentalisatie van een hydrogelator in beweegbare waterdruppels. In deze studie ontdekten we dat de interne Marangoni-stromen die de druppels aandrijven, de bundeling van nanovezels versterken en een sol-gel overgang induceren, wat leidt tot interne fasenscheiding binnen het watercompartiment. De vorming van deze Janusdruppels resulteert in versneld beweging door symmetriebrekende effecten, die de hydrodynamische instabiliteit die het Marangoni-proces aandrijft, versterken. Inzichten in het versnellingsmechanisme worden verkregen door het bestuderen van de micellaire oplosbaarheidsoptimalisatie in aanwezigheid van de hydrogelator en de effecten ervan op de oppervlakte spanning. De rol van mechanische kracht bij het bevorderen van gellering wordt bevestigd door bulk- en microrheologie-experimenten, waarbij de deeltjesvolgvelocimetrie wordt gebruikt om de schuifspanning te schatten die door interne Marangoni-stromen wordt geproduceerd. Dit hoofdstuk laat zien hoe de integratie van complexe biomimetische systemen, zoals mechanisch actieve supramoleculaire materialen en beweegbare compartimenten, kan leiden tot synergetische effecten en complexe functionele responsen.

652563-L-bw-Pataleone
Processed on: 5-9-2024

Ps

Popular science summary

Motors are machines used to convert energy. If you are thinking about the engine of your car, this is a good starting point. Without any prior knowledge of thermodynamics everyone knows what an engine does: it uses fuel (chemical energy) to drive you home (mechanical work). Far more complex engines are present in cells but their task is fairly similar. These molecular machines can transform the chemical potential stored in our food into the energy for a workout. The most obvious difference between combustion engines and molecular machines is of course their dimensional scale. The first challenge to be faced when operating machines in the microscopic world is the Brownian storm. As suggested by its name the Brownian storm describes a very chaotic environment where molecules fly in any direction colliding and randomly exchanging energy and trajectories. To picture this storm let's imagine that the wind is blowing over 300 km/h. Operating molecular machines at the nanoscale is like driving your car in such a hurricane. Even if you could start the engine and control some molecular movements, for example the rotation of the wheels, it would be impossible to maneuver the vehicle.

A possible solution for driving through the Brownian storm consists in using more motors working together, as if they were powering a large cruise ship, large enough to withstand this hurricane. However, assembling a larger machine from smaller components comes with an additional problem: how do we coordinate the movement of these motors? Answering this question requires a brief explanation of what we mean by "anisotropy" and, since we already moved into analogies with ships and sailing, we will define this concept using a metaphor on canoeing. Let's imagine that a sailing club is having a party on a boat. Despite there is a lot of movement on the deck the boat doesn't move significantly. In fact, at this "Brownian party" each movement is cancelled out: for every crew member splashing port there is another one splashing starboard (Figure 1a). However, when the party is over, all the members of the sailing club line up and start rowing in one direction. The same amount of movement that was previously

652563-L-bw-Pataleone
Processed on: 5-9-2024

*Figure 1: (**a**) Members of the sailing club having a "Brownian party" on a boat. (**b**) When sailors organize in an "anisotropic structure", their individual contributions combine to propel the boat.*

dissipated by the chaotic environment is now effectively transferred to the motion of the boat (Figure 1b). This directionality emerging from organization is what we mean by anisotropy.

The last concepts you need to grasp to understand the topic of this dissertation are those of polymerization and depolymerization motor. It is worth mentioning that in the microscopic world there are different types of motors. Recalling our previous analogy with the sailing club the process of lining up resembles what happens during a polymerization. Individuals (molecules) assemble together into a larger structure of a line (polymer). What is special about a polymerization motor is that the energy comes, rather than individual movements (rowing, splashing), from the process of assembling the line itself. How is this possible? When a crowd assembles very fast the front line can exert quite some pressure on a barricade. Think about a concert or a ticket sale. Who works in crowd control knows how much energy is required to keep the doors closed until the last moment. When the space becomes packed, somehow there is always a person who will manage to squeeze in and grow the line a bit further. Afterall, individuals and molecules do not behave so differently.

That is in short what it means exploring "The role of anisotropy in artificial polymerization motors". In the conclusions of this section we must answer one last (difficult) question: why do we want to study such a thing? The easiest way to address this question is pointing at the possible applications that may have an impact on our society. Surely, studying these mechanisms may eventually lead to advancements in soft nanorobotics, innovative drug delivery systems, or even

energy storage solutions. However, it is important to acknowledge that this work is primarily fundamental research, which means that its main drive is to expand our scientific knowledge. In my opinion, technology is something that naturally develops at a later stage of research, sometimes even with unexpected outcomes. For this reason it is very important to continue, alongside more application-oriented studies, to explore what at the moment is just a matter of genuine scientific curiosity. Who knows what the future has in store.

Acknowledgements

I wish to thank L. D'Ippolito for the art work represented in Figure 1.

Ack

Acknowledgements

A wise colleague once told me that for their experiments, PhD students typically have one good day each month. That's how often things work. I can't say if that average is accurate, but I've found this journey to be quite challenging. Fortunately, I was lucky to have many supportive people around me during the times when chemistry didn't cooperate, and I wish to extend my thanks to all of them.

I would like to start the acknowledgments by thanking my supervisor, **Prof. Tibor Kudernac**. You have always been open, positive, and supportive of new ideas, and you gave me almost unlimited freedom to express my creativity and curiosity during these years of work together. I am grateful for that. I deeply admire your vision of science, and the humanity you showed in your approach to leadership. It takes a lot of courage to lead a group in a non-conventional way, which I always found progressive and inspiring.

I would also like to express my gratitude to my co-supervisor, **Prof. Wesley Browne**. In addition to being a tremendous support in numerous projects and teaching me everything I know about spectroscopy, you knew how to push me when I needed to walk that extra mile. I will always remember how, after my Erasmus stay in the Netherlands, I was seeking a PhD position to return to Groningen, and you helped me a great deal with that. For all of this, I am eternally grateful.

I am grateful to the members of the assessment committee, **Prof. Ben Feringa**, **Prof. Thomas Hermans**, and **Prof. Clemens Mayer**, for reading this thesis and for their valuable feedback.

I would like to express my gratitude to **Prof. David Goodsell** for creating the beautiful artworks that decorate this thesis and for his generosity in sharing them under an open Creative Commons license (CC-BY-4.0).

I would like to thank **Alexandra Elbakyan** for her courage and dedication in the fight for an open science.

The people I had around at work have become more than colleagues in these last four years, so I wish to call them friends and thank them all for their support, for a laugh during the lunch break, or simply for making me feel welcome from the very first day I moved to this country. I would like to start with the members of my group. **Federico** and **Anamarija**, even though we crossed paths briefly, your advice was precious and encouraged me to start my PhD during the troubled times of the pandemic. Thank you. I want to thank **Nicolas** for being, especially in my first two years, a lasting point of reference. I admire your passion for science and the way you have always cared for the other members of the group. **Qin**, what can I say, you are the sweetest guy in the group. Then there is **Julien**, I think I never saw you upset or frustrated, and I spent three years figuring out how you manage to always approach every trouble with so much perspective. **Baptiste**, heart of a lion, if I could only have three paranymphs, I would have asked you. I only spared you because a lot of people wanted you by their side on the day of their defense, and for a reason, because you are a great friend. **Jacopo**, you are our wild card: you are a great experimentalist who's not afraid of computational work and enjoys solo travel around Latin America. I always found this combination truly remarkable. **Yaroslava**, your calm and maturity are essential components for the balance of our group. I really enjoy working with you, and thank you for teaching me so many things about the surface.

I want to thank my master students, **Ning**, for being simply the best, and **Robert**, for being simply the worst. Robert, you know I like messing with you. I loved working with both of you. Teaching can be a wonderful experience with the right students, and I am aware I was extremely lucky.

I wish to thank my paranymphs, Victor and Thomas. **Victor**, you joined the group when I was halfway through my PhD, and still, I learned immensely from you. You are a smart guy and you know it, but you are also incredibly humble, and this is a rare quality in the scientific community. You can also be quite funny. I came to realize that pretty quickly when I found my desktop trashed one morning for one of your pranks. At the time, I barely knew you, so it was quite a bold move for ice-breaking. Well, thanks for reaching out. **Thomas**, you are capable of incredible things, both genius and on the edge of stupidity, and you definitely know how to make me laugh and cheer me up. For the important things though, you are very serious, and I know we share a lot of common values. To both of you, thank you for accepting to be my paranymphs. I feel honored.

Acknowledgements

I would like to thank **Prof. Nathalie Katsonis** for her scientific input in the projects that we shared, but also for promoting the nice social atmosphere between our groups. I take this chance to thank **Hasnaa**, **Chanikan**, **Manee**, and all the members of the **Katsonis group** for the fun activities we did together. I would also like to thank **Foteini** for our interesting discussions about Σκλαβενίτης and Βασιλόπουλος.

A special thanks goes to **Dr. Alexander Ryabchun**, who always found the time to help me. Besides the countless times you came with a good idea or your expert advice, there are only a few people I enjoy discussing science with as much as you, especially if it is in front of a coffee.

I would like to thank **Dr. Marc Stuart** for introducing me to electron microscopy. I have met a few people with your enthusiasm and passion for transferring their knowledge and experience. Thank you, Marc; your EM course was a blast.

I wish to thank **Dr. Kasia Tych** for trusting an organic chemist sitting behind the optical tweezers. It was a great pleasure to collaborate with you. I have learned immensely from you and your amazing group. In this regard, I would also like to thank **Lyan** for her precious help and for her patience.

I am grateful to **Prof. Giuseppe Portale**, whose expertise was crucial for many projects in this thesis. Thanks to our collaborations, my interest in X-ray scattering techniques has constantly grown.

A special thanks goes to all the members of my cluster. I found that **MOLAN** is an incredible repository of knowledge and skilled people that created a working atmosphere I can only describe as positive, cooperative, and inclusive. In particular, I want to thank **Kristopher**, **Taegeun**, **Isaac**, **Silene**, and **Liliana** for integrating me as a part of their own group. I want to thank **Hugo**, **Anouk**, **Ruben**, **Yanrong**, **Andy**, and all the Brownies for sharing their coffee machine.

Then, I wish to thank **Nol**, **Isa**, **Niels**, **Daniel**, **Maurits**, and **Carlijn**. **Niels** was the first person I met during my Erasmus stay in Groningen. He introduced me to my Dutch friends. This group of people is one of the reasons why I wanted to come back to the Netherlands for my PhD.

I would like to thank my expat friends **Marika**, **Eleonora**, **Gianni**, **Sofia**, **Ilaria**, **Rachael** and **Giorgia**. We worked together; we had so many fun nights between concerts, parties, karaoke, and board games nights. A special thanks goes to Marika and Eleonora. **Marika**, for a lasting friendship that started the very first day I stepped into a research lab, and **Eleonora**, for introducing me to Gianni.

I would like to gratefully acknowledge **Renze**, **Johan**, **Pieter**, **Folkert**, **Jacob**, and all the staff members of our Institute(s) for their incredible skills and constant willingness to help me with countless measurements. Thank you.

Then, I would like to thank my family.

Tia **Denise**, obrigado por acreditar em mim e por todas as maravilhosas experiências que contribuíram a ampliar a minha visão do mundo. Os contos das suas viagens e as que fizemos juntos me ajudaram a chegar até aqui.

I wish to thank my brother, **Pedro**, for the beautiful cover of this dissertation. Even though we chose different paths, we ended up doing something quite similar: building things (at different scales). As you browse through this thesis, you will see that I am not the only one who noticed this analogy. One of the molecules pictured in Chapter 4, fullerene C_{60}, was named after Buckminster Fuller, an architect and great thinker who was not afraid to cross the fields of design, science, and philosophy. I am very proud of you.

Ai miei genitori, grazie per aver sempre incoraggiato la mia curiosità, per avermi spinto a studiare e a crescere, facendolo senza mai impormi nulla, ma con amore e naturalezza. Questo lavoro è frutto dell'educazione che mi avete dato e del vostro immancabile sostegno. La vostra generosità è fonte di ispirazione. Grazie di cuore.

The last and most important person I want to thank is **Beatrice**. I feel you have been my paranymph in the last four years. It is hard to express the extent of your support, your love, and your care, with which you backed me up since day one. You are the person who knows me best and with whom I shared all my joyful moments and all my struggles. We embarked on this journey together, and we will finish it together. Thank you.